

Adaptive computational reduction framework for the
unsteady aerodynamics of lifting surfaces

PhD Thesis

Gaetano Pascarella

FASTT Lab

Mechanical And Aerospace Engineering

University of Strathclyde, Glasgow

June 3, 2021

*To my family I dedicate this work,
to express all my gratitude for their infinite love
so often I take for granted.*

*Alla mia famiglia dedico questo lavoro,
per esprimerle tutta la mia gratitudine per il loro infinito amore
che così spesso do per scontato.*

*“If I have seen further,
it is by standing upon the shoulders of giants. ”*
— Isaac Newton[†]

[†]I would like to thank University of Strathclyde, James Weir Building, for this quote I used to read so many times on my way to the office.

This thesis is the result of the author's original research. It has been composed by the author and has not been previously submitted for examination which has led to the award of a degree.

The copyright of this thesis belongs to the author under the terms of the United Kingdom Copyright Acts as qualified by University of Strathclyde Regulation 3.50. Due acknowledgement must always be made of the use of any material contained in, or derived from, this thesis.

Gaetano Pascarella

June 3, 2021

Abstract

The development and use of Reduced Order Models (ROMs) has attracted lots of attention among the engineering and scientific community in the past decades. Indeed, these models are able to significantly reduce the original complexity of a system, without severely affecting the accuracy. A crucial point to consider when elaborating Reduced Order Models (ROMs) for unsteady (e.g. transient) nonlinear problems in fluid dynamics is the definition of a proper set of dominant features, alias modes or basis functions, that can project the fluid system behaviour in a low-dimensional space without losing essential dynamics. To ensure that this is the case, a quantitative assessment is often necessary to define how well the low-dimensional space is approximating the underlying dynamics. For transient nonlinear flows, elaborating such a ROM, equipped with an efficient and reliable measure of its accuracy, can be a rather challenging task.

To address these aspects, the present work reports a heuristic study of ROM performance, targeted for transient nonlinear fluid flows, when using different low-dimensional spaces, that are defined using different algorithms for the extraction of dominant features and different sorting of dominant features within each algorithm. An analysis is also performed to assess quantitatively such ROMs. In particular, the reliability of an error measure is investigated, namely the residual error, based on a specific discretisation of the initial set of equations of the fluid system, as opposed to an error measure that requires the computation of high-fidelity reference solution to obtain information about the accuracy of the ROM.

The results of these analyses have shown that different linear low-dimensional spaces, identified by a specific set of global basis functions, are able to solve for different dy-

dynamic features with a good degree of accuracy. Moreover the residual error has demonstrated to be a reliable means to assess the relative performance of the various ROMs considered. As a consequence, a Model-Based Adaptive ROM Framework has been introduced. The novel framework combines the strengths of several linear ROMs in a unique monolithic structure by selecting the best low-dimensional space, among a collection of available ones, based on the specific time window where the low-dimensional reconstruction is needed. The term Model-Based refers to the residual error that is used to drive the selection of the basis.

The performance of the Model-Based Adaptive ROM has been finally assessed on a set of test-cases relevant for the aeronautical field, that exhibit transient nonlinear dynamics with advection-diffusion and interaction of flow structures. Namely, a multi-element airfoil, also in a 3D wing-body configuration, an isolated delta wing and three delta wing geometries in a formation flight configuration have been considered. The Adaptive ROM has shown promising capabilities in promoting strong dimensionality reduction (degrees of freedom less than 10-15, compared to the $10^6 - 10^8$ degrees of freedom (DOFs) of a common three dimensional CFD problem), while preserving good accuracy and physical consistency. Such a reduction in terms of DOFs will have a substantial impact on the reduction in computational cost to achieve any low-dimensional solution within the time window where the ROM has been trained. It is worth noting that, being the method data-driven, the overall advantage in terms of computational cost has to be filtered with the upfront cost of generating the training dataset.

The Adaptive ROM has demonstrated to be able to solve more details in terms of flow structures present in the field, which can be of advantage when design and/or flow control problems are addressed.

Acknowledgements

First and foremost I would like to thank my first supervisor, Dr Marco Fossati, who gave me the opportunity to enrol in this challenging PhD project. Thanks for guiding me through a very challenging path, trusting me and accepting all my weaknesses. Many thanks to my second supervisor Dr Gabriel Barrenechea, for all the valuable discussions and support on fundamental aspects of this research project. I would also like to thank the other lecturers in the ACE lab for the many pieces of advice and support that helped me cope with the struggles and stress of my adventure as a PhD.

I am grateful to all the other people in the ACE lab that were there throughout my PhD or for a limited time. You contributed creating a very nice work environment inside and outside the office and made much less painful being far away from home. The list is long but I reckon you know if you are in it.

I am also thankful to all the other people of Glasgow, coming from all over the world, that I crossed the path with. Each one of you brought something new to my life.

I would like now to acknowledge personally some people and places that signed this path the most.

Thanks, Jimmy John, for nicely welcoming me in the ACE department and introducing me to the vibrant Glasgow.

Thanks, Giuseppe and Catarina, for being real friends before being colleagues and co-workers. Our team-building capabilities should be used as an example.

Thanks, Cristian, Lorenzo, Gianluca and Simona. I could not have been any luckier to start this adventure with you.

Thanks, Giacomo, Abhishek, Matteo, Francesco, for the very last good times I had in

Glasgow before the pandemic separated us.

Thanks, Carmelo. Living with you for almost two years has been like being at home. You have been a mentor, a real friend, the one taking care of me when I was in desperate need, before being my flatmate.

Thanks, my lifetime friends, Andrea, Felice, Dominga, Antonio, for always being present, cheering me up and giving me positive energies.

Thanks, my university friends, Fabio, Davide, Ciro. I am so grateful we have always been in touch during these challenging times despite the distance, and I hope it will be the same also in the future.

Thanks, Francesca, mom and dad. You are the infinite source of unconditional love and the driving force that keeps me always on track while trying to pursue my dreams, despite my insecurities. Francesca, you are my guardian angel on earth, the one who understands the most my deepest anxieties, the faithful companion in our struggle to be our better selves.

Thanks, Terra Mia, for always being a safe harbour. So far away, I felt even more how close you are to my heart.

Thanks, Glasgow, for all the people, places, stories to tell, bad and good times that I will always keep in my heart.

Thanks to all the others I did not mention, but have always been close to me, no matter the distance.

Gaetano

*“Al mio cuore malandato
almeno a lui ho messo le ali . . .*

Io, padrone di un bel niente

Neppure di me stesso.”

— Al mio cuore, Poeta Massimo

Contents

List of Figures	viii
List of Tables	xviii
1 Introduction	1
1.1 Motivation	1
1.1.1 Why Reduced Order Models in fluid dynamics	2
1.1.2 Transient nonlinear aerodynamic flows: motivation and challenges	5
1.2 Objective and Research Questions	8
1.3 Outline	11
1.4 Publications arising from this thesis	13
2 Background and Literature Review	15
2.1 Low-dimensional Modeling in fluid dynamics	15
2.2 Prerequisites for dimensionality reduction	17
2.3 Reduced Order Models for fluid analysis and discovering time dynamics	20
2.3.1 Methods based on POD	22
2.3.2 Methods based on DMD	24
2.3.3 Recent developments using machine learning algorithms	26
2.4 Reduced Order Models for fast simulations	28
2.4.1 Intrusive techniques	28
2.4.2 Non-Intrusive techniques	31

3	Assessment of different Basis Extraction Methods	34
3.1	The importance of using different basis functions	34
3.2	Methods for Basis Extraction	35
3.2.1	Proper Orthogonal Decomposition	36
3.2.2	Spectral Proper Orthogonal Decomposition	38
3.2.3	Dynamic Mode Decomposition	39
3.2.4	Recursive Dynamic Mode Decomposition	41
3.3	Non-Intrusive Reconstruction method	42
3.3.1	A note on rank reduction	43
3.4	Comparative Analysis on the accuracy in reconstruction	44
3.4.1	NACA0012 test-case	47
3.4.2	30P30N test-case	50
3.5	Remarks	53
4	Ranking of Modes	56
4.1	Ranking of POD and SPOD modes	57
4.1.1	Numerical Test-Cases	57
4.1.2	Remarks	65
4.2	Ranking of DMD modes	68
4.2.1	DMD Modes classification for reconstruction of early transition in Channel flow	69
4.3	Ranking of RDMD modes	81
5	Model-Based Adaptive Reduced Order Model	82
5.1	Adaptive Reduced Order Models	83
5.1.1	Adaptive Framework based on different sets of basis functions	84
5.2	Estimating the accuracy of a ROM	85
5.2.1	Projection error	86
5.3	Direct error	87
5.4	Residual error	90
5.4.1	A note on Time Integration	93

Contents

5.5	A comparative study of residual and direct error	98
5.5.1	Sensitivity Analysis	99
5.5.2	NACA0012	101
5.5.3	30P30N	107
5.5.4	Remarks	113
5.6	Adaptive Framework equipped with residual error	114
6	Residual Analysis varying the number of modes	117
6.1	Adaptive ROM residual analysis varying the number of modes	118
6.2	NACA0012 test-case	120
6.3	30P30N test-case	122
6.4	Grid sensitivity study	125
6.5	Remarks	130
7	Impulsively started lifting bodies	132
7.1	Unsteady problems typical of aeronautical field	132
7.2	30P30N	134
7.2.1	Volume Analysis	136
7.2.2	Surface Analysis	139
7.3	High-Lift Wing-Body Configuration	140
7.3.1	Volume Analysis	143
7.3.2	Surface Analysis	145
7.4	Delta Wing	145
7.4.1	Volume Analysis	149
7.4.2	Surface Analysis	151
7.5	Formation Flight featuring Delta Wing geometries	151
7.6	Remarks	159
8	Conclusions and Outlook	164
	Bibliography	174

List of Figures

1.1	Examples of 3D CFD problems with millions of Degrees of Freedom, whose unsteady and/or parametric analysis promptly leads to <i>curse of dimensionality</i> . From left to right: High-Lift Wing-Body configuration; Delta Wing geometry featuring vortex breakdown phenomenon; Delta Wing geometries in Formation Flight configuration.	4
3.1	Evolution in time in terms of Mach number of an impulsive start of the 30P30N geometry, used later as a test-case, on two different meshes. Left column represents the solution on mesh M1 (coarse), right column represents the solution on mesh M2 (fine). The first two rows report a close-up view near the flap at earlier instants of time. The last two rows report the flow around the entire geometry once the starting vortex has fully developed and is propagating downstream.	47
3.2	Plots of Pressure Coefficient C_p on the surface of the 30P30N geometry at different instants of time for mesh M1 (coarse) and mesh M2 (fine). .	48
3.3	Qualitative comparison of different ROMs using 30 modes at time $t = 10^{-3}$ s, Velocity Magnitude (filled contours CFD, lines ROM), NACA0012.	51
3.4	Qualitative comparison of different ROMs using 30 modes at time $t = 2.11 \times 10^{-3}$ s, Velocity Magnitude (filled contours CFD, lines ROM), NACA0012.	51
3.5	Qualitative comparison of different ROMs using 30 modes at time $t = 4 \times 10^{-4}$ s, Velocity Magnitude (filled contours CFD, lines ROM), 30P30N.	53

List of Figures

3.6	Qualitative comparison of different ROMs using 30 modes at time $t = 3.51 \times 10^{-2}$ s, Velocity Magnitude (filled contours CFD, lines ROM), 30P30N.	54
4.1	Energy redistribution among modes as a function of the SPOD filter N_f , with $N_f \in [0; 60]$	58
4.2	Comparison between velocity magnitude contours from CFD and ROM reconstruction with different values of the SPOD filter N_f , using $En = 95\%$ at time $t = 3.5$ s from the impulsive start. Solid line: CFD coloured with the value of the error ϵ ; Dashed line: ROM reconstruction.	60
a	$N_f = 0$	60
b	$N_f = 10$	60
c	$N_f = 20$	60
d	$N_f = 30$	60
4.3	Comparison between velocity magnitude contours from CFD and ROM reconstruction with different values of the SPOD filter N_f , using $En = 99.9\%$ at time $t = 3.5$ s from the impulsive start. Solid line: CFD coloured with the value of the error ϵ ; Dashed line: ROM reconstruction.	61
a	$N_f = 0$	61
b	$N_f = 10$	61
c	$N_f = 20$	61
d	$N_f = 30$	61
4.4	Comparison between velocity magnitude contours from CFD and ROM reconstruction with different values of the SPOD filter N_f , using $En = 95\%$ at time $t = 6.5 \times 10^{-2}$ s from the impulsive start. Solid line: CFD coloured with the value of the error ϵ ; Dashed line: ROM reconstruction.	63
a	$N_f = 0$	63
b	$N_f = 10$	63
c	$N_f = 30$	63
d	$N_f = 40$	63

List of Figures

4.5	Comparison between velocity magnitude contours from CFD and ROM reconstruction with different values of the SPOD filter N_f , using $En = 99.9\%$ at time $t = 6.5 \times 10^{-2}$ s from the impulsive start. Solid line: CFD coloured with the value of the error ϵ ; Dashed line: ROM reconstruction.	64
a	$N_f = 0$	64
b	$N_f = 10$	64
c	$N_f = 30$	64
d	$N_f = 40$	64
4.6	Comparison between velocity magnitude contours from CFD and ROM reconstruction with different values of the SPOD filter N_f , using $En = 99.9\%$ at time $t = 8.1 \times 10^{-2}$ s from the impulsive start. Filled contours: CFD velocity magnitude; Solid black lines: ROM reconstruction.	65
a	$N_f = 0$	65
b	$N_f = 6$	65
c	$N_f = 12$	65
d	$N_f = 18$	65
4.7	Comparison between velocity magnitude contours from CFD and ROM reconstruction with different values of the SPOD filter N_f , using $En = 99.9\%$ at time $t = 8.1 \times 10^{-2}$ s from the impulsive start. Filled contours: CFD velocity magnitude; Solid black lines: ROM reconstruction.	66
a	$N_f = 0$	66
b	$N_f = 6$	66
c	$N_f = 12$	66
d	$N_f = 18$	66
4.8	Q-criterion isosurfaces coloured by the velocity magnitude at 4 instants of time and depicting the bypass transition process. From top-left to bottom right: $t = 1450 L_h u_b^{-1}$ ($Q = 10^{-4}$), laminar; $t = 1480 L_h u_b^{-1}$ ($Q = 10^{-4}$) and $t = 1530 L_h u_b^{-1}$ ($Q = 5 \times 10^{-4}$), transition; $t = 1700 L_h u_b^{-1}$ ($Q = 0.05$), fully developed.	71

List of Figures

4.9	Shear stress evolution for the time interval used in DMD (left). Full time window from transition to a fully developed turbulent flow (right). . . .	72
4.10	DMD eigenvalues and time dynamics.	72
	a DMD eigenvalues on the unit circle	72
	b time dynamics of DMD modes	72
4.11	DMD modes selection using t -envelope method (left) and energy spectrum of all the extracted DMD modes (right): the red circles highlight the modes selected using the energy norm, the black circles the ones selected using the t -envelope method with 8 levels of selection.	75
4.12	DMD spectrum (ω):(left) whole spectrum and (right) detailed view on the selected modes. Red circles highlight the DMD modes selected on the DMD spectrum using the t -envelope method (first row) and the energy method (second row).	76
4.13	Amplitude of α coefficients. Red circles highlight the DMD modes selected using the t -envelope method (left) and the energy method (right).	76
4.14	Selected modes via the t -envelope approach coloured by ϕ magnitude. Modes are ordered from left-to-right, from top-to-bottom, according to the corresponding energy content.	78
4.15	Selected modes via the energy approach coloured by ϕ magnitude. Modes are ordered from left-to-right, from top-to-bottom, according to the corresponding energy content.	79
4.16	Comparison of the onset of transition described through numerical simulation (first row), DMD t -envelope (second row), DMD energy (third row); $t = 1430L_h u_b^{-1}$ (first column), $t = 1480L_h u_b^{-1}$ (second column), $t = 1530L_h u_b^{-1}$ (third column).	80
4.17	Relative error of the Energy and t -envelope method with respect to simulations, for the velocity vector: velocity magnitude and velocity components.	81

List of Figures

5.1	Examples of Direct and Projection Error for the NACA0012 test-case presented in Chapter 3. Direct Error ϵ is reported in 5.1a, the difference between the two $\epsilon - \epsilon_P$ is reported in 5.1b. Errors are computed using the leave-n-out strategy (error in the mid-points of the training snapshots).	89
	a	89
	b	89
5.2	Examples of Direct and Projection Error for the 30P30N test-case presented in Chapter 3. Direct Error ϵ is reported in 5.2a, the difference between the two $\epsilon - \epsilon_P$ is reported in 5.2b. Errors are computed using the leave-n-out strategy (error in the mid-points of the training snapshots).	90
	a	90
	b	90
5.3	Conceptual difference between direct and residual error. RBM indicates a Reduced Basis Method, alias ROM.	91
5.4	Comparison of residual plots using spatial and spatio-temporal residual error for various ROMs and conservative variable density, NACA0012 test-case.	96
5.5	Bar plots with Basis Functions selection versus time using spatial residual error (first row) and spatio-temporal residual error (second row) for the set of conservative variables, NACA0012 test-case.	96
5.6	Comparison of residual plots using spatial and spatio-temporal residual error for various ROMs and conservative variable density, 30P30N test-case.	97
5.7	Bar plots with Basis Functions selection versus time using spatial residual error (first row) and spatio-temporal residual error (second row) for the set of conservative variables, 30P30N test-case.	97
5.8	Sensitivity with respect to the choice of Δt_{res} (left), number of modes and choice of method for density (right).	100

List of Figures

5.9	NACA0012 sensitivity with respect to number of modes and choice of method for density. Residual error = $\log_{10}(\epsilon_R(\rho))$ (left column), direct error = $\log_{10}(\epsilon_D(\rho))$ (right column).	104
5.10	NACA0012 minimum envelope of errors. Residual error = $\log_{10}(\epsilon_R(\rho, \rho u, \rho v, \rho e))$ (left column), direct error = $\log_{10}(\epsilon_D(\rho, \rho u, \rho v, \rho e))$ (right column).	105
5.11	NACA0012 momentum magnitude reconstructions at two different instants of time within the sampled time window. Coloured contours report the CFD reference solution, line contours represent the ROM reconstruction. The top row reports the reconstruction with the choice of methods and number of modes driven by the pseudo-algorithm based on residual error, the bottom row uses the pseudo-algorithm based on direct error.	106
a	$t = 0.05s$	106
b	$t = 0.05s$	106
5.12	30P30N sensitivity with respect to number of modes and choice of method for density. Residual error = $\log_{10}(\epsilon_R(\rho))$ (left column), direct error = $\log_{10}(\epsilon_D(\rho))$ (right column).	110
5.13	30P30N minimum envelope of errors. Residual error = $\log_{10}(\epsilon_R(\rho, \rho u, \rho v, \rho e))$ (left column), direct error = $\log_{10}(\epsilon_D(\rho, \rho u, \rho v, \rho e))$ (right column).	111
5.14	30P30N momentum magnitude reconstructions at two different instants of time within the sampled time window. Coloured contours report the CFD reference solution, line contours represent the ROM reconstruction. The top row reports the reconstruction with the choice of methods and number of modes driven by the pseudo-algorithm based on residual error, the bottom row uses the pseudo-algorithm based on direct error.	112
a	$t = 0.0159s$	112
b	$t = 0.0507s$	112
5.15	Schematic of the adaptive approach distinguished in the offline and online phases.	115

List of Figures

6.1	$\log_{10}(\epsilon_{R,T})$ varying the number of modes, for Adaptive ROM and POD, NACA0012 test-case.	122
6.2	$\log_{10}(\epsilon_{\text{diff}})$ considering POD as reference Single ROM, versus time and number of modes, NACA0012 test-case. White regions correspond to $\epsilon_{\text{diff}} = 0$, i.e. the Model-Based Adaptive ROM selects POD.	123
6.3	Volume reconstruction of density at time $t = 0.06\text{s}$ for 2 modes (left) and 28 modes (right), NACA0012 test-case. Coloured contours represent the CFD reference solution.	123
6.4	$\log_{10}(\epsilon_{R,T})$ varying the number of modes, for Adaptive ROM and POD, 30P30N test-case.	126
6.5	$\log_{10}(\epsilon_{\text{diff}})$ considering POD as reference Single ROM, versus time and number of modes, 30P30N test-case. White regions correspond to $\epsilon_{\text{diff}} = 0$, i.e. the Model-Based Adaptive ROM selects POD.	127
6.6	Volume reconstruction of density at time $t = 0.0054\text{s}$ for 6 modes (left) and 17 modes (right), 30P30N test-case. Coloured contours represent the CFD reference solution.	127
6.7	Fine and coarse grids for the NACA0012 test-case, used to investigate the influence on the residual error behaviour with the number of modes.	128
6.8	$\log_{10}(\epsilon_{R,T})$ versus number of modes, considering only POD, for the two different grids reported in Figure 6.7, NACA0012 test-case.	129
6.9	$\log_{10}(\epsilon_{R,T})$ varying the number of modes, for Adaptive ROM and POD on the coarse grid, NACA0012 test-case.	130
7.1	Contours of pressure for the impulsive start over the 30P30N airfoil at different instants of time.	135
7.2	Volume residual evaluation (left column) and choice of methods (right columns) for all the conservative variables (excluding turbulence), fixed number of modes $N_m = 10$, 30P30N test-case.	138

List of Figures

7.3	Comparison of the volume solution in terms of ρ . coloured lines show the ROM reconstruction while the black lines show the reference CFD solution. The left column shows the adaptive reconstruction, the right columns shows the pure POD reconstruction. Number of modes fixed, $N_m = 10$	139
7.4	Surface residual evaluation (left column) and choice of methods (right columns) for the conservative variables ρ and ρE , fixed number of modes $N_m = 10$, 30P30N test-case.	140
7.5	Surface reference solution in terms of ρE , 30P30N test-case. The shaded rectangle highlights the region where a zoomed comparison between methods is reported, see Figure 7.6.	141
7.6	Contour comparison of the surface solution in terms of ρE for (top to bottom) $t = 0.0073s, 0.0178s, 0.0250s$ for the 30P30N test-case. Coloured lines show the ROM reconstruction while the black lines show the reference CFD solution. The left column shows the adaptive reconstruction, the right columns shows the pure POD reconstruction. Number of modes fixed, $N_m = 10$	141
7.7	Contours of Mach number at different instants of time for the impulsive start of the High-Lift configuration.	142
7.8	$\log_{10}(\epsilon_{R,T})$ varying the number of modes, for Adaptive ROM and POD, High-Lift Wing-Body Configuration test-case.	144
7.9	Volume residual evaluation (left column) and choice of methods (right columns) for all the conservative variables (excluding turbulence), fixed number of modes $N_m = 10$, High-Lift Wing-Body test-case.	146
7.10	Contours comparison of volume solution in terms of ρU for the High-Lift Wing-Body test-case. Black contours show the CFD reference solution, colour contours report the ROM reconstruction. Left column shows the adaptive reconstruction, right column shows the POD pure reconstruction. Number of modes fixed, $N_m = 10$	147

List of Figures

7.11	Surface residual evaluation (left column) and choice of methods (right columns) for the conservative variables ρ and ρE , fixed number of modes $N_m = 10$, High-Lift Wing-Body test-case.	148
7.12	Detail of wing tip surface solution in terms of ρE for the High-Lift Wing-Body test-case. Black contours report the CFD reference solution, line contours show the ROM reconstruction. Left column is adaptive reconstruction, right column is pure POD reconstruction. Number of modes fixed, $N_m = 10$	148
7.13	Contours of Q-criterion $Q = 800s^{-2}$ coloured with velocity magnitude for different time instants, Delta Wing test-case.	149
7.14	$\log_{10}(\epsilon_{R,T})$ varying the number of modes, for Adaptive ROM and POD, Delta Wing test-case.	150
7.15	Volume residual evaluation (left column) and choice of methods (right columns) for all the conservative variables (excluding turbulence), fixed number of modes $N_m = 10$, Delta Wing test-case.	152
7.16	Comparison of volume solution in terms of ρ for the Delta Wing test-case. The black contours report the CFD reference solution, the coloured contour lines show the ROM reconstruction. Left column shows the adaptive reconstruction, right column shows the pure POD reconstruction. Number of modes fixed, $N_m = 10$	153
7.17	Surface residual evaluation (left column) and choice of methods (right columns) for the conservative variables ρ and ρE , fixed number of modes $N_m = 10$, Delta Wing test-case.	154
7.18	Detail of surface solution in terms of ρE for (top to bottom) $t = 0.0096s$, $0.0153s$, $0.0198s$ for the Delta Wing test-case. Black contours indicate the CFD reference solution, coloured contours show the ROM reconstruction. Left column is Adaptive reconstruction, right column is pure POD reconstruction. Number of modes fixed, $N_m = 10$	155
7.19	Contours of Q-criterion $Q = 800s^{-2}$ coloured with velocity magnitude (m/s) for different time instants, Formation Flight test-case.	156

List of Figures

7.20	$\log_{10}(\epsilon_{R,T})$ varying the number of modes, for Adaptive ROM and POD, Formation Flight test-case.	157
7.21	Volume residual evaluation (left column) and choice of methods (right columns) for all the conservative variables (excluding turbulence), fixed number of modes $N_m = 15$, Formation Flight test-case.	158
7.22	Comparison of volume solution in terms of ρ for the Formation Flight test-case. The black contours report the CFD reference solution, the coloured contour lines show the ROM reconstruction. Left column shows the adaptive reconstruction, right column shows the pure POD reconstruction. Slice taken at 0.45m from the plane of symmetry. Number of modes fixed, $N_m = 15$	159
7.23	Detail of volume solution in the region of vortices interaction, in terms of ρ for the Formation Flight test-case. The black contours report the CFD reference solution, the coloured contour lines show the ROM reconstruction. Left column shows the adaptive reconstruction, right column shows the pure POD reconstruction. Slice taken at 0.45m from the plane of symmetry. Number of modes fixed, $N_m = 15$	160

List of Tables

3.1	NACA0012 simulation parameters	48
3.2	30P30N simulation parameters	52
4.1	Error in reconstruction for the square cylinder, computed according to Equation 4.2 for u and v component of velocity, for two different energetic contents and varying the SPOD filter size.	62
4.2	Error in reconstruction for the 30P30N, computed according to Equation 4.2 for u and v component of velocity, for two different energetic contents and varying the SPOD filter size.	62
4.3	Error in reconstruction for the 3D High-Lift Wing-Body configuration, computed according to Equation 4.2 for u , v and w component of velocity, with fixed energetic content and varying the SPOD filter size.	67
5.1	NACA0012 ROM setting	102
5.2	NACA0012 choice of ROM for each conserved quantity according to the residual or direct error.	107
5.3	30P30N ROM setting	108
5.4	30P30N choice of ROM for each conserved quantity according to the residual or direct error.	109

List of Tables

- 7.1 Comprehensive time breakdown for the Adaptive Framework in terms of time required for the database generation (T_{datagen}), time required for features extraction and residual database computation ($T_{\text{FE-RE}}$) and time required for the reconstruction of one ROM solution ($T_{\text{ROM-online}}$). The last two columns define the time requirements for the computation of the error database at one single point when a residual error ($T_{\text{Res-Eval}}$) or a direct error (T_{CFD}) are used. The time for the database generation is reported in CH, all the other times are considered on a single core. . . 162

Nomenclature

Acronyms

2D	Two Dimensional
3D	Three Dimensional
BDF	Backward Difference Formula
CFD	Computational Fluid Dynamics
CH	core/hours
CNR	Crank Nicholson Residual
DFT	Discrete Fourier Transform
DMD	Dynamic Mode Decomposition
DNS	Direct Numerical Simulation
DOFs	Degrees of Freedom
DTR	Dual Time Residual
FOM	Full Order Model
FV	Finite Volume
MRA	Multi-Resolution Analysis
NS	Navier-Stokes

Nomenclature

ODE	Ordinary Differential Equation
PDE	Partial Differential Equation
POD	Proper Orthogonal Decomposition
RANS	Reynolds Averaged Navier-Stokes
RBF	Radial Basis Function
RBM	Reduced Basis Method
RDMD	Recursive Dynamic Mode Decomposition
RIC	Relative Information Content
ROM	Reduced Order Model
SPOD	Spectral Proper Orthogonal Decomposition
SST	Shear Stress Transport
SVD	Singular Value Decomposition

Greek Symbols

α	angle of attack
α_i	i -th DMD mode amplitude
ϵ_{diff}	Difference between Adaptive ROM and Single ROM residual error
ϵ_{D}	Direct Error
ϵ_{P}	Projection Error
$\epsilon_{\text{R,A}}$	Residual Error for the Adaptive Framework
$\epsilon_{\text{R,S}}$	Residual Error for a single ROM
$\epsilon_{\text{R,T}}$	Residual Error integral over time

Nomenclature

ϵ_R	Residual Error
λ_i	i -th eigenvalue
Λ	Eigenvalues matrix
Φ	matrix of modes
ϕ_i	i -th modal basis
Σ	Singular values matrix
μ	generic parameter
ω_i	i -th DMD continuous time eigenvalue
ρ	density
σ_i	i -th singular value
τ_w	Wall shear stress

Roman Symbols

$\hat{\mathbf{F}}$	vector of numerical fluxes
$\hat{\mathbf{u}}$	approximated ROM solution vector for a generic physical quantity
$\tilde{\mathbf{T}}$	low-dimensional time dynamic matrix
\mathbf{A}	matrix of coefficients
\mathbf{e}	exact error vector
\mathbf{e}_\perp	exact error component perpendicular to the low-dimensional space
\mathbf{F}	vector of analytical fluxes
\mathbf{n}	edge normal
\mathbf{P}_ϕ	Projection Operator

Nomenclature

\mathbf{R}	temporal correlation matrix
\mathbf{R}_f	filtered temporal correlation matrix
\mathbf{R}_i	spatial residual vector at point i
$\mathbf{R}_{\Delta t, i}$	spatio-temporal residual vector at point i
\mathbf{T}	time dynamic matrix
\mathbf{T}_{dyn}	matrix with DMD time coefficients evolution
\mathbf{U}	snapshots matrix
\mathbf{u}	solution vector for a generic physical quantity
\mathbf{U}'	time shifted snapshots matrix
\mathbf{V}	Vandermonde matrix
\mathbf{w}	vector of conservative variables
a_i	i -th modal coefficient
d_n	Kolmogorov n -width
En	Energy content
f	radial basis function
g_k	SPOD filter function
L_b	reference length for channel flow
L_h	channel half-height
M	Mach number
N_f	SPOD filter size
N_m	Number of modes

Nomenclature

N_p Number of grid points

N_s Number of snapshots

$p(t)$ polynomial of low degree

Q Q-criterion value

Re Reynolds number

Re_b Reynolds number based on bulk velocity

Re_τ Reynolds number based on friction velocity

S_j j -th cell edge surface

t time

u_b bulk velocity

u_τ friction velocity

V_i i -th cell volume

Chapter 1

Introduction

1.1 Motivation

The development of algorithms capable of reducing the computational effort required to characterize the behaviour of complex systems has attracted lots of attention in the past decades [1, 2, 3]. Reduced Order Model (ROM) is the denomination used to indicate this wide class of algorithms, whose aim is to find a good trade-off between accuracy in describing the system behaviour and reduction of the complexity of the system itself. The complexity reduction is often associated with a reduction of dimensionality of the original system, which might have a very large number of degrees of freedom (DOFs). This fundamental aspect of a ROM has determined its widespread usage over almost all fields of engineering, including modeling of electrical circuits [4, 5, 6] and Micro-Electro Mechanical Systems (MEMS) [7, 8, 9], applications to structural problems [10, 11, 12], processing and compression of videos and images [13, 14], aeroelasticity [15, 16, 17, 18, 19], other than fluid dynamics [20, 21, 22]. For these problems, where a lot of high-dimensional data are usually produced by experiments or computationally demanding high-fidelity simulations, it is indeed possible in some cases to define a low-dimensional space where to describe the system dynamics. It is crucial to prove that the behaviour of the system is in fact confined within a low-dimensional manifold since reliability and accuracy of a ROM depend on it. This has proven to be the case for many systems where the dynamics in time or the behaviour over a parameter space is confined within

an attractor [23]. The attractor represents a subset of the whole vector space where solutions of the system lie. This subset is usually very low-dimensional (i.e. dependent on very few parameters with respect to the high-fidelity model of the system) and therefore paves the way for a definition of a low-dimensional model.

The elaboration of a ROM often represents the starting point to perform further analysis later, for example in the phase of the conceptual and preliminary design of engineering devices, where it is fundamental to have algorithms able to provide solutions in a real-time manner [17, 19], as opposed to computational demanding high-fidelity simulations or time demanding experiments that need to be set up [24, 25, 26, 27].

1.1.1 Why Reduced Order Models in fluid dynamics

Model reduction in fluid mechanics can be discussed from two fundamental conceptually different, yet linked, points of view:

1. identify patterns and physical primitives governing the nonlinear behaviour of the flow system;
2. approximate the detailed dynamics of the system for a range of operating conditions in a much faster yet physically consistent manner.

The research on ROMs in the fluid dynamic field has widely covered both aspects. The former is quite important due to the huge amount of data coming from both experiments and high-fidelity models. This makes the extraction of meaningful information about time dynamics, as well as parametric system behaviour, unmanageable without relying on any algorithm for projecting initial data on a low-dimensional manifold, where data can be more interpretable. The problem has been historically introduced in the fluid dynamics community through the analysis of turbulent flows, where it became rather soon clear that the very chaotic behaviour hides an underlying more organized motion happening in the flow [28, 29, 30]. This observation led for the first time to define a procedure that allow identifying some coherent structures in space and time, which are the main responsible for the flow time dynamics [23, 31, 32]. Since then, isolation of dominant flow features, and often also the extraction of important dynam-

ical information (e.g. frequencies and growth/decay rates) associated to them, was introduced in many fields of fluid dynamics, in order to visualize essential dynamics and/or parametric behaviour with only few degrees of freedom. The effort has been put in defining extraction algorithms for the identification of flow features that provide correct information about the actual physics underlying the collected data. For the specific case of pure unsteady flows, it has been shown that being able to define dominant structures on the basis of important physical consideration was a key point to extract physically meaningful information from the fluid system [33, 34, 35, 36, 37]. Dominant flow features not only provide a deeper understanding of the flow physics but also put the basis to act on specific spatial structures that have a strong impact on the overall flow dynamics. This last aspect is strongly related to the many applications of ROMs for flow control problems [20, 38, 39, 40, 41, 42].

When the focus is only on the numerical aspect of fluid dynamics problem, the second point listed above becomes important. The need to elaborate ROMs in this case is linked to the very high computational demand of CFD simulations. Solving a fluid dynamics problem using CFD techniques requires the discretisation of the original system of Partial Differential Equations (PDEs), i.e. the set of Navier-Stokes equations for the general case of a viscous compressible flow, over a specific computational domain. When dealing with complex geometries and three dimensional (3D) problems, the computational mesh can count up to hundreds of millions grid points leading to an equivalently large number of Degrees of Freedom (DOFs). The very high number of points in the computational mesh is linked to the need to resolve important spatial scales, catch all the meaningful dynamics and limit numerical diffusion. Figure 1.1 shows some examples of CFD problems of this kind. It becomes clear that retaining the entire description of the system in the high-dimensional space, when unsteady behaviours need to be described or the system behaviour needs to be explored over a large parameter/design space, makes the analysis unfeasible due to the well-known *curse of dimensionality* problem. Therefore, approximating the system evolution over a low-dimensional space with few degrees of freedom is fundamental for these kind of problems.

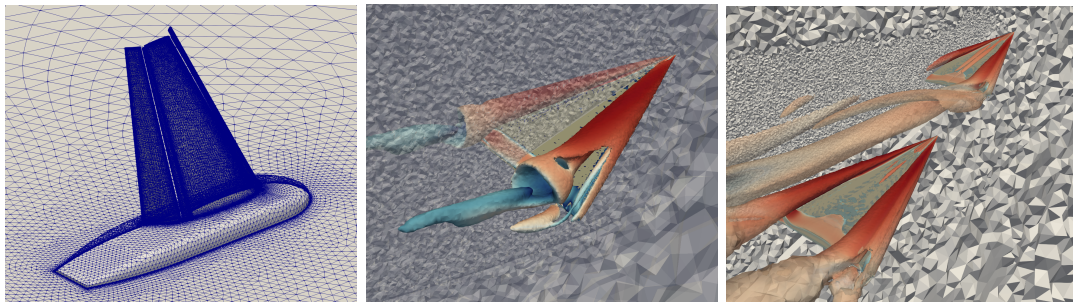


Figure 1.1: Examples of 3D CFD problems with millions of Degrees of Freedom, whose unsteady and/or parametric analysis promptly leads to *curse of dimensionality*. From left to right: High-Lift Wing-Body configuration; Delta Wing geometry featuring vortex breakdown phenomenon; Delta Wing geometries in Formation Flight configuration.

Despite the definition of the low-dimensional space is also open to the introduction of a wide range of analytical approximation methods (e.g. response surfaces, polynomial approximations, etc.), the possibility to take advantage of the information embedded into a set of few dominant primitives (data-driven ROMs) has proven to be both more efficient and more effective in the development of reduction techniques, showing superior performance while making detailed reconstructions of the flow physics. In this last case, few “physically” meaningful flow features that are able to span the low-dimensional space are identified and then used for projecting the system onto such space. This highlights how the two aspects of ROMs in fluid dynamics discussed in this section are strongly interconnected. The definition of a good low-dimensional space is indeed linked to how well the extracted features describe the underlying physics of the problem and therefore are at the basis of generating a robust and reliable ROM. Nevertheless, it is worth noting that, when the focus is only on the approximation of complex fluid systems, dominant features do not need to be “physically meaningful”, i.e. they do not necessarily need to have a physical interpretation (such as coherent structures in a turbulent flow) in order to provide a sufficiently accurate approximation of the flow physics. This is for example the case of the impulsively started dynamics associated to particular geometries, which is investigated in the present work. Although it is difficult to extract features that alone can be representative of specific structures present in the flow due to its purely transient nature, the combination of these features is able

to reconstruct the overall dynamics preserving the essential physics (see for examples results presented in Section 3.4 and Chapter 7). There are instead cases where a clearer connection can be made between structures appearing in the flow and the flow features extracted by a specific algorithm. Section 4.2 reports an example of this kind, where some of the features extracted and eventually used to build the low-dimensional model unveil coherent structures actually present in the flow.

1.1.2 Transient nonlinear aerodynamic flows: motivation and challenges

Dominant flow structures in unsteady nonlinear flows can undergo significant changes in terms of their intensity, e.g. the energy associated to them. They can appear and/or disappear or be relevant only over a specific time window. All of this makes their identification and the consequent definition of a low-dimensional model a nontrivial problem. This difficulty is exacerbated when performing the numerical study of the unsteady aerodynamic environment developing around lifting bodies. The generation of starting vortices, the coalescence and interaction of such vortical structures, the occurrence of possible separation regions determine a rather nonlinear scenario. Moreover, the description of such nonlinear spatio-temporal dynamics in a very high-dimensional space, like the one arising from the discretisation of the original computational domain, can be very inefficient in terms of both computational cost and memory storage required. It is worth noting that the degree of nonlinearity of the considered spatio-temporal dynamics is difficult to quantify in local terms, e.g. defining the degree of nonlinearity of interacting and/or advecting vortices developing in the flow field. Therefore the term nonlinear used hereafter will refer more in general to the nonlinear nature of the original system of equations solved, i.e. the full set of Navier-Stokes equations, which dictates the formation and evolution of such flow structures. The term transient will instead refer to the unsteady behaviour of flow structures generated by fixed geometries in flow fields with constant boundary conditions.

The scientific community has built a strong awareness of the difficulties linked to the extraction of physically meaningful flow structures from fluid flows that exhibit a com-

plex dynamics, with many features interacting and mixing together in a nonlinear manner [33, 36, 43, 44, 45]. The debate has been focused on the limitations of two widely used techniques in the fluid dynamics community, that are Proper Orthogonal Decomposition (POD) [23, 31] and Dynamic Mode Decomposition (DMD) [46, 47]. POD has been recognized to have limitations in extracting all the important dynamic information from a set of collected snapshots. Indeed its optimal property promote the most energetic structures of the flow, which are not always the only structures responsible for fundamental dynamics. Rowley et al. [48] points out for examples how fluid flows where acoustic resonances occur, acoustic waves play a crucial role, even though their energy content is much smaller than other pressure fluctuations that can be present in the flow. In their work they demonstrate the beneficial effect of combining POD with a balanced truncation algorithm in extracting physically meaningful flow feature for a linearized channel flow problem. Sieber et al. [36] also introduces an alternative to POD that is able to deal with flows exhibiting complex dynamics, where complexity is mainly linked to intermittent dynamics, frequency modulations, to mention a few. This leads to a condition where dominant flow structures cannot be easily isolated. In particular, examples of such complex flows are given, that are the flow near the region of a gurney flap, the flow in a swirl-stabilized combustor and the flow resulting from a sweeping jet generated by a fluidic oscillator. In all these cases, the authors propose an alternative to POD which reveals to be better in separating flow structures, facilitating its ranking on the basis of their dynamic importance. The work of Rowley et al. [48] and Sieber et al. [36] will be also better discussed in Chapter 2, where a literature review of methods is presented.

The isolation of pure coherent structures is also a limitation of DMD, since it extracts flow features with single frequencies that might not exactly reproduce their complex dynamics. Besides this, it has been recognized also how DMD can fail in describing transient dynamics. In particular Bagheri [43] has shown how DMD fails in describing the dynamics of a cylinder wake when the DMD observation window is stretched too far from the limit of the characteristic periodic oscillations. Moreover, Page and Kerswell [45] have discussed more in general how DMD can fail when describing a system

dynamics over an observation window that contains crossover points of the dynamical system.

In the context of isolating dominant flow features, and more in general defining an accurate and efficient ROM when complex dynamics associated to flow structures mixing, advection and diffusion is considered, it is possible to identify four main challenges:

Challenge 1. The identification of dominant flow features that are able to describe transient nonlinear dynamics in a low-dimensional space in a consistent, i.e. systematic and automatic, manner. Complex unsteady flows, expressed by the full set of Navier-Stokes equations, often present dynamics happening on several spatial and temporal scales. Defining low-dimensional manifolds through data-driven techniques that are close to the physical one, if it exists, needs careful considerations in order not to miss essential dynamical information [33, 35, 36, 44, 46, 49].

Challenge 2. Advection-dominated phenomena are common in unsteady fluid flows and they are mainly characterised by the convection of flow structures over the computational domain. For this specific class of flows, using conventional ROM approaches leads to reduced models that still need quite a large number of degrees of freedom to achieve a satisfactory accuracy [50, 51, 52, 53]. The ability to obtain a reduced model that has a rather small number of DOFs but retains CFD-like accuracy in the reconstructed solution is still one important open problem in model reduction techniques for advection-diffusion PDEs.

Challenge 3. Intrusive ROMs, i.e. ROMs that project the original governing equation of the system on a low-dimensional space through the set of basis functions computed, are widely used in the literature [54, 55, 56, 57]. Using an intrusive ROM allows to convert the high-dimensional system of ODEs coming from the spatial discretisation of the original PDEs in a system of few ODEs that describes the evolution of the system in a low-dimensional space. The main challenge for this class of ROMs, when unsteady dynamics is considered, is how to deal with stability issues linked to the integration in time of the low-dimensional system of equations [39, 58, 59, 60, 61, 62]. This is also

better clarified in Section 2.4.1.

Challenge 4. Defining a set of flow features requires an initial phase of training, where a set of high-dimensional solutions, i.e. snapshots, are computed at various instants of time. When dealing with transient nonlinear flows, a uniform sampling in time might not be the best choice. Moreover, differently from what happens in the case of parametric problems, where each solution over the parameter space can be computed independently, a specific sampling for unsteady problems might require also to define an adaptive time step for the solution of the initial set of equations, in order to make the sampling procedure more efficient [63].

1.2 Objective and Research Questions

The present research work focuses on the exploration of the first two challenges reported above by studying a class of flows exhibiting significant nonlinear features in space and time and characterised by the interaction and advection of complex structures. Indeed, the analysis of this kind of flows raises the problem of defining a proper low-dimensional space that is able to take into account the essential dynamics, including advection phenomena, while keeping the number of DOFs as small as possible. The work is also originating from a more engineering context and its relevance can be assessed both in terms of applied research, as it tackles a series of challenges relevant to the design of air vehicles, and in terms of fundamental research, as it aims at exploring the methodological and numerical aspects of computational reduction techniques.

Research questions. The following interconnected research questions will be addressed:

- 1) “*When identifying the fundamental flow structures at the basis of the reduction process, what is the impact of explicitly considering the time correlation between snapshots on the accuracy of the reduced solution?*”
- 2) “*Is it possible to define an error measure, both computationally efficient and reli-*

able, that allows to perform a quantitative assessment of the accuracy of different sets of flow features in the reduced order reconstruction of complex unsteady dynamics?”

- 3) *“If no best-in-class ROM can be identified, is there a way to formulate a computational reduction technique that is able to combine the strengths of diverse existing methods, in terms of resolving specific dynamic features in time, in a unique and cohesive reduction framework?”*

The first research question is linked to the well-known problem in the ROM community of defining a low-dimensional model that is able to isolate the essential dynamics of the fluid system. Many efforts have been indeed devoted to this task in the recent past, all mainly focusing on extracting pure dynamical information and describing the dynamics of conceptually simple problems, or at least problems where some important information are known a-priori [35, 36, 47]. The present work instead represents an effort more focused on the reconstruction accuracy that can be achieved by these newer techniques when they are applied to problems featuring relevant nonlinear transient in time, e.g. impulsive starts, and complex dynamics in space, with structures advecting and interacting over the computational domain. The study related to the first research question is therefore strongly connected to the first two challenges presented above, since it provides a more in depth insight on the limitations and advantages of diverse extraction techniques in describing the evolution of advection-dominated phenomena. The second research question addresses the problem of defining a quantitative assessment of the various ROMs considered. In the literature many examples can be found addressing the problem of defining ROM accuracy through the definition of a-priori and a-posteriori error bounds, which make the method certified and reliable [64, 65, 66, 67, 68]. Nevertheless, comparable rigorous error estimations have not been addressed in the same detail for problems governed by the full set of Navier-Stokes equations applied to impulsive start problems of aeronautical relevance. The present work represents an effort in this direction, tackling the general problem of defining error measures in these cases with a more engineering rather than mathematical approach. With respect to

the first two challenges presented above, the second research question provides also a quantitative study of the performance of diverse algorithms for feature extraction to target transient nonlinear flows with advecting flow structures.

The last research question represents an effort to offer a possible solution to the first two challenges and it is also a natural consequence of the first two research questions. It explores the problem of how different reduced methods should be regarded and possibly combined together to generate a single monolithic ROM that improves the description of transient nonlinear dynamics. The improvements are measured not only in terms of accuracy, but also in terms of reduction of degrees of freedom. Namely a trade-off between the two will be used in the present work to define the capabilities of such new ROM when compared to single reduced order techniques.

Overarching objective. Stemming from the last of the research questions above, *the overarching objective of the present work is to formulate and implement a non-intrusive ROM able to describe the dynamics of impulsively started aeronautical geometries with superior accuracy when compared with the different existing methods, and capable to ensure a significant reduction in the number of degrees of freedom of the original problem* [69, 70]. The identification of a low-dimensional space that is able to preserve all the essential dynamics developing over several spatial and temporal scales represents a central challenge, which can hardly be addressed by relying on a single reduction technique. Research efforts have been put in defining a framework able to exploit capabilities of different reduction techniques and the associated low-dimensional spaces. Information obtained addressing the two first research questions are crucial in the effort to define this unique framework.

Contribution to knowledge. The research needed to address the above research questions allows identifying the following specific objectives, each one providing an original contributions to the field of computational reduction:

- Investigate how a range of classical and more recent linear decomposition techniques compare with respect to the widely used POD in reconstructing complex

- dynamics in time, for the specific case of complex unsteady aerodynamics flows;
- Explore how different ranking of modes for the specific case of POD and DMD influence the accuracy in reconstruction of unsteady complex aerodynamics flows;
- Define an error estimation formula derived from the Navier-Stokes equations that allows for a consistent ranking of available reduction methods in reconstructing the solution for untried condition;
- Introduce a synergistic integration of low-dimensional spaces coming from different reduction techniques to improve the reconstruction of complex dynamics.

The list will be also mirrored in the final Chapter, where conclusions are reported, in terms of what has been done to build these contributions.

1.3 Outline

The remainder of this thesis is structured as follows:

- **Chapter 2** reports some background about Reduced Order Modeling in fluid dynamics, literature review, and state of the art of ROMs used for the specific case of unsteady fluid dynamics problems.
- **Chapter 3** presents a list of ROMs used to extract physically meaningful features from a set of snapshots of the fluid flow, namely POD, Spectral Proper Orthogonal Decomposition (SPOD), DMD, and Recursive Dynamic Mode Decomposition (RDMD). It also shows the qualitative performances of these different algorithms in reconstructing unsteady complex dynamics, namely the impulsive start of a NACA0012 airfoil evolving to a quasi-periodic behaviour, and the impulsive start of a 30P30N multi-element airfoil.
- **Chapter 4** presents methods for ranking flow features extracted using the algorithms presented in Chapter 3. In particular, a qualitative and quantitative analysis is carried out for the specific case of POD and DMD. The effect of energy redistribution among POD modes is investigated when reconstructing the

dynamics of a set of impulsively started geometries and the vortex shedding of a cylinder. A novel approach is also presented for properly selecting physically meaningful DMD modes in describing the dynamics of the early transition in a channel flow.

- **Chapter 5** introduces the novel approach for non-intrusive low-dimensional modeling of complex unsteady fluid dynamics. The technique is an Adaptive ROM that exploits the best aspects of the various linear ROMs introduced in Chapter 3, in the effort to create a synergy among them. Two different definitions of the error are introduced to complete the Adaptive Framework. A comparative study is also performed to investigate the Adaptive ROM performances when it is equipped with such error definitions. Namely a residual error that does not require reference solutions, and a direct error that instead requires a set of reference solutions, are considered. The Model-Based Adaptive ROM is finally introduced. The term Model-Based refers to the residual error eventually used within the Adaptive Framework.
- **Chapter 6** presents a preliminary analysis of the features of the Model-Based Adaptive Framework as the number of modes retained is changed. The analysis represents an effort to achieve a good trade-off between solution accuracy and dimensionality reduction of the initial problem. An investigation is also provided regarding the influence of the initial mesh resolution on the performance of the Model-Based Adaptive ROM.
- **Chapter 7** finally shows the performance of the Model-Based Adaptive framework when applied to impulsively started aeronautical geometries, exhibiting complex dynamics in time and space. Geometries are indeed investigated that generate complex vortical structures, namely the 30P30N multi-element airfoil and its 3D version in a Wing Body configuration, as well as simple geometries in configurations that generate complex dynamics in time, namely Delta Wing exhibiting vortex breakdown and Delta Wings geometries in Formation Flight configuration exhibiting vortex interactions.

Chapter 1. Introduction

- **Chapter 8** draws the conclusions, summarizing results presented from Chapter 3 to Chapter 7, and providing answers to the research questions presented in Section 1.2. Possible further developments of the novel Adaptive Framework introduced in Chapter 5 are also discussed.

1.4 Publications arising from this thesis

Journal Papers

- In Preparation

G. Pascarella, G. Barrenechea, M. Fossati. Model-based Adaptive Reduced Order Modeling for Unsteady Aerodynamics. Part I: Concepts and Formulation. *Journal Of Computational Physics*.

G. Pascarella, G. Barrenechea, M. Fossati. Model-based Adaptive Reduced Order Modeling for Unsteady Aerodynamics. Part II: Applications. *Journal Of Computational Physics*.

- Published

G. Pascarella, M. Fossati, G. Barrenechea. Impact of POD modes energy redistribution on flow reconstruction for unsteady flows of impulsively started airfoils and wings. *International Journal of Computational Fluid Dynamics*, 34(2):108-118,2020.

G. Pascarella, I. Kokkinakis, M. Fossati. Analysis of transition for a flow in a channel via reduced basis methods. *Fluids*, 4(4):202, 2019.

G. Pascarella, M. Fossati, G. Barrenechea. Adaptive reduced basis method for the reconstruction of unsteady vortex-dominated flows. *Computers & Fluids*, 190:382-397, 2019.

Chapter 1. Introduction

Conference Papers

G. Pascarella, M. Fossati. Model-based adaptive MOR framework for unsteady flows around lifting bodies . In *MODRED 2019*. (In press)

G. Pascarella, M. Fossati, G. Barrenechea. Model-based adaptive reduced basis methods for unsteady aerodynamics studies. In *AIAA Aviation 2019 Forum*, 2019-3332.

Chapter 2

Background and Literature Review

2.1 Low-dimensional Modeling in fluid dynamics

Although there are many assumptions as starting points to elaborate low-order models, the main assumption that will be used in the present work is that the generic quantity $\mathbf{u}(\mathbf{x}, t, \mu)$ can be expressed as a sum of N_m products of parameter-dependent coefficients and parameter-independent basis functions, namely

$$\mathbf{u}(\mathbf{x}, t, \mu) = \sum_{i=1}^{N_m} a_i(t, \mu) \phi_i(\mathbf{x}) \quad (2.1)$$

where N_m represents the number of basis functions used in the ROM, i.e. the number of degrees of freedom of the low-order model, ϕ_i is the generic set of basis functions, alias modes, a_i is the generic coefficient associated to the basis function, which dictates the system evolution into the low-dimensional space. The time dependence t of coefficients a_i is separated from the generic parameter μ , since different considerations need to be taken and different algorithms can be implemented depending on whether the problem is steady or unsteady. \mathbf{x} represents a discrete vector of points where the solution vector \mathbf{u} is computed, i.e. the points of the computational mesh if considering the high-fidelity solution coming from a CFD simulation. The vector \mathbf{u} will be hereafter used to indi-

cate the generic physical quantity under study on a set of discrete points and it is often a very high-dimensional vector for fluid dynamics problems. The assumption in Equation 2.1 is crucial to elaborate a low-order model that is able to capture essential behaviour of the system using as few DOFs as possible, still preserving a good degree of accuracy and physical consistency, as opposed to low-fidelity methods, e.g. vortex-lattice or panel methods. Indeed, although they can provide enough accuracy if some underlying conditions are met (e.g. negligible 3D effects), these low-fidelity methods might provide misleading results when strong separations and important cross-flows occur in the flow field, which leads to the necessity of full CFD (high-fidelity) simulations. It is worth to highlight that, even if the basic assumption in Equation 2.1 is “linear”, since it decomposes the solution \mathbf{u} as a linear combination of basis functions through some coefficients a_i , it is also able to treat “nonlinearity”. Indeed, the basis functions ϕ_i can represent nonlinear spatial structures that evolve through nonlinear function a_i over the time and parameter space. Recent literature [71] has also pointed out the importance of having spatio-temporal basis functions, i.e. $\phi_i = \phi_i(\mathbf{x}, t)$, in order to enrich the description of the low-dimensional subspace and take into account more complex nonlinearities. Nevertheless, the extraction of features of this kind still remains an open question. Furthermore, while increasing the complexity in modeling flow physics through accurate spatio-temporal features, attention has to be paid in order not to define models that have a level of complexity comparable to the one of the original set of equations.

The two main components of Equation 2.1 allow to distinguish each ROM in two main phases: an *offline* phase and an *online* phase. The *offline* phase consists of a training step, where usually high-fidelity solutions are computed and fed into an algorithm that provides the set of basis functions ϕ . This procedure is performed once and for all, therefore the time required for the training and extraction stage is usually of minor importance. It is worth noticing that the training is the most delicate step in building a ROM, since the resulting low-dimensional model will be at most capable of describing behaviours contained in the collected solutions, independently from the specific algorithm used. Therefore, the more the solutions span all the possible behaviours of the

original system, the more the ROM is able to accurately describe the system behaviour in a low-dimensional manner. The *online* phase, instead, represents the true computational speedup of the method. It allows indeed to compute coefficients a_i in Equation 2.1 and therefore describes the system evolution in a low-dimensional manifold. Equation 2.1 can be used then to project the solution in the low-dimensional space to the high-dimensional space once coefficients are provided.

It is worth noting at this stage that the Equation 2.1 will be used in the present work only to elaborate a ROM that is able to compute low-dimensional solutions within the space sampled and used to train the ROM. No prediction capabilities, in terms of testing the ROM when new solutions are computed out of the sampled space, will be developed or investigated. The remainder of the Chapter reports an overview of ROMs implementation and usage in fluid dynamics for both the aspects highlighted in Section 1.1.1. In particular: Section 2.2 provides the main aspects that have to be considered before trying to define a Reduced Order Model; Section 2.3 provides a review of ROMs used for fluid modal analysis; Section 2.4 provides instead a review of reduced models for describing the system behaviour in a fast, yet accurate, low-dimensional manner.

2.2 Prerequisites for dimensionality reduction

Although ROMs are a very powerful method to provide quantitatively and qualitatively accurate descriptions of a system behaviour, there are some considerations that need to be done before trying to elaborate algorithms for dimensionality reduction. All these considerations stem from the actual existence of low-dimensional manifolds where to describe the system behaviour. Lassila et al. [72] provides a good overview of the main aspects to be considered before building a ROM for a generic high-dimensional system. The most important one is the Kolmogorov n -width. It mathematically represents the distance $d_n(M, X)$ of the low-dimensional manifold M and the corresponding high-

dimensional space X , defined as follows

$$d_n(M, X) := \inf_{X_n \subset X} \sup_{\mathbf{u} \in M} \inf_{\tilde{\mathbf{u}} \in X_n} \|\mathbf{u} - \tilde{\mathbf{u}}\|_X \quad (2.2)$$

Here, $\tilde{\mathbf{u}}$ represents the low-order reconstruction of the quantity \mathbf{u} , while n is the same as N_m defined in Equation 2.1. Therefore, the faster d_n tends to zero as $n \rightarrow \infty$, the stronger the dimensionality reduction that can be achieved using a ROM. Naturally, knowing or computing a-priori the Kolmogorov n -width is not an easy task, especially for very complex problems originating from the full set of Navier-Stokes equations. Indeed, this last problem is usually characterized by many spatial and temporal scales and only numerical approximations or substitute quantities to Kolmogorov n -width can be computed, which are still able to provide an indication of the existence of low-dimensional manifolds. There have been efforts for very simple problem to provide a mathematical computation of the Kolmogorov n -width. Unger and Gugercin [73] have tried to define $d_n(M, X)$ for a Linear Time Invariant (LTI) system, showing that the quantity in Equation 2.2 for such systems equal their $(n + 1)$ st Hankel singular values. Brown et al. [74] and Combettes and Dũng [75] define Kolmogorov widths for subspaces generated by a particular class of smooth functions and non-degenerate differential operator, respectively. Lassila et al. [76] and Bachmayr and Cohen [77] also provided estimates of the Kolmogorov widths for parametric and elliptic PDEs, showing the important link between the n -width of the solution manifold and the fast convergence of reduced basis methods. For complex problems generating from Navier-Stokes equations, a quantity that is considered a good substitute to Kolmogorov width is the set of singular values produced by a collection of snapshots of the system. To compute a set of singular values of the system that represents a reliable measure of the low-dimensional structure, it is necessary to have a good number of solutions available from the original system and a proper sampling of these solutions. The rate of decay of the singular values provides then a measure of how much the dimensionality of the system can be reduced. Many works use singular values decay as an estimate of the capability to reduce dimensionality of a complex systems and singular values are often

used to define the rank of the reduced model through the Relative Information Content (RIC) defined as follows [72, 78],

$$\text{RIC} = \frac{\sum_{i=1}^r \sigma_i^2}{\sum_{i=1}^{n_{\text{tot}}} \sigma_i^2} \quad (2.3)$$

where r represents the number of flow features eventually used in the ROM, therefore equivalent to the quantity N_m in Equation 2.1, n_{tot} is the total number of collected solutions, σ_i is the i -th singular value. Peherstorfer [50] uses the different rate of decay of singular values with local versus global approaches to elaborate a fast and accurate adaptive reduced model for convection dominated flows.

The introduction of local ROMs stems from another important guideline for dimensionality reduction stated in [72], that is “Divide and conquer whenever possible”. It is well known, indeed, that accuracy and reliability of a ROM often decays as new evaluation are searched for in the low-dimensional space, far away from the range of parameters value with which the model has been trained. Therefore, taking into account that a global Kolmogorov width cannot be found for very complex problems but more low subspaces can be found for different ranges of time and parameters, local adaptive strategies are to be preferred and usually lead to more accurate and reliable results. In order to detect and check for low-dimensionality in complex problem, Williams et al. [79] proposed also an hybrid ROM integrator that uses two independent reduced order algorithm, namely Proper Orthogonal Decomposition and Dynamic Mode Decomposition (DMD), to elaborate a criterion able to determine if the ROM is accurate or not without directly evaluating the underlying system governing equations. Specifically, DMD and POD low-dimensional results are compared and if the two models produce different solutions, the algorithm switches back to the Full Order Model (FOM). The rationale behind the algorithm is that POD and DMD are two independent methods whose dynamics should agree on attractors. Therefore, the disagreement of the two methods should be an indicator that the dynamics does not lay anymore on a low-dimensional attractor and a Full Order Model is required again. It is worth noting that the method still remains heuristic and based on the assumptions that POD and

DMD are widely used models in the literature, with their efficacy tested on several problems exhibiting low-dimensional behaviour. Checking for the actual convergence of both POD and DMD to the low-dimensional attractors of complex nonlinear systems still remains an open mathematical question. This leads to possible uncertainties when the hybrid model needs to be generalized to any class of problems. In conclusion, the hybrid integrator represents only a step forward achieving a more reliable ROM in terms of detecting and describing low-dimensionality, but still not a final solution to the problem of identifying and reconstructing nonlinear attractors. This is also justified by the presence of different hybrid ROMs in the literature, which target problems with different complexities [80, 81, 82].

2.3 Reduced Order Models for fluid analysis and discovering time dynamics

As already stated in Section 1.1.1, one of the main objective of ROMs is to gain more physical insight into system dynamics. The current section offers a review of how this can be performed for fluid systems, focusing on the extraction of different sets of basis functions. Indeed, the ϕ presented in Equation 2.1 can be extracted using several different methods, and each algorithm used for their computation brings different information that can be useful to gain an understanding of the physical behaviour of the system. It is worth to highlight that the techniques reviewed here are data-driven based techniques, i.e. they compute the basis functions ϕ from a collection of available snapshots of the system. Naturally, there are ways to define the set of basis functions analytically, using for example Fourier or Wavelet Decomposition, but this will not explicitly consider the dynamics of the system, as it can be learned from actual realization of the system itself. One of the techniques most used and first to be introduced in the fluid dynamics community as a data-driven algorithm to compute basis functions ϕ is Proper Orthogonal Decomposition (POD). POD was introduced by Lumley [31] as a means to extract coherent structures in turbulent flows. Its widespread usage in many fields and fluid dynamics is strictly related to the main properties of the ex-

tracted basis. The set of ϕ is indeed optimal with respect to a specific norm (usually an L^2 or euclidean norm) and defines an orthonormal basis [23, 83]. The optimality property guarantees that the POD basis is the closest basis to the original dataset with respect to any other linear basis obtained adopting the same norm and for a given rank. Moreover, if velocity fields are processed, for the specific case of fluid dynamics problems, the euclidean norm used in the process represents the kinetic energy of the flow. Therefore the POD basis can be interpreted also as the one able to describe the most energetic structures in a fluid flow. The orthonormality of the basis set, instead, makes the POD basis very attractive to build ROMs, especially the ones based on projection techniques [54, 55, 56, 84, 85, 86]. Although its desirable properties and the simplicity of its algorithm, which is basically equivalent to a Singular Value Decomposition, it has been widely recognized in the literature that POD has limitations in extracting meaningful dynamical information, e.g. specific frequencies or stable/unstable behaviour in time. The energy criterion of POD does not always allow to isolate coherent structures with pure frequencies, assuming such structures are present in the flow field. What the method often extracts in this case instead is spatial features having multiple frequencies (frequency mixing). Moreover, the energy ranking of POD might also neglect the importance of less energetic structures that, despite their low energy content, are still important for the system dynamics. To deal with the frequency mixing problem and the lack of important dynamical information, Dynamic Mode Decomposition (DMD) was introduced by Schmid [46] in the fluid dynamics community. DMD takes directly into account the time dynamics underlying the collected data by considering a linear regression in time over all the set of available snapshots [87]. Each state is assumed to propagate in time by a constant matrix. From its basic assumption, DMD is able to extract spatial modes, namely dynamic modes, with associated frequencies and growth/decay rates. Differently from a Discrete Fourier Transform (DFT), which only extracts pure frequencies from data, DMD is therefore able to spot also transient dynamics of specific spatial structures through information coming from growth and decay rate coefficients, thanks to its linear system dynamics assumption. As for POD, also DMD has its limitations. When dealing with complex nonlinear dynamics, with-

out any specific frequency components, the spectral purity of DMD can indeed provide misleading information. Coherent structures that are mixed in frequencies might be possible in complex nonlinear flows, as well as dynamic features existing only in particular time windows, therefore a pure frequency decomposition might not be the most suitable for a dynamic analysis. As pointed out by Noack [71], a crucial point in fluid modal decomposition is how to bridge the energy optimality promoted by the POD and the spectral purity promoted by DMD and DFT, as these are both fundamental aspects to gain the correct understanding of the physics of a fluid flow. In the following, methods that try to correct the optimal property of the POD and the spectral purity of the DMD are reviewed.

2.3.1 Methods based on POD

The POD variants mentioned in the present section represent an effort to overcome the two main limitations of the POD algorithm: the energy ranking criterion used to classify the POD modes importance, which might neglect important dynamical features having low energy content; the frequency mixing in the set of flow features extracted. The Balanced POD (BPOD), proposed by Rowley [33], represents mainly an effort to overcome the first limitation. It combines balanced truncation [88] and POD in order to obtain a good approximation of balanced truncation for very high-dimensional systems, like the one arising from problems in fluid dynamics. Balanced truncation aims at finding a basis transformation where to represent the system dynamics. It has the main feature that observable and controllable states have the same importance. Here, controllability refers to the ability of an input to control the evolution of a state, observability, instead, measures the effect of a given initial state on future outputs. These two quantities are measured through two matrices, called controllability and observability Gramians, and the role of POD is to provide a low-dimensional approximation of these two Gramians. Considering the new system of coordinates defined by the BPOD basis, where observable and controllable states are balanced, showed to be an important aspect for describing transient dynamics in non-normal system [89], as more observable states are able to capture important dynamics features that are neglected by the energy based

modes coming from pure POD. Spectral POD, introduced by Sieber et al. [90], puts the effort in overcoming the frequency mixing limitation. Not to be confused with the POD in the frequency domain [91], it tries to bridge energy optimality of the POD and spectral purity of the DFT through the application of a filter in the POD algorithm. Since the dimension of the applied filter can be changed continuously, it is possible to gradually switch from POD to DFT. This should allow to extract also coherent features responsible for the flow dynamics that have multiple frequencies. Sieber et al. [36] show indeed for the case of a gurney flap configuration, a swirling combustor and a sweeping jet, how intermediate dimensions of the filter are able to extract coherent features and related dynamic information better than the DMD algorithm. Sieber et al. conclude that SPOD allows for a better separation of fluid structures into single modes, can solve for temporal dynamics also for partially recorded phenomena and ensures a smooth evolution of modes in time, as opposite to the chaotic evolution usually provided by POD. Nevertheless, the choice of the right filter dimension is something that cannot be defined a-priori and requires some knowledge of the problem at hand. A further step in isolating coherent features and bridging optimality and spectral purity was taken by Mendez et al. [37], introducing Multiscale Proper Orthogonal Decomposition (mPOD). The basic idea of mPOD is to apply a multi resolution analysis to the temporal correlation matrix of the POD in order to split contribution coming from different scales. Each contribution is then processed with the common POD algorithm, obtaining an orthonormal basis for each scale. The bases of each scale are finally merged together into a temporal basis and spatial structures are found. The algorithm proposed was applied to a synthetic dataset, a numerical and an experimental test-case and for each problem showed a good extraction capability of coherent features, a good time localization of these features and good convergence to the actual solution. Mendez et al. [37] therefore conclude that mPOD represents an excellent compromise between energy optimality and spectral purity, while also preserving the orthogonality of the basis set. All the POD variants presented are usually targeted to specific applications and generalization of these methods still provide room for further research and investigation. Indeed, Balanced POD requires specific datasets (inputs coming from impulsive re-

sponses of the systems) and its application is quite limited to experimental data, even if some additional work has already been envisaged in the direction of solving these limitations [21]. SPOD requires some previous knowledge of the problem at hand in order to exploit at best its capabilities. Moreover, non-orthogonality of its modes might represent a strong limitation for specific applications (e.g. projection-based ROM). Finally, Multiscale POD introduces additional complexities in the algorithm of feature extraction through elements of Multi-Resolution Analysis (MRA). This paves the way for further investigation on the specific parameters used for the MRA step, i.e. how to break different scales [92]. Nevertheless, mPOD remains one of the best methods proposed to isolate specific structures associated to different scales, while still preserving the original orthogonality property of the POD.

2.3.2 Methods based on DMD

The drawbacks of the DMD method for dynamical features extraction mainly derive from the assumption of linear dynamics. Moreover, it has been shown that data used for generating dynamic modes need to have specific properties in order for the DMD to be considered valid [93]. Although DMD has shown to approximate eigenvalues and eigenfunctions of Koopman operator [94, 95], which is an infinite dimensional linear operator for describing nonlinear dynamics, and therefore able to handle also nonlinear phenomena of some kind, it might generate misleading results for complex nonlinear and transient phenomena. Several variants of the DMD algorithm have been proposed to overcome its limitations. Optimal Mode Decomposition (OMD) by Wynn et al. [34] is presented as a generalization of the DMD algorithm. The DMD algorithm for fluid dynamics problems, where a huge number of DOFs have to be treated, needs a further reduction step to obtain eigenmodes and eigenvalues from the dynamic matrix of the linear system. This reduction step is usually performed projecting the dynamic matrix in the low-dimensional space identified by POD modes. OMD tries instead to define an optimal low rank space where to project the system dynamics and extract eigenvalues and eigenmodes of the system. The optimal low rank space is searched for using a conjugate-gradient based algorithm and tools from manifold theory. Although Wynn

et al. [34] were not able to prove if OMD is able also to provide a better estimation of the Koopman modes for a general nonlinear system, they showed how OMD outperforms DMD in terms of accuracy in describing system dynamics, even in presence of measurement noise, and also in spotting higher frequency modes in turbulence. Variants of DMD have been proposed also to address the specific problem of sensor noise, when dealing with experimental data, as the algorithm has shown to be quite sensitive to it [96]. MultiResolution Dynamic Mode Decomposition (mrDMD), introduced by Kutz et al. [97], represents the equivalent of mPOD in the realm of DMD algorithms, and allows to provide a separation of dynamics happening on different time scales. It combines tools from multi resolution analysis and the DMD algorithm. The mrDMD method recursively removes low-frequency content from the collected snapshots, providing a separation of dynamic phenomena that either have different temporal scales or are happening only on specific time intervals. It has been shown on different cases that mrDMD can perform very well in spotting localized dynamics, separating fast and slow modes and handling invariances in data such as translation and rotation. The Recursive Dynamic Mode Decomposition (RDMD) by [44] represents another method that, like the SPOD by Sieber et al., directly tries to bridge the POD optimality and DMD spectral purity. It is based on a recursive DMD modes extraction, where the mode that produces the least time-averaged error in reconstructing the initial snapshots data is selected at each step of recursion. Differently from SPOD, RDMD has the advantage to provide orthogonal modes, such as the POD algorithm, and does not need any filtering parameter to be tuned. Therefore, it is presented as a good compromise between POD and DMD. The High Order Dynamic Mode Decomposition (HODMD), introduced by Le Clainche and Vega [98], represents an extension of the DMD algorithm able to deal with systems presenting a very wide spectrum of frequencies that cannot be solved using the standard DMD algorithm. The spectral complexity of DMD, which is the maximum number of frequencies it is able to extract from available data, is indeed limited by the maximum number of available snapshots of the system. This might not be enough to describe the entire frequency spectrum. The HODMD enlarges this spectrum considering a matrix of time-lagged snapshots and applying the DMD algorithm

to it. As for the POD variants, also the algorithms proposed to overcome the limits of the DMD are targeted to solve specific limitations, usually related to the specific problem at hand. OMD is presented as a method that can introduce major improvements when measurement noise and high frequencies contribution are present in the collected data (specifically high frequencies related to turbulent flow dynamics). Multi-resolution DMD can isolate structures and dynamics happening on different scales, but it can easily incur in the problem of extracting many flow features since DMD on different scales needs to be applied. This can represent a drawback when a low-dimensional approximation is searched for and many different spatial and temporal scales need to be resolved. HODMD is presented as an alternative to DMD when not enough data are available to solve their entire spectral content and its applications are limited to instability analysis and identification of flow patterns in transient evolving towards attractors [98, 99, 100]. Finally RDMD has shown greater performance only when describing dynamics on attractors [44], with some degradation when transient behaviour is considered.

2.3.3 Recent developments using machine learning algorithms

POD, DMD and their variants presented in the previous Sections are all linear methods, as also stated in Section 2.1, where the main assumption is introduced in Equation 2.1. Nevertheless, high-dimensional data coming from nonlinear dynamics usually lie on low-dimensional manifolds that are nonlinear and therefore not well described by linear subspaces. The detection of nonlinear manifolds allows to extract more coherent spatial and temporal structures from data and furtherly reduces the space where the system dynamics is projected. It is natural to expect that to describe nonlinear manifolds with linear bases would require more DOFs to ensure a good accuracy. Recently, deep learning algorithms are also used to extract coherent features and are based on Convolutional Neural Networks (CNNs), mainly autoencoders [101]. They can lead to non-orthogonal spatial modes but they are still capable of describing the nonlinear embedding of low dimension [102]. Deep learning has also been used in the literature to improve the DMD approximation of the Koopman eigenvalues and eigenmodes [103].

Many other nonlinear algorithms have been introduced to build the low-dimensional embedding, which belong instead to the class of manifold learning techniques [104, 105], the most widely used being Self-Organizing Maps (SOMs) [106], ISOMAP [107], Locally Linear Embeddings (LLE) [108, 109] and Kernel methods, like Kernel Principal Component Analysis (kPCA [110]). The first two are based on the computation of geodesic distances to learn the shape of the manifold. Therefore a graph needs to be constructed and usually a Multi Dimensional Scaling (MDS) [111] is applied to define the actual dimension of the nonlinear manifold. The kernel methods, instead, are still based on euclidean distances and use nonlinear functions from a defined dictionary in order to take into account the nonlinearity of the manifold.

A good review of methods used in nonlinear dimensionality reduction is reported in [110]. Examples of applications and recent advances in the field of fluid mechanics are well described and summarized by [102]. Future perspectives for deep learning in fluid dynamics are also given by [112]. It is worth noting that all these methods will lose the characteristic linear modal decomposition reported in Equation 2.1 and therefore not always allow to compute a back mapping from the low-dimensional nonlinear manifold to the high-dimensional physical space. Moreover, it is also worth noting that the research on deep learning algorithms in fluid flows is still at its early stage and many aspects need to be further investigated. The main challenge is related to the many parameters to handle, which can easily lead to a condition where the level of complexity is comparable to that of the original high-dimensional model. Additional criticism addressed to models based on machine learning algorithms and deep learning is also related to: how to perform latent parameter searching; how to carry out a proper training that avoid overfitting; optimization issues that can be related to the presence of local minima, especially when very high-dimensional systems are treated [113]. All the points mentioned have led a wide part of the scientific community to continue using linear models, like the ones presented in Sections 2.3.1 and 2.3.2.

2.4 Reduced Order Models for fast simulations

The fluid modal analysis can be considered as the first step to elaborate ROMs, i.e. trying to define a low-dimensional space through some meaningful features able to catch the essential dynamics. Once some considerations related to what stated in Section 2.2 have been appropriately made and the ϕ have been determined through one of the algorithms presented in Section 2.3, a way to compute the coefficients a_i needs to be defined, in order to describe the dynamics into the low-dimensional space. The back mapping to the high-dimensional physical space is then easily done through Equation 2.1, considering only linear methods. These last two step represent the true computational speedup of the ROM. Indeed, the coefficients that need to be computed are only a few compared to the high number of DOFs of the original system, especially when dealing with problems in fluid dynamics, where very refined meshes are used in CFD simulations or PIV experimental measurements are performed with very high resolution cameras. Considering the time required for state-of-the-art CFD solver, the computational speedup a ROM can provide is therefore of several orders of magnitude. The current Section will present the various methods that have been used in the literature to compute the coefficients a_i . They can be classified in two categories, namely intrusive and non-intrusive methods, the former using the governing equation of the system, the latter being completely equation-free.

2.4.1 Intrusive techniques

Techniques classified as intrusive use the system governing equations to compute the coefficients a_i . Therefore these equations need to be known and careful considerations need to be taken in order to obtain stable and reliable ROMs.

Projecting the system of equations into the low-dimensional linear space defined by the ROM has been widely used in the literature as a means to compute the coefficients of the model [78, 114]. The two main preferred basis used as a starting point for the solution decomposition have been the POD basis [115] and the basis coming from the Reduced Basis Method [66, 116]. Depending then on the basis used for the projection

operation, the methods can be classified in Galerkin methods [55, 62], if the basis used for projection is the same used for the decomposition, and Petrov-Galerkin methods [117], if the basis for the projection and the basis for the decomposition are different. In both cases, low-dimensional operators depending only on spatial basis functions are computed offline once and for all, and a system of Ordinary Differential Equations (ODEs) is obtained for the set of coefficients a_i , that is much smaller than the original system of ODEs originating from the direct discretization of the original Partial Differential Equations (PDEs).

Galerkin methods have been widely studied in the literature for the incompressible Navier-Stokes equations. In this case, indeed, the entire set of reduced order Navier-Stokes equations is reduced to the momentum equation only, since the divergence property coming from the continuity equation is identically satisfied by the POD or ROM modes and the energy equation decoupled from momentum. Despite the apparent simplicity deriving from the reduction of the full set of Navier-Stokes equation to only one equation, there are issues related to the elaboration of Galerkin ROMs also for the case of incompressible flows. The main problem of such models is instability, especially on long time integrations, which is mainly related to the presence of transient dynamics, not properly described when higher order modes are truncated [33], and the pressure term appearing in the momentum equation [85]. This aspects need the introduction of ad hoc fixes. Cazemier et al. [118] addressed the problem of unsolved POD modes adding a damping term to the ROM to elaborate a closure model for long term prediction of a lid-driven cavity flow. This damping coefficient is a function of the retained modes and is computed from an energy conservation equation. In [86] instead, the pressure term problem is addressed, introducing a pressure extended ROM that takes into account a possible modeling of such term. Moreover, the problem of modeling finer scales associated to dissipation and enrichment of POD basis when changing some parameters of the system is considered. Caiazzo et al. [119] also proposes a novel velocity-pressure ROM, which uses pressure POD modes and shows improvements with respect to an only velocity POD modes based Galerkin ROM. Further developments on the stabilization of the pressure term are also presented by Ballarin et al. [60]. Also

a recent work [120] on POD-Galerkin models has investigated the problem of instabilities due to long time integration. Rubini et al. [120] showed that a specific data-driven sparsification and calibration of a Galerkin based ROM is able to improve the temporal stability of the model. Specifically, the method has shown to outperform Galerkin dense models (i.e. not involving sparsification) in predicting the turbulent kinetic energy and its power spectrum. Examples are present in the literature that try to expand Galerkin models to the case of compressible flows [59, 61]. Rowley et al. [48] shows a particular definition of the POD norm, which links all the independent variables in a consistent way, to define a Galerkin model for slightly compressible flows. Nevertheless, a common issue when dealing with the full set of Navier-Stokes equations or for complex flows in general, is the treatment of the nonlinear term, which strongly compromises the efficiency of the ROM as it has to be updated at each step of the computation. Also elaborating Galerkin models considering the full set of Navier-Stokes equations represents a very cumbersome task [114], as the projection operations required increase exponentially with the number of modes retained, due to the presence of the nonlinear terms. The work of Rubini et al. [120], already cited above, also addressed this problem, introducing an l_1 regularised regression approach that aims at retaining only important quadratic interactions between modes, which are resulting from the nonlinear term. To avoid the problem of nonlinearities of the full set of Navier-Stokes equations, techniques have also been proposed in the literature that introduce an *hyper-reduction* step, focused on how to accelerate the computation of the nonlinear term. A widely used method has been the Discrete Empirical Interpolation Method (DEIM) [121] that tries to describe the nonlinear term through the evaluation of the nonlinear function only at some meaningful points. Another class of intrusive techniques is based on a residual minimization step. Coefficients a_i are computed as the solutions of a minimization problem once the decomposition in Equation 2.1 is substituted into the governing equations of the system. The residual, coming from the particular discretization of the system of PDEs, is computed as a function of the coefficients a_i and the optimization problem is solved [24]. Residual minimization techniques have been used also to elaborate hyper-reduction models for the compressible set of Navier-Stokes equations and

usually belong to the class of nonlinear model reduction methods based on POD and using Petrov-Galerkin projection [122]. A well known residual minimization method is the Gauss-Newton method of approximated tensors (GNAT), introduced by Carlberg et al. [57]. Amsallem et al. [123] also reported a discussion on the importance of defining a proper norm for the residual involved in the minimization procedure. Specifically the work introduces a new residual norm definition in the effort to make the model reduction process independent from mesh spacing consideration, i.e. different influence of small and large cells.

2.4.2 Non-Intrusive techniques

To avoid the problems arising from acting directly on the governing equations of the system under study, which for fluid dynamic problems means the need to access the source code of the CFD solver, and to circumvent all the issue related with projection operation, non-intrusive ROMs have been widely implemented and used in the literature. The coefficients a_i are in this case computed with completely equation free techniques that involve regression or interpolation. The *online* phase of the final ROM, therefore, becomes completely independent from the original system of equations. Non-intrusive ROMs might be very useful when governing equations of the system are unknown, in case of data collected through experiments, and can be also used to infer dynamic equations of the system, using techniques from symbolic regression. A recent introduced algorithm that operates in this direction is the Sparse Identification of Nonlinear Dynamics (SINDy), introduced by Brunton et al. [124]. Despite its great success, marked by the combination of symbolic regression techniques with algorithms to promote sparsity, SINDy has its own limitations. Indeed, the accuracy of the method strongly depends on the sampling, how the time derivatives used to train the dynamic model are computed, and the dictionary of functions defined before the sparse algorithm is executed. Although a dictionary of polynomial functions has been quite extensively tested on fluid dynamics problems [125], this has been limited to problem exhibiting periodic and/or quasi-periodic behaviour, for which the existence of a low-dimensional attractor is known a-priori. Extension to problems with stronger nonlinearities and

transient [126], as well as adapting the algorithm for very high-dimensional problems as the one arising from complex fluid dynamics, is still an open field of research. Indeed SINDy and similar algorithms are usually applied after an initial reduction step is carried out, e.g. using POD or other techniques from machine learning.

Other techniques for non-intrusive ROMs, specifically oriented to the computation of coefficients, can be interpolation based or operator based. Stochastic regression and interpolation based techniques mainly used in ROMs are kriging [127, 128, 129] and Radial Basis Functions (RBF) [130, 131, 132] respectively. This last technique will be the one used in the present work and will be introduced in detail in Chapter 3, when discussing about the online Reconstruction methods. More recently, also regression techniques based on Gaussian Processes [133] have been introduced to define the mapping between time-parameters inputs and the coefficients of the ROM [134].

Operator based techniques provide an analytical expression for the coefficients. The DMD algorithm belongs to this class, which extracts a set of coefficients a_i with a particular frequency and growth/decay rate and amplitude that can be computed with specific algorithms [35, 87]. Cammilleri et al. [135] applies the DMD algorithm on the POD coefficients to determine the time dynamics in the low-dimensional attractor identified by POD. Limitations of using DMD operator based techniques are linked to the discussion already reported in Section 2.3 and can be summarized with the difficulty of expressing transient and nonlinear dynamics with a linear operator. Other examples of operator based techniques come from Global Stability Analysis [136, 137, 138], which allows to express the time evolution of global stability modes in an analytical manner, together with its complementary method for nonlinear problems, that is resolvent analysis [139, 140]. However, their application is limited to the identification of growth and/or decay rates of perturbations with respect to a given base or mean flow. Moreover, both approaches require discretized operators from the Navier–Stokes equations to perform the modal stability analysis.

Koopman operator is instead a nonlinear operator, which represents a good alternative to the linear operators presented above in order to express nonlinear dynamics [141]. Although it has been investigated in the literature for a long time [95, 142, 143], the

definition of a Koopman operator, i.e. Koopman eigenmodes and eigenfunctions, for fluid dynamics problem is an open field of research. The main challenge is related to the main characteristic of the Koopman operator, which is an infinite-dimensional operator.

Recent developments in Neural Network have also paved the way to compute coefficients of a ROM in a non-intrusive manner using deep learning algorithms. Besides extracting coherent features using CNNs, as already shown in Section 2.3.3, Neural Networks are also used to compute the evolution of the coefficients. Many techniques are usually hybrid, combining a POD extraction stage with a Neural Network for computing coefficients [42, 144, 145, 146]. Other non-intrusive techniques use instead an entire ML framework from the extraction stage till the online phase [101, 147]. In both cases, machine learning algorithms used for the definition of reduced order models are still an early area of research and present some limitations linked to overfitting, lack of interpretability, many hyper-parameters and challenges in introducing physical constraints as opposed to linear techniques.

In conclusion, non-intrusive techniques based on interpolation methods represent a good compromise in terms of generalizability and level of complexity of the model. Indeed, they do not need to access the set of underlying governing equations of the problem while computing ROM solutions and they do not require the tuning of many hyper-parameters, which is instead needed for machine learning approaches. As regards instead the intrusive techniques reviewed in Section 2.4.1, they are usually targeted to very specific class of problems and require remodelling on the basis of the specific set of equations at hand, and therefore they are less prone to generalization. For the specific case of fluid dynamic problems, ad hoc intrusive techniques need to be defined depending on the compressible or incompressible nature of the flow, the specific discretisation used for the set of equations(e.g. Finite Volume, Finite Element, Finite Difference), and considerations on time stability issues related to long time integration.

Chapter 3

Assessment of different Basis Extraction Methods

Central to linear reduced modeling is the identification of a number of flow primitives, also referred to as flow structures, modes or basis functions, capable of representing the essential dynamics of complex fluid flows. The algorithm used to obtain these flow features is crucial in defining the quality of dynamic information extracted and also the accuracy in the final reconstruction of the system dynamics. Different algorithms are presented and a comparative analysis is carried out to assess the performance of the resulting flow features in capturing the essential dynamics of unsteady flows. The impulsive start of a NACA0012 airfoil converging to a periodic attractor and a multi-element airfoil converging to a steady state flow will be used in this chapter to carry out the assessment. The key message resulting from this analysis is that for problems of unsteady aerodynamics presenting nonlinear advection and interaction of spatial structures, such as the dynamics resulting from impulsively started airfoils, there is not a unique set of modes that can be considered the best in describing such dynamics.

3.1 The importance of using different basis functions

As already pointed out in Chapter 2, the flow features, alias modes or basis functions ϕ of a fluid system, can be extracted using different methods. Each method performs

a transformation of system coordinates that tries to compress the information content coming from the collected snapshots in only few modes. Then, depending on the specific algorithm used, the compression of data can unveil different patterns. The present Chapter reports a numerical study of the influence of a particular set of basis functions on the accuracy in reconstructing complex dynamics of fluid flows. All the methods considered are linear methods and therefore can be fully described through Equation 2.1. The Chapter is structured as follows: Section 3.2 presents in more details the linear methods considered for the comparative study; Section 3.3 describes the non-intrusive formula used to compute the evolution coefficients of the low-dimensional model; Section 3.4 reports a comparative study on two 2D test-cases, typical of aeronautical flows, namely the impulsive start of a NACA0012 airfoil, converging to a periodic limit cycle, and a multi element 30P30N airfoil, converging to a steady flow state.

3.2 Methods for Basis Extraction

The present Section offers a more detailed description of the ROMs used to perform the comparative study. Among the several algorithms available in the literature for feature extraction, the ones that promote a strong dimensionality reduction and decompose the flow according to Equation 2.1, i.e. linear methods, are considered. Specifically Proper Orthogonal Decomposition (POD) [83] for its optimality property, Dynamic Mode Decomposition (DMD) [46] for its ability to extract pure dynamic information, Spectral POD [36] and Recursive DMD [44], since they try to bridge the optimal property of POD and spectral purity of DMD. All the methods, with the specific quantities involved, will be introduced for the specific case of fluid dynamics problems for which CFD solutions are available. Nevertheless, an extension is straightforward to any kind of problems that exhibit temporal dynamics and for which data can be collected. In the following, \mathbf{u} will indicate a column vector that collects the solution of a fluid dynamic problem at each point of a computational grid. When more than one variable is considered in the process, they can be processed in two different ways: either they are stacked in a unique vector, for example when dealing with vector quantities such

as velocity, momentum, vorticity, etc, and projected in the same low-dimensional space elaborating a unique ROM, or they are processed independently and a ROM is defined for each quantity. The first approach will be the one considered for the analysis presented in the current Chapter, since the velocity vector will be the quantity processed by the ROM. The second approach will be adopted when different physical quantities will be considered in the process, such as the entire set of conservative variables coming from the Navier-Stokes equations. For this case, indeed, it can be unphysical to define a unique norm and consider the same low-dimensional evolution for the entire vector \mathbf{u} .

3.2.1 Proper Orthogonal Decomposition

POD allows to extract an optimal basis from a given set of snapshots in terms of a specific norm, defined over the N_p -dimensional space spanned by the snapshots. For a CFD simulation, N_p is the number of grid points defined by the mesh times the number of unknowns chosen to build the reduced basis. The unknowns can be the entire set of conservative variables, coming from the set of Navier-Stokes equations, or a specific kinematic or thermodynamic variable. The norm used hereafter is the 2-norm based on the euclidean distance, therefore for each snapshot

$$\|\mathbf{u}\|_2 = \sqrt{\sum_{i=1}^{N_p} u_i^2} \quad (3.1)$$

According to the discussion reported above, \mathbf{u} can be a vector containing the solution of a scalar field in each point of the computational mesh or, in case of vector fields, a unique vector containing each scalar component stacked on top of each other (see also Equation 3.19). Therefore N_p can be either the number of grid points or the number of grid points times the number of scalar fields considered. The POD optimality condition, which allows to extract the closest basis to the initial dataset, is then defined

$$\max_{\phi_i \in \mathbb{R}^n} \langle \mathbf{U}, \phi_i \rangle \quad \text{with} \quad \|\phi_i\|_2 = 1 \quad i = 1, 2, \dots, N_s \quad (3.2)$$

where $\langle \cdot, \cdot \rangle$ represents the average over time, \mathbf{U} is the matrix of the collected snapshots, $\{\mathbf{u}_1, \mathbf{u}_2, \dots, \mathbf{u}_{N_s}\}$ with size $N_p \times N_s$ and N_s represents the number of collected snapshots, with $N_s \ll N_p$ for fluid dynamic problems. The solution of the optimal problem in Equation 3.2 can be found using different algorithms. The most widely used is SVD. Once the matrix \mathbf{U} has been filled with the computed snapshots \mathbf{u}_i , the POD modes are computed with the following matrix decomposition

$$\mathbf{U}_{N_p \times N_s} = \mathbf{\Phi}_{N_p \times N_s} \mathbf{\Sigma}_{N_s \times N_s} \mathbf{A}_{N_s \times N_s}^* \quad (3.3)$$

where the matrix $\mathbf{\Phi}$ contains the POD spatial functions, i.e. POD modes, the matrix \mathbf{A} their relative time dynamics (the * indicates the transpose conjugate) and the matrix $\mathbf{\Sigma}$ is a diagonal matrix containing the square root of the POD eigenvalues, which give a quantitative measure of the energy associated to each mode. Specifically, the energetic content of each mode is given by $E_i = \sigma_i^2$, where σ_i is the generic diagonal element of the matrix Σ . The SVD is the most robust and stable algorithm to compute POD modes [2], nevertheless it can be very computationally expensive for vectors coming from fluid dynamics problems (the computational cost scales with $O(N_p^3)$), where the row size of matrix \mathbf{U} can be very high, of the order of the DOFs of the CFD simulations. A much less expensive method for very huge problems is the method of snapshots from Sirovich [148]. The method is based on the assumption that POD modes can be expressed as a linear combination of the initial snapshots

$$\phi_i(\mathbf{x}) = \sum_{i=1}^{N_s} b_i \mathbf{u}_i \quad (3.4)$$

therefore the procedure used to extract POD modes is equivalent to solving the following eigenvalue problem

$$\mathbf{R} \mathbf{a}_i = \lambda_i \mathbf{a}_i \quad (3.5)$$

where \mathbf{R} is the POD temporal correlation matrix, defined as $\mathbf{R} = \mathbf{U}^* \mathbf{U}$ and therefore with size $N_s \times N_s$, $\lambda_i = \sigma_i^2$ are the POD eigenvalues. The vectors \mathbf{a}_i are the eigenvectors of the temporal correlation matrix and are equivalent to the right singular vectors in

Equation 3.3. Once the eigenvalue decomposition problem is solved, the POD modes can be recovered as follows

$$\phi_i = \frac{1}{\sqrt{\lambda_i}} \mathbf{U} \mathbf{a}_i \quad (3.6)$$

The division by $\sqrt{\lambda_i}$ represents a normalization of the POD modes and the ϕ_i in formula 3.6 are equivalent to the modes collected in the columns of matrix Φ in Equation 3.3. For fluid dynamics problems, the size of the matrix \mathbf{R} is considerably lower than the matrix of snapshots \mathbf{U} ($N_s \ll N_p$), therefore the eigenvalue problem defined through the method of snapshots represents a faster method to compute POD modes and it is also the algorithm that will be used in the present work. The Eigen Library [149] is used in the present work to solve the eigenvalue problem in Equation 3.5 and perform all the matrix operations needed for the basis extraction. This will also be the library used for the implementation of the algorithms presented hereafter.

3.2.2 Spectral Proper Orthogonal Decomposition

The Spectral POD is structured around the POD approach using the method of snapshots. The idea behind Spectral POD is to introduce a filter applied to the correlation matrix \mathbf{R} , which leads to the following filtered matrix

$$R_{f_{i,j}} = \sum_{k=-N_f}^{N_f} g_k R_{i+k,j+k} \quad (3.7)$$

Boundary conditions need to be defined for the matrix \mathbf{R} in order to apply the filter to all the elements of the matrix. For more in-depth discussion on how to impose boundary condition to the matrix \mathbf{R} and alternatives to the zero-padded boundary condition the reader can refer to [36]. The rationale behind the filtering process is to circumvent the POD limit in separating spatial structure and temporal evolution. The SPOD, in fact, considers a spatio-temporal evolution across a time span related to the size of the filter during the modes extraction. This leads to the main difference between snapshot POD and SPOD: the former reveals the more likely states of the system among all the collected snapshots [31], whereas the latter reveals similar space-time trajectories

within the original data [90].

From Equation 3.7 it can be noticed how the SPOD filter acts along the diagonal of the temporal correlation matrix, which is equivalent to weight elements characterized by the same Δt in time (the function $R(t_1, t_2)$ evaluated for different t_1 and t_2 , keeping $t_1 - t_2 = \Delta t$ constant). This procedure leads to a redistribution of the energy levels E_i defined above within the modes with respect to POD. The weights g_k can be defined in different ways, but the most reasonable choice is either a box filter, with $g_k = \frac{1}{1+N_f} = const.$, or a Gaussian filter with certain variance. The choice of the weights should reflect the evolution of specific spatial structures over time sub-windows and, therefore, it can take advantage of some previous knowledge about the investigated flow dynamics. When no considerations about the evolution of specific fluid structures can be inferred a-priori from the fluid flow, which is the case of the problems considered later in this Chapter, the simplest assumption of a box filter is made and the behaviour of the method is also investigated varying the size of the filter N_f (see Sections 3.4.1 and 3.4.2).

Once the \mathbf{R}_f matrix is computed, the procedure to extract spatial and temporal modes proceeds in the same way as POD. The new eigenvectors extracted from the filtered matrix \mathbf{R}_f are still orthogonal (the filtering operation preserves the symmetry of the correlation matrix), whereas the spatial modes ϕ are not anymore, at least in a POD sense [90]. It is worth to notice that, when the filter in Equation 3.7 acts over the entire correlation matrix, the SPOD is equivalent to a Discrete Fourier Transform (DFT) [150, 151]. Therefore, hereafter, every time the SPOD is performed, using N_f equal to the size of the matrix \mathbf{R} , it will be referred to as DFT.

3.2.3 Dynamic Mode Decomposition

The DMD extraction technique is based on the following assumption

$$\mathbf{u}^{n+1} = \mathbf{T}\mathbf{u}^n \quad (3.8)$$

where \mathbf{u}^{n+1} represents solution at discrete time $n + 1$, \mathbf{u}^n the solution at discrete time n and \mathbf{T} is a linear time dynamics matrix with size $N_p \times N_p$. Equation 3.8 therefore defines the linear dynamics that best fits the initial set of snapshots. The DMD algorithm to extract dynamic modes and eigenvalues was first introduced by Schmid [46] and Rowley et al. [94] as a variant of the standard Arnoldi algorithm. It aims at computing Ritz eigenvalues and eigenvectors of a companion matrix coming from the assumption that the last snapshots \mathbf{u}^n at time t_n can be expressed as a linear combination of the previous $n - 1$ ones. Nevertheless, the procedure is numerically unstable, especially for very large problems, since it has to deal with an eigenvalue problem applied to a matrix in companion form. Therefore, an alternative algorithm will be briefly presented, following the one reported in [87, 93], and it will be the one used in the present work. A straightforward way to extract DMD modes is indeed to compute the eigenvalue decomposition of the matrix \mathbf{T} , which will be called the dynamic matrix of the approximated linear system. For fluid dynamics problems, the dimension of this matrix might be very high ($N_p \gg 1$), therefore a reduction step is performed in order to circumvent such an expensive step, as it will be shown below. The set of initial snapshots is collected into two matrices whose columns differ by a time shifting of Δt , namely $\mathbf{U} = [\mathbf{u}_1 \ \mathbf{u}_2 \ \dots \ \mathbf{u}_{N_s-1}]$ and $\mathbf{U}' = [\mathbf{u}_2 \ \mathbf{u}_3 \ \dots \ \mathbf{u}_{N_s}]$. Equation 3.8 can be expressed for the entire set of snapshots

$$\mathbf{U}' = \mathbf{T}\mathbf{U} \quad (3.9)$$

An SVD is then applied to the matrix \mathbf{U} , expressed as in Equation 3.3, and the following similarity transformation is applied to express the time dynamics in a low-rank space

$$\tilde{\mathbf{T}}_{N_m \times N_m} = \mathbf{\Phi}_{N_p \times N_m}^* \mathbf{T}_{N_p \times N_p} \mathbf{\Phi}_{N_p \times N_m} \quad (3.10)$$

where the $\mathbf{\Phi}$ are the equivalent of the POD spatial modes as defined in Equation 3.3. Combining Equation 3.9 with the SVD of \mathbf{U} , Equation 3.3, and solving for \mathbf{T} , the following expression is obtained for the low rank matrix $\tilde{\mathbf{T}}$, which circumvents the

computation of the high-dimensional matrix \mathbf{T} [87]

$$\tilde{\mathbf{T}}_{N_m \times N_m} = \mathbf{\Phi}_{N_p \times N_m}^* \mathbf{U}'_{N_p \times N_s} \mathbf{A}_{N_s \times N_m} \mathbf{\Sigma}_{N_m \times N_m}^{-1} \quad (3.11)$$

It becomes clearer, at this stage, that the new matrix $\tilde{\mathbf{T}}$ might be of many order of magnitude smaller than the initial matrix \mathbf{T} for fluid dynamics problems ($N_m \leq N_s \ll N_p$). A further reduction step is implicitly considered in Equation 3.11, where only the first N_m columns of the matrix $\mathbf{\Phi}$ are retained on the basis of the singular values, $N_m \leq N_s$ (the reader can refer for example to the singular value hard threshold method [152]).

An eigenvalue problem is then solved on the reduced matrix $\tilde{\mathbf{T}}$ and the computed eigenvectors can be projected again on the high-dimensional space using the similarity transformation in Equation 3.10, obtaining the spatial DMD modes. In particular, the i -th DMD mode is recovered as follows

$$\phi_i = \frac{1}{\lambda_i} \mathbf{U}' \mathbf{A} \mathbf{\Sigma}^{-1} \mathbf{w}_i \quad (3.12)$$

defined as the exact DMD mode in [93]. In Equation 3.12, λ_i and \mathbf{w}_i represent the i -th eigenvalue and eigenvector respectively of the reduced dynamic matrix $\tilde{\mathbf{T}}$. The time dynamics is recovered from the eigenvalues λ_i , whose real and imaginary part provide the growth/decay rate and the frequency of each mode. Since it is a linear regression over the entire set of snapshots, the DMD might not be the best choice to express complex evolution in time even if all the modes coming from the presented algorithm are used.

3.2.4 Recursive Dynamic Mode Decomposition

The Recursive DMD introduces a procedure for feature extraction that combines the extraction algorithm coming from the DMD with the optimality condition of the POD. The modes are extracted recursively selecting at each step of recursion the DMD mode that is the closest to the set of data. The closest mode at each step of the recursion is

selected in terms of the minimum of the vector of residuals

$$\min_{i \in \{1, 2, \dots, N_s - 1\}} = \|\mathbf{U}_r - \phi_{i,r} \mathbf{a}_{i,r}\|_2 \quad (3.13)$$

where \mathbf{U}_r is the set of data the DMD extraction is applied to at the r -th step of recursion, whereas $\phi_{i,r} \mathbf{a}_{i,r}$ represents the reconstruction computed considering only the i -th DMD mode at the r -th step of recursion. The quantity \mathbf{U}_r is calculated by subtracting the contribution of the first $r - 1$ modes from the set of initial snapshots. The RDMD technique has shown to outperform even the POD in the description of the limit cycle [44], which will be proved also for the test-cases presented in this work.

3.3 Non-Intrusive Reconstruction method

Depending on the method chosen to extract the basis, two distinct expressions for reconstruction have to be considered

$$\mathbf{u}(\mathbf{x}, t) \approx \hat{\mathbf{u}} = \sum_{i=1}^{N_m} a_i(t) \phi_i(\mathbf{x}) \quad (3.14)$$

$$\mathbf{u}(\mathbf{x}, t) \approx \hat{\mathbf{u}} = \sum_{i=1}^{N_m} \alpha_i \phi_i(\mathbf{x}) e^{\omega_i t} \quad (3.15)$$

Both equations are in accordance with the linear decomposition presented in Equation 2.1, with the main difference that Equation 3.15 provides an explicit analytical expression for the time evolution of coefficients a_i . Equation 3.14 is used in the case of POD, SPOD and RDMD and it performs an interpolation to calculate solutions outside the training points (non-intrusive technique). Equation 3.15, used in the case of DMD, represents an explicit function of time and does not require any further operation to reconstruct the flow field, once the basis is extracted and the constant coefficients α_i are computed, as shown below. Therefore, in all cases a completely equation-free approach is adopted for the online phase of the ROM and governing equations are not considered to compute online solutions. The interpolation technique used for Equation

3.14 is radial basis function (RBF)

$$a_i(t) \approx p(t) + \sum_{j=1}^{N_s} w_j f(|t - t_j|) \quad (3.16)$$

where $p(t)$ is a polynomial of low degree and the basis function f is a real valued function on $[0; \infty)$ [153]. The basis functions used in the present work are mainly linear or gaussian functions, namely $f_j = |t - t_j|$ and $f_j = e^{|t - t_j|}$. The t_j are referred to as the centers of the RBF and they are the time instants corresponding to the components of the POD eigenvectors \mathbf{a}_i in Equation 3.5. For the coefficients α_i in the Equation 3.15 the following optimization problem is solved

$$\min_{\alpha_i \in \mathbb{R}^r} \|\mathbf{U}' - \Phi \mathbf{D}_\alpha \mathbf{V}\|_2 \quad (3.17)$$

where \mathbf{D}_α is a diagonal matrix containing the DMD coefficients α_i , r is DMD rank, i.e. the number of DMD modes extracted, and \mathbf{V} is the Vandermonde matrix built with DMD eigenvalues

$$\mathbf{V} = \begin{bmatrix} 1 & \lambda_{1,\text{DMD}} & \lambda_{1,\text{DMD}}^2 & \cdots & \lambda_{1,\text{DMD}}^{N_s-1} \\ 1 & \lambda_{2,\text{DMD}} & \lambda_{2,\text{DMD}}^2 & \cdots & \lambda_{2,\text{DMD}}^{N_s-1} \\ \vdots & \vdots & \vdots & \ddots & \vdots \\ 1 & \lambda_{N_s-1,\text{DMD}} & \lambda_{N_s-1,\text{DMD}}^2 & \cdots & \lambda_{N_s-1,\text{DMD}}^{N_s-1} \end{bmatrix} \quad (3.18)$$

The optimization in Equation 3.17 is convex and can be solved analytically for the coefficients α_i in matrix D_α . The reader can refer to [35] for further details.

3.3.1 A note on rank reduction

The number of modes N_m used in the reconstruction formulae (3.14) and (3.15) defines the further rank reduction performed by the single ROM, $N_m \leq N_s \ll n$, with n the number of DOFs of the initial high-dimensional problem. The main aim of the rank reduction is to reduce as much as possible the computational cost and the number of DOFs to deal with, while preserving sufficient accuracy in describing the dynamics of

the system. There is not a universally recognized criterion to define the rank reduction due to the lack of rigorous a-priori error bounds, especially when the ROM is used for predicting solutions out of the training samples. Indeed, the accuracy of ROMs is usually reported varying the number of modes [118, 122]. Since the aim of Section 3.4 is to highlight how different methods perform while using a low-dimensional space of the same rank, the number of modes is fixed and chosen to be less than the initial number of snapshots. These modes are selected in terms of the N_m highest contributions in the reconstruction formulae (see Equations 3.14 and 3.15), which is equivalent to keep the modes associated to the highest eigenvalues for POD, the modes with the highest euclidean norm for SPOD and the first N_m modes for RDMD. For the specific case of DMD, instead, the reduction step preserves the N_m columns of the matrix Φ associated to the highest singular values σ_i in Equation 3.10, and all the modes extracted from the low-rank dynamics are retained (singular value truncation).

3.4 Comparative Analysis on the accuracy in reconstruction

It has been widely discussed in the literature how POD-based methods provide the optimal basis to describe an ensemble of collected snapshots in terms of the least square error between the original data set and the basis extracted. Nonetheless, this optimality condition is defined on an average over all the set of snapshots and it could penalize snapshots that are not important in an energetic sense but fundamental for the unsteady dynamics. Therefore, relaxing this optimality condition could sometimes lead to better results in terms of reconstruction over the whole time interval. The comparison of different methods is presented in terms of the ability to reconstruct a flow field at various time steps. Two test-cases will be considered here, namely the impulsive start of a NACA0012 airfoil and the high-lift configuration 30P30N [154].

For the specific case of SPOD, for each test-case a box filter will be considered, using also different sizes, and zero-padded boundary conditions will be used for the temporal correlation matrix. Each reduced model will be built for the velocity field only, treated

as a unique vector. A unique low-dimensional space is therefore defined for all the components of velocity and the column vector \mathbf{u} will be arranged as follows

$$\mathbf{u} = \begin{bmatrix} \mathbf{u}_x \\ \mathbf{u}_y \\ \mathbf{u}_z \end{bmatrix} \quad (3.19)$$

where \mathbf{u}_x , \mathbf{u}_y and \mathbf{u}_z represent the velocity components, each one a vector containing the discretised solution over the computational domain.

The CFD snapshots used to build the ROM are computed using the open-source Finite Volume solver SU2 [155]. A C++ code based on the Eigen library [149] for matrix operations implements the various algorithms presented in Section 3.2 and the non-intrusive reconstruction reported in Section 3.3, and it is used for the comparative analysis performed in the current Section. A configuration file is provided as an input to the code, which allows to define the ROM method to be performed and its specifications (e.g. number of snapshots to use, rank of the ROM, query points where to reconstruct the solution, etc.). A run of the code consists of reading the snapshots computed by the SU2 solver, extracting flow features ϕ_i and training coefficients a_i/α_i for the specified method, compute the reconstruction at desired query points in time.

A note on the convergence study of CFD solutions. The main aim of the work presented throughout this thesis is to demonstrate the ability of linear ROM methods, targeted for unsteady fluid flows, to resolve the essential dynamics contained in the initial snapshots. Therefore, the reference dynamics is assumed to be the one contained in the snapshots, regardless of how they are computed. The only aspect worth to highlight is that the snapshot computation often requires both high computational effort and high memory storage, which defines the need for a ROM. On the basis of these observations, a rigorous unsteady convergence study, in terms of resolution in space and time, has not been carried out for the test-cases presented in the later Sections and Chapters of the thesis. Nevertheless, for each test-case, an effort has

been put in defining the mesh used in order to solve as much as possible the expected dynamics, both in terms of time and space resolution of the original CFD simulation. In this effort, also some choices in terms of maximum space-time resolution have been done on the basis of the computational resources available for the present work.

For the specific case of the 30P30N geometry presented for the first time in Section 3.4.2, an unsteady CFD solution is reported on two different meshes, in order to practically show the effort invested in the choice of the mesh for the different test-cases. The mesh indicated with M1 has 559,652 elements and 327,733 grid points, while the mesh indicated with M2 has 1,221,067 elements and 688,721 grid points. Details of the simulation setup are given later in Section 3.4.2 when the test-case is introduced. Figure 3.1 shows the solution on the two different meshes in terms of filled contours of the Mach number for four instants of time. An impulsive start from freestream conditions is considered. In particular, the first two rows report a close-up view of the flow field near the flap region of the 30P30N geometry at two instants after a small time from the impulsive start. The last two rows report instead two later time instants, when the starting vortex is almost fully developed and it is only convecting downstream. It can be observed how, despite the small differences on the two meshes, the coarse one (left column in Figure 3.1) is able to describe with good resolution the dynamics that is expected from the specific geometry and the specific setup defined. For expected dynamics of this test-case, it is intended for example the formation of small vortical structures generated from the various component of the 30P30N geometry, namely slat, main component and slat, two of which are visible on both meshes at the first two time instants represented in Figure 3.1. Another feature visible on both meshes is the merging of the vortex structures generated from the flap and main component in a single starting vortex propagating downstream, together with the convection of the vortex generated by the slat towards the wake formed downstream of the flap (last two rows in Figure 3.1). For completeness, Figure 3.2 reports also the plots of the Pressure Coefficient on the surface of the 30P30N geometry for the same time instants reported in Figure 3.1. These results show in practice what have been the aspects considered in defining the mesh for the various test-cases together with the limitations linked

to the computational resources available (especially for the 3D test-cases), without considering a rigorous grid convergence study. It is worth highlighting again that the practical choice of space-time resolution for the various test-cases is not an alternative to a rigorous space-time convergence study, but it is the solution taken in the present work in order not to remove the focus from the main aim of the analysis.

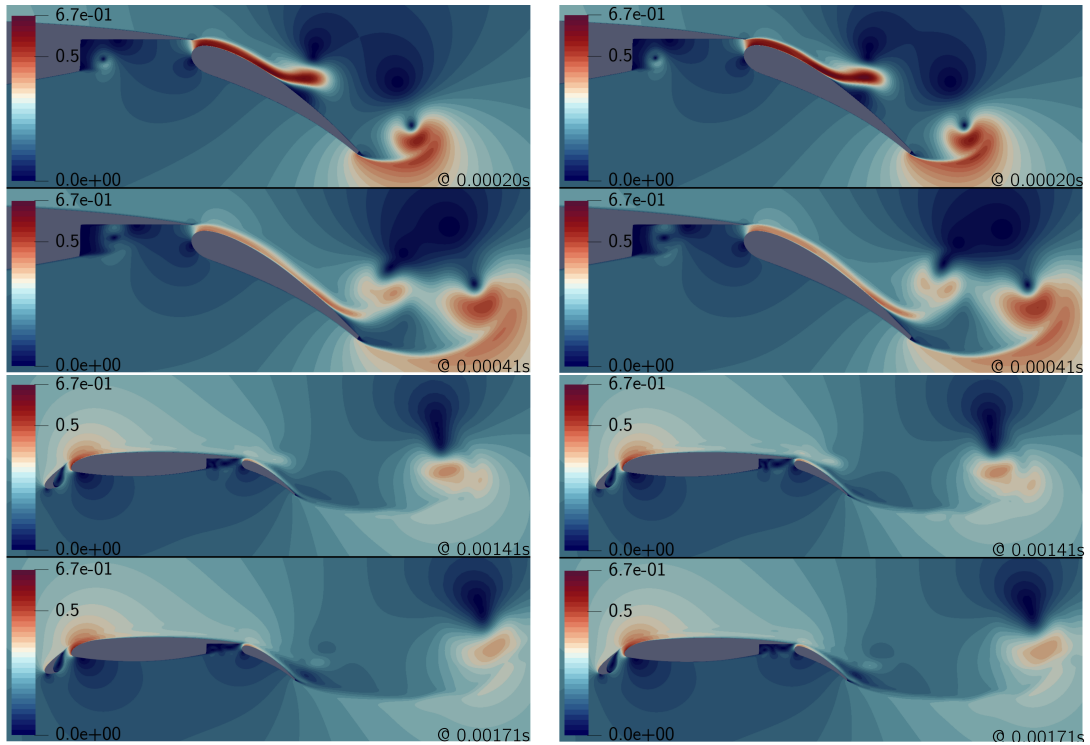


Figure 3.1: Evolution in time in terms of Mach number of an impulsive start of the 30P30N geometry, used later as a test-case, on two different meshes. Left column represents the solution on mesh M1 (coarse), right column represents the solution on mesh M2 (fine). The first two rows report a close-up view near the flap at earlier instants of time. The last two rows report the flow around the entire geometry once the starting vortex has fully developed and is propagating downstream.

3.4.1 NACA0012 test-case

The impulsive start of a NACA0012 airfoil is considered first. The parameters used for the unsteady simulation are summarized in Table 3.1. The Mach number, Reynolds number and angle of attack are fixed respectively to $M = 0.1$, $Re = 10,000$, $\alpha = 15$ deg. Under these conditions, a vortex-dominated flow is established. In particular, the flow

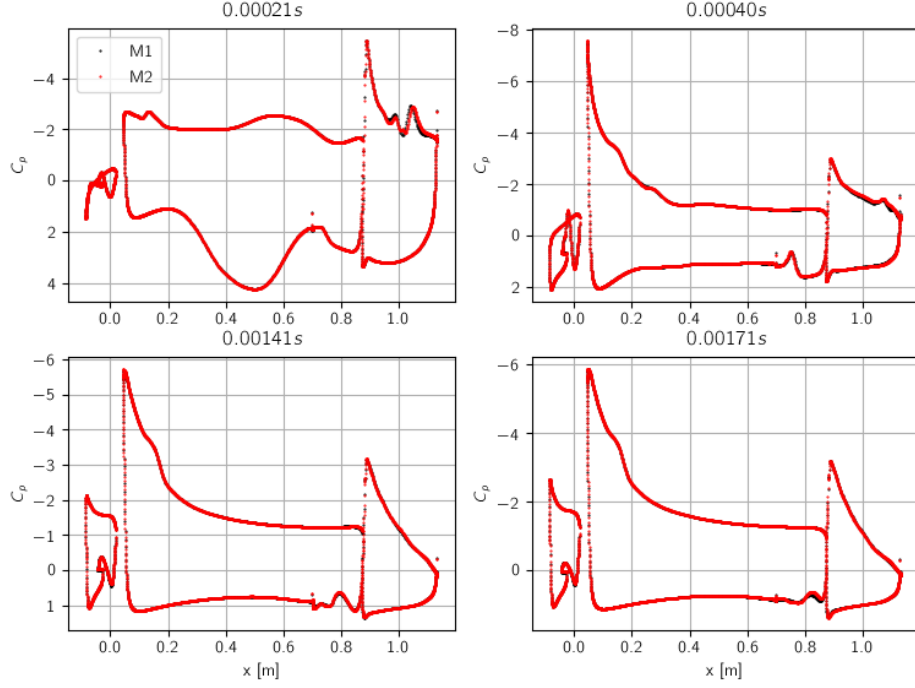


Figure 3.2: Plots of Pressure Coefficient C_p on the surface of the 30P30N geometry at different instants of time for mesh M1 (coarse) and mesh M2 (fine).

field is characterized by an initial laminar bubble that grows gradually in time until it interacts with the separated region near the trailing edge. This eventually leads to the onset of an instability in the airfoil wake, causing the development of a quasi-periodic vortex shedding like motion.

The mesh used for the domain discretisation is a viscous structured mesh with 91,039

Table 3.1: NACA0012 simulation parameters

Mach	α [deg]	Reynolds	T_∞ [K]	Time [s]	Δt [s]	CFL
0.1	15	10,000	288.15	0.3	10^{-3}	5

elements and 91,650 grid points. The time discretisation is obtained using a constant time step, $\Delta t = 10^{-3}$ s, for advancing the unsteady simulation. As regards the numerical setup for the high-fidelity simulation, the laminar Navier-Stokes equations have been solved, using a second order Finite Volume Discretisation for the fluxes (MUSCL

approach) and a second order Dual-time stepping scheme to deal with the unsteady part. In particular, the convective fluxes have been discretised using Roe scheme. As initial condition, the entire domain is initialized to freestream quantities, while the boundary conditions on the body and at the domain borders are no-slip (for momentum equations) adiabatic (for energy equation) and free stream quantities respectively. The time interval investigated with the ROM ranges from the very initial transient to the development of the vortex shedding flow past the airfoil, $t \in [0; 0.3]$ s. The performances of the different techniques are therefore tested for both a transient and periodic behavior. Within this time window the ROM is built using a sampling Δt of 2×10^{-3} , which results in a number of snapshots $N_s = 150$, equispaced in time. It is worth noting at this stage that the time window is defined on the basis of some dynamics of interest happening, for which a low-dimensional description is looked for. This is the same rationale used for all the test-cases presented in this thesis. Additional valuable analysis can be carried out on the influence of how the sampling is performed within the fixed time window, e.g. changing the sampling frequency of the snapshots or defining a non-uniform sampling based on adaptive strategies, but this is out of the scope of the present work. A uniform sampling is implemented for all the test-cases presented hereafter, with a sampling frequency depending on the CFD solutions available within the fixed time frame.

The time required for the database generation is 60 core/hours (CH). The time required for the extraction of flow features, instead, depends on the different algorithms used and, for the specific case of DMD and RDMD, it depends also on the number of modes extracted. For the test-case reported here, the number of modes extracted has been fixed to 30, which requires, on a single core, ~ 1 s for POD and SPOD, ~ 6 s for DMD and ~ 8 min for RDMD. RDMD is the most costly algorithm, since it needs to iteratively apply the full rank DMD algorithm for each extracted feature. Overall, the time required for the generation of the reduced basis is negligible when compared to the time required for the database generation. Therefore this last time can be considered a good approximation of the computational cost of the offline phase. The time required for the online phase is approximately a tenth of a second to compute a reconstructed

ROM solution and it does not change with the specific algorithm used.

Figure 3.3 and 3.4 show respectively a qualitative comparison of different ROMs during the initial transient, at time $t = 10^{-3}$ s after the impulsive start, and once the quasi-periodic motion is established, at time $t = 0.211$ s, with the number of modes of each reduced basis fixed to 30. It can be noted how the DMD and RDMD are not able to reconstruct the dynamics of the starting vortex with sufficient accuracy at the very initial time steps (Figure 3.3). Many higher order oscillations are introduced near the wall of the aerodynamic body and spurious spatial oscillation are also visible around the starting vortex, which is solved with very poor accuracy. The POD basis is instead able to reconstruct with a good resolution the starting vortex, and only slight differences are introduced with the application of the SPOD filter. In particular, the effect of the SPOD filter for the initial transient seems to slightly reduce the reconstruction accuracy. Moving forward in time, once the transient is vanished and the quasi-periodic vortex shedding has settled (Figure 3.4), the DMD and RDMD reproduce the flow considerably better than at the beginning of the time window. SPOD and DMD present overall a reconstruction accuracy that is comparable to the one provided by POD. Moreover, RDMD gives slightly better results than POD at this specific time according to the results in [44].

3.4.2 30P30N test-case

The impulsive start of a 30P30N airfoil is considered [154]. Table 3.2 summarizes the parameters used for the unsteady simulation. The Mach number, Reynolds number and angle of attack are fixed respectively to $M = 0.2$, $Re = 9 \times 10^6$, $\alpha = 19$ deg. Under these conditions, a nearly-steady state field is established in the region near the airfoil after the initial transient. The initial transient is instead characterised by formation and shedding of vortices from the various lifting surfaces, which eventually interact and merge together in the wake of the airfoil. As regards the numerical setup, a dual-time stepping method is used for the unsteady simulation with a $\Delta t = 10^{-4}$ s. A second order discretisation in space is used (MUSCL approach) with Roe scheme for fluxes computation. As initial condition, the entire domain is initialized to freestream

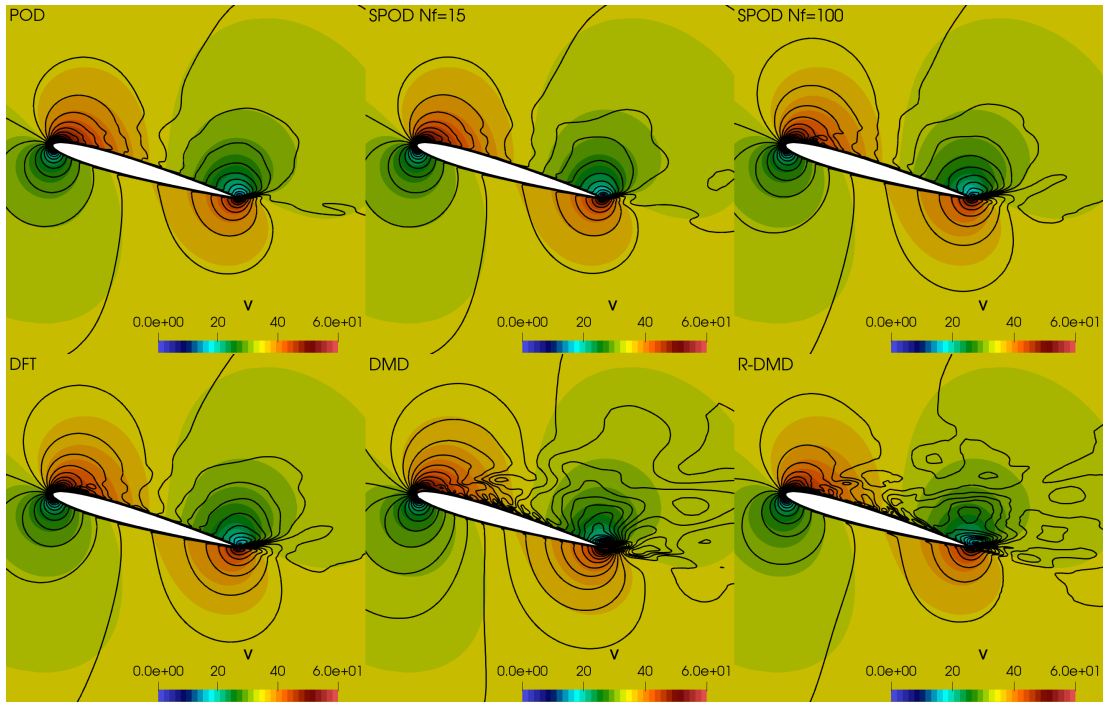


Figure 3.3: Qualitative comparison of different ROMs using 30 modes at time $t = 10^{-3}$ s, Velocity Magnitude (filled contours CFD, lines ROM), NACA0012.

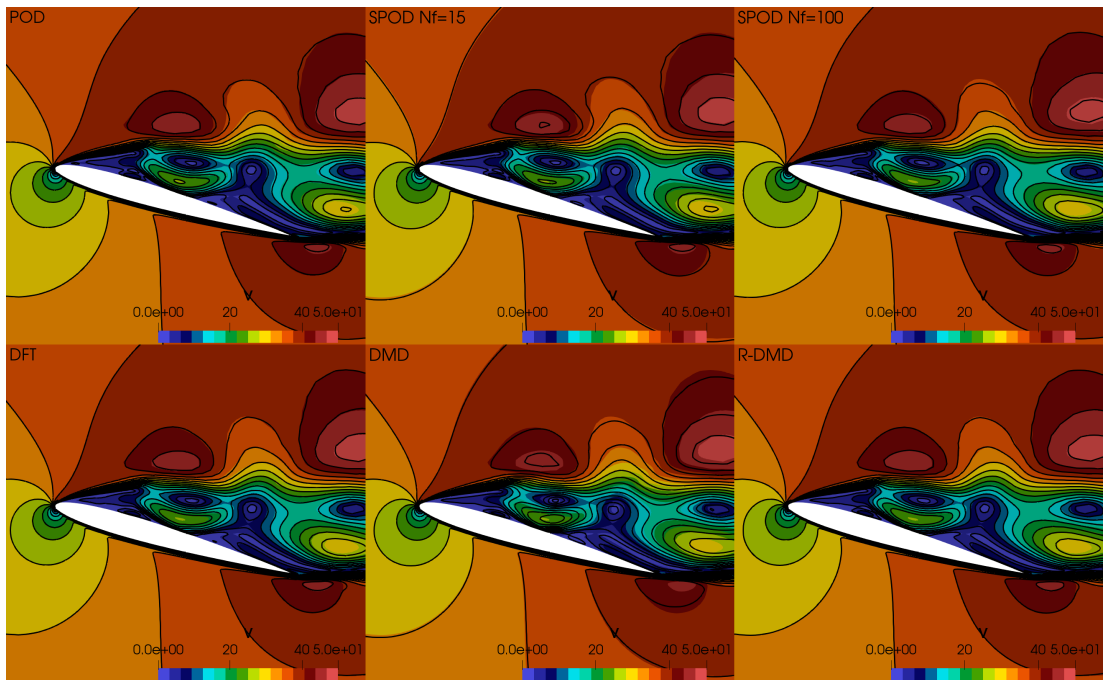


Figure 3.4: Qualitative comparison of different ROMs using 30 modes at time $t = 2.11 \times 10^{-3}$ s, Velocity Magnitude (filled contours CFD, lines ROM), NACA0012.

quantities, while the boundary conditions on the body and at the domain borders are no-slip (for momentum equations) adiabatic (for energy equation) and free stream quantities respectively. The simulation is run as fully turbulent, using the SST model [156]. The mesh used is a viscous hybrid mesh with 559,652 elements and 327,733 grid points.

The time interval investigated with the ROM ranges from the very initial transient to the steady state condition around the airfoil, with one big resulting vortex propagating downstream, $t \in [0; 0.06]$ s. The reduced basis is built within this interval using a sampling Δt equal to 6×10^{-4} , which results in $N_s = 100$ equispaced in time.

The time required for the database generation is 7200 CH. The number of modes

Table 3.2: 30P30N simulation parameters

Mach	α [deg]	Reynolds	T_∞ [K]	Time [s]	Δt [s]	CFL
0.2	19	9×10^6	288.15	0.06	10^{-4}	0.4

extracted has been fixed to 30, which requires, on a single core, ~ 3 s for POD and SPOD, ~ 20 s for DMD and ~ 25 min for RDMD. It can be noticed again how the time for the database generation can be considered as a good approximation of the whole cost of the offline phase. The online phase requires approximately few tenths of a second to compute a reconstructed ROM solution and it does not change with the specific algorithm used.

Following the same qualitative analysis as the one presented for NACA0012, Figure 3.5 shows the reconstruction of the different reduced order techniques at a very early stage of the transient, namely $t = 4 \times 10^{-4}$ s. It can be noticed again how DMD is not able to recover the initial unsteady dynamics and RDMD is less accurate than POD and SPOD. DMD presents many high order spatial oscillation, both near the wall and in the region around the aerodynamic body. RDMD is performing poorly in the resolution of the starting vortex, even if it is capable of removing the spatial oscillation caused by DMD. Moreover, also for this test-case, it can be noticed how the application of the SPOD filter slightly lowers the performance of the model in reconstruction accuracy of the very initial transient. In particular, accuracy is decreasing in solving features

around the main component of the airfoil and in reconstructing the starting vortex dynamics. After the strong initial transient, instead, Figure 3.6, the SPOD filter seems to have more beneficial effects on solution accuracy, especially in solving the region around the starting vortex. The higher order spatial oscillations of the DMD vanishes and its performance is much higher than in the initial time window. Finally, RDMD performs slightly better than POD.

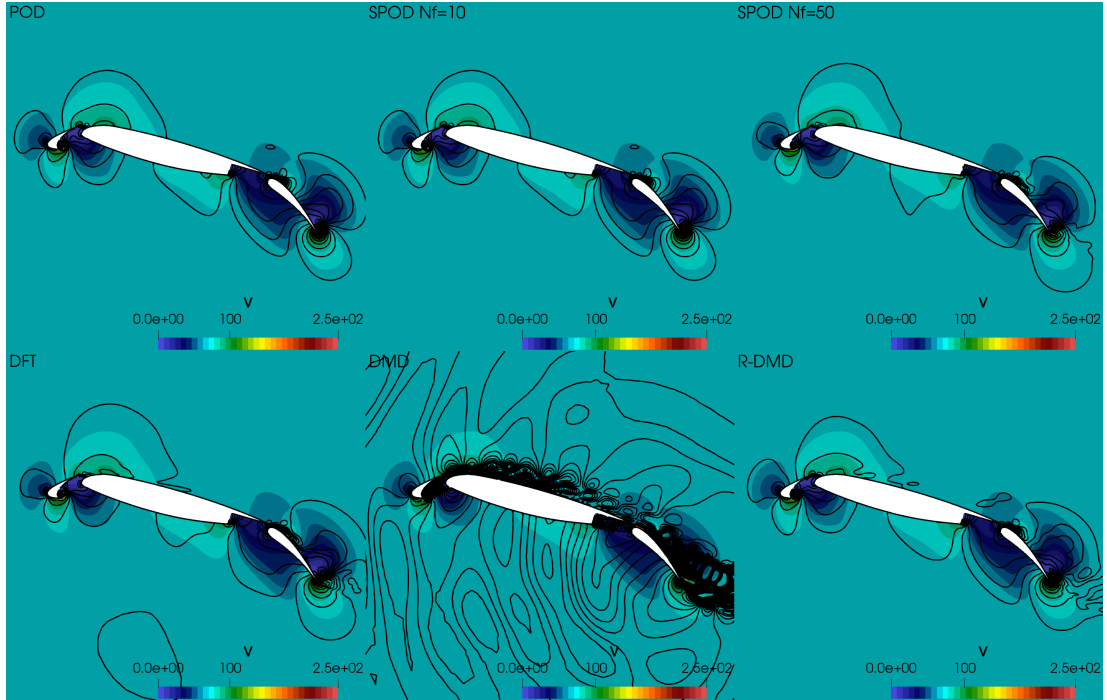


Figure 3.5: Qualitative comparison of different ROMs using 30 modes at time $t = 4 \times 10^{-4}$ s, Velocity Magnitude (filled contours CFD, lines ROM), 30P30N.

3.5 Remarks

A qualitative analysis of accuracy in reconstruction while using basis functions coming from different reduction algorithms has been presented for two test-cases, namely the impulsive start of the NACA0012 airfoil and the impulsive start of 30P30N multi-element airfoil. To perform this analysis, the number of modes has been fixed, in order to investigate the performances of the various methods when dealing with the same DOFs of the reduced order model. The output of this analysis has shown that

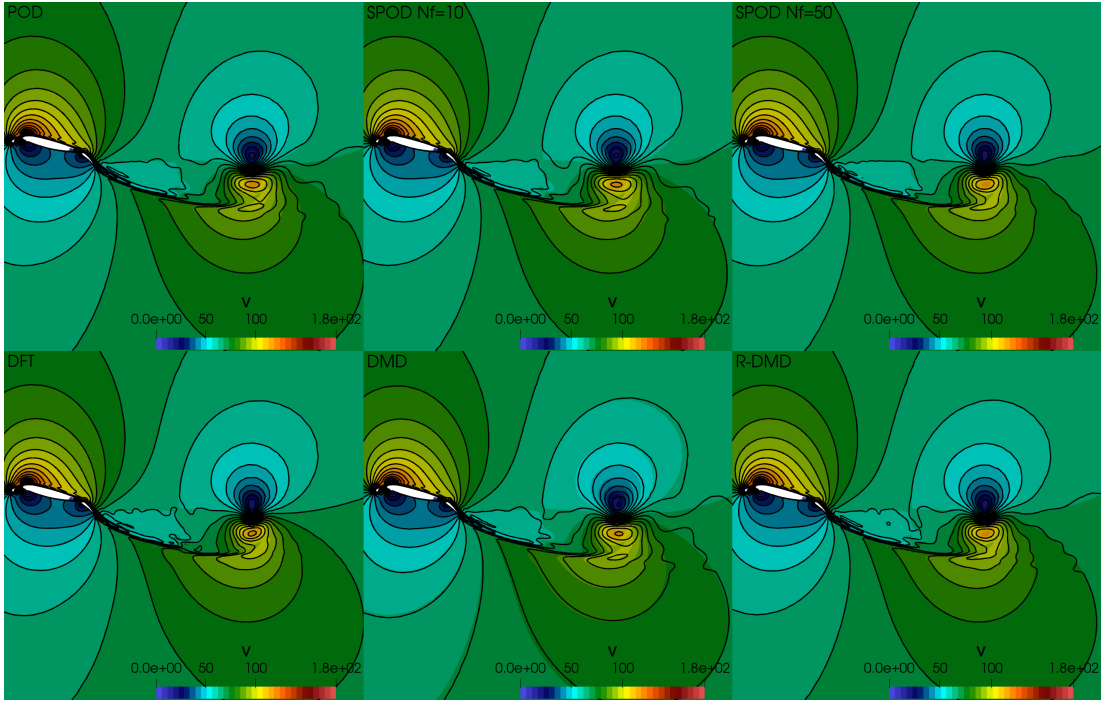


Figure 3.6: Qualitative comparison of different ROMs using 30 modes at time $t = 3.51 \times 10^{-2}$ s, Velocity Magnitude (filled contours CFD, lines ROM), 30P30N.

performance of a single ROM varies over time when looking at large time windows where different dynamical phenomena are happening. This statement holds also for POD, despite it gives a basis that is the closest one to the initial set of snapshots, according to its optimality property. Indeed, the optimality is defined over the entire set of snapshots, and the average operation that defines the optimality condition in Equation 3.2 might miss meaningful dynamics at specific time instants. For the case of NACA0012, for instance, there is an initial time dynamics linked to the formation of laminar bubble on the upper part of the airfoil that eventually interacts with the trailing edge and lead to the formation of a quasi-periodic motion, namely the vortex shedding. For the 30P30N test-case, there is a small initial time window where vortices are first detaching from the various lifting surfaces, and then eventually they merge together in the far wake of the airfoil. In the near field, instead, the flow converges to a steady state, with a well defined stable wake over the main component linked to the slat positioned upstream, and a separated flow on the flap. The dynamics in both

cases is therefore not showing any repeating patterns or specific periodic motions when looking at the entire investigated time window. The qualitative analysis shows how the very first instant of the initial transient are better resolved by POD and SPOD, while DMD and RDMD present lots of spurious oscillation in representing such dynamics. Moving to the second half of the investigated time window, which means getting closer to the final solution attractor, instead, DMD and RDMD improve significantly their performances in catching meaningful dynamics in the flow. In conclusion, there is not a unique ROM that can be considered the best technique for the fixed number of modes chosen, in order to describe the dynamic over the entire investigated time window. A possible synergy among all the linear methods considered can be therefore created and will be at the basis of the framework presented later in Chapter 5.

Computational requirements have also been reported for the two test-cases considered. It has been shown that, although the time required for the extraction of features is dependent on the specific algorithm used, this time is negligible when compared to the time required for the database generation. Therefore a good approximation of the time required for the offline phase is the time associated with the computation of the training snapshots. Moreover, it has been shown that the online phase is able to provide reconstructed ROM solutions in a real-time manner ($t < 1s$), with no differences among the various algorithms used.

Chapter 4

Ranking of Modes

The choice of the number of modes to use to express the dynamics of a complex flow in a low-dimensional space, i.e. the rank of the ROM, is another key element for the ROM to be accurate, stable, reliable and fast. In order to select only few meaningful features among the entire set of the ones available, a specific ordering needs to be defined on the basis of their importance in expressing the final dynamics. An overview of the different methods used in the literature to perform the ranking of fundamental flow features is presented. An analysis is performed on POD modes for three different test-cases, changing the modes ranking through the application of a filter, and a new approach for DMD modes selection, based on their time dynamics, is presented for the specific case of turbulent transition in a channel flow. Two key conclusions can be drawn from the analysis conducted here. The first is that the energy redistribution among POD modes, promoted by the application of the filter, is improving the description of some dynamics in time through the new set of modes retained. The second is that a newly proposed selection criterion proves to be able to identify the most meaningful DMD modes in describing a quasi-linear dynamic in time. In particular, the early transition phase happening in a channel flow is considered and an actual improvement of the proposed selection criterion is observed with respect to the common energy based ranking criterion.

4.1 Ranking of POD and SPOD modes

The ranking of POD modes has been always based on the eigenvalues extracted from the algorithm reported in Section 3.2.1. Indeed, following also the normalization of the modes ϕ_i as in Equation 3.6, each eigenvalue λ_i brings the energy content, alias the actual euclidean norm, of the corresponding mode. A cumulative sum is therefore defined

$$En = \frac{\sum_{i=1}^{N_m} E_i}{\sum_{i=1}^{N_s} E_i} \times 100 = \frac{\sum_{i=1}^{N_m} \lambda_i}{\sum_{i=1}^{N_s} \lambda_i} \times 100 \quad (4.1)$$

that represents the percentage of the full energy retained by the first N_m modes and is equivalent to the RIC defined in Equation 2.3. The full energy represents the whole amount of energy contained in the original training snapshots. It has been already widely discussed in Chapter 2 how the energy criterion can penalize dynamics, especially when there are very complex phenomena to model in a low-dimensional manner. Therefore the ranking of POD modes, despite straightforward and very intuitive, might not be a very accurate way to describe complex underlying dynamics. Christensen et al. [157] proposed a weighted POD in the effort to be able to select modes important for the dynamics that have less energetic content. The Spectral POD method introduced in Section 3.2.2, instead, operates on the energy ranking criterion promoting a different energy distribution among the original POD modes, through the application of the filter to the POD temporal correlation matrix (see Equation 3.7). Figure 4.1 shows the effect of the SPOD filter N_f on the cumulative sum En reported in Equation 4.1. It is clearly visible how, for a specific energetic content, SPOD selects a different set of modes with respect to POD. This will be shown to improve the description of some dynamics.

4.1.1 Numerical Test-Cases

The effect of the energy redistribution among POD modes is assessed using as snapshots set of CFD solutions computed using the open-source solver SU2. Roe scheme is used for the convective terms, while a central scheme is used for the viscous part. A Monotonic Upwind Scheme for Conservation Laws (MUSCL) approach and a dual time-stepping

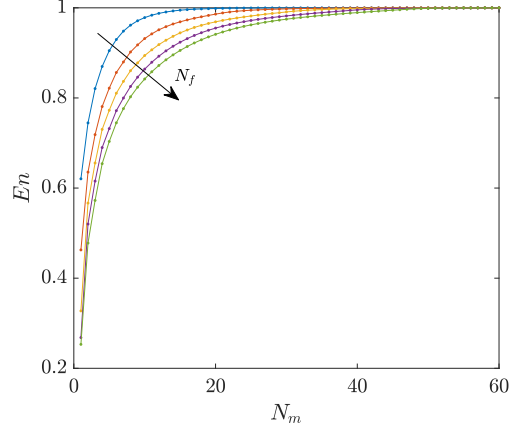


Figure 4.1: Energy redistribution among modes as a function of the SPOD filter N_f , with $N_f \in [0; 60]$.

method based on the Backward Differentiation Formula (BDF) are used to obtain second order accuracy in space and time. Three test-cases are considered to evaluate the ability of POD and SPOD in reconstructing the unsteady flow field. One case considers a canonical flow around a 2D square cylinder developing a von Karman vortex street, i.e. with vortices periodically detaching from its upper and lower edges, while the other two refer to flows around impulsively started lifting bodies with no characteristic frequency. The velocity vector is the quantity considered to build the ROM. The components are processed as a unique vector (see Equation 3.19) and, therefore, a unique low-dimensional space is identified for the entire velocity vector. For each test-case, the global error in reconstruction, defined as

$$\epsilon = \frac{\|\mathbf{u}_{\text{CFD}} - \mathbf{u}_{\text{ROM}}\|_2}{\|\mathbf{u}_{\text{CFD}}\|_2} \quad (4.2)$$

is reported for a specific time instant, where the \mathbf{u}_{ROM} is the reduced basis reconstruction obtained with either POD or SPOD, fixing the energetic content in Equation 4.1, whereas \mathbf{u}_{CFD} is the exact CFD solution. Moreover, qualitative results in terms of reconstruction are also reported, comparing the contour lines of the ROM and CFD solution. Information about the time required for the offline and online phase are also reported, in order to highlight the computational speed-up of the ROM with respect to

the high-fidelity simulation, once the basis is extracted. All the reconstructed time instants are computed out of the training points but still within the time window where the sampling is performed, in order to test how the ROM performs in reconstructing new solutions, i.e. not used to build the reduced basis. It is worth noting that the ROMs presented are not able to make predictions and, therefore, all the reconstructions presented are always computed within the sampled time window.

Square cylinder The periodic flow past a square cylinder is considered. The solution is initialized using the far field conditions and only the snapshots after the initial transient, once the vortex shedding has established, are considered for the training of the ROM. The domain discretisation is performed through a completely structured mesh with 190,244 elements and 191,040 grid points. A dual time-stepping method is used for the unsteady simulation with $\Delta t_{\text{CFD}} = 1.5 \times 10^{-3}\text{s}$ and the Mach number, Reynolds number and angle of attack are respectively $M = 0.1$, $Re = 22,000$ and $\alpha = 0$ deg. At the fixed Reynolds number, the vortex street is turbulent, therefore the simulation is run as fully turbulent using SST turbulence model [156]. To build the ROM, a sampling Δt equal to $6 \times 10^{-3}\text{s}$ is used within the time window [3.4575; 3.9975]s, which corresponds to almost two complete shedding cycles, resulting in a number of snapshots $N_s = 30$, equispaced in time. The time required for the database generation is approximately 60 CH, considering for the dual-time stepping 10^{-6} as the residuals tolerance and a maximum of 1,000 inner iterations, which mainly determines the computational effort needed for the offline phase. Indeed, for both POD and SPOD, the time required to extract the basis is approximately 0.3s on a single core, while 0.12s is the time required, still on a single core, to obtain one reconstructed snapshot during the online phase. Table 4.1 reports the error for the two components of velocity as defined in Equation 4.2 and the number of modes required for two fixed energetic contents, namely 95% and 99.9%. It can be clearly noticed how the main effect of the application of the filter is a redistribution of the initial POD energy on a higher number of modes, according to what was reported in Figure 4.1, with a consequent reduction of the global error in reconstruction ϵ (ϵ_u and ϵ_v in Table 4.1). Figures 4.2 and 4.3

report contours of the CFD and reconstructed solution (solid lines and dashed lines respectively). There is no visible improvements in solving local features when setting the energy level to 99.9% (Figure 4.3), while slightly increased accuracy can be noticed in reconstructing features further downstream in the von Karman vortex street when retaining 95% of the energy (Figure 4.2).

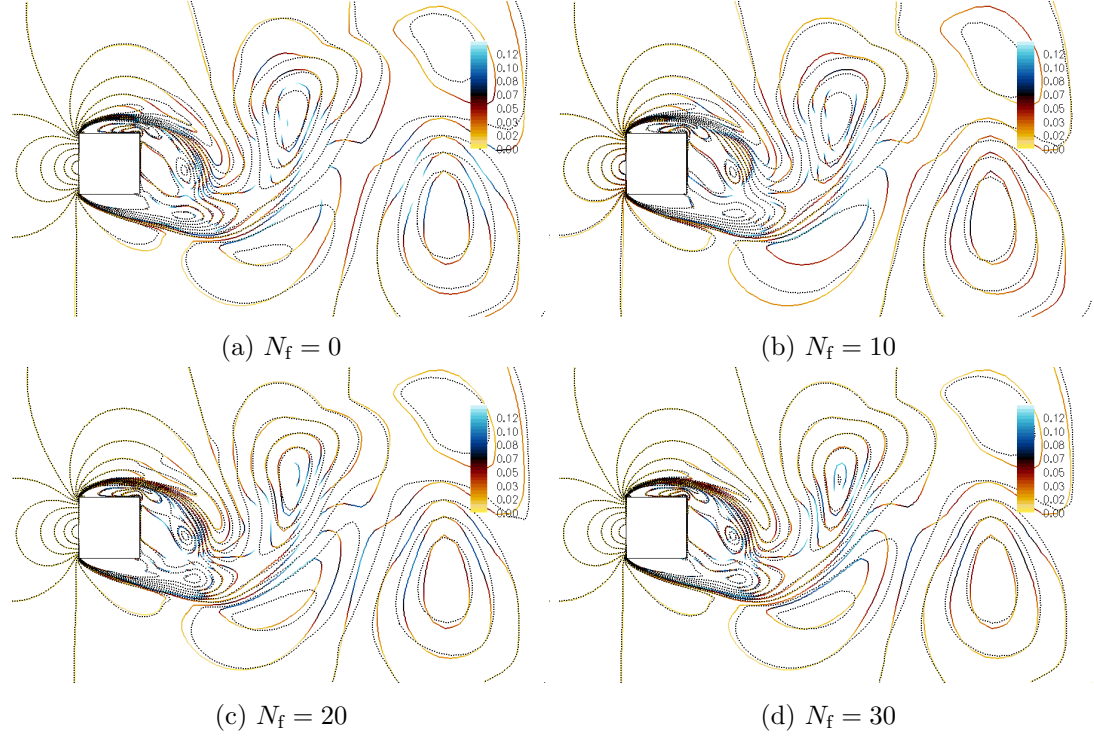


Figure 4.2: Comparison between velocity magnitude contours from CFD and ROM reconstruction with different values of the SPOD filter N_f , using $En = 95\%$ at time $t = 3.5$ s from the impulsive start. Solid line: CFD coloured with the value of the error ϵ ; Dashed line: ROM reconstruction.

30P30N The impulsive start of the three component 30P30N airfoil is now investigated [154]. Differently from the square cylinder case, where the time window considered for the snapshots refers to the periodic regime only, excluding the initial transient, in this case, the time window includes the entire initial transient, from the initial condition up to an instant of time when the flow is almost stationary in proximity of the airfoil. The test-case is equivalent to the one reported in Section 3.4.2, with the only difference in the Δt_{CFD} used for the physical time step, which is 10^{-3} s. The ROM is

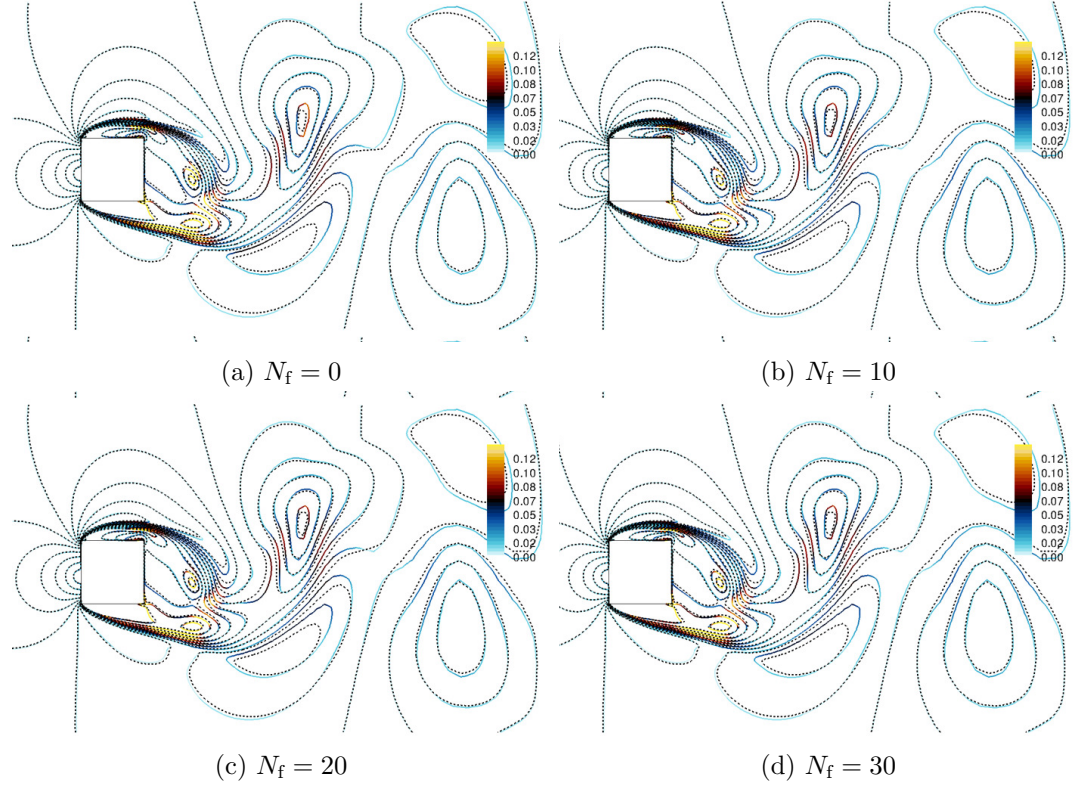


Figure 4.3: Comparison between velocity magnitude contours from CFD and ROM reconstruction with different values of the SPOD filter N_f , using $En = 99.9\%$ at time $t = 3.5$ s from the impulsive start. Solid line: CFD coloured with the value of the error ϵ ; Dashed line: ROM reconstruction.

built using a sampling Δt equal to 3×10^{-3} s within the time window $[0, 0.12]$ s where the dynamics of interest is happening, which results in a number of snapshots $N_s = 40$, equispaced in time. The time required for the database generation is approximately 150 CH, considering for the dual-time stepping 10^{-6} as the residuals tolerance and a maximum of 1,000 inner iterations. For both POD and SPOD, the time required for features extraction is approximately 0.7 s on a single core, which, together with the time required for the database generation, completes the information about the time needed for the offline phase. The online phase, instead, requires 0.32 s on a single core to obtain one reconstructed snapshot. Table 4.2 reports the error for the two components of velocity as defined in Equation 4.2 and the number of modes required for two fixed energetic contents, namely 95% and 99.9%. The same trend, in terms of number of modes

N_f	$N_m/N_s(En = 99.9\%)$	$\epsilon_u(\%)$	$\epsilon_v(\%)$	$N_m/N_s(En = 95\%)$	$\epsilon_u(\%)$	$\epsilon_v(\%)$
0 (POD)	22/30	1.5	4.0	6/30	3.4	8.4
10	28/30	1.4	3.8	10/30	4.3	9.4
20	29/30	1.4	3.8	12/30	2.7	7.5
30 (DFT)	29/30	1.4	3.8	13/30	2.0	5.7

Table 4.1: Error in reconstruction for the square cylinder, computed according to Equation 4.2 for u and v component of velocity, for two different energetic contents and varying the SPOD filter size.

retained as the filter increases, can be observed also for this test-case. Additionally, a major improvement in terms of error is present, with the value of ϵ falling from 0.4% to 0.2% for the u component of velocity, and from 0.98% to 0.53% for the v component of velocity, when setting the energy content to 99.9%. A strong improvement is also achieved when lowering the energy level retained to 95%. The main reason for the strong reduction of the error can be better explained looking at the contours reported in Figures 4.4 and 4.5, where both CFD and reconstructed solutions are represented. It can be clearly observed how the main effect of the filter is in both cases a better resolution of the vortex structure propagating downstream.

N_f	$N_m/N_s(En = 99.9\%)$	$\epsilon_u(\%)$	$\epsilon_v(\%)$	$N_m/N_s(En = 95\%)$	$\epsilon_u(\%)$	$\epsilon_v(\%)$
0 (POD)	20/40	0.4	0.98	7/40	2.8	4.9
10	32/40	0.3	0.72	14/40	1.7	3.2
20	35/40	0.2	0.53	18/40	0.8	1.9
30	38/40	0.2	0.53	22/40	0.5	1.2
40 (DFT)	40/40	0.2	0.53	25/40	0.5	1.2

Table 4.2: Error in reconstruction for the 30P30N, computed according to Equation 4.2 for u and v component of velocity, for two different energetic contents and varying the SPOD filter size.

High-Lift Wing-Body Configuration The impulsive start of a High-Lift Wing-Body configuration is finally considered [158]. Only half of the geometry is retained and a symmetry boundary condition is imposed on the plane of symmetry. The mesh used is a viscous unstructured mesh with 21,492,137 elements and 3,652,657 grid points. Similarly to the 30P30N test-case, the time window considered for the ROM analysis

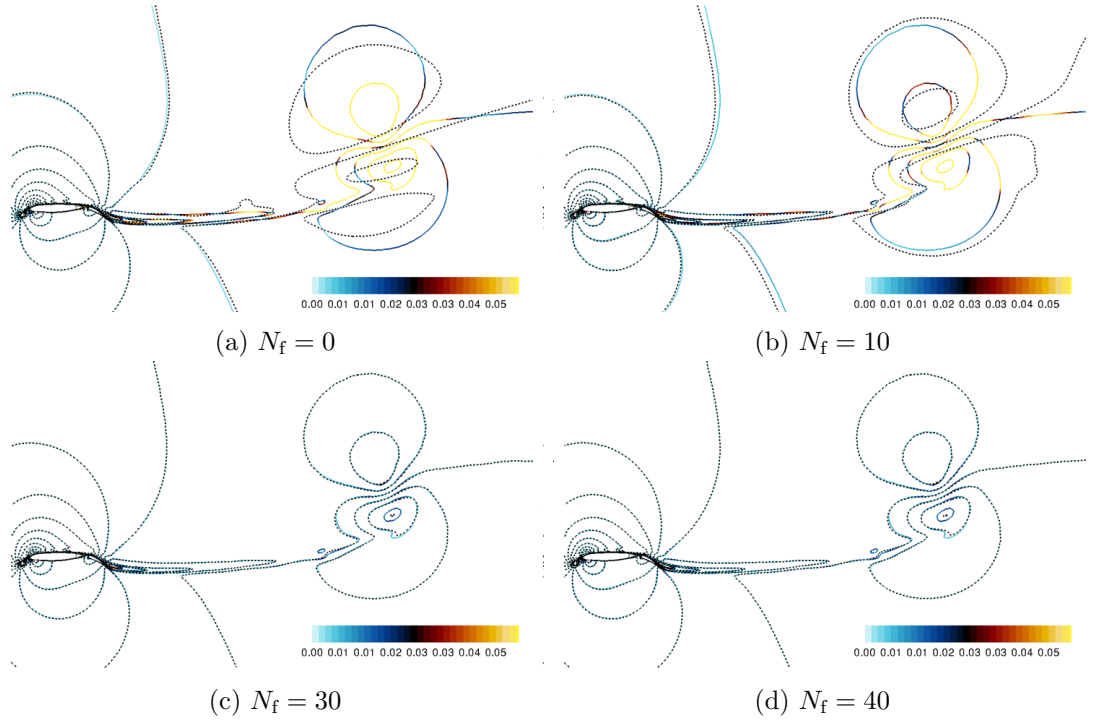


Figure 4.4: Comparison between velocity magnitude contours from CFD and ROM reconstruction with different values of the SPOD filter N_f , using $En = 95\%$ at time $t = 6.5 \times 10^{-2}$ s from the impulsive start. Solid line: CFD coloured with the value of the error ϵ ; Dashed line: ROM reconstruction.

ranges from the initial transient, when the wing is impulsively set into motion, up to the point where a nearly steady state is reached near the wing and the unsteadiness is only coming from the advection of the vortical structures shed by the wing. A dual time-stepping method is used for the unsteady simulation with $\Delta t_{\text{CFD}} = 10^{-3}$ s and the Mach number, Reynolds number and angle of attack are respectively $M = 0.2$, $Re = 4.3 \times 10^6$ and $\alpha = 13$ deg. The turbulence is modeled using SST turbulence model. The ROM is built using a sampling Δt equal to 6×10^{-3} s within the time window $[0, 0.108]$ s where the dynamics of interest is happening, which results in a number of snapshots $N_s = 18$, equispaced in time. The time required for the database generation is approximately 8600 CH, considering for the dual-time stepping 10^{-6} as the residuals tolerance and a maximum of 1,000 inner iterations. For both POD and SPOD, the time required for features extraction is approximately 12s on a single core, still negligible with respect to the computational effort required for the database generation. The online phase,

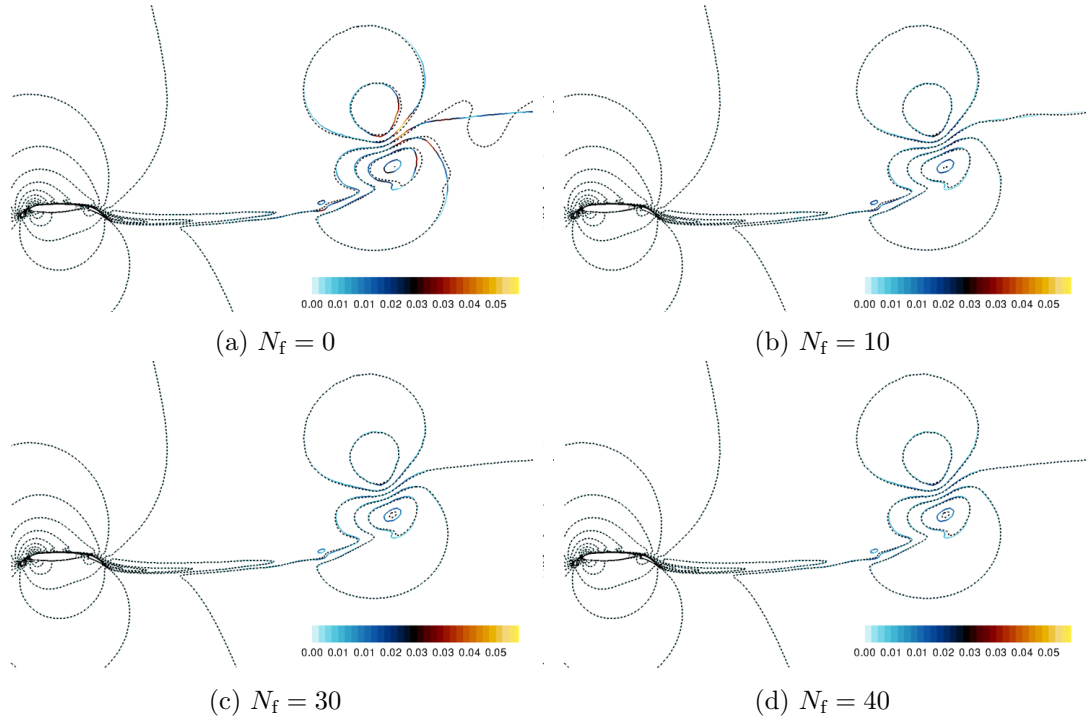


Figure 4.5: Comparison between velocity magnitude contours from CFD and ROM reconstruction with different values of the SPOD filter N_f , using $En = 99.9\%$ at time $t = 6.5 \times 10^{-2}$ s from the impulsive start. Solid line: CFD coloured with the value of the error ϵ ; Dashed line: ROM reconstruction.

instead, requires 8.2s on a single core to obtain one reconstructed solution. Table 4.3 reports the error for the three components of velocity as defined in Equation 4.2 and the number of modes required for a fixed energetic content of 99.9%. There is no significant improvement in terms of global error for all the components of velocity. Nevertheless, looking at Figures 4.6 and 4.7, which report contours of the exact and reconstructed solution on two different slices in the span wise direction, it can be observed how SPOD is able to better resolve features of the starting vortex further downstream of the wing (second slice in Figure 4.7). The almost constant behaviour of the global error as the filter increases might be linked to the low resolution of the mesh in the wake region of the wing and for the entire far field. This hampers a good resolution of important spatial features in the original spatial snapshots used to build the ROM. Having a good description of these spatial features is fundamental to exploit at best the capabilities of the SPOD filter. Indeed, a local improvement of the SPOD can still be seen from

the reconstruction of the entire flow field, but it cannot be noticed when an integral measure is used, such as the global error ϵ .

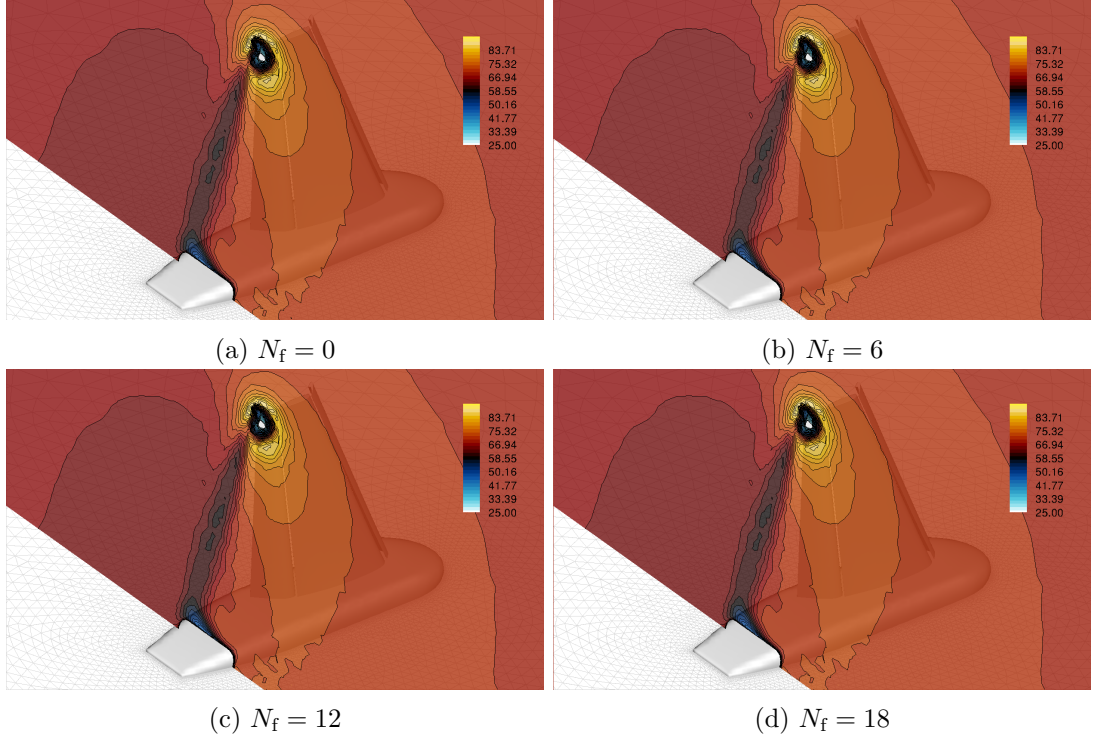


Figure 4.6: Comparison between velocity magnitude contours from CFD and ROM reconstruction with different values of the SPOD filter N_f , using $En = 99.9\%$ at time $t = 8.1 \times 10^{-2}$ s from the impulsive start. Filled contours: CFD velocity magnitude; Solid black lines: ROM reconstruction.

4.1.2 Remarks

The energy redistribution due to the filter applied to the POD correlation matrix entails a greater number of modes to reach a fixed energetic content for each test-case, as it can be noticed from Tables 4.1, 4.2 and 4.3. Nevertheless, the computational cost of the two techniques is almost the same, both for the offline and online steps, since the main dimensionality reduction is performed in terms of considering at most N_s modes, instead of the n initial DOFs coming from the CFD simulation. There is no significant effect on the global error as the filter is varied for the three test-cases but differences can be noticed locally, looking at the contour fields. For the periodic case, vortex shedding

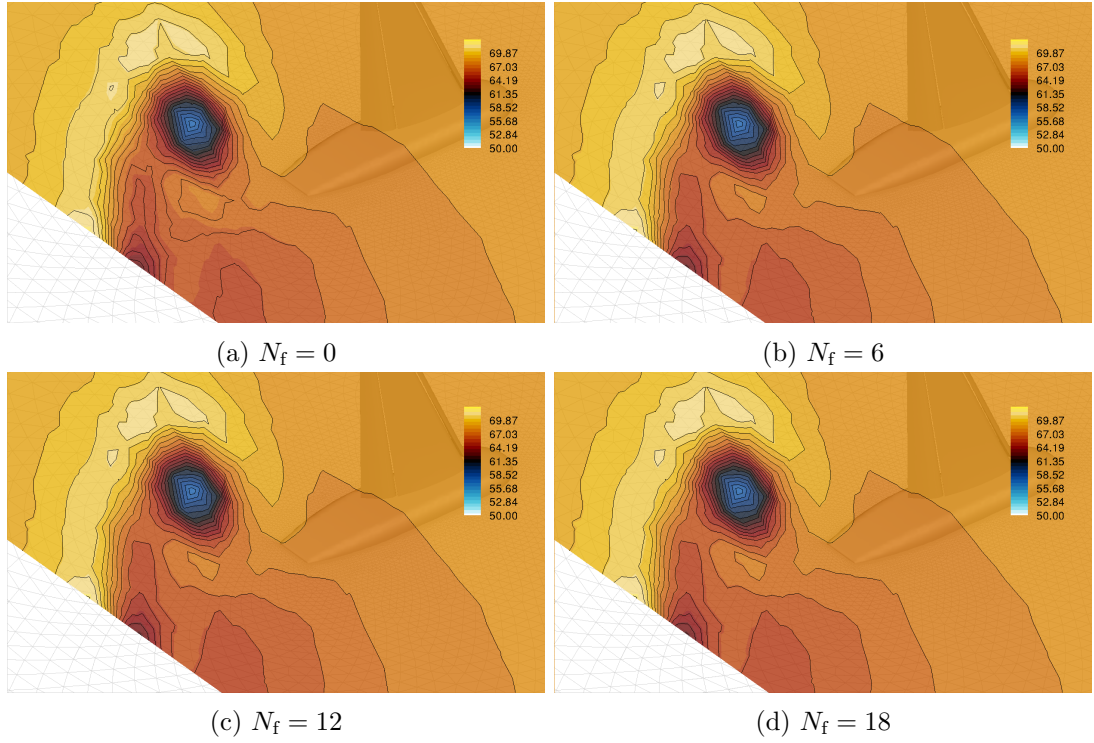


Figure 4.7: Comparison between velocity magnitude contours from CFD and ROM reconstruction with different values of the SPOD filter N_f , using $En = 99.9\%$ at time $t = 8.1 \times 10^{-2}$ s from the impulsive start. Filled contours: CFD velocity magnitude; Solid black lines: ROM reconstruction.

past a square cylinder, an energetic content of 99.9% shows no difference between POD and SPOD (Figure 4.3). However, as the energetic content is lowered to 95% (Figure 4.2) a fine difference can be noticed between the two techniques in resolving the coherent structures more downstream in the von Karman vortex street. For the case of the impulsive start of the 30P30N airfoil, the same behaviour can be highlighted for both the energetic contents (Figure 4.4 and 4.5). The POD does not perform as well as SPOD in reproducing the dynamic of the starting vortex as it propagates downstream and dissipates. The difference between the two techniques is much more remarkable when an energetic content of 95% is fixed (Figure 4.4), where it can be noticed how the performance in resolving the starting vortex dynamics improves significantly as the filter increases. Finally, for the 3D High-Lift Wing-Body configuration, the Figures 4.6 and 4.7, corresponding to an energetic content of 99.9%, highlight again how the

N_f	$N_m/N_s(En = 99.9\%)$	$\epsilon_u(\%)$	$\epsilon_v(\%)$	$\epsilon_w(\%)$
0 (POD)	14/18	1.20	1.35	3.65
6	17/18	1.22	1.35	3.65
12	18/18	1.22	1.35	3.65
18 (DFT)	18/18	1.22	1.35	3.65

Table 4.3: Error in reconstruction for the 3D High-Lift Wing-Body configuration, computed according to Equation 4.2 for u , v and w component of velocity, with fixed energetic content and varying the SPOD filter size.

POD fails in reconstructing the whole dynamics of the starting vortex. As a matter of fact, Figure 4.7 shows how the reconstruction improves as the filter increases, i.e. more details of the flow field are recovered. This behaviour, common over the three test-cases, can be easily explained considering the optimization procedure the POD algorithm is based on. Since the POD modes represent a set that maximize in average the energy kept from the set of initial snapshots (for the specific test-cases analyzed, kinetic energy, since the velocity vector is considered), coherent structures that are less energetic might not be recovered properly. This can be clearly seen comparing the two slices reported in Figures 4.6 and 4.7 for the 3D test-case. Closer to the wing, where the coherent structures have an higher energetic content, POD is able to recover the flow field with the same level of detail as SPOD. On the slice far away from the wing, instead, the coherent structures are less energetic and SPOD performs better. Same considerations apply to the 30P30N test-case, where it is evident the better performance of SPOD in catching the advection of the starting vortex as it dissipates and becomes less energetic. Downstream of these observations, the following conclusions can be drawn:

- The energy-based POD mode truncation has limitations in recovering the whole unsteady dynamics of less energetic structures;
- It is relevant to take into account the temporal dependency of snapshots at the modes extraction level (SPOD filter applied to the temporal correlation matrix);
- The energy-based SPOD mode truncation allows a better reconstruction of less energetic flow structure dynamics.

4.2 Ranking of DMD modes

DMD extracts only pure frequencies and possible transient behaviour through growth/decay rate information coming from the dynamic matrix eigenvalues. Therefore it is not an easy task to recognize a-priori the subset of DMD modes that are important for describing the essential dynamics. If there is some a-priori knowledge of the system dynamic behaviour, in terms of characteristic frequencies, it is possible to spot the important DMD modes as the ones corresponding to the expected frequencies. If the dynamics is completely unknown, instead, it becomes tricky to provide a classification of DMD modes as done for POD. Besides the truncation performed on the basis of the singular values, which is when the dynamic matrix is projected into the low-dimensional space where DMD information is extracted, the further selection of modes meaningful for the dynamics, at the end of DMD algorithm, has been mainly performed in the literature trying to mimic the energy criterion from POD. Classifications have been proposed on the basis of DMD modes norm or DMD coefficients α_i (see Equation 3.15) [93, 98], that do not take into account the DMD modes dynamic and therefore could penalize transient linked to strong decay rates. Integral measures have also been used in the effort to take into account also the time evolution of DMD modes [159, 160]. Specifically, the following integral has been used to perform a DMD mode ranking

$$E_i = \frac{1}{T} \int_0^T \|\phi_i\|_2 e^{2\sigma_i t} dt = \|\phi_i\|_2 \frac{e^{2\sigma_i T} - 1}{2T\sigma_i} \quad (4.3)$$

where T is the time interval over which DMD is applied and σ_i is the real part of the i -th DMD eigenvalue. Nevertheless, also in this case, being the final measure an integral over time, local importance of DMD modes, which might be related to the transient behaviour dictated by the real part of DMD eigenvalues, is not considered. Moreover, it is worth noticing that both the rankings based on the integral measure and DMD coefficients or modes norm are neither related directly to the total energy content of the initial snapshots set nor they can be used to define a cumulative sum as in Equation 4.1. Other methods have also been proposed, that try to isolate meaningful DMD modes at the extraction stage of the method, using optimization algorithms. Optimized-

DMD [161], recently proposed also for the case of snapshots unevenly spaced in time [162], uses a global optimization algorithm that has shown to extract more physical frequencies when applied to the case of the transient and post-transient dynamics of a cylinder wake. Sparsity promoting DMD (spDMD) [35] tries to induce sparsity through regularization of the least-squares deviation between the matrix of snapshots and the linear combination of DMD modes, with an additional term that penalizes the l_1 -norm of the vector of DMD amplitude α_i . The algorithm was successfully applied to three test-cases showing an improvement in the extraction of dynamical information. Nevertheless, both the algorithms rely on numerical optimization procedures, where the rank of DMD modes is user defined and other few parameters need to be tuned in the process. A new approach, that exploits the local time dynamics of DMD modes and does not use any optimization algorithm for modes extraction or energy ranking criteria for modes selection, is the t -envelope method, presented in the following for the specific case of describing the dynamics of early transition in a Channel flow. Even if the specific flow considered is not a flow of aeronautical interest, it is a good demonstration case which shows in a tangible manner the importance of the selection of appropriate DMD modes from a set of available ones, in order to express some dynamics of interest. Indeed, for this specific case, some connections will be also introduced between the modes extracted by DMD and the underlying physics of the flow.

4.2.1 DMD Modes classification for reconstruction of early transition in Channel flow

The DMD algorithm is applied to a collection of snapshots coming from the Direct Numerical Simulation (DNS) of a by-pass type transition in a channel flow [163, 164]. In the following details of the simulation are briefly described. The 9th-order WENO scheme and 128^3 mesh resolution are employed, for which the accuracy of the results were previously shown to be DNS-like [163]. The Reynolds number based on the friction velocity (u_τ) and the channel half-height (L_h) is equal to $Re_\tau \approx 395$, whereas the one based on the bulk velocity (u_b) is $Re_b \approx 6887$. The y^+ value of the first point from the wall is equal to 0.74, resulting in a resolved mean friction Reynolds number of just over

393, within less than 0.5% of the target value. The employed grid and numerical scheme were previously shown to be capable of accurately resolving the turbulence properties of the test-case and set-up considered in this study [163]. In order to obtain a sufficient number of flow snapshots of the bypass transition, the initial velocity field is perturbed with white noise in all directions by 5% of the local streamwise velocity (instead of the 10% used in [163]), which in turn is obtained by a laminar Poiseuille parabolic profile. The quantity used to describe the entire transitional process is the wall shear stress τ_w (see Figure 4.9).

DMD characterization

The DMD method is applied to 1000 snapshots of the numerical simulation sampled in the time interval highlighted in Figure 4.9, using an equispaced non-dimensional $\Delta t = 10^{-3} L_h u_b^{-1}$. This is the maximum value admissible to have time-resolved data, i.e. the maximum Δt that still allows to follow the evolution in time of flow structures. Each snapshot consists of all the three components of the velocity arranged in a unique column vector, $\mathbf{u} = [u, v, w]^T$. The time interval selected considers the early stage of transition, when the vortical laminar tubes that appear in the left half of the channel start showing spatial oscillations. These oscillations are then amplified and eventually determine the interaction and breakdown of the laminar tubes, which rearrange in more chaotic yet coherent turbulent structures. The reader can refer to the first three time instants reported in Figure 4.8 to have a direct visualization of the described process. Since a transient phenomenon is considered, it is worth noticing here that another crucial aspect of DMD recently discussed in the literature is how much it is capable to provide consistent results when transient phenomena are considered [43]. Specifically Page and Kerswell [45] have shown, for a simple Couette flow, how DMD can fail when trying to describe the dynamics of a fluid system moving between two equilibria along an heteroclinic orbit. Nevertheless, in the same work it was also shown how the DMD looks accurate if applied to very short time windows not containing cross-over points of the dynamical system. This is why the DMD extraction method applied in the present work is focusing on a small window at the early stage of transition. The whole

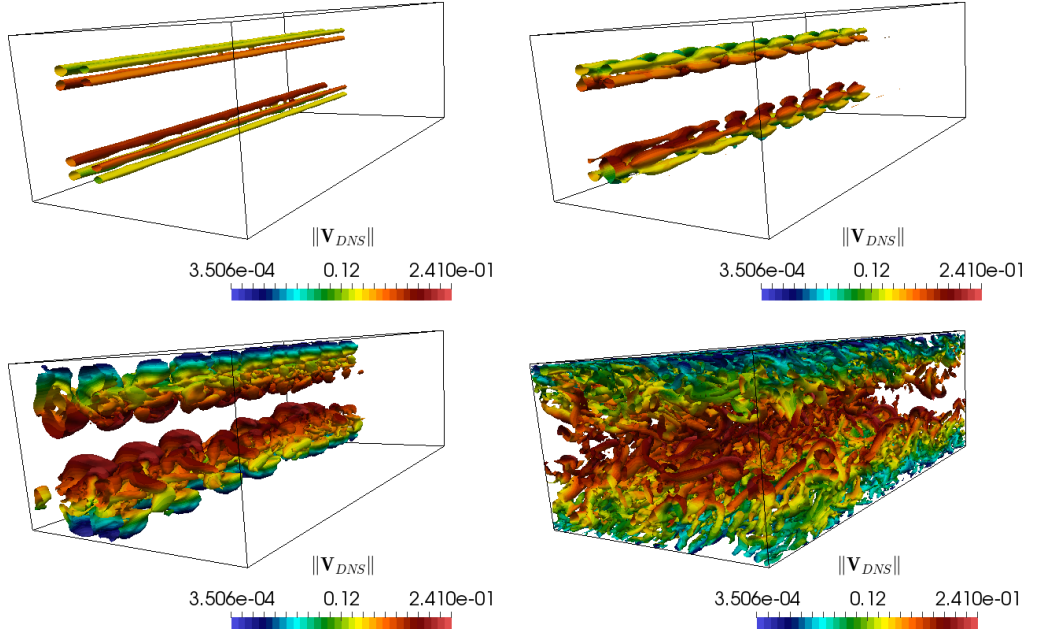


Figure 4.8: Q -criterion isosurfaces coloured by the velocity magnitude at 4 instants of time and depicting the bypass transition process. From top-left to bottom right: $t = 1450 L_h u_b^{-1}$ ($Q = 10^{-4}$), laminar; $t = 1480 L_h u_b^{-1}$ ($Q = 10^{-4}$) and $t = 1530 L_h u_b^{-1}$ ($Q = 5 \times 10^{-4}$), transition; $t = 1700 L_h u_b^{-1}$ ($Q = 0.05$), fully developed.

transition process is indeed an heteroclinic orbit going from the unstable equilibrium of the laminar flow to the stable limit cycle of the fully-turbulent flow. Therefore, applying DMD to the entire time window is very likely to give results that are not consistent. Figure 4.10 reports the information coming from the DMD in terms of the eigenvalues λ_i and the time dynamics $\alpha_i e^{\omega_i t}$ of the dynamic modes extracted. Since the DMD modes are normalized, the time dynamics is a direct indication of the importance of each mode with respect to the others at all time instants.

The t -envelope method

The DMD algorithm reported in Section 3.2.3 extracts 999 dynamic modes out of the 1000 snapshots collected in the chosen time window. The selection of the relevant modes among the ones available is the aim of the present section. The method here introduced, which represents an effort to take into account the local dynamics of DMD modes and will be hereafter referred to as t -envelope, will respond to two important

Chapter 4. Ranking of Modes

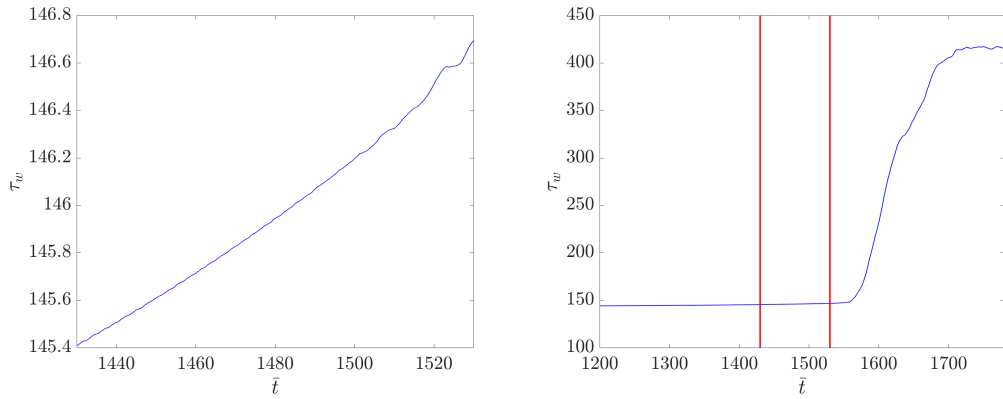
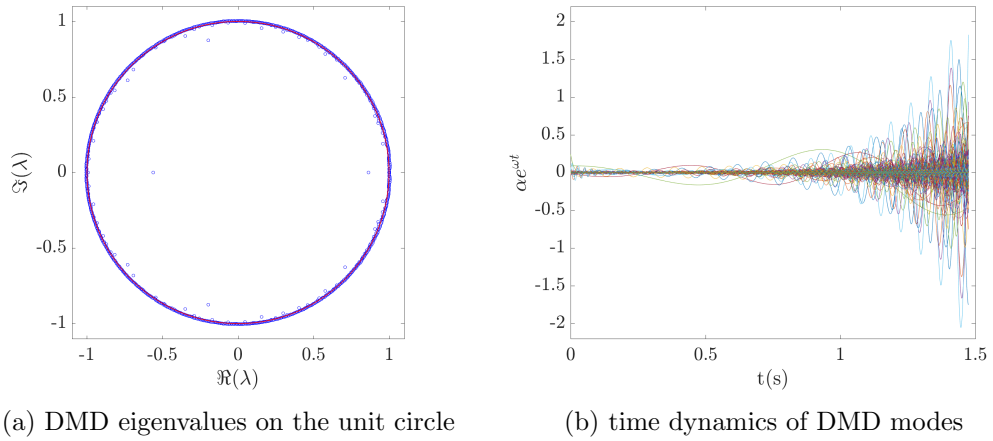


Figure 4.9: Shear stress evolution for the time interval used in DMD (left). Full time window from transition to a fully developed turbulent flow (right).



(a) DMD eigenvalues on the unit circle

(b) time dynamics of DMD modes

Figure 4.10: DMD eigenvalues and time dynamics.

questions: 1) can we identify DMD modes associated to physical flow structures that characterize the onset of transition and 2) can we identify those few DMD modes that better allow reconstructing the flow field in the region leading to the transition phase. The assessment and evaluation of DMD modes with respect to the two above criteria will be carried out by looking at the similarity between the reconstructed flow field using a few selected modes and the actual flow field in the time window preceding the actual transition zone, where turbulent structures will already show a chaotic behaviour. Moreover, a comparison with the energy ranking criterion by Tissot et al. [159] will be performed to show the improvements of the proposed method in expressing a specific

dynamics.

The proposed t -envelope method allows to perform a modes selection that is based on a criterion that is local in time and does not rely on an integral quantity, such as the one reported in Equation 4.3. The algorithm is straightforward and does not imply any computational step, besides the selection of local maxima. It can be schematized with the following few steps

- 1 The time dynamics of all the DMD modes, namely the functions $\alpha_i e^{\omega_i t}$, are evaluated at the sampling points and their amplitude is collected in a matrix \mathbf{T}_{dyn} , where on each row there are the time amplitudes of the corresponding DMD mode;
- 2 Since the DMD modes ϕ_i are normalized, these functions represent the actual contribution of each mode to the resulting flow field; therefore the maxima for each column of the matrix \mathbf{T}_{dyn} are computed and the corresponding modes are selected;
- 3 Once these modes have been selected, the positions of the maxima in the matrix \mathbf{T}_{dyn} are set to zero, the new maxima are computed and the corresponding modes selected;
- 4 The procedure can be iterated for any levels of selection, depending on how much resolution is desired for the coherent structures in the flow field.

The criterion for modes selection at each level can be expressed with a mathematical formula as follows:

$$Id_m(t) = \arg \max_{i=1, \dots, N_m} \|\alpha_i e^{\omega_i t}\| \quad \text{with} \quad 0 < t < T. \quad (4.4)$$

Once the $Id_m(t)$ is built at each level, all the modes are collected and used as inputs in the Equation 3.15 to obtain an approximation of the dynamic of the transition.

Analysis of DMD eigenvalues and modes

The selection process presented in the previous section is compared with the energy ranking criterion in Equation 4.3 in terms of differences of modes and corresponding eigenvalues selected among the entire set of the available ones.

Figure 4.11 reports, on the left, the t -envelope selection of DMD modes using 8 levels of selection and, on the right, the energy spectrum of DMD modes computed according to Equation 4.3. On the energy spectrum the modes selected with the t -envelope method, highlighted with black circles, are also reported together with the same number of the most energetic ones, highlighted in red. Here it can be noticed how some of the modes selected with the t -envelope method are not the most energetic ones but yet important for the dynamics. The total number of modes used, with a number of levels fixed to 8 for the t -envelope, is 32. Figure 4.12 shows the DMD spectrum, where the red circles indicate the growth/decay rate and frequencies of the DMD modes selected through the t -envelope and the energy method. Similarly, Figure 4.13 shows the α_i amplitudes versus the frequencies (imaginary part of ω_i eigenvalues) of the DMD modes selected with the two methods. It is worth noting that the spectra reported in Figures 4.12 and 4.13 are symmetric since the original data processed through the DMD algorithms are real. This generates outputs that appear always in complex conjugate pairs.

Figures 4.14 and 4.15 report the DMD modes selected with the t -envelope and the energy methods respectively and used to compute the approximated flow field with the Equation 3.15. All the modes are represented in terms of the Q-criterion computed on the three components of each mode. Since each complex mode appears in the list of the selected modes with its complex conjugate, only half of the modes is showed, excluding the one related to the mean, which does not vary over time ($\omega_{\text{DMD}} = 0$). Therefore, being the number of selected modes 32, only the real part of 15 of them is reported. All the selected modes are sorted according to the energy level defined in Equation 4.3. Comparing Figures 4.14 and 4.15 it can be observed how among the modes selected by the t -envelope method, modes exist that are closely related to the stream tubes characterizing the flow field at the beginning of the time window considered, which are not present in the energy selection process.

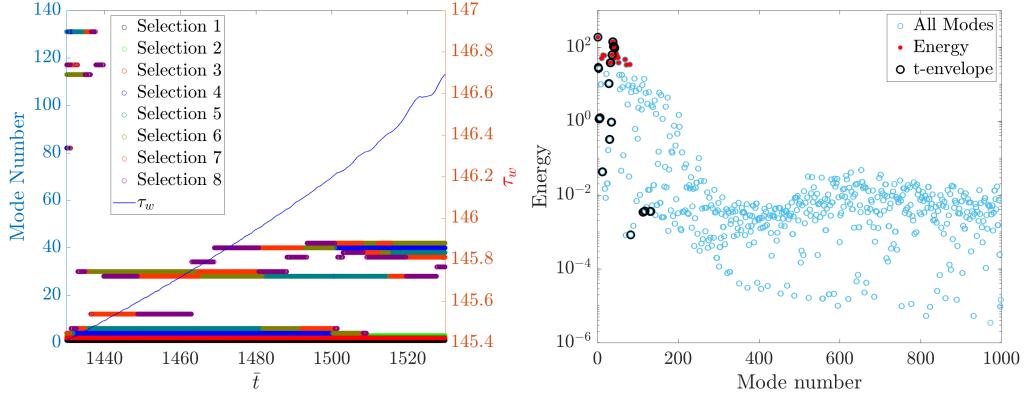


Figure 4.11: DMD modes selection using t -envelope method (left) and energy spectrum of all the extracted DMD modes (right): the red circles highlight the modes selected using the energy norm, the black circles the ones selected using the t -envelope method with 8 levels of selection.

Reconstruction of the flow field

The difference among the selected modes becomes evident in Figure 4.16 where a more explicit comparison of the onset of transition, as obtained through the numerical simulation and as it is reconstructed by the two set of modes, is presented. The DMD reconstruction is computed according to Equation 3.15, where the multiplication and summation of complex terms is treated using the complex matrix algebra implemented in the Eigen Library [149]. The top row in Figure 4.16 reports the DNS-like solutions at three distinct instants of time in the time window of Figure 4.9. The left plot refers to a time instant at the beginning of the window, the central plot to an intermediate one and the right plot to a time at the end of the time window, right at the beginning of the actual transition phase as indicated by the shear stress plot. The middle row is the reconstructed flow field using the t -envelope method and the bottom row reports the reconstructed fields using the Energy method. In these Figures, the Q-criterion of the reconstructed velocity field is shown.

Remarks

It can be noticed how the t -envelope method is able to provide reconstructed flow fields that are closely related to the actual flow field. Indeed, the modes identified by the

Chapter 4. Ranking of Modes

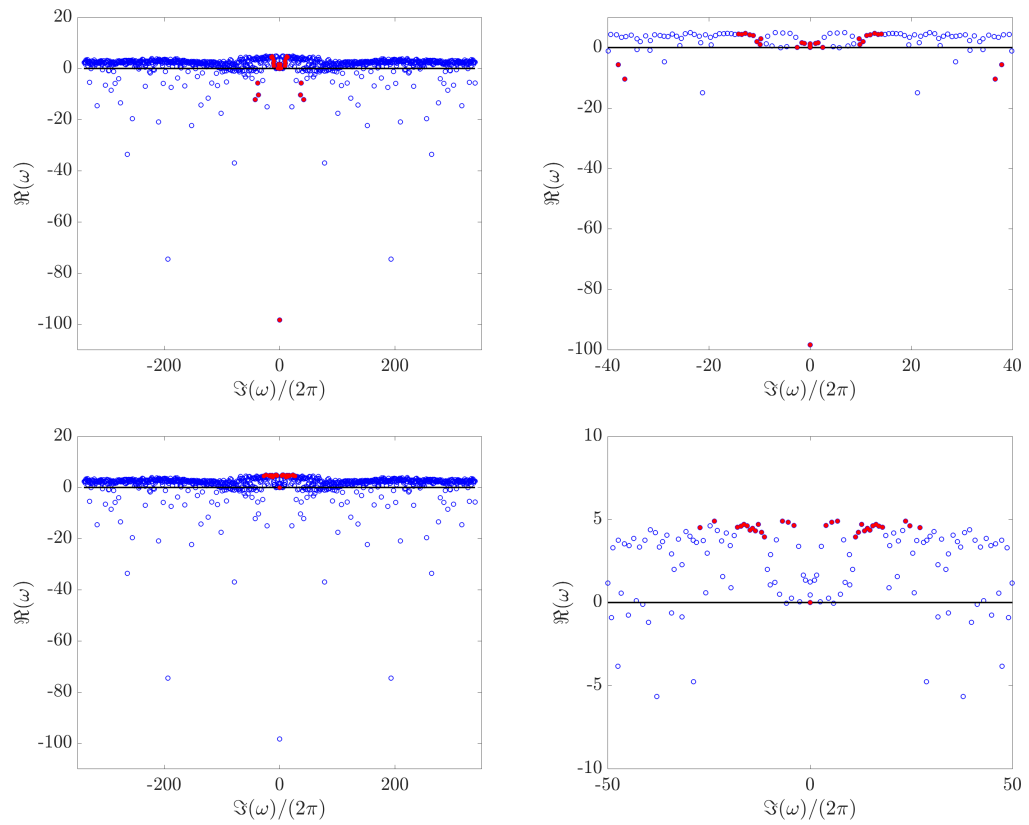


Figure 4.12: DMD spectrum (ω):(left) whole spectrum and (right) detailed view on the selected modes. Red circles highlight the DMD modes selected on the DMD spectrum using the t -envelope method (first row) and the energy method (second row).

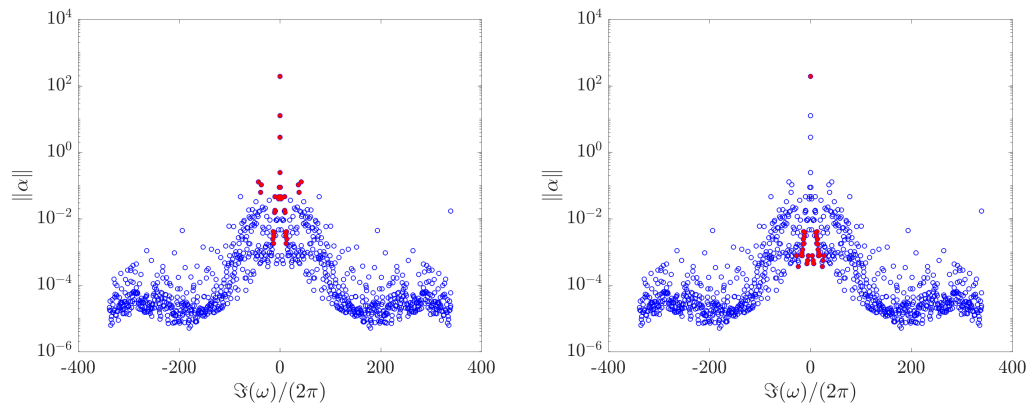


Figure 4.13: Amplitude of α coefficients. Red circles highlight the DMD modes selected using the t -envelope method (left) and the energy method (right).

t -envelope clearly isolate the instabilities of the laminar streaks as they grow, as time progresses and transition becomes evident. Also, it is worth noticing how the reconstructed flow field by the t -envelope at the last instant of time of the time window is visually very similar to the actual flow field. These elements support the case for the adoption of the t -envelope method for the identification of structures leading to transition and also for the identification of the few relevant modes for a fairly accurate reconstruction. This is quite evident when a comparison with the energy-based reconstruction is presented, where the identification of relevant flow structures and their evolution in time is not quite possible and also the reconstruction at the last instant of time seems to be less accurate than in the case of the t -envelope. Moreover, for the first two instants of time reconstructed with the Energy method, a different value for the Q-criterion isosurfaces is used in order to be able to visualize the streamwise streaks, while for all the other cases this value is kept constant. Also a quantitative analysis has been carried out to prove that the t -envelope method is performing better than the energy selection criterion. Figure 4.17 shows the error defined in Equation 4.2. The error is reported over time for both the velocity magnitude and each component of the velocity vector. It can be noticed how the t -envelope method always outperforms the energy method also in terms of ϵ .

Chapter 4. Ranking of Modes

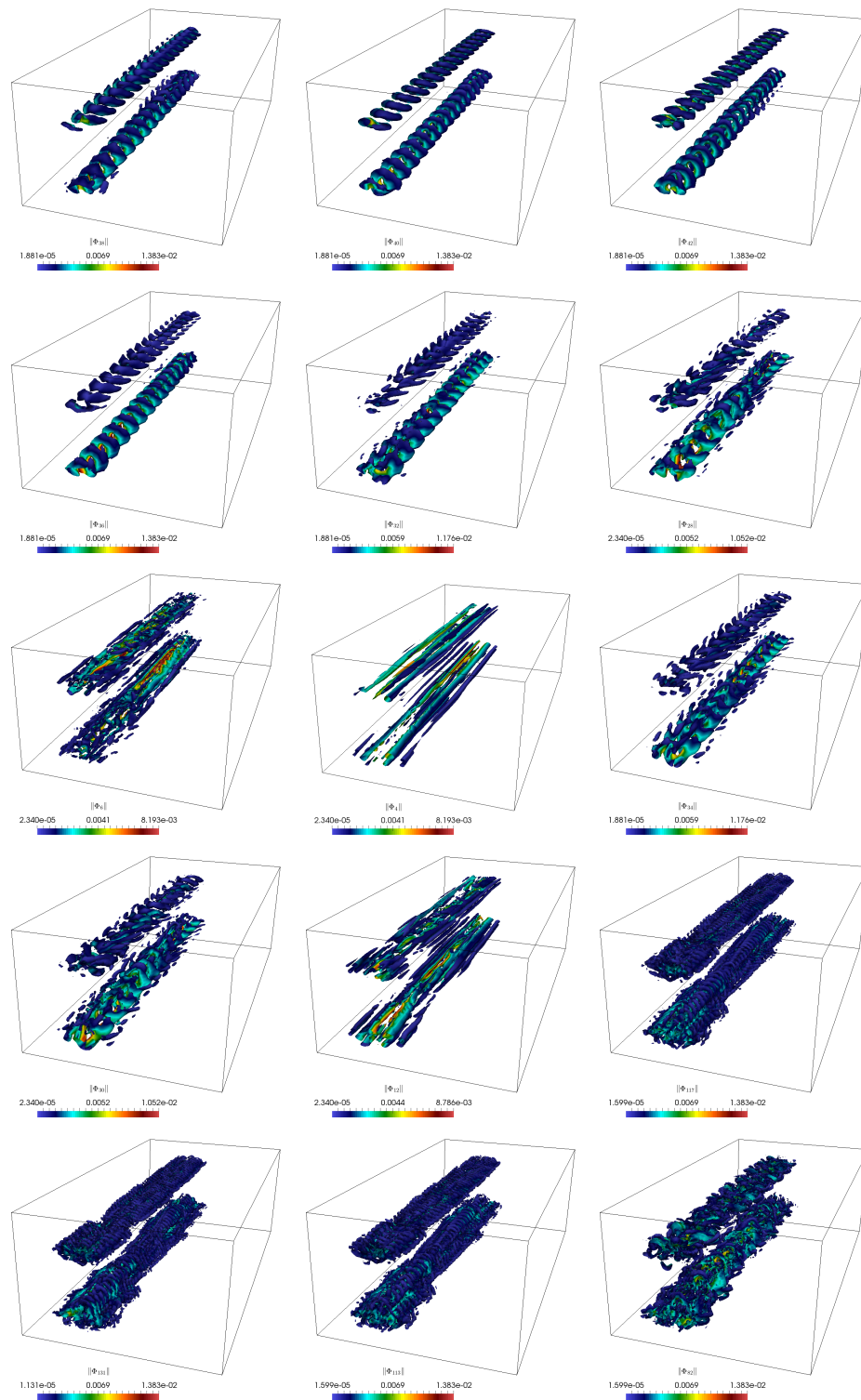


Figure 4.14: Selected modes via the t -envelope approach coloured by ϕ magnitude. Modes are ordered from left-to-right, from top-to-bottom, according to the corresponding energy content.

Chapter 4. Ranking of Modes

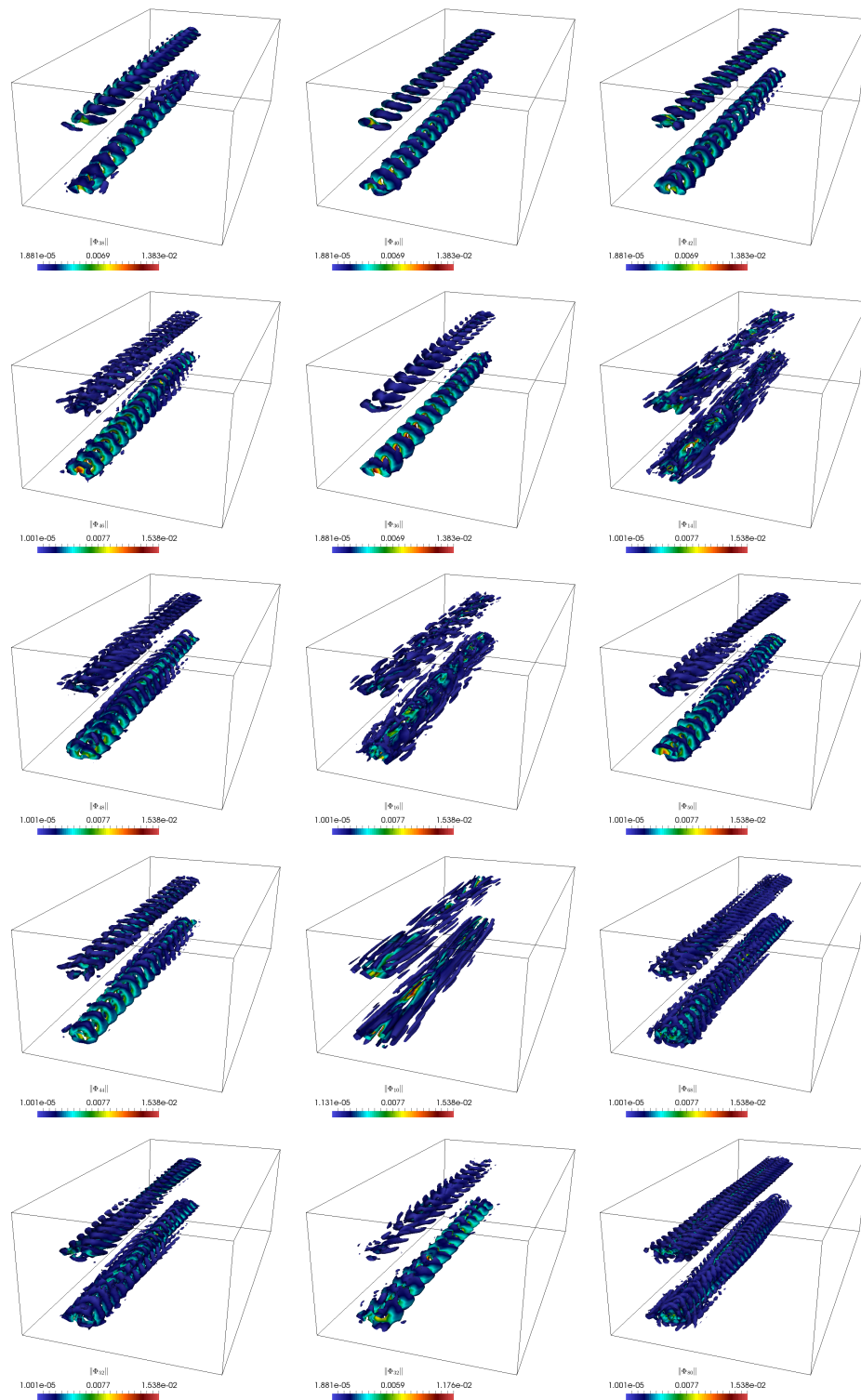


Figure 4.15: Selected modes via the energy approach coloured by ϕ magnitude. Modes are ordered from left-to-right, from top-to-bottom, according to the corresponding energy content.

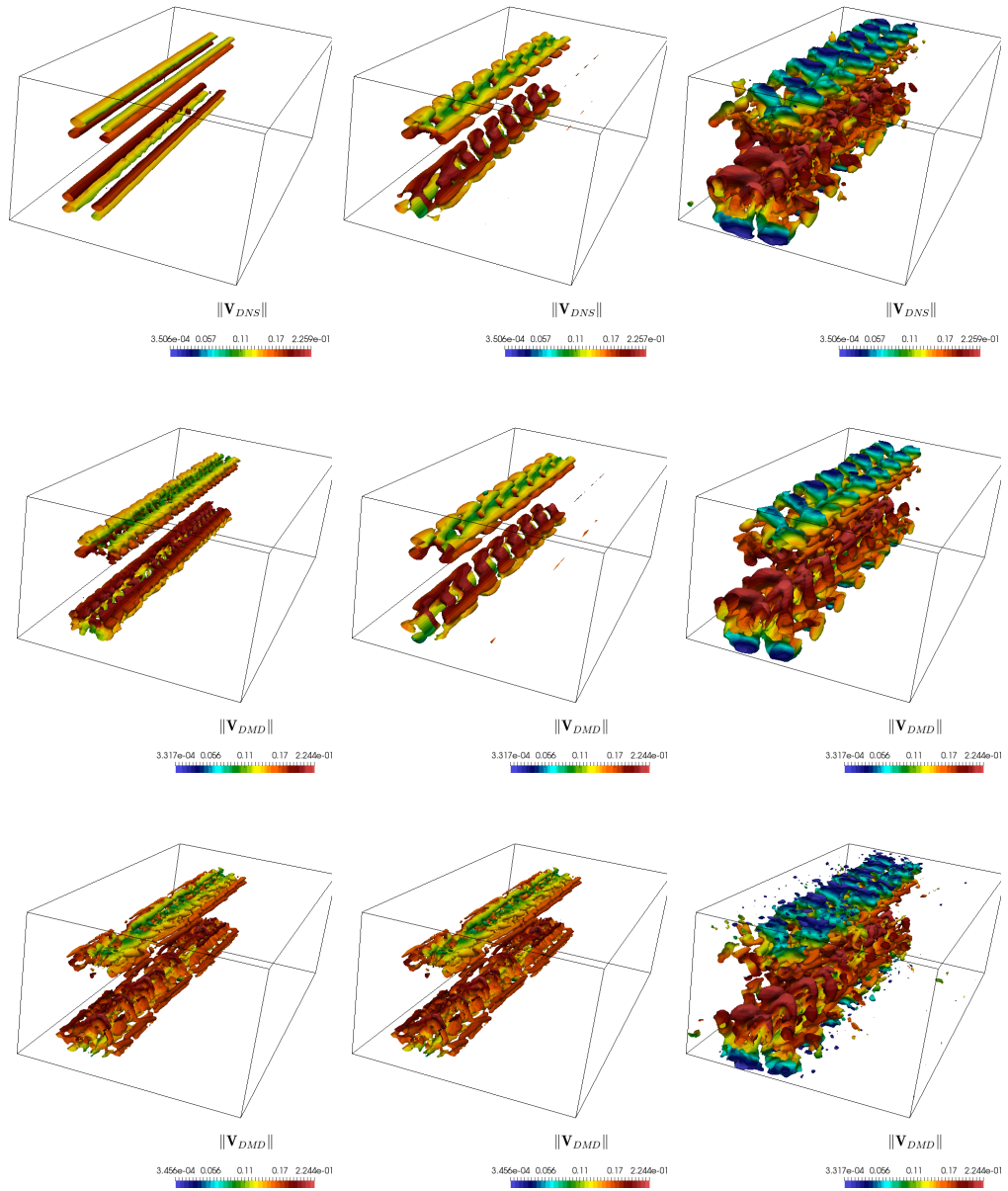


Figure 4.16: Comparison of the onset of transition described through numerical simulation (first row), DMD t -envelope (second row), DMD energy (third row); $t = 1430L_h u_b^{-1}$ (first column), $t = 1480L_h u_b^{-1}$ (second column), $t = 1530L_h u_b^{-1}$ (third column).

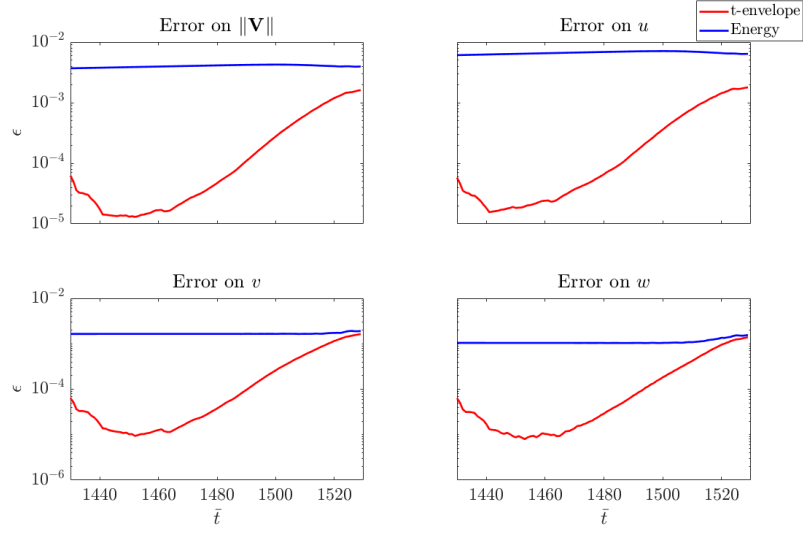


Figure 4.17: Relative error of the Energy and t -envelope method with respect to simulations, for the velocity vector: velocity magnitude and velocity components.

4.3 Ranking of RDMD modes

Since RDMD inherits the optimality property of POD, an energy criterion for modes ranking can be defined, with an ordering that follows the recursion procedure. The modes are normalized during the extraction step as described by Noack et al. [44] and the associated energy content is linked to the singular values extracted during the recursion [69]. Indeed, differently from DMD, the equivalence between singular values and modes norm still holds as in the case of POD. The singular values are the ones computed at each step of the recursion when the DMD algorithm is applied (see Section 3.2.4) and are eventually used to define the cumulative energy of the RDMD modes as follows

$$E_{r-1} = \frac{\sum_{i=1}^{N_s-1} \sigma_i^2 - \sum_{j=1}^{N_s-1} \sigma_{i,r}^2}{\sum_{i=1}^{N_s-1} \sigma_i^2} \quad (4.5)$$

where E_r is the energetic content of the first r modes (at the r -th step of recursion), σ_i are the singular values at the first step of recursion, $\sigma_{i,r}$ the ones at the r -th step of recursion.

Chapter 5

Model-Based Adaptive Reduced Order Model

A novel technique that aims at creating a synergy among different sets of basis functions to reconstruct the dynamics of complex nonlinear unsteady flows is here formulated. Different ROMs are combined together to build a unique Adaptive Framework that selects the most accurate method to reconstruct the solution at every untried/unsaved instant of time within the sampled time window. Central to this novel Framework will be the introduction of an error estimation to drive the adaptive choice of methods. Different formulations for estimating ROM accuracy are presented, together with a comparative analysis of the performance of the adaptive technique equipped with different error formulas. The comparative analysis reported will show how an error measure based on the evaluation of the FV residual is a good candidate when used as a means to drive the adaptive selection in time of the low-dimensional space. The main advantage of such formula is that it does not need any reference solution to be computed, as opposed to a formulation where the reduced solution is compared directly to a set of reference solutions. The comparative study leads to the definition of a hereinafter called Model-Based Adaptive ROM, where the term Model-Based refers to the intrusive definition of the error based on a residual evaluation. Although the error introduces a component of intrusion, this is restricted to the offline phase when the error database is computed,

whereas the online phase still remains non-intrusive.

5.1 Adaptive Reduced Order Models

When trying to use ROMs on parameter spaces that have large parameter variations or over extended interval of time, the low-dimensional model is likely to have very low performance in resolving local nonlinearities. There are different strategies to address this problem using adaptive ROMs. Examples are present in the literature where an adaptive sampling of snapshots is performed. Many are the algorithms that have been proposed for a parametric adaptive sampling, often based on physical considerations. Snapshots are added iteratively in regions of the design space where the ROM is less accurate, according to an error estimator. Examples of such strategies are leave-one-out [165, 166] and methods based on Gaussian Process Regression [167]. The starting point can be a uniform sampling over the parameter space or a non-uniform sampling, like Latin Hypercube, Centroidal Voronoi Tessellation (CVT), Halton sequence, Sobol sequence and many others [107, 129, 168, 169, 170]. There is scarcity of methods instead to perform an adaptive sampling in time, which often implement ad hoc functions depending on the specific dynamics at hand [146]. Usually the sampling is performed uniformly, since proper techniques for the adaptive sampling in time need to define an adaptive time step also for the solution of the initial set of equations [63]. Besides the adaptive sampling, there are also techniques that try to implement local low-dimensional spaces, in order to deal with localized nonlinear phenomena. These techniques usually extract local basis functions. Rewienski and White [171] presented a trajectory piecewise linear approach that aims at giving a low-order piecewise linear approximation of the nonlinear function appearing on the right hand side of the dynamic equations of the system. Rewieński and White [172] also offered a study of error bounds for the proposed technique. Washabaugh et al. [173] proposed nonlinear ROMs based on local approaches for parametric problem, using unsupervised learning algorithm to cluster solutions and define sub-spaces over the entire parameter space. Zhan et al. [174] implemented a similar approach to conduct a comprehensive exploration of

the in-flight icing certification envelope. Local approaches are also often implemented for advection dominated phenomena, where global basis functions usually show very low performances as opposed to local approaches [175]. Examples of this effort are the work of San and Borggaard [176], which proposed a Principal Interval Decomposition to compute different set of basis functions on different time window, and the work of Peherstorfer [50], which used an adaptive approach able to switch continuously between the low-order and full-order model on the basis of an error estimator. Each time the switch is performed, either a new basis is computed or the original basis is updated with additional information. Recent effort to deal with advection problems have been also oriented on defining Lagrangian ROMs, based on widespread techniques in the fluid dynamics community [52, 53], or on computing advection modes [51].

A different approach, that goes beyond the idea of both adaptive sampling over time and parameter space and the idea of defining local basis function, is the adaptive h -refinement proposed by Carlberg [177], which borrows idea from h -adaptation of computational meshes, generalizing it for POD basis functions. With this method, an original set of basis functions coming from POD is recursively split until a certain error tolerance is reached in the ROM solution. In particular, the selected reduced basis vectors are split into multiple vectors with disjoint discrete support and the splitting technique is based on a tree structure computed by applying k -means clustering to the state variables. Differently from all the other methods, the h -adaptivity ROM proposed by Carlberg ensures convergence to the full-order model, which is when the splitting method leads to the same DOFs of the full-order solution. Etter and Carlberg [178] further developed this idea using vector-space sieving for splitting the original set of basis functions.

5.1.1 Adaptive Framework based on different sets of basis functions

The present chapter introduces a different idea of adaptive ROM, that is neither local nor focused on the sampling procedure. Following the analysis performed in Chapter 3, it has emerged that different set of global basis functions, coming from different algorithms for dimensionality reduction, provide different performances in describing

the time dynamics over the selected time interval. For instance, RDMD has shown to outperform POD when the solution is converging to the final attractor, once the initial transient is vanished. Overall, considering the entire dynamics, it is clear that a unique winner cannot be found to describe the whole dynamics with only one set of basis functions. This is why all the methods presented in Chapter 3 will be used in synergy to create a monolithic ROM framework, which will be referred hereafter as Adaptive, able to select the best linear method for the computation of the online solution. Naturally, the method that drives the selection is based on a particular definition of the error, which is crucial for any adaptive strategy. Section 5.2 provides an overview of ways to estimate ROM accuracy; Section 5.2.1 introduces a measure of how well a generic ROM is approximating the high-dimensional space defined by the original snapshots; Sections 5.3 and 5.4 focus on two particular definitions of the error, namely a so-called direct error, which has been already used in Chapter 4 to show the quantitative influence of modes ranking on ROM reconstructions, and a so-called residual error [70]; Section 5.5 compares the performances of these two error definitions when used in the Adaptive Framework, which is schematized in Section 5.6 [69].

5.2 Estimating the accuracy of a ROM

A reliable definition of the error to estimate the accuracy of a ROM is crucial for every adaptive technique [65]. Indicating with \mathbf{v} the exact solution and with $\hat{\mathbf{v}}$ the reduced order approximation, a straightforward definition of the error is

$$\mathbf{e} = \mathbf{v} - \hat{\mathbf{v}} \quad (5.1)$$

All the quantities reported in Equation 5.1 are vectors, i.e. discretised solutions over the computational domain. The quantity \mathbf{e} can be then decomposed as [179, 180]

$$\mathbf{e} = \mathbf{e}_{\parallel} + \mathbf{e}_{\perp} \quad (5.2)$$

\mathbf{e}_\perp is the component of the error perpendicular to the low-dimensional space built with the ROM and therefore it depends on the information content the extracted basis is able to preserve. \mathbf{e}_\parallel represents the component of the error that lies in the low-dimensional space defined by the reduced basis, and it is a contribution to the error linked to the method used to compute the coefficients a_i of the expansion in Equation 2.1. Many efforts have been put in the literature to find a-posteriori error bounds and a-posteriori error estimators for the quantity \mathbf{e} in order to elaborate certified and reliable ROMs. Nevertheless, the a-posteriori error estimators proposed have usually been ad hoc for particular partial differential equations, such as parabolic [67, 68] or elliptic [64, 65] problems, or linear and nonlinear systems of ODEs. The ad hoc a-posteriori error estimator is also linked to the specific discretisation used. Usually a-posteriori ROMs error estimation inherits a-posteriori error estimators from finite element methods [64, 65, 181], but efforts have been put to define estimators also for Finite Volume discretisation [85, 182, 183].

It is worth noticing that all these a-posteriori and a-priori error bounds and error estimators have been so far introduced in the context of intrusive ROMs, therefore they bring information about the accuracy of the ROM with respect to the exact solution of the original system of equations. Since a non-intrusive online procedure is implemented in the present work, the errors used are neither bounds nor estimators of the actual accuracy of ROM with respect to the exact solution. They instead represent an effort to define ROM accuracy with respect to the high-fidelity solution obtained through some discretisation process of the initial system of governing equations, namely the Finite-Volume discretisation of the set of Navier-Stokes equations. Therefore all the errors introduced hereafter will consider the CFD solution as the exact reference solution.

5.2.1 Projection error

A compact expression approximating the perpendicular component of the error \mathbf{e}_\perp in Equation 5.2 is here provided. Indicating with \mathbf{P}_ϕ the projection operator defined by

a general linear basis, the quantity \mathbf{e}_\perp can be written as

$$\mathbf{e}_\perp = \mathbf{v} - \mathbf{P}_\phi \mathbf{v} \quad (5.3)$$

If Φ is the matrix whose columns are the basis functions ϕ , extracted with one of the algorithms reported in Section 3.2, an approximation to the projection operator \mathbf{P}_ϕ can be computed as (see also [161])

$$\tilde{\mathbf{P}}_\phi = \Phi(\Phi^* \Phi)^{-1} \Phi^* \quad (5.4)$$

A compact measure can be finally defined, the so-called projection error,

$$\epsilon_P = \frac{\|\mathbf{u} - \tilde{\mathbf{P}}_\phi \mathbf{u}\|_2}{\|\mathbf{u}\|_2} \quad (5.5)$$

where \mathbf{u} here represents a generic CFD reference solution. A low projection error indicates that the set of basis Φ retains a large amount of information coming from the original training snapshots. It is worth noticing that, since the projection error is only an approximation of the actual \mathbf{e}_\perp , it is not an indicator of a good accuracy of the ROM with respect to the underlying physics. The set of basis functions is built from available data \mathbf{u} that might not span the entire low-dimensional space, therefore a low ϵ_P does not guarantee accuracy at new untrained points where online solutions from the ROM are computed. Nevertheless, a high projection error is still a good measure to define inaccurate ROMs, as it indicates that the set of basis ϕ does not define properly the low-dimensional space or that a low-dimensional space for the specific problem under investigation cannot be found.

5.3 Direct error

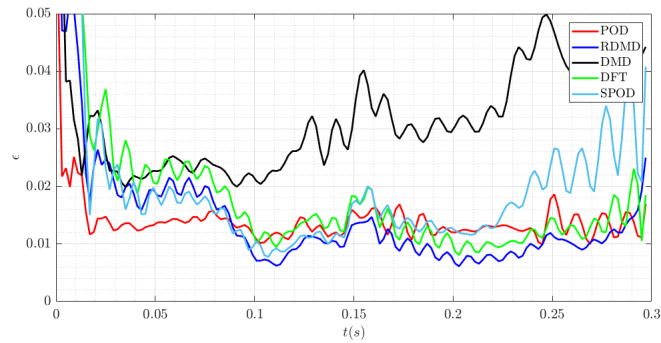
The direct error is defined as the norm of the error in Equation 5.1, normalized by the norm of the exact solution,

$$\epsilon = \frac{\|\mathbf{u} - \hat{\mathbf{u}}\|_2}{\|\mathbf{u}\|_2} \quad (5.6)$$

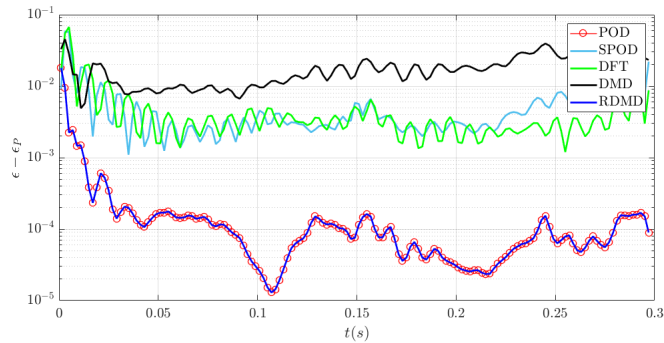
where \mathbf{u} represents a generic CFD reference solution. It represents the most reliable way to estimate the accuracy of a ROM, but it is also the most expensive to compute at untrained points as it requires additional full-order simulations to be run. The definition is equivalent to the error estimation provided in Chapter 4, when quantitative results on the accuracy in reconstruction have been reported. In order to evaluate error plots that are also able to test the predictive capabilities of the ROM, a leave-n-out approach is implemented, where $N_s/2$ equispaced snapshots over the entire investigated time window are used to build the basis, while the remaining $N_s/2 - 1$, still equispaced in time and in the mid-points between snapshots used for the ROM, are used to compute the error (see also Figure 5.3). The strategy is similar to the leave-one-out approach, implemented for example in [166, 174]. In this case, in order to compute the direct error at a specific location, the corresponding snapshot is excluded from the training of the reduced basis and is used to estimate the accuracy of the ROM using Equation 5.6. Nevertheless, for the specific case of unsteady flows, iteratively excluding one snapshot can lead to a situation where the sampling is not equispaced in time and inconsistencies are present in the unsteady algorithms to extract flow features, which is why a leave-n-out approach is implemented instead.

Figure 5.2 reports examples of direct error and projection error for the two test-cases presented in Chapter 3. The first two rows report the direct error ϵ and the difference $\epsilon - \epsilon_P$ between direct and projection error in logarithmic scale for the NACA0012 test-case, over the entire investigated time window. Analogously, the last two rows show the same quantities for the 30P30N test-case. The DMD projection error is reported for completeness, since no meaningful information can be inferred in this case. Indeed, the different reconstruction formula used for DMD (see Section 3.3), does not allow a straightforward decomposition of the error as the one presented in Section 5.2. For all the other methods, once the rank has been fixed, it is worth noticing the higher overall performance in defining a low-dimensional space when the set of basis functions is orthogonal, i.e. for the case of POD and RDMD. These are indeed the cases that show the lowest projection error for both NACA0012 and 30P30N, which means that the main error source is principally linked to the computation of coefficients in the

low-dimensional space. The behaviour of the SPOD basis is different instead, since it shows comparable contribution to the final error linked both to the projection operation and the computation of coefficients. Another aspect worth noticing from Figure 5.2 is that for both test-cases there is no common pattern that allows to define a particular ROM as the best one to approximate the evolution over the whole time-interval. This consideration is at the basis of the adaptive strategy finally introduced in the present Chapter, as the only possible way to combine best accuracy at each time step desired for reconstruction.



(a)



(b)

Figure 5.1: Examples of Direct and Projection Error for the NACA0012 test-case presented in Chapter 3. Direct Error ϵ is reported in 5.1a, the difference between the two $\epsilon - \epsilon_P$ is reported in 5.1b. Errors are computed using the leave-n-out strategy (error in the mid-points of the training snapshots).

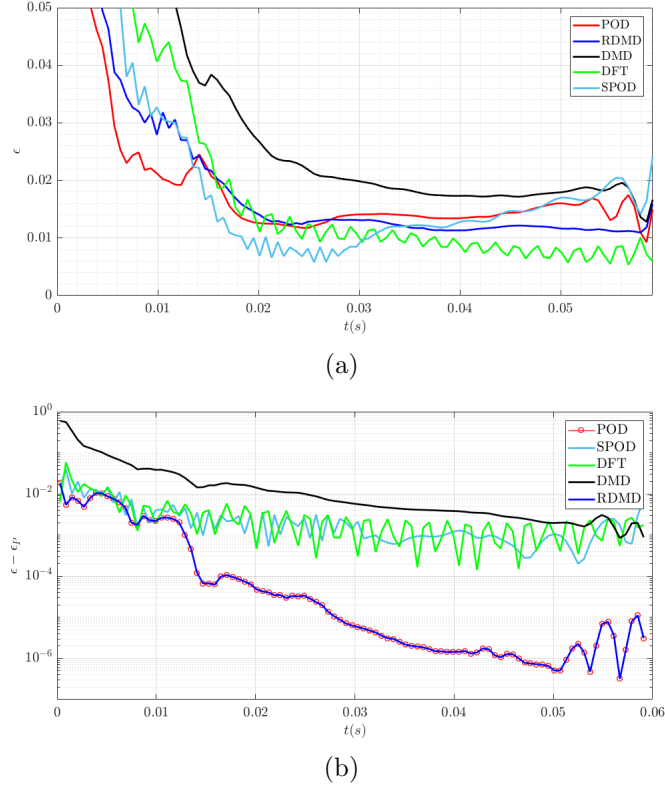


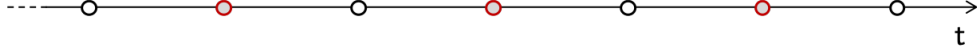
Figure 5.2: Examples of Direct and Projection Error for the 30P30N test-case presented in Chapter 3. Direct Error ϵ is reported in 5.2a, the difference between the two $\epsilon - \epsilon_P$ is reported in 5.2b. Errors are computed using the leave-n-out strategy (error in the mid-points of the training snapshots).

5.4 Residual error

The leave-n-out approach based on the direct error often leads to a severely depleted set of snapshots to be actually used in the basis construction. A different definition of the error is introduced instead in the present Section, i.e. the residual error, that does not require any reference solution and therefore allows the ROM to use all the available snapshots to build the low-dimensional space. The conceptual difference between the two errors is illustrated in Figure 5.3. The residual error is computed substituting the general ROM solution provided by Equation 2.1 in a particular discretisation of the Navier-Stokes equations. Therefore it introduces a component of intrusion that might limit its application to situations where the snapshots are based on CFD calculations.

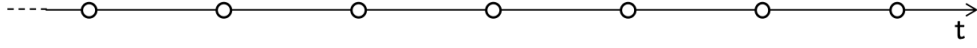
“Direct” error

*Provides exact measure of error if exact solution is known; **DOES** require knowing a set of reference solutions to compare with*



“Residual” error

*Provides a measure of how well the RB solution resolves the discrete form of the equations; **DOES NOT** require any reference solutions*



○ Indicates a snapshot, i.e. the solution of the PDE at an instant of time **used to build the RBM**

○ Indicates a solution needed to assess the RBM

Figure 5.3: Conceptual difference between direct and residual error. RBM indicates a Reduced Basis Method, alias ROM.

It is worth noticing that the residual produced by the original set of governing equations of a fluid system has been already used in the literature to elaborate ROMs, even if for completely different aims [24, 184]. Indeed, a residual minimization algorithm is often used to compute the set of coefficients for the reduced basis, namely the a_i in Formula 2.1, and therefore it is a part of an online phase that gives as output the final solution reconstructed at the querying point. Other usage of residual evaluation includes also stabilization techniques [185]. In the present work instead, the residual is used as a measure to assess the performances of different ROM techniques. Since the focus is on unsteady fluid problems, an edge-based Finite Volume formulation is considered for the residual error, equipped with a Backward Difference Formula (BDF) for the unsteady term, which ensures second order accuracy. The formula is briefly derived in the following. A strong formulation of the Navier-Stokes equations in conservative form is

$$\frac{\partial \mathbf{w}}{\partial t} + \nabla \cdot \mathbf{F}(\mathbf{w}) = 0 \quad (5.7)$$

where \mathbf{w} indicates the vector of conservative variables, namely $\mathbf{w} = [\rho, \rho u, \rho v, \rho w, \rho E]$ and \mathbf{F} represents the vector of convective and viscous fluxes. Considering a Finite Volume approach, Equation 5.7 is integrated over the generic cell V_i of the computational

domain, obtaining

$$\int_{V_i} \frac{\partial \mathbf{w}}{\partial t} dV_i + \int_{\partial V_i} \mathbf{F} \cdot \mathbf{n} d(\partial V_i) = 0 \quad (5.8)$$

where the second integral is obtained applying the Divergence Theorem. Equation 5.8 is still exact and approximations are introduced to compute the volume and surface integrals. Specifically a linear variation of the quantity \mathbf{w} is considered over the generic cell V_i and the generic flux $\mathbf{F}(\mathbf{w})$ is evaluated over the edges of cell V_i considering an intermediate state $\hat{\mathbf{w}}$, which is computed on the basis of the value of \mathbf{w} in the actual cell and the one in the neighbor cell sharing the same edge. The following approximations are therefore introduced

$$\mathbf{w}(\mathbf{x}) \approx \mathbf{w}_i + (\mathbf{x} - \mathbf{x}_i) \cdot \nabla \mathbf{w} \quad (5.9)$$

$$\int_{\partial V_i} \mathbf{F} \cdot \mathbf{n} d(\partial V_i) \approx \sum_{j=1}^{N_{\text{edges}}} \hat{\mathbf{F}}_j \cdot \mathbf{S}_j \quad (5.10)$$

where $\hat{\mathbf{F}}_j$ is the flux computed at the intermediate state $\hat{\mathbf{F}}_j = \mathbf{F}(\hat{\mathbf{w}})$, and $\mathbf{S}_j = \mathbf{n}S_j$, with S_j the area of the generic edge. Substituting in Equation 5.8 and defining as \mathbf{R}'_i the residual produced by the approximations introduced,

$$\frac{\partial \mathbf{w}_i}{\partial t} V_i + \sum_{j=1}^{N_{\text{edges}}} \hat{\mathbf{F}}_j \cdot \mathbf{S}_j = \mathbf{R}'_i \quad (5.11)$$

A second order Backward Difference Formula (BDF) is finally considered for the temporal derivative, obtaining the final expression of the residual \mathbf{R}_i for the generic cell V_i and for the entire set of the conservative variables,

$$\mathbf{R}_i = V_i \frac{3\mathbf{w}_i^{n+1} - 4\mathbf{w}_i^n + \mathbf{w}_i^{n-1}}{2\Delta t_{\text{res}}} + \left(\sum_{j=1}^{N_{\text{edges}}} \hat{\mathbf{F}}_j \cdot \mathbf{S}_j \right)_{n+1} \quad \text{with } i = 1, 2, \dots, N_p \quad (5.12)$$

where $\mathbf{R}_i = \mathbf{R}'_i + \mathbf{r}$ and \mathbf{r} represents the additional contribution to the residual coming from the discretisation of the temporal derivative. N_p represents the number of points of the computational domain. The residual is evaluated at time instant $t = t_{n+1}$ and

it will be referred to as Dual Time Residual (DTR). To obtain a final measure of the residual error, the norm of \mathbf{R}_i over the entire computational domain is computed, normalized by the number of points. Therefore, for each conservative variable

$$\epsilon_{R,j} = \sqrt{\frac{1}{N_p} \sum_{i=1}^{N_p} R_{j,i}^2} \quad (5.13)$$

with $R_{j,i}$ the residual produced by the j -th conservative variable, in the i -th cell, according to Equation 5.12. The Δt_{res} in the Equation 5.12 represents an additional parameter for this particular error definition and dictates where the ROM reconstructions are computed to evaluate the residual. For turbulent simulations using turbulence models, new conservative quantities need to be added to the vector \mathbf{w} . In the present work, only the residuals for mass, momentum and energy will be considered hereafter, but turbulence variables are also computed (e.g. eddy viscosity, k and/or ε and/or ω according to the turbulent model used for the simulation), since they are involved in the computation of the residuals of the primary conservative variables.

It is worth noting that the computation of the quantity ϵ_R introduces a component of intrusion in the process, since the original set of governing equation of the system is needed. Despite that, the evaluation of Formula 5.13 will be always performed during the offline phase of the ROM, in order to maintain the online process genuinely non-intrusive (see Section 5.6).

5.4.1 A note on Time Integration

The residual presented in Equation 5.12 derives from an only spatial integration of the initial set of Navier-Stokes equations, Equation 5.8. Therefore the error defined in Equation 5.13 only accounts for a spatial measure of how well the ROM satisfies the discretized equation. It is worth considering also a temporal contribution to the residual previously introduced [186], to better understand if the ROM is introducing an additional error while evolving the solution in time. The formulation of a residual that accounts for both spatial and temporal contribution can be still derived from Equation

5.7, integrating in space and time

$$\int_t^{t+\Delta t} \left(\int_{V_i} \frac{\partial \mathbf{w}}{\partial t} dV_i + \int_{\partial V_i} \mathbf{F} \cdot \mathbf{n} d(\partial V_i) \right) dt = 0 \quad (5.14)$$

Considering the same spatial approximations introduced for Equation 5.8, it is legitimate to consider directly the integral in time of Equation 5.11 for computing the new expression of the residual, obtaining

$$\int_t^{t+\Delta t} \left(\frac{\partial \mathbf{w}_i}{\partial t} V_i \right) dt + \int_t^{t+\Delta t} \left(\sum_{j=1}^{N_{edges}} \hat{\mathbf{F}}_j \cdot \mathbf{S}_j \right) dt = \int_t^{t+\Delta t} \mathbf{R}'_i dt \quad (5.15)$$

Since the first integral in time can be computed analytically using the fundamental theorem of calculus, the only further approximation that needs to be introduced for the computation of the final residual is related to the computation of the integral in time of the flux term. For this term a trapezoidal formula is considered

$$\int_t^{t+\Delta t} \phi dt = \frac{1}{2} (\phi_t + \phi_{t+\Delta t}) \Delta t \quad (5.16)$$

Applying the fundamental theorem of calculus for the first integral and the trapezoidal formula for the second integral and dividing by the integration interval Δt , an expression for the space-time residual is obtained

$$\mathbf{R}_{\Delta t, i} = V_i \frac{\mathbf{w}_i^{t+\Delta t} - \mathbf{w}_i^t}{\Delta t} + \frac{1}{2} \left(\sum_{j=1}^{N_{edges}} \hat{\mathbf{F}}_j \cdot \mathbf{S}_j \right)_t + \frac{1}{2} \left(\sum_{j=1}^{N_{edges}} \hat{\mathbf{F}}_j \cdot \mathbf{S}_j \right)_{t+\Delta t} \quad (5.17)$$

that is also known as the Crank-Nicholson formula [186]. Therefore this new residual will be referred to as Crank Nicholson Residual (CNR). Comparing Formula 5.17 to the Equation 5.12, the evolution over time of the fluxes is explicitly taken into account. This provides additional information about the temporal contribution to the integral measure of the error.

The computation of the two residual formulas, namely the DTR reported in Equation 5.12 and the CNR reported in Equation 5.17, is performed within SU2, introducing

some modifications to the source code. The computation of fluxes and unsteady terms appearing in the residual equations are performed using SU2 functions (e.g. Roe, JST for the fluxes, or Backward Difference Formula for the unsteady term). Two separate routines are introduced in the SU2 code, one for reading the input fields to substitute in the residual formulas, the other to assemble together the different terms appearing in the two residual formulas. The inputs come from the ROM code also used for the analyses presented in the previous chapters, which reconstructs the conservative fields at the time instant needed by the residual formulation. The cost associated to one residual evaluation is mainly linked to the time required for the computation of convective and viscous fluxes.

Figures 5.4-5.7 report a comparative analysis of the two residuals formulations, for the two test-cases already presented in Sections 3.4.1 and 3.4.2. The same Δt is considered for both time discretisation in Equation 5.12 and time integration in Equation 5.17. POD, DMD and RDMD are considered as methods for dimensionality reduction and the residual error is computed over the time window investigated, on a set of test points equispaced in time. To build each of the reduced models, 20 modes are considered for the NACA0012 test-case, while 10 modes are considered for the 30P30N test-case. Figure 5.4 clearly shows a very slight difference between the two residuals formulations for the case of the conservative variable density. Similar behaviour is shown also for all the other primary conservative variables, namely momentum and energy, even if not reported. This is also supported from Figure 5.5, where bar plots are reported for all the conservative variables, that indicate the method selected at each time instant on the basis of the lowest residual. In particular, the first row shows the selection driven by Formula 5.12, second row shows the selection driven by Formula 5.17. There are no significant differences between the bar plots reported on the two rows, which means that the various ROM considered do not add any significant residual in time. Same conclusions can be drawn from Figures 5.6 and 5.7, which report the same plots for the 30P30N test-case.

The performed analysis allows to define which of the two residual formulas introduced above should be considered to build an adaptive framework composed of different

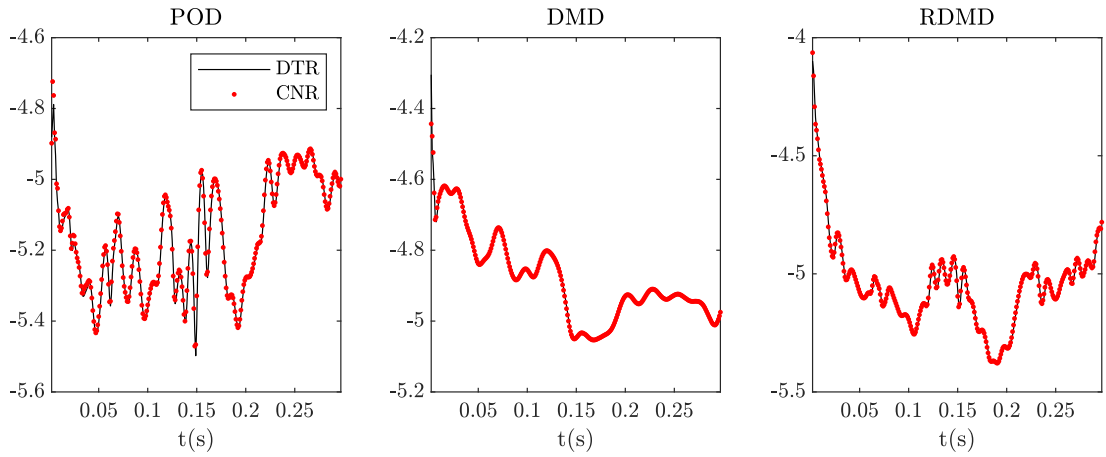


Figure 5.4: Comparison of residual plots using spatial and spatio-temporal residual error for various ROMs and conservative variable density, NACA0012 test-case.

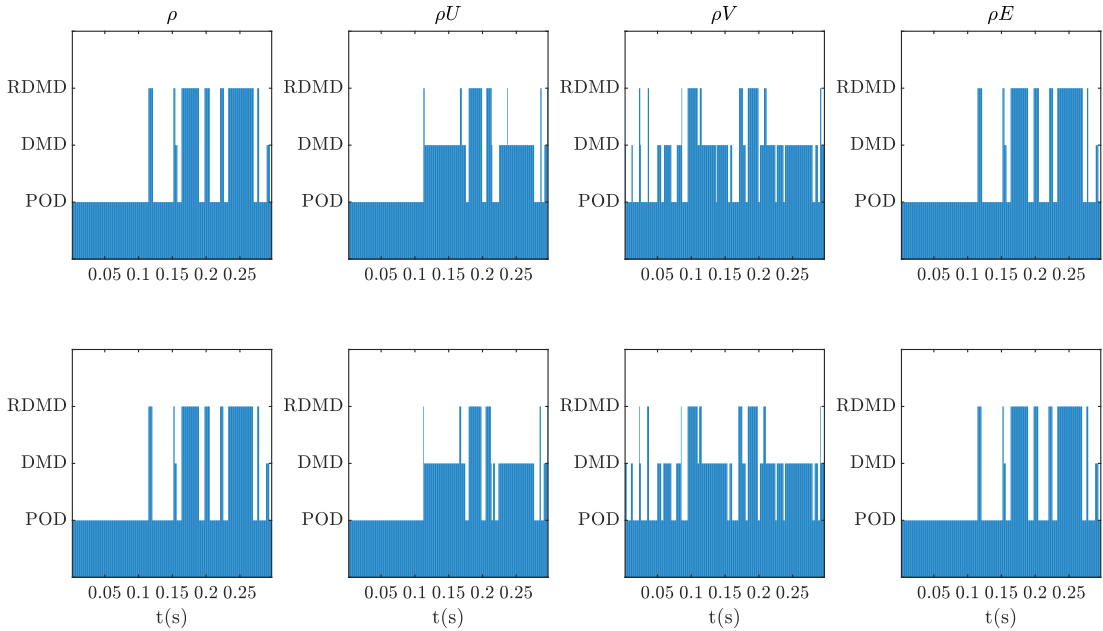


Figure 5.5: Bar plots with Basis Functions selection versus time using spatial residual error (first row) and spatio-temporal residual error (second row) for the set of conservative variables, NACA0012 test-case.

sets of global basis functions. Since there is no significant temporal contribution to the residual from each of the ROMs considered, Formula 5.12 should be used in the adaptive framework for the following reasons:

- Formula 5.12 is faster, since it involves the computation of fluxes only at one time

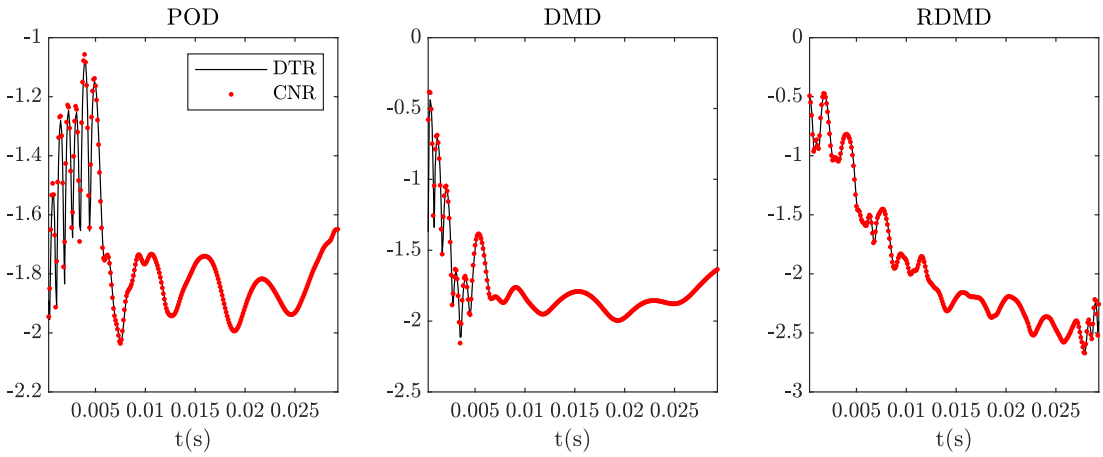


Figure 5.6: Comparison of residual plots using spatial and spatio-temporal residual error for various ROMs and conservative variable density, 30P30N test-case.

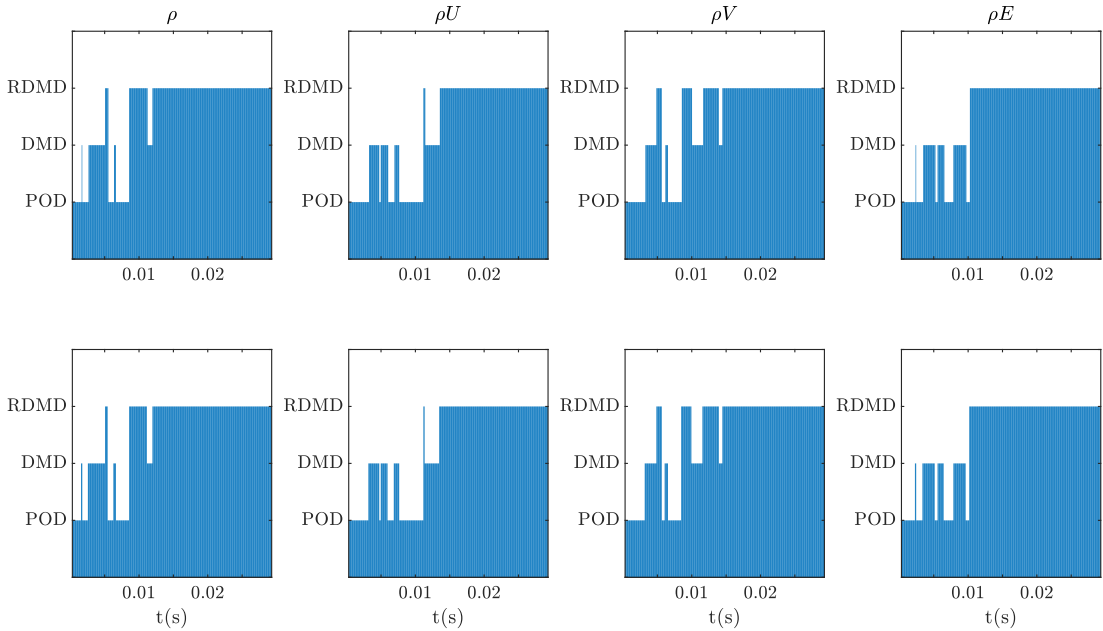


Figure 5.7: Bar plots with Basis Functions selection versus time using spatial residual error (first row) and spatio-temporal residual error (second row) for the set of conservative variables, 30P30N test-case.

instant, while the Crank-Nicholson formula requires computation of fluxes at two different time instants. The time required for the spatio-temporal formulation is therefore almost twice the time required for the spatial formulation only;

- Formula 5.17 introduces some ambiguity since it represents an integration over

a time interval, while Formula 5.12 is evaluated at a specific time instant. This is more in line with the underlying idea of the Adaptive Framework that will be introduced, since the main aim is to reconstruct the solution at a desired time instant with the set of global basis functions producing the lowest residual at that specific time instant.

In view of these considerations, Formula 5.12 will be the one used hereafter to define the Adaptive Framework equipped with an equation-based error and will be the one tested on various test-cases later in Chapter 7.

5.5 A comparative study of residual and direct error

The present Section offers a comparative study of the performances of two different ROM Frameworks, both based on the idea of adaptation introduced in Section 5.1.1 that is an adaptive framework able to combine different sets of global basis functions. The two frameworks are equipped with two different errors, namely the direct error introduced in Section 5.3 and the residual error introduced in Section 5.4. A slight modification of Equation 5.6 will be considered for this specific analysis, in order to make the normalization of the two errors consistent, namely

$$\epsilon_D = \frac{1}{\sqrt{N_p}} \|\mathbf{u} - \hat{\mathbf{u}}\|_2 \quad (5.18)$$

A prior sensitivity analysis is presented for the number of modes, i.e. the rank of each single ROM that will be eventually used in the Adaptive Framework, which has as final aim the identification of the set of modes that generates the lowest error possible. A further sensitivity analysis is also carried out for the Δt_{res} quantity for the specific case of the residual error. The performance of the Adaptive Framework with the two definition of the error is then assessed on two different 2D test-cases. The reason for this last analysis is to investigate accuracy of an Adaptive Framework equipped with an error definition, namely residual error, that might be less reliable than the direct

error, since it uses the equations of the governing system in its weak formulation and does not compare to any reference exact solution.

5.5.1 Sensitivity Analysis

The error estimation depends on a number of parameters. In the case of direct error, the sensitivity of the error is analysed with respect to the choice of the number of modes in the reconstruction and the method used for the reconstruction. In this analysis, the choice of modes is based on their ranking according to the relative energy content of each mode [23, 69], the output of such analysis being the optimal number of modes to be used for each set of basis function at a specific instant of time, that guarantees the lowest error. In the case of residual error, an additional parameter that is considered is the choice of the time step used to evaluate the BDF formula. The latter is quite a relevant parameter since it will affect the error measure as a consequence of the necessity of having two additional solutions to evaluate the BDF formula. This has been achieved here by using the same ROM to reconstruct the three solutions, i.e. the one at the instant of time of interest and two previous instants of time. Figure 5.8 left reports an example of the analysis done to assess the sensitivity of the residual error on the choice of Δt_{RES} . Results in this Figure refers to the NACA0012 test-case (Section 5.5.2). In all the analyses presented later, an iterative process has been put into place to reach a state where the changes in residual error, as Δt_{RES} is reduced, is below a specific tolerance set for all cases to 10^{-8} . The right plot of the same Figure shows instead the analysis done to assess the impact of the choice of the number of modes in the evaluation of the error. The latter has been done both for residual and direct error. On the basis of these considerations, an algorithm to compute the error associated to a specific method has been proposed that, on one side, automatically identifies the maximum Δt_{res} allowing for independence of the residual error from the choice of Δt_{res} , while on the other, allows considering the optimal number of modes to be used for a specific method during the reconstruction as the number of modes guaranteeing the lowest error. The Pseudo-algorithm for error estimation is

Pseudo-algorithm

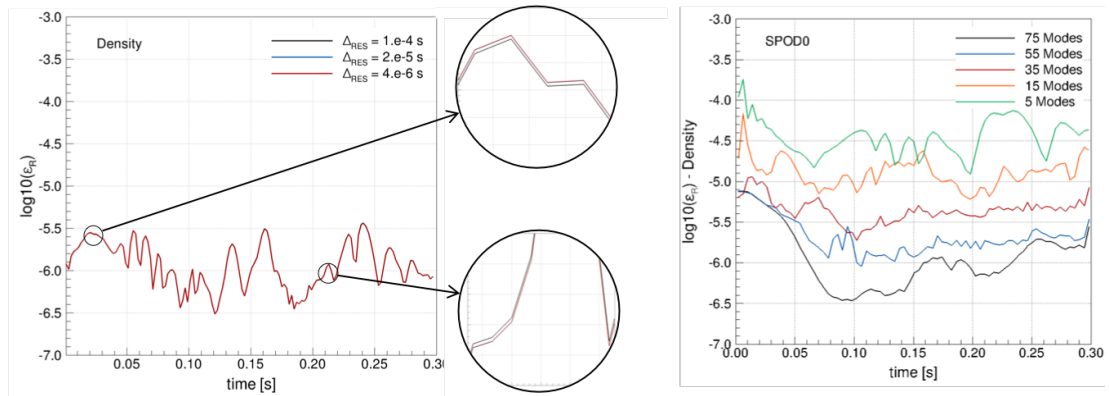


Figure 5.8: Sensitivity with respect to the choice of Δt_{res} (left), number of modes and choice of method for density (right).

```
for t = 1, N_t
```

```
  if  $\exists u_{\text{REF}}(t)$  then
```

```
     $\epsilon_d(t) = \min \epsilon_d(t; N_m, N_{\text{met}}) \quad \forall N_m, N_{\text{met}}$ 
```

```
  end
```

```
  if  $u_{\text{REF}}(t)$  .or. Resid then
```

```
     $\Delta t_r = \Delta t_{r0}$ 
```

```
     $\epsilon_r(t; \Delta t_r) = \min \epsilon_r(t; \Delta t_r, N_m, N_{\text{met}}) \quad \forall N_m, N_{\text{met}}$ 
```

```
     $\epsilon_{r,p} = 0$ 
```

```
     $\Delta \epsilon_r(t; \Delta_r) = \text{abs}(\epsilon_r - \epsilon_{r,p})$ 
```

```
    while  $\Delta \epsilon_r(t; \Delta_r)$  .gt. threshold
```

```
       $\Delta t_r = \Delta t_r / K$ 
```

```
       $\epsilon_{r,p} = \epsilon_r(t; \Delta t_r)$ 
```

```
       $\epsilon_r(t; \Delta t_r) = \min \epsilon_r(t; \Delta t_r, N_m, N_{\text{met}}) \quad \forall N_m, N_{\text{met}}$ 
```

```
       $\Delta \epsilon_r(t; \Delta_r) = \text{abs}(\epsilon_r - \epsilon_{r,p})$ 
```

```
      if  $\Delta \epsilon_r(t; \Delta_r)$  .lt. threshold
```

```
        exit
```

end

end

end

end

The pseudo-algorithm is performed offline (error estimation step in the left box in Figure 5.15). The expected outcome for the direct error ϵ_D is the method N_{met} and its corresponding number of modes N_m that guarantees the lowest ϵ_D . Equivalently, for the residual error the result will be the method N_{met} and its corresponding number of modes N_m that guarantees the lowest ϵ_R , with the only difference that a preliminary sensitivity analysis is performed, as stated above, to compute the best Δt_{res} for the evaluation of the residual. The selection of the best values for all these parameters goes through a manual exploration of the parameter space, where a set of N_m , Δt_{res} and all the methods N_{met} are considered. Convergence of the pseudo-algorithm to a global optimal solution is expected as the number of points in the parameter space is increased.

5.5.2 NACA0012

The conditions of the simulation for the NACA0012 airfoil are the same presented for the test-case in Section 3.4.1 (Table 3.1), the corresponding details of the reduced basis method are reported in Table 5.1. For additional details on the numerical setup and computational mesh the reader can still refer to the test-case presented in Section 3.4.1. The time required for computing a single time step using high-fidelity CFD is approximately 15 minutes on 1 core, while the time required to compute a single time step with ROM is in the order of a tenth of a second on 1 core. The ROM has been built in the time window where the dynamics of interest is happening, ranging from the very initial transient to the development of the vortex shedding flow past the airfoil, $t \in [0; 0.3]$ s. Within this time interval, a sampling Δt has been used equal to 4×10^{-3} , which results in 75 snapshots equispaced in time. It is worth noting that

Table 5.1: NACA0012 ROM setting

N_s	Δt_{NS} [s]	N.modes	Δt_{res} [s]	DOF_{CFD}	DOF_{ROM}	ROM [s]
75	$4 \cdot 10^{-3}$	Error-based	10^{-5}	242,600	$\mathcal{O}(10^2)$	1.8

the number of DOFs of the resulting ROM, reported in Table 5.1, is based only on the pseudo-algorithm presented in Section 5.5.1, and therefore it can range from very few modes retained to a maximum value which is linked to the number of snapshots used. Additional considerations on further reducing the number of modes retained, and therefore the resulting DOFs of the ROM, will be made later in the analysis presented in Chapter 6. The sensitivity analysis on the time step used for the residual evaluation led to a Δt_{res} of 10^{-5} seconds. Figure 5.9 reports the sensitivity of the reconstruction error for the density with respect to the choice of the number of modes and with respect to the different methods. While not reported in the Figure, the same analysis has been performed for all the other conserved quantities. The way plots have been represented reflects the steps of the pseudo-algorithm reported in section 5.5.1. Indeed for each plot in Figure 5.9, the minimum envelop of the curves related to different modes is taken as first step of the pseudo-algorithm. A general trend is observed where the error tends to reduce as the number of modes employed for the reconstruction is increased. This is not always observed in the case of DMD, where time windows exist for which the reconstructed flow with as few as 5 modes is the one that globally has the lowest direct error. This is supposed to happen as a consequence of the specific flow dynamics that has a very specific frequency captured by the few DMD modes. In Figure 5.9 the first column represents the sensitivity analysis on the number of modes performed using the direct error, while the second column reports the same sensitivity performed with the residual error, according to Equations 5.18 and 5.13. It can also be observed that the direct error evaluation tends to be in general lower than the residual error when comparing the same ROM. This difference is obviously related to the fact that the two error definitions have different units. Indeed, the direct error refers to the actual physical quantity, while the residual error refers to the conservation equation associated

to the specific physical quantity considered.

Figure 5.10 represents the second and ultimate step of the pseudo-algorithm. Indeed all the minimum envelopes obtained from Figure 5.9 for each method in the adaptive framework are combined together to obtain the minimum envelopes reported in the first row of Figure 5.10. The procedure is repeated for each conservative variable, obtaining the remaining rows reported in Figure 5.10. Therefore, these final envelopes represent the minimum error among all the considered methods and all the number of modes used in the reconstruction. Also for this final step, results considering both error definitions (residual error on the left, direct error on the right), are reported. Table 5.2 reports the percentage values of the choice of the best method over the time window explored for each one of the conserved quantities, which better clarifies the contribution of each of these methods to the minimum envelopes represented in Figure 5.10. It can be observed that for this type of flow, POD and RDMD are the most used methods. Some instants of time are best reconstructed using SPOD with a filter of 10 and only very few instants of time are best reconstructed with DMD. Overall the behaviour in terms of choice of methods is erratic, and it also depends on the specific conservative variable, which justifies the need of the pseudo-algorithm introduced in Section 5.5.1 for elaborating a classification of methods. Finally, Figures 5.11a and 5.11b report the reconstruction of the flow field by means of the adaptive approach for two different instants of time. A comparison with a reference high-fidelity solution not used in the definition of the ROM is presented. The momentum magnitude is shown as obtained by reconstructing independently the two components ρu and ρv . Coloured contours refer to the high-fidelity solution while solid black lines the reconstructed field. The Figure also reports the number of modes and the method used for the reconstruction of the two components of the momentum. Overall, the agreement is good and minor differences are observed between the reconstruction based on the direct error and the one based on the residual error.

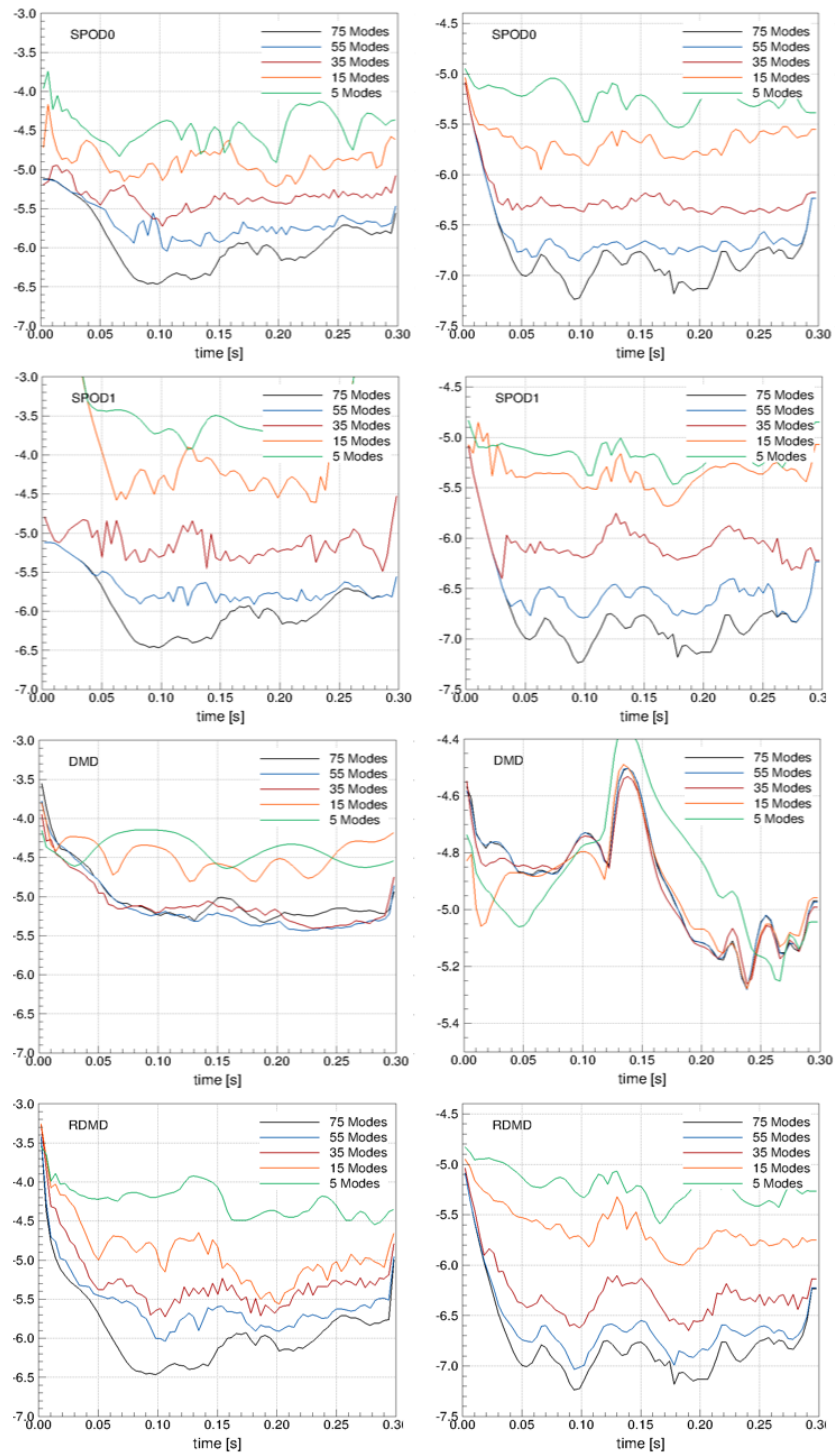


Figure 5.9: NACA0012 sensitivity with respect to number of modes and choice of method for density. Residual error = $\log_{10}(\epsilon_R(\rho))$ (left column), direct error = $\log_{10}(\epsilon_D(\rho))$ (right column).

Chapter 5. Model-Based Adaptive Reduced Order Model

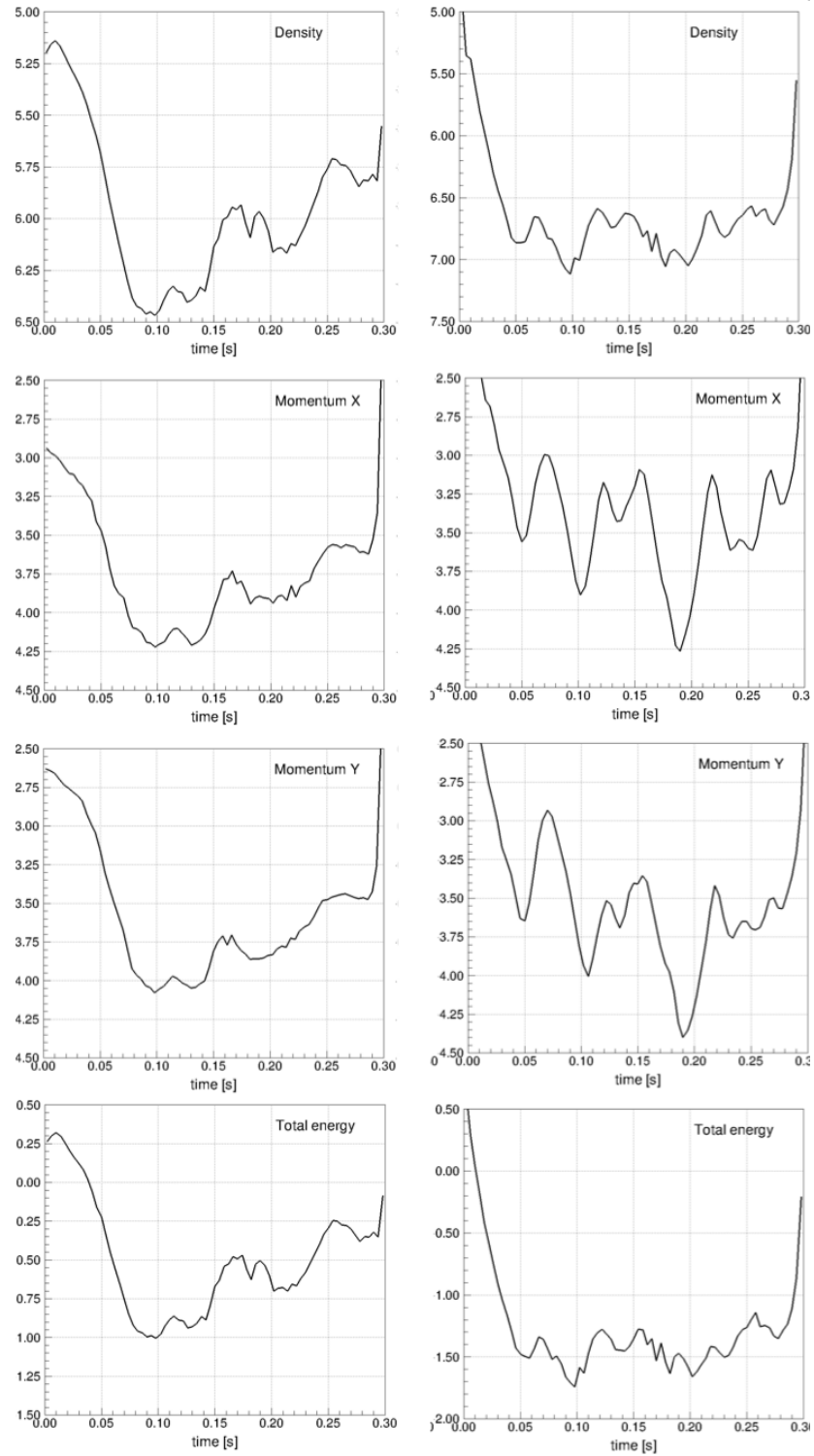


Figure 5.10: NACA0012 minimum envelope of errors. Residual error = $\log_{10}(\epsilon_R(\rho, \rho u, \rho v, \rho e))$ (left column), direct error = $\log_{10}(\epsilon_D(\rho, \rho u, \rho v, \rho e))$ (right column).

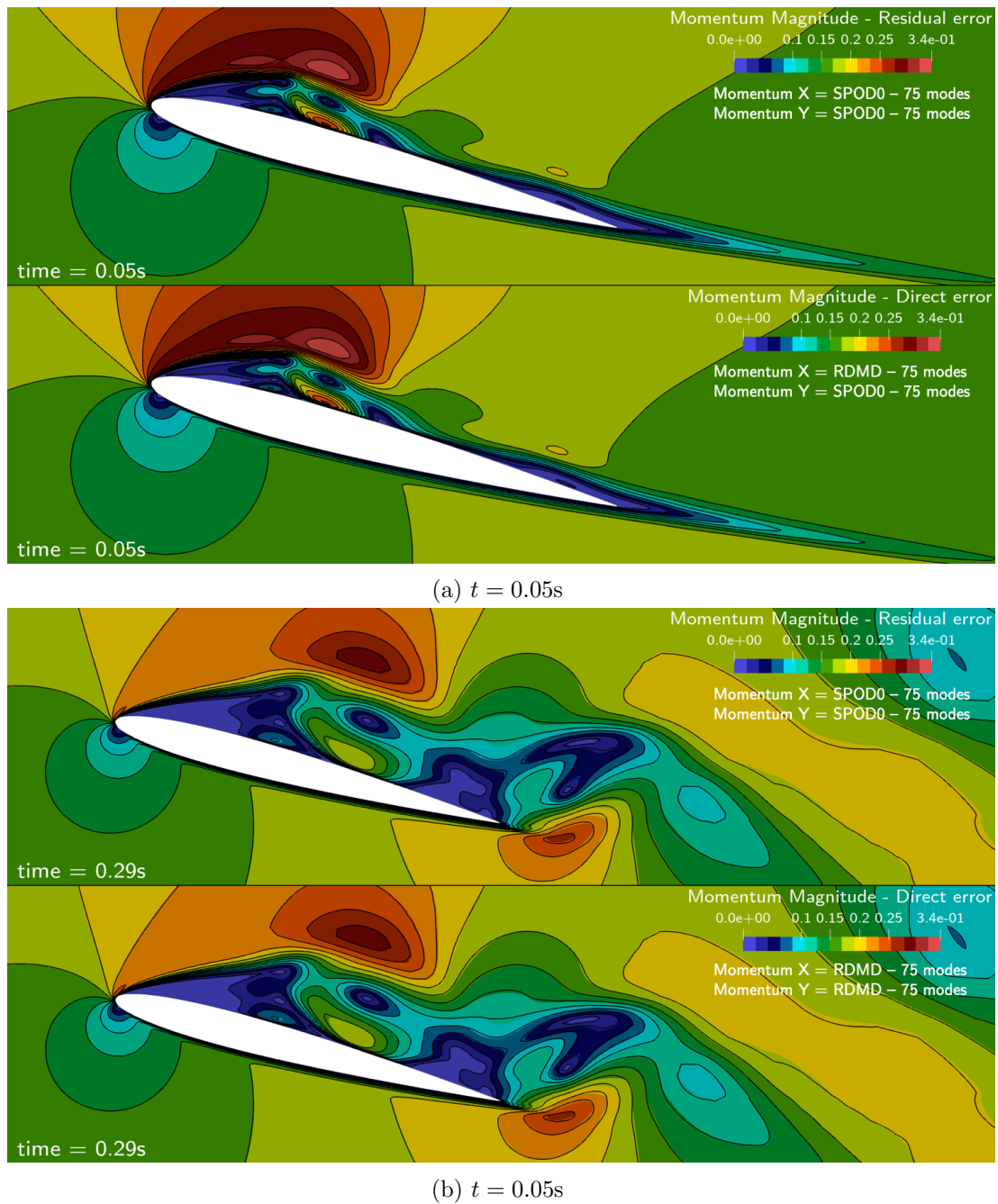


Figure 5.11: NACA0012 momentum magnitude reconstructions at two different instants of time within the sampled time window. Coloured contours report the CFD reference solution, line contours represent the ROM reconstruction. The top row reports the reconstruction with the choice of methods and number of modes driven by the pseudo-algorithm based on residual error, the bottom row uses the pseudo-algorithm based on direct error.

Table 5.2: NACA0012 choice of ROM for each conserved quantity according to the residual or direct error.

	POD	SPOD1	DMD	RDMD
ρ_D	48%	4%	0%	48%
ρ_R	55%	9%	0%	36%
ρu_D	54%	1%	0%	45%
ρu_R	55%	4%	0%	41%
ρv_D	48%	8%	0%	44%
ρv_R	55%	4%	1%	40%
ρe_D	32%	4%	0%	64%
ρe_R	56%	7%	0%	37%

5.5.3 30P30N

The conditions of the simulation for the 30P30N airfoil are equivalent to the one presented for the test-case reported in Section 3.4.2 (Table 3.2), the corresponding details of the reduced basis method are reported in Table 5.3. The time required for computing a single time step using high-fidelity CFD is approximately 12.5h on 1 core, while the time required to compute a single time step with ROM is in the order of a tenth of a second on 1 core. It is worth noting that no further investigation has been carried out on the specific numerical setup of the CFD simulation on the basis of its time requirements, although it is believed that the definition of a more appropriate numerical setup can drastically reduce the computational cost. This is out of the scope of the work presented here. The huge time requirement for this 2D test-case is related to the high number of inner iterations used in the dual-time stepping strategy and the stringent stopping criteria for the residual, which, together with the complexity of the geometry investigated and the specific numerical setup used, makes the computation very time costly.

The ROM has been built in the time window where the dynamics of interest is happening, ranging from the very initial transient where vortices are forming from the various lifting surfaces, to the coalescence and advection of the final vortex in the wake of the airfoil, $t \in [0; 0.06]$ s. Within this time interval, a sampling Δt has been used equal to 6×10^{-4} s, which results in 100 snapshots equispaced in time. The number of DOFs of

Table 5.3: 30P30N ROM setting

N_S	Δt_{NS} [s]	N.modes	Δt_{res} [s]	DOF _{CFD}	DOF _{ROM}	ROM [s]
100	6×10^{-4}	Error-based	5×10^{-6}	1,966,398	$\mathcal{O}(10^2)$	24

the resulting ROM reported in Table 5.3 represents only the maximum value of DOFs of the ROM. As already explained in the previous test-case, its actual value is provided by the pseudo-algorithm reported in Section 5.5.1. The sensitivity analysis on the time step used for the residual evaluation led to a Δt_{res} of 5×10^{-6} seconds. As for the previous test-case, Figure 5.12 reports the sensitivity of the reconstruction error for the density with respect to the choice of the number of modes and with respect to the different methods. Differently from the NACA0012 case, no general trend can be observed with respect to the reduction of reconstruction error as the number of modes increases. This may be related to the different unsteady dynamics of this flow that reaches an advection-dominated status as the vortices coalesce and then get transported downstream. The strong oscillations appearing for the DMD residual error as the number of modes increases (third row on the left column of Figure 5.12) might be due to the addition of higher frequency modes as the rank in the DMD algorithm increases, which might not be representative of the actual dynamics and introduce spurious oscillation in the time and space derivatives in the Formula 5.12 for the evaluation of the residual. An investigation of the terms in Equation 5.12 that primarily contribute to these spurious oscillation is out of the scope of the present work. Similarly to the NACA0012 case, the direct error evaluation tends to be in general lower than the residual error when comparing the same ROM.

Also similarly to the previous test-case, Figure 5.13 reports the error curves obtained as a result of the application of the pseudo-algorithm in Section 5.5.1. The steep increase in the direct error envelope in the final part of the investigated time window (Figure 5.13, right columns) can be related to interpolation issues at the border. In particular, for this specific dynamics, where unsteadiness is more dominant in the first half of the time window considered, the almost constant behaviour of the selected modes

Table 5.4: 30P30N choice of ROM for each conserved quantity according to the residual or direct error.

	POD	SPOD1	DMD	RDMD
ρ_D	81%	11%	0%	8%
ρ_R	38%	26%	29%	7%
ρu_D	82%	10%	0%	8%
ρu_R	65%	26%	8%	1%
ρv_D	90%	9%	0%	1%
ρv_R	36%	43%	17%	4%
ρe_D	69%	19%	0%	12%
ρe_R	38%	28%	29%	5%

for the reconstruction can lead to oscillations among training points at the border of the interpolated interval. This tendency is less pronounced in the residual error, at the end of the time window, since the computation of the unsteady term might be transparent to the oscillations linked to the interpolation if a very small Δt_{res} is used. Table 5.4 reports the percentage values of the choice of the best method over the time window explored for each one of the conserved quantities. Also for this flow, it can be observed that POD is the most used method, but differently from the previous case SPOD with a filter of 10 is the second best choice over the specified time window in terms of percentage of use. Finally, Figures 5.14a and 5.14b report the reconstruction of the flow field by means of the adaptive approach for two different instants of time. A comparison with a reference high-fidelity solution that is not used in the definition of the ROM is presented. The momentum magnitude is shown as obtained by reconstructing independently the two components ρu and ρv . Coloured contours refer to the high-fidelity solution while solid black lines the reconstructed field. The Figure also reports the number of modes and the method used for the reconstruction of the two components of the momentum. Despite the different choice of methods as opposite to what happens in the previous test-case (see Figure 5.11a and 5.11b), overall, the agreement is good and minor differences are observed between the reconstruction based on the direct error and the one based on the residual error.

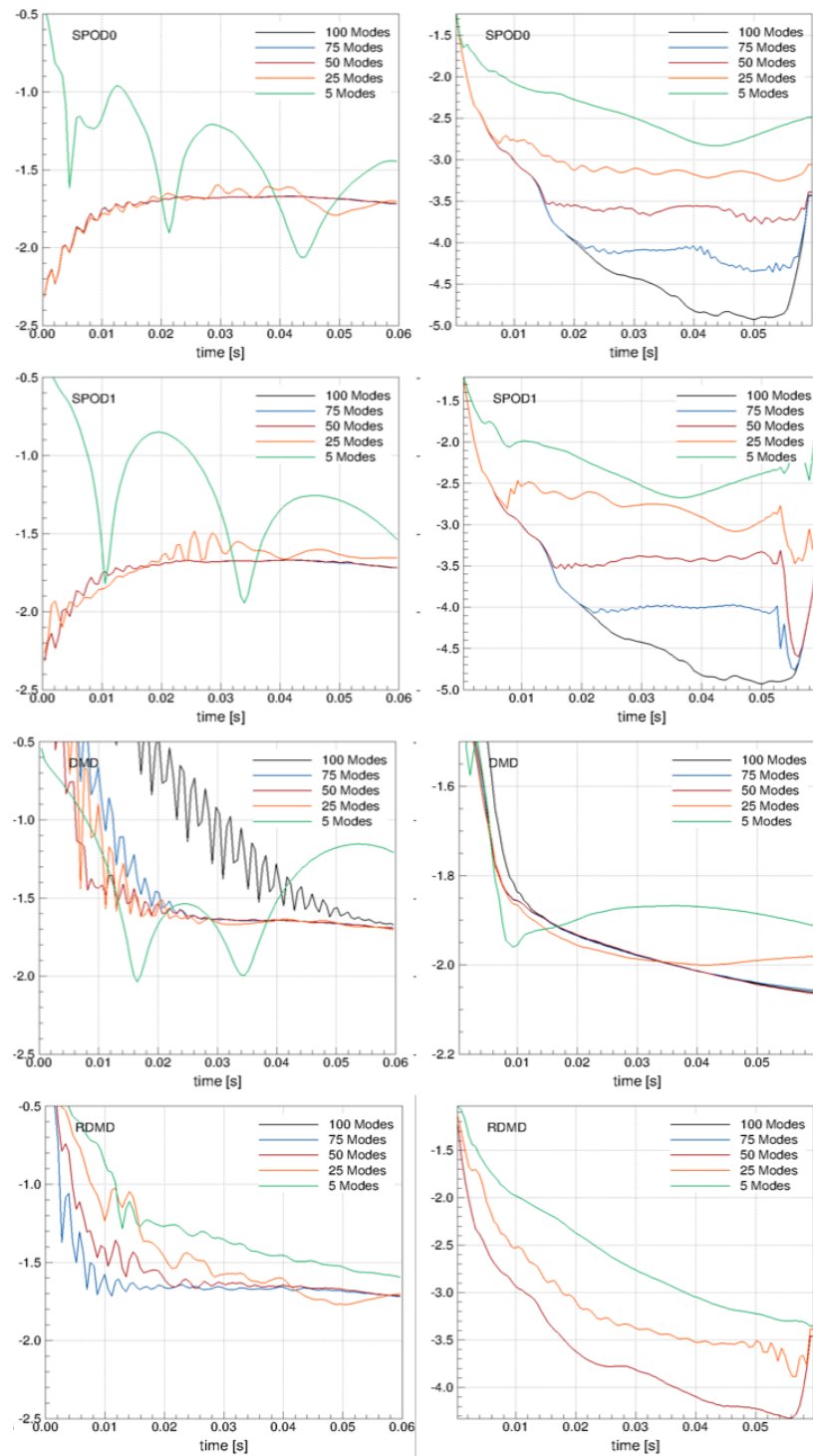


Figure 5.12: 30P30N sensitivity with respect to number of modes and choice of method for density. Residual error = $\log_{10}(\epsilon_R(\rho))$ (left column), direct error = $\log_{10}(\epsilon_D(\rho))$ (right column).

Chapter 5. Model-Based Adaptive Reduced Order Model

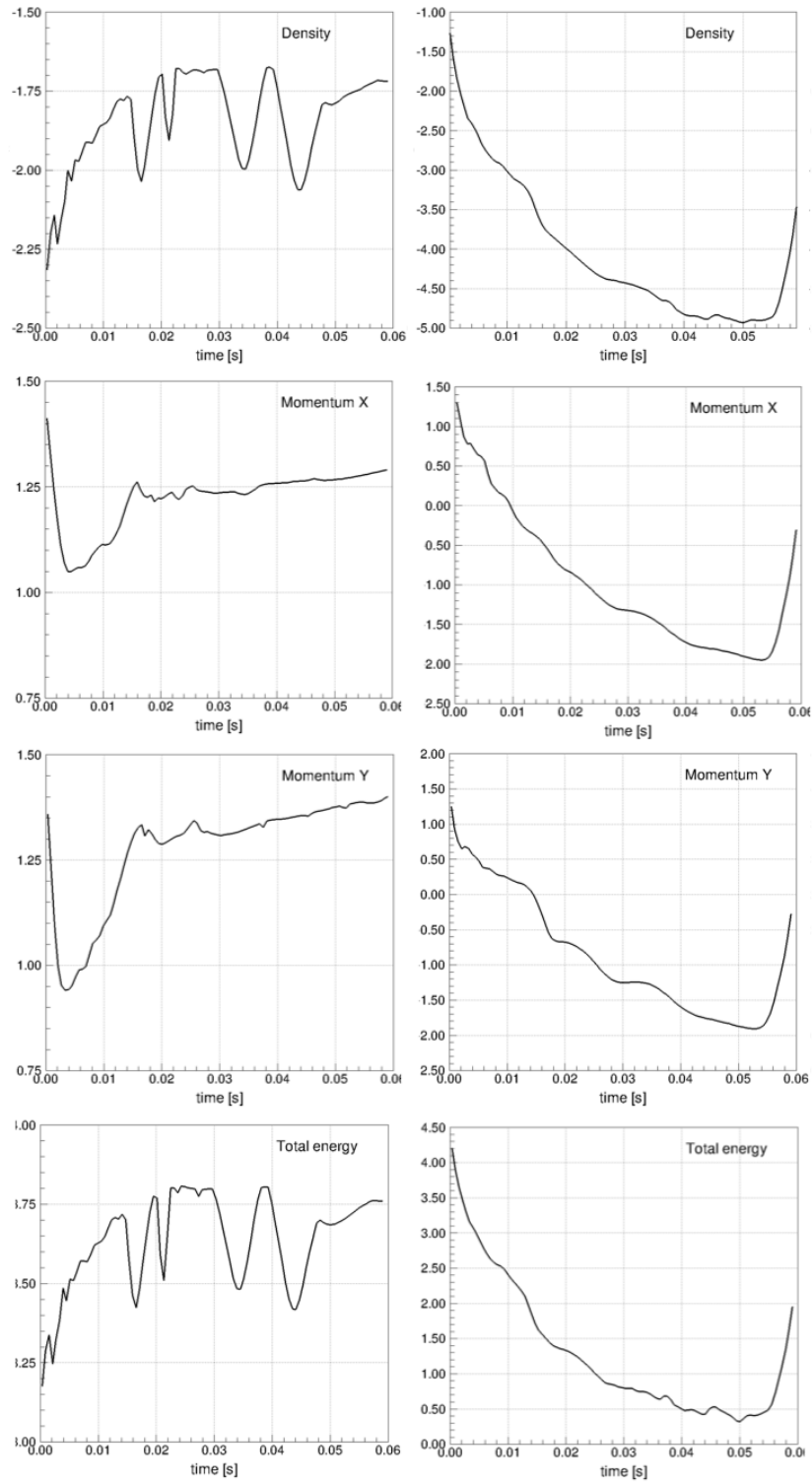
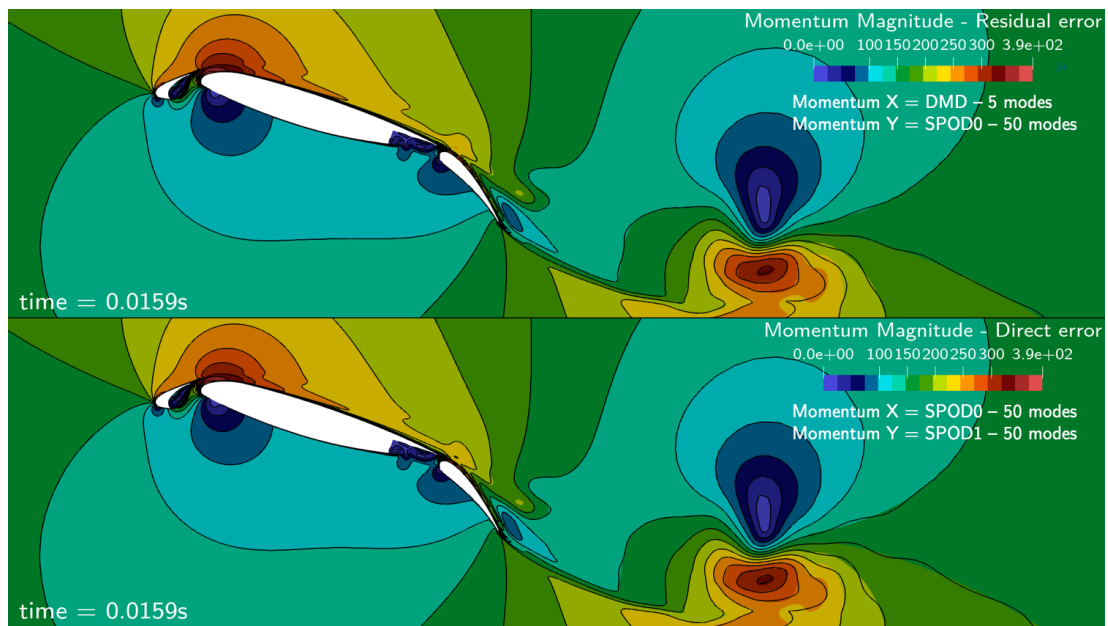
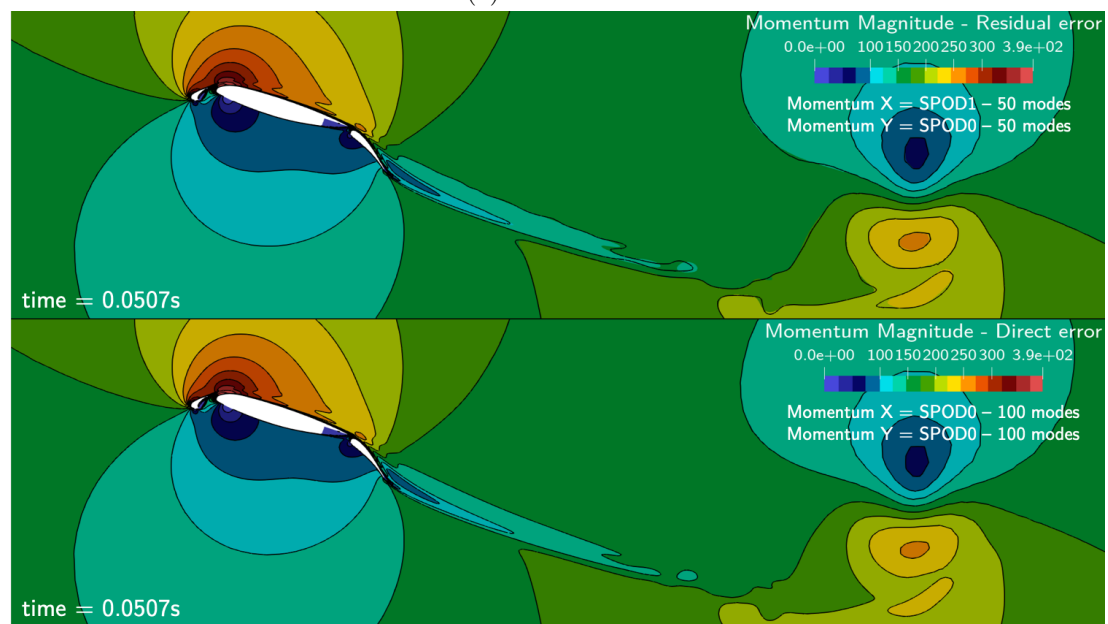


Figure 5.13: 30P30N minimum envelope of errors. Residual error = $\log_{10}(\epsilon_R(\rho, \rho u, \rho v, \rho e))$ (left column), direct error = $\log_{10}(\epsilon_D(\rho, \rho u, \rho v, \rho e))$ (right column).



(a) $t = 0.0159s$



(b) $t = 0.0507s$

Figure 5.14: 30P30N momentum magnitude reconstructions at two different instants of time within the sampled time window. Coloured contours report the CFD reference solution, line contours represent the ROM reconstruction. The top row reports the reconstruction with the choice of methods and number of modes driven by the pseudo-algorithm based on residual error, the bottom row uses the pseudo-algorithm based on direct error.

5.5.4 Remarks

The choice of the error estimator is non trivial and sometimes driven by engineering/practical considerations and a combination of direct and residual error can be considered to find the optimal trade-off between the ability to obtain a consistent estimation of the reconstruction error and the number of snapshots that need to be excluded for the ROM due to the evaluation of the direct error. It is worth noticing that the two definitions of the error introduced, which define the two different Adaptive Frameworks, can be compared only in an heuristic way, since they refer to different quantities. In particular the direct error represents an actual measure of the error associated to the specific physical quantity considered, while the residual error represents a measure of how well a particular discretisation of the conservation equation associated to the specific physical quantity considered is satisfied. Overall, the trends in terms of choice of method between direct and residual error are consistent but differences are observed when looking at specific time windows, i.e., for the 30P30N test-case, the choice reported in figures 5.14a and 5.14b are different for the two definition of the error. The direct error tends to be a more reliable estimation of the error since no pollution is expected, nevertheless, it requires a bigger database of snapshots to be able to use some of them only for error estimation and the rest for the ROM construction. In practice, despite the difference in the methods selection, the reconstructed solutions show a good agreement with a reference CFD solution using both error definitions. The present analysis was based on conservative quantities, i.e. error estimation and reconstruction was performed for mass, momentum and total energy. In case the ROM is required to obtain a primitive or another derived quantity, these can be obtained from the conservative ones.

The analysis carried out in the current Section also highlighted the importance of the number of modes retained for each method within an Adaptive Framework, in terms of its influence on the residual and direct error. In particular, the pseudo-algorithm defined in Section 5.5.1 included the number of modes as a parameter, whose value needs to be computed for each method in order to obtain the lowest error possible.

5.6 Adaptive Framework equipped with residual error

The main idea of the present Chapter is to lay the foundations for formulating a new concept of Adaptive ROM, that uses different sets of global basis functions and a residual evaluation to be able to select the most suitable reduced model among the ones presented. The residual of each ROM is computed substituting its reconstruction into the residual formula presented in 5.4. This is different from the direct error definition introduced in Section 5.3, which requires an extended database to build the adaptive framework. The offline phase consists of three steps, each one repeated for all the selected ROMs:

- 1) Extraction of flow primitives for each conservative variable;
- 2) Computation of the ROM reconstruction for all the conserved quantities on fixed training points;
- 3) Construction of the database of residuals on these fixed training points, substituting the ROM reconstructions into the Finite Volume approximation of the equations, Formula 5.12.

There is no limitation in the number and kind of ROMs to include into the Adaptive Framework, and methods can be added and removed at any time, also on the basis of the specific problem at hand. Consequently, at the end of the offline phase, a certain number of different basis sets are extracted and each of them will have a residual error database associated. The residual database is constructed feeding ROM solutions to the same solver used to obtain high-fidelity snapshots for the training phase. The specific solver used in the present work is the open source SU2 CFD solver [187].

The online phase consists of two very fast steps:

- 1) Selection of the best ROM at the desired time and for each conserved quantity desired for reconstruction, using the residual database;
- 2) Reconstruction computation using either Equation 3.15 or Equation 3.14 on the basis of the method selected.

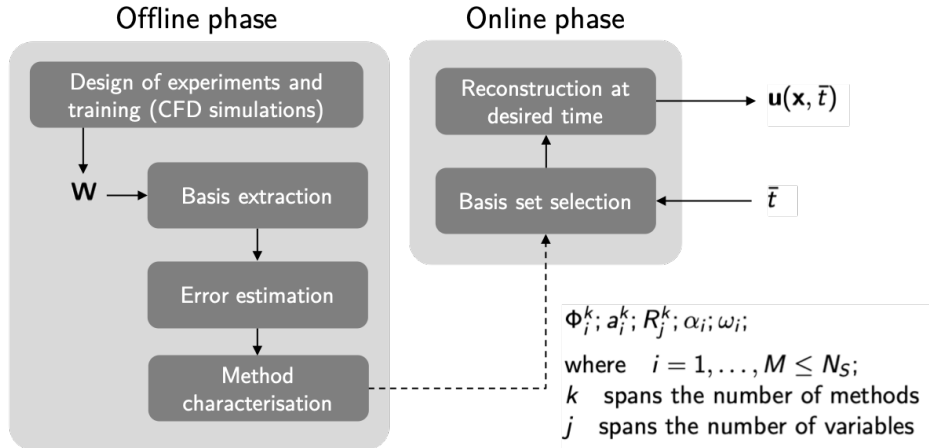


Figure 5.15: Schematic of the adaptive approach distinguished in the offline and online phases.

A schematic of the complete offline and online procedure is reported in Figure 5.15. Since the error definition the Adaptive strategy is equipped with is equation-based, i.e. it uses the original set of governing equations of the system, the Adaptive Framework implemented will be referred to as Model-Based Adaptive ROM. Moreover, considering the definition of the residual error given in Equation 5.12, it will be always assumed hereafter that the Adaptive Framework is applied to the entire set of conservative variables, namely the vector \mathbf{w} in Equation 5.12, all treated as independent variables to build the low-dimensional space.

Two main C++ modules have been developed on top of the code already implemented for the previous analyses, which handle the offline and online phase of the Model-Based Adaptive ROM:

- The *offline module* performs the following steps
 1. Generation of the snapshot matrix;
 2. Extraction of the flow primitives for the various ROM algorithms;
 3. Computation of the residual database for each ROM using an SU2 wrapper.
A slightly modified version of SU2 with the additional routines discussed in Section 5.4.1 is used.
- The *online module* performs the following steps

Chapter 5. Model-Based Adaptive Reduced Order Model

1. Reading residual database and database for reconstruction, i.e. modes and coefficients for linear ROMs;
2. Defining best method at each selected point, i.e. method with lowest residual;
3. Computing online reconstruction at selected points using the best method.

Chapter 6

Residual Analysis varying the number of modes

An analysis on the influence of the number of modes used within the Adaptive Framework is presented to assess the impact of such a choice on the evaluation of the residual error and the accuracy in the final reduced order reconstruction. The study is made by considering the impulsive start of a NACA0012 airfoil and of a 30P30N airfoil. In order to interpret the specific behaviour of the residual error, some flow field reconstructions are computed and, for the specific case of the NACA0012, also a grid dependence study is carried out. One key conclusion is that the choices made within the Adaptive Framework strongly depend on the initial mesh resolution, as this is linked to how well the dynamics of spatial structures in time is captured. A second key message emerging from the present analysis is the major improvement obtained by employing an Adaptive Framework instead of a Single ROM, when very few modes are retained. This is a key result contributing to the identification of the best trade-off between computational reduction and accuracy of the resulting prediction.

6.1 Adaptive ROM residual analysis varying the number of modes

The choice of the number of modes to be used in the Adaptive Framework is mainly related to two fundamental aspects:

- Accuracy in terms of error estimates;
- Reduction of degrees of freedom.

It is worth noting at this stage that the number of modes finally retained does not sensibly impact the time required for the online phase of the ROMs defined in the present work. Indeed, unless the number of training snapshots is potentially very high ($N_s \sim N_p$), the further reduction associated to the value of N_m (number of modes) in Equation 3.14 and 3.15 has a negligible influence on the computational time. Nevertheless, this reduction can be beneficial in terms of the final number of parameters to handle in order to describe the flow evolution in the low-dimensional space, when for example an optimal state is looked for and the set of coefficients need to be optimized. The further reduction will reveal to be also a crucial point when the Adaptive Framework with different sets of global basis functions is used. In this case, indeed, promoting a further reduction will still preserve more essential physics than if this reduction is performed on a Single ROM. This will lead to a situation where, retaining only few modes will introduce more improvements of the Adaptive Framework with respect to a Single ROM, as opposed to a condition where all the modes are retained and a Single ROM might be able to describe the dynamics with similar accuracy. Here, the expression Single ROM refers to any ROM that extracts one set of global basis function from the original set of snapshots. According to this discussion and the two points listed above, the analysis performed here focuses on defining a good trade-off between solution accuracy and dimensionality reduction of the Adaptive Framework, in order to preserve enough physical consistency while using as few degrees of freedom, i.e. number of modes, as possible. Therefore, differently from the analysis reported in Section 5.5, where the final objective has been only to identify an Adaptive ROM

Framework with the best possible accuracy, the present Chapter offers also a view of the importance of considering only a subset of modes.

It is also worth to mention that the number of modes finally retained, and therefore the reduction of degrees of freedom introduced by a ROM, is strongly problem dependent. Some aspects that influence the reduction are for example the time window investigated and how complex the dynamics happening in this time window is.

An analysis is presented on the two 2D test-cases NACA0012 and 30P30N, which investigate the influence of the number of modes used in the Adaptive Framework on the Residual Error introduced in Chapter 5. An important assumption is also made for changing the number of modes: while defining the parameters of the final Adaptive Framework, once the number of modes has been fixed, it will be considered constant for all the methods included. This means that all the ROMs that define the Adaptive strategy, such as POD, DMD, SPOD and RDMD, will use the same number of modes. To perform the study, an integral in time of the residual error will be presented varying the number of modes

$$\epsilon_{R,T} = \int_{t_0}^T \epsilon_R dt \quad (6.1)$$

where $[t_0, T]$ is the time interval used to train each ROM, ϵ_R is the residual error defined in Equation 5.13 for a generic conservative variable. To compute the integral, the residual error ϵ_R is computed on set of test points equispaced in time and with a resolution $\Delta t \leq \Delta t_{\text{CFD}}$, which represents the same procedure adopted to build the residual error database for the Adaptive ROM. The integral is then approximated using a trapezoidal rule. An additional quantity will be reported, which provides a better understanding of the improvements introduced by the Adaptive Framework over the investigated time window, varying the number of modes. The quantity represents the difference of the residual error produced by the Adaptive ROM and the residual error produced by a Single ROM,

$$\epsilon_{\text{diff}} = \epsilon_{R,S} - \epsilon_{R,A} \quad (6.2)$$

where the subscripts A and S stand for Adaptive and Single respectively, while ϵ_R still represents the residual error as defined in Equation 5.13, for a generic conservative

variable. In the following analysis $\epsilon_{R,S}$ will be considered as the residual error of the POD method. This is because POD has been the most widely used method in the literature for implementing ROMs in the case of unsteady problems and it represents a good reference point for the community, even if the $\epsilon_{R,S}$ can represent the error of any Single ROM. For the same reason, also the analysis reported on $\epsilon_{R,T}$ for the Adaptive Framework will be compared with the POD technique.

6.2 NACA0012 test-case

The NACA0012 test-case is considered first. Details for the computational mesh and setup used to compute the training snapshots can be retrieved from Section 3.4.1. For the analysis of $\epsilon_{R,T}$ and ϵ_{diff} an Adaptive Framework is built within the time window $[0, 0.3]$ s where the dynamics of interest is happening, using a sampling Δt of 4×10^{-3} s, which results in a number of snapshots $N_s = 75$ equispaced in time. The maximum number of modes that can be used in the Adaptive ROM is therefore 75. Figure 6.1 reports the quantity $\epsilon_{R,T}$ for the Adaptive ROM, red curve, and the POD, black curve, for the entire set of conservative variables. An interesting aspect to discuss for these plots is the presence of a non monotonic trend as the number of modes is increased. Indeed, the residual integral starts from relatively lower values when using very few modes and increases as other modes are added. Starting from a particular number of modes, the overall trend is then decreasing, reaching a minimum when the entire set of modes is used. The non monotonic behaviour can be linked to a physical interpretation of the modes. Following the modes ranking described in Chapter 4, the most important modes should carry information about large spatial structures, while higher modes solve for smaller spatial structures. When using very few modes, small spatial structures are not resolved and something closer to the mean field with little variation in time is reconstructed, which might be responsible for the lower residual. It is worth to highlight at this point that Formula 5.12 represents a weak discretization of the set of initial governing equations of the system (the space of possible solutions is therefore expanded), and moreover it is completely blind to the actual physical time

considered. As more modes are added, new spatial structures start to be resolved, even if with very low resolution, which cause the residual integral to increase. Once the number of modes is reached where all the spatial structures are present in the reconstructed flow field, adding additional modes will decrease the integral residual, since also small structures start to be better resolved. A proof of this discussion can be seen in Figure 6.3, where a reconstruction at a specific time instant, provided by the Adaptive ROM, is reported using two different number of modes that show the same residual integral from Figure 6.1, namely 2 modes (on the left) and 28 modes (on the right). The reconstruction in the wake of the airfoil with 2 modes shows only averaged flow features, where the region of separated flow is clearly visible, but no structures in the wake are resolved. Moving to 28 modes, it can be noticed how more structures in the wake are resolved, but also new oscillations not present in the reference field are added. These oscillations will vanish only adding additional modes, with a consequent reduction of the residual error.

The trend of $\epsilon_{R,T}$ with the number of modes is not a unique feature of the Adaptive ROM. As a matter of fact, considering the number of modes in the same way as the degrees of freedom of the computational mesh, the non monotonic behaviour has been observed also for the case of error estimators used for a steady linear advection-diffusion equation [188]. In particular, Allendes et al. [188] define error estimators that show a non monotonic behaviour while increasing the size of the initial computational mesh. Another important result from Figure 6.1 is that the improvement of the Adaptive ROM with respect to the POD Single ROM is higher when using a number of modes that is much less than the entire set of modes available (10 – 15 out of 75, on the basis of the distance between the red and black curves reported in Figure 6.1). Overall the Adaptive Framework always performs better than pure POD in terms of residual integrals. Figure 6.2 shows ϵ_{diff} , in log scale, in the box $t \times N_m = [0, 0.3] \times [2, 75]$. White spaces correspond to $\epsilon_{\text{diff}} = 0$, which means that POD has been chosen from the Adaptive Framework for that combination of time and number of modes. Details of ROMs used over the space of different times and number of modes is not reported, since no common pattern has been identified in switching among different ROMs and the behaviour is erratic, similar

to what has been shown for the analysis in Sections 5.5.2 and 5.5.3. Also from the ϵ_{diff} contours it is visible how the Adaptive Framework introduces improvements with respect to the Single ROM ($\epsilon_{\text{diff}} > 0$) when using a subset of all the modes available. As the number of modes is increased, the improvements introduced by the Adaptive Framework with respect to POD are less and less visible. This is obviously linked to the enrichment of the POD basis with the whole information content coming from the training snapshots, which is eventually able to reconstruct the entire dynamics contained in them.

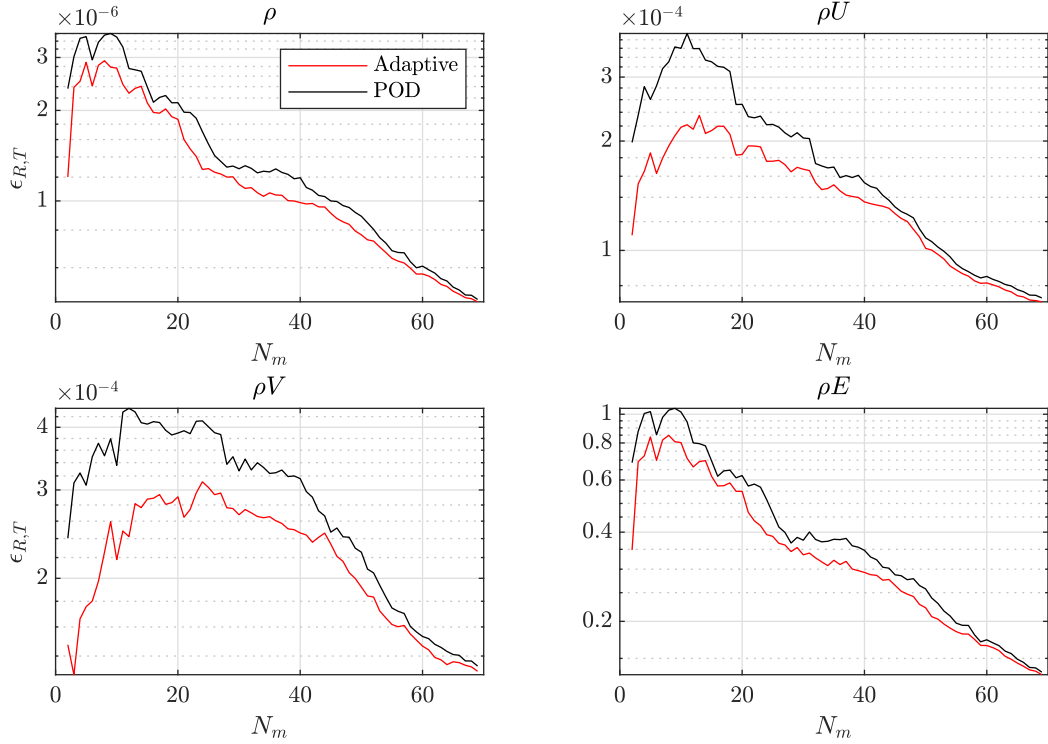


Figure 6.1: $\log_{10}(\epsilon_{R,T})$ varying the number of modes, for Adaptive ROM and POD, NACA0012 test-case.

6.3 30P30N test-case

The 30P30N test-case is now considered. For details on the computational mesh and setup used to compute high-fidelity training snapshots the reader can refer to Section 3.4.2. An Adaptive Framework is built within the time window $[0, 0.03]$ s where the

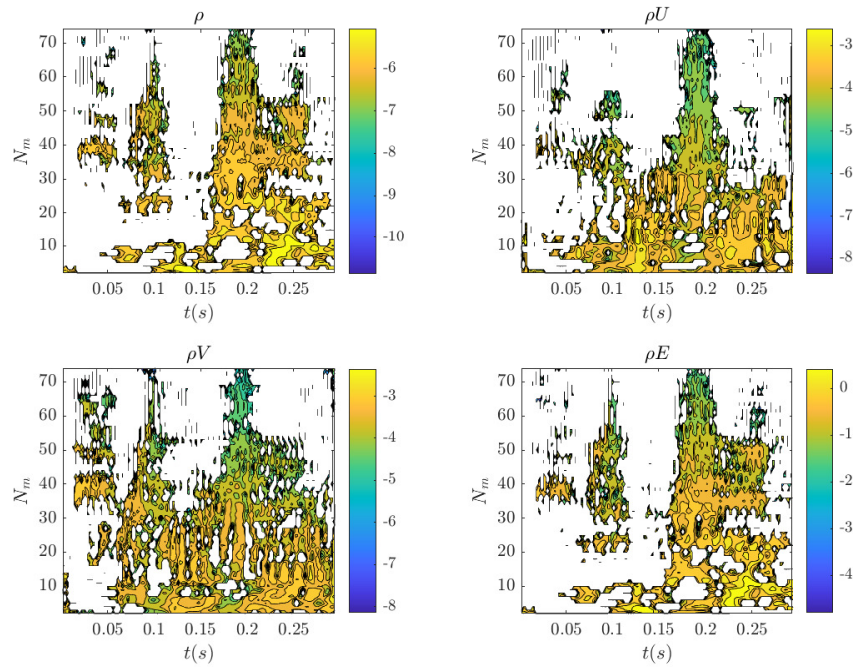


Figure 6.2: $\log_{10}(\epsilon_{\text{diff}})$ considering POD as reference Single ROM, versus time and number of modes, NACA0012 test-case. White regions correspond to $\epsilon_{\text{diff}} = 0$, i.e. the Model-Based Adaptive ROM selects POD.

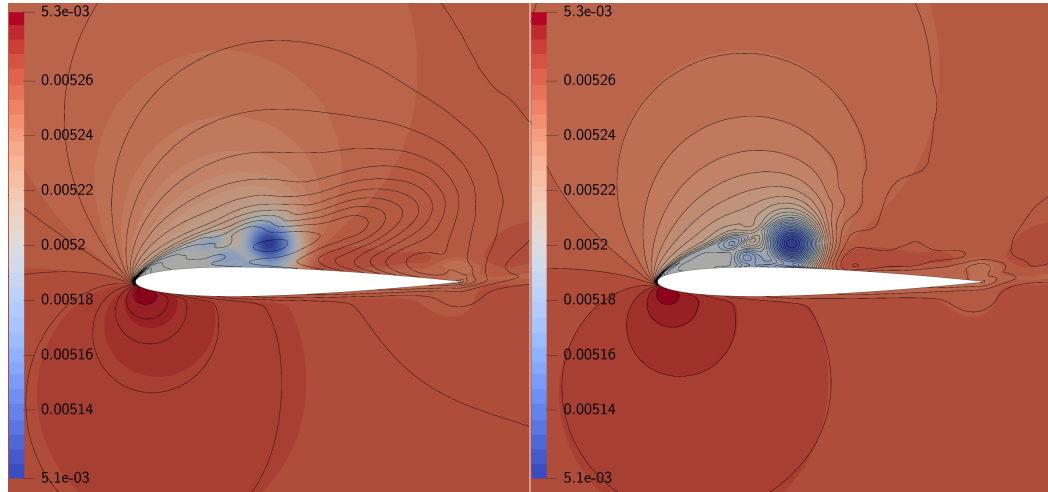


Figure 6.3: Volume reconstruction of density at time $t = 0.06$ s for 2 modes (left) and 28 modes (right), NACA0012 test-case. Coloured contours represent the CFD reference solution.

dynamics of interest is happening, using a sampling Δt of 6×10^{-4} s, which results in a number of snapshots $N_s = 50$ equispaced in time. Analogously to the previous test-case, Figure 6.4 reports the quantity $\epsilon_{R,T}$ for both Adaptive and POD ROM and for all the primary conservative variables. Since high-fidelity solutions for the 30P30N are computed using RANS, modeling turbulence with SST, the turbulent variables are considered in the computation of the residual error for the primary variables, even if a separate analysis for them is not reported. Also in this case a non monotonic behaviour with the number of modes is clearly visible in the plots and a similar discussion can be done considering Figure 6.4. Moreover, Figure 6.6 shows the reconstruction of the flow field provided by the Adaptive Framework at a specific instant of time, for two sets of modes that present the same value of $\epsilon_{R,T}$. Namely, 6 modes are used for the reconstruction on the left, 17 modes for the one on the right. The reconstruction of the conservative variable density is reported and the filled contours represent the CFD reference solution, while the black line contours are the Adaptive ROM reconstructions. Using only 6 modes details of the vortices detaching from the multiple airfoil surfaces, namely slat, main component and flap, are completely lost, since these vortices are represented as a single large spatial structure. Switching to 17 modes (same value of $\epsilon_{R,T}$) adds more details in terms of vortices detaching from the airfoil, still not merged, but also introduces additional oscillations in space, which will vanish only adding more modes. This balance between resolving only for large spatial structures (6 modes case) and resolving also for smaller structures but introducing spatial oscillations in other regions of the flow field (17 modes case) explains the non monotonic behaviour in Figure 6.4. It is worth noticing that, since the most important dynamics is linked to the advection of the vortices detaching from the various lifting surfaces, another important aspect to consider is the advective nature of the problem. The spatial oscillations downstream of the starting vortices, visible on the right contours in Figure 6.6, are indeed not linked to the low resolution of spatial structures actually present in the flow field at that specific time instant, instead they are due to the advection of the starting vortices, which are transported to those regions in the following time instants. These oscillations vanish when adding higher order modes.

Figure 6.5 shows finally the quantity ϵ_{diff} , in log scale, in the box $t \times N_m = [0, 0.03] \times [2, 50]$. As for the previous test-case, no common pattern can be identified in switching from one ROM to another over the various times and number of modes used, therefore details on that are not reported. From the contours in this Figure, but also looking at the integral results in Figure 6.4, it can be noticed how the improvement of the Adaptive Framework with respect to the Single ROM ($\epsilon_{\text{diff}} > 0$) is much more evident when using a small subset of modes, while the performances of the two methods (Adaptive and Single ROM) becomes similar as the number of modes is increased. This is in accordance with what has been already observed for the previous test-case and an equivalent explanation can be provided. Moreover, a particular trend can be observed on the contours reported in Figure 6.5. Specifically, the transition line between $\epsilon_{\text{diff}} = 0$ and $\epsilon_{\text{diff}} > 0$ can be approximated as a straight line with a specific slope. This particular behaviour is linked to the specific dynamics that this test-case exhibits, which presents an initial transient where many structures are forming, advecting and interacting, and a very simple evolution in time after all these structures have merged together in a single vortex propagating downstream. A possible interpretation for the specific trend shown in Figure 6.5 is provided in the following. The energetic content associated to the initial structures is higher than the one associated to the final vortex propagating downstream since some energy is dissipated due to viscosity effects. As the number of modes retained is increased, the POD basis is able to solve also for less energetic structures present in the flow, which appear later in time, determining the quasi-linear trend on the ϵ_{diff} contours.

6.4 Grid sensitivity study

The present Section investigates the influence of the mesh used to compute the high-fidelity snapshots on the residual integral error $\epsilon_{R,T}$ versus the number of modes. Besides the influence of the modes extracted by a generic ROM algorithm, as already discussed in the previous Sections, the initial mesh resolution is indeed another main element responsible for the resolution of all the spatial structures present in the flow

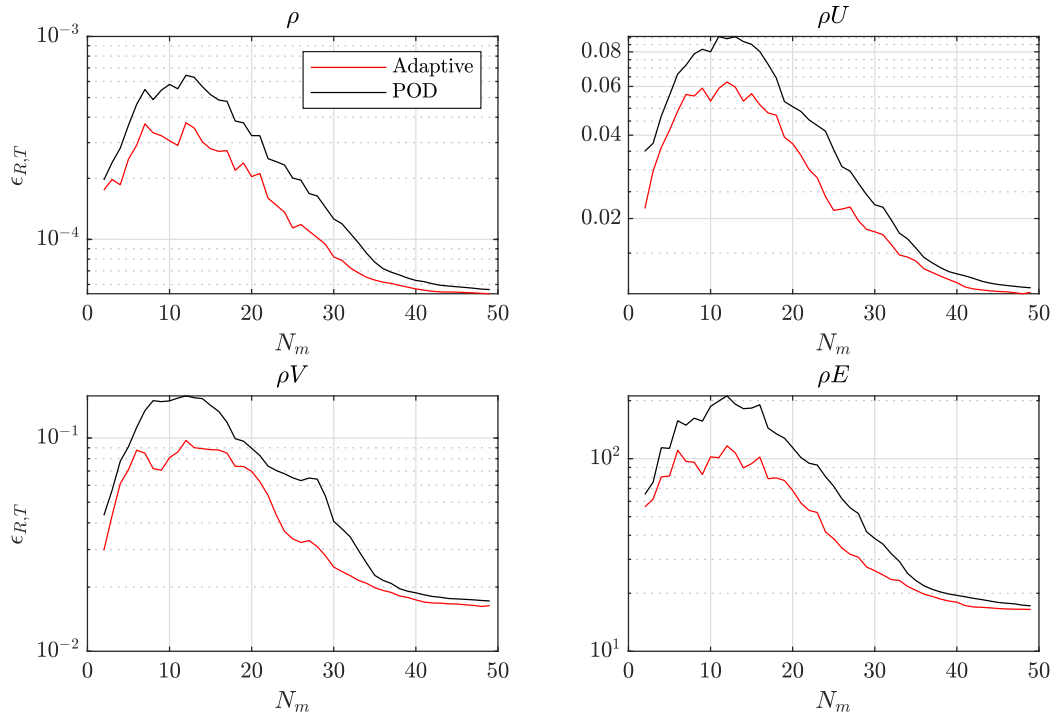


Figure 6.4: $\log_{10}(\epsilon_{R,T})$ varying the number of modes, for Adaptive ROM and POD, 30P30N test-case.

field. The use of a very coarse mesh might lose the description of all the spatial scales, which is also reflected on the spatial basis functions extracted by the ROM. According to that, the peaks present in the plots reported in Figures 6.4 and 6.1 should narrow and in the limit of very coarse meshes, completely disappear. Indeed, if the spatial basis functions are extracted on very coarse meshes, very few modes are already capable of resolving all the spatial scales encoded in the initial snapshots, and higher order spatial oscillations introduced by the advection phenomena are no longer present or of minor importance. As a direct consequence, the residual integral error $\epsilon_{R,T}$ should start the monotonic decrease earlier and in the limit of very coarse meshes, present a monotonic decrease over the entire set of modes.

For the specific test-case of the NACA0012 a much coarser mesh has been considered (see Figure 6.7) and the integral quantity $\epsilon_{R,T}$ has been computed varying the number of modes. All the settings for the CFD simulation and the ROM construction have been left unchanged, in order to study the particular effect of mesh coarsening.

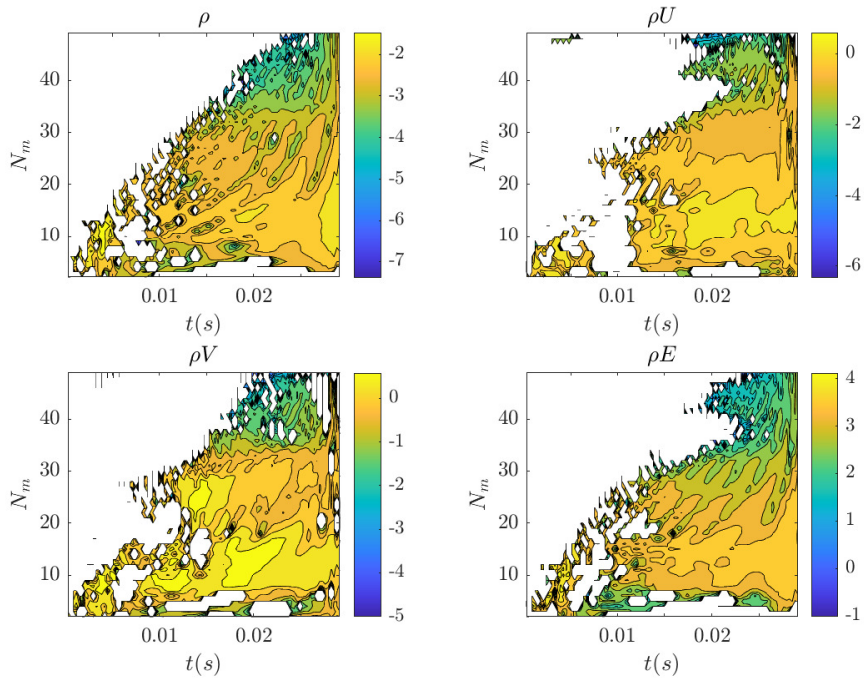


Figure 6.5: $\log_{10}(\epsilon_{\text{diff}})$ considering POD as reference Single ROM, versus time and number of modes, 30P30N test-case. White regions correspond to $\epsilon_{\text{diff}} = 0$, i.e. the Model-Based Adaptive ROM selects POD.

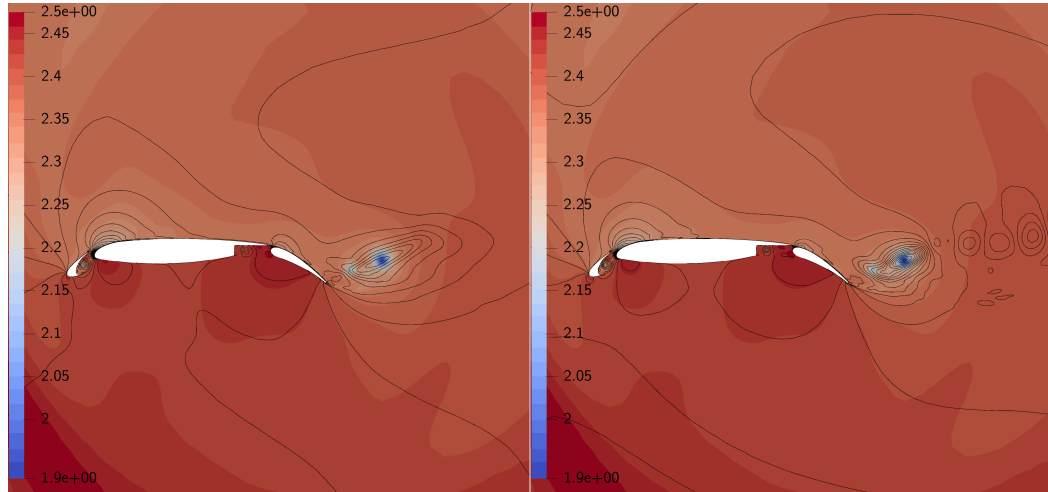


Figure 6.6: Volume reconstruction of density at time $t = 0.0054$ s for 6 modes (left) and 17 modes (right), 30P30N test-case. Coloured contours represent the CFD reference solution.

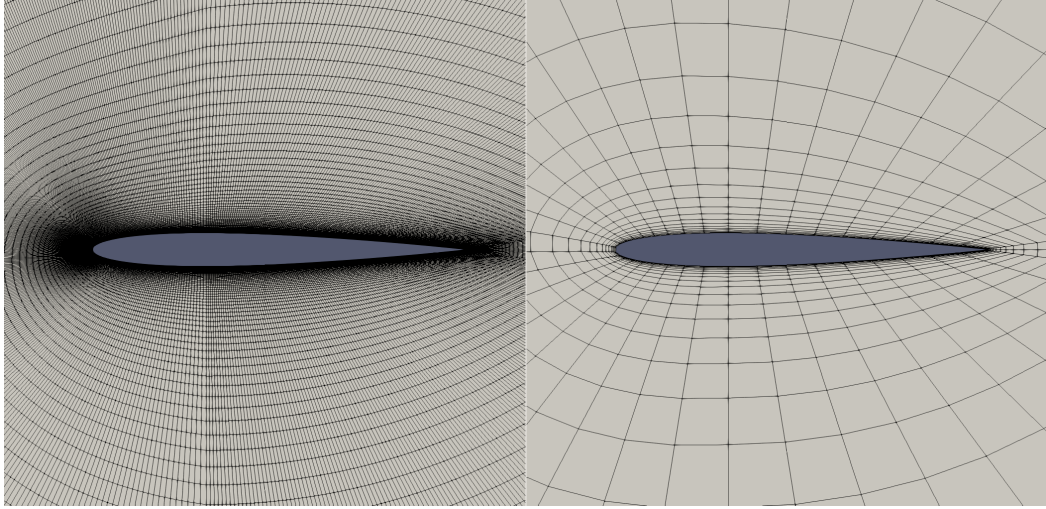


Figure 6.7: Fine and coarse grids for the NACA0012 test-case, used to investigate the influence on the residual error behaviour with the number of modes.

Therefore 75 snapshots have been sampled equispaced in time, with $\Delta t = 4\Delta t_{\text{CFD}}$. Figure 6.8 reports the residual integral error $\epsilon_{\text{R,T}}$ computed for a Single ROM, namely POD, on the Fine and Coarse meshes represented in Figure 6.7. Results are showed for the entire set of conservative variables. It can be noticed how the black curve that is computed on the coarse mesh present a narrower peak, especially for the two momentum components ρU and ρV , when compared with the red curve computed on the finer mesh. Moreover, the hyperbolic trend after the small initial peak for the coarse case, as opposed to the almost linear trend for the finer case, highlights the minor importance of higher order modes, which are not resolving any other additional spatial structures, but are only refining the large spatial structures already resolved by the very first few modes. Equivalently, the very low resolution allows to describe the advection of physical quantities without introducing significant spurious oscillations in space, even when using few modes.

These aspects can be used as an additional proof of the discussion presented for the two test-cases reported in Sections 6.2-6.3, where an initial explanation for the non monotonic behaviour with the number of modes is provided looking also at the reconstruction of the entire flow field at some time instants. Another important aspect to discuss, that is linked to the initial grid used to compute the initial training snapshots,

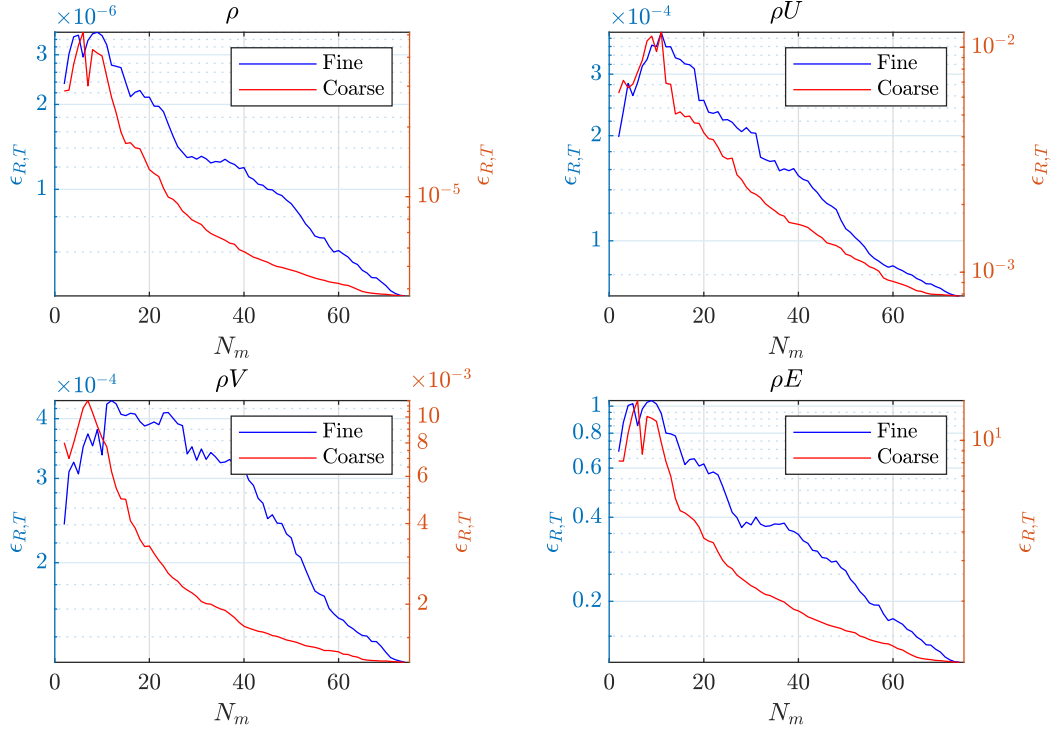


Figure 6.8: $\log_{10}(\epsilon_{R,T})$ versus number of modes, considering only POD, for the two different grids reported in Figure 6.7, NACA0012 test-case.

is the improvement of the Adaptive ROM with respect to a Single ROM. Figure 6.9 reports on the coarse mesh the same plot showed for the NACA0012 test-case in Figure 6.1. It can be noticed that a direct effect of losing resolutions of both some spatial structures, i.e. the smaller ones, and their advection in time, reduces drastically the improvements introduced by the Adaptive ROM with respect to a Single ROM. As a matter of fact, the two curves reported in Figure 6.9 are much closer than in Figure 6.1. This is strongly linked to the Adaptive Framework rationale, that is using different sets of basis functions in order to catch dynamics in time linked to different spatial structures. It is therefore natural to conclude that part of the improvements introduced by the Adaptive framework are lost when some spatial structures are missing or poorly resolved and only a few of them are present in the original snapshots used to train the model. It is worth noticing that all the discussion reported here has been carried out on the integral quantity $\epsilon_{R,T}$ and therefore provide a preliminary indication of the performance of the Adaptive Framework, without doing any local consideration

in time.

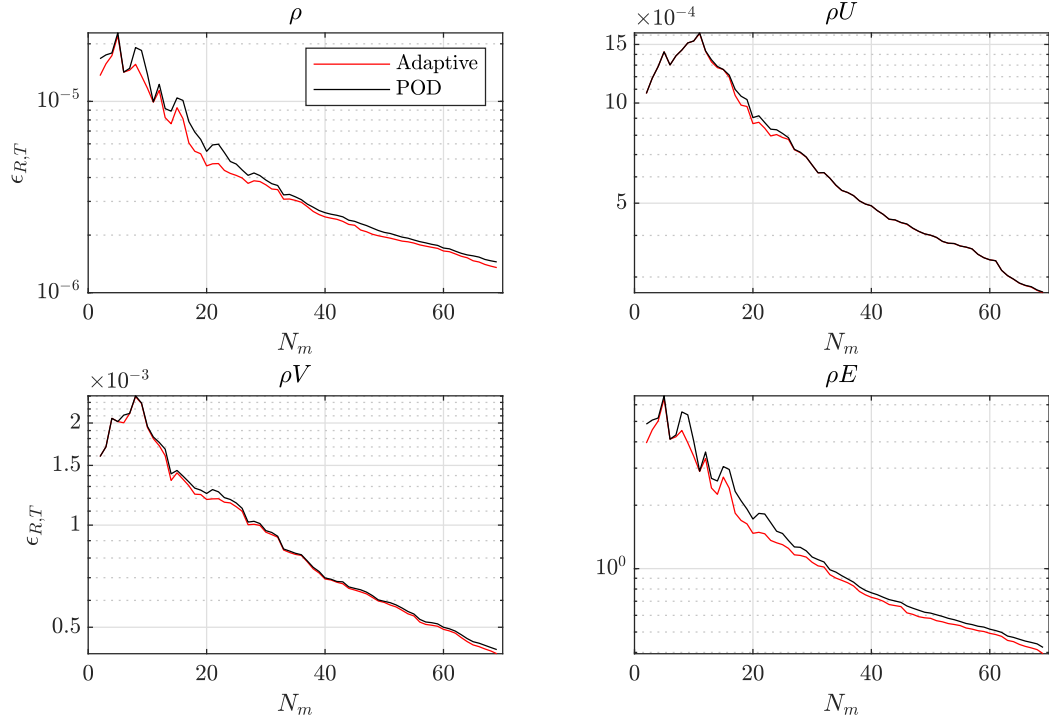


Figure 6.9: $\log_{10}(\epsilon_{R,T})$ varying the number of modes, for Adaptive ROM and POD on the coarse grid, NACA0012 test-case.

6.5 Remarks

An analysis on the influence of the number of modes used in the Adaptive ROM has been performed in the present Chapter. The common two 2D unsteady test-cases, namely NACA0012 and 30P30N, have been considered. It has been shown in both cases how the Adaptive Framework outperforms a Single ROM (specifically POD) and that better improvements can be achieved with respect to the Single ROM when using a subset of all the modes available, Figures 6.1 and 6.4. An explanation for the non monotonic behaviour with the number of modes appearing in the plots of $\epsilon_{R,T}$ has been provided also looking at some flow field reconstructions (see Figures 6.6 and 6.3). From these reconstructions emerged that resolving only for very large spatial structures, i.e. when using very few modes, produces a residual error from Equation 5.12 that is

comparable with a case where other modes are added. Indeed, in the former case, a solution is obtained that solves only for large spatial features, while in the former case the reconstructed solution solves for more spatial structures, namely the smaller ones, but also introduces spurious oscillation in the flow field. These spurious oscillations are not only due to low resolution of existing spatial structures, but they are also linked to the advective nature of the problems, as it is clearly visible from Figure 6.6 left, where spurious spatial oscillations appear in regions where physical quantities are transported. A further analysis has been presented in Section 6.4, for the specific case of NACA0012, in order to investigate the influence of the grid resolution used to compute the initial snapshots on the performance of the Adaptive Framework. It has been shown how unresolved smaller spatial structures have a direct effect on the monotonicity of the error curve (see Figure 6.8) and on the overall improvement of the Adaptive Framework with respect to a Single ROM (see Figure 6.9). These results are also an additional proof of concept for the explanation provided about the presence of the extended peak in the finer case, since it tends to disappear in the limit of very coarse meshes.

Besides investigating on the qualitative behaviour of the $\epsilon_{R,T}$ as the number of modes is changed, the additional aim of the analysis reported is to provide a suitable number of modes to retain within the Adaptive Framework, in order to achieve a good trade-off between accuracy and physical consistency of the final ROM solution on one side, and a strong reduction of degrees of freedom on the other. On the basis of the results shown, it has emerged that a small subset of the original set of modes available should be used, to exploit at best the improvements of the Adaptive Framework with respect to a Single ROM.

Chapter 7

Impulsively started lifting bodies

The Model-Based Adaptive framework is here applied to a number of unsteady complex problems, typical of the aeronautical field where lifting bodies are considered. The importance of using different sets of basis functions will be highlighted, in order to reconstruct the dynamics over the entire investigated time window when dealing with complex transient dynamics. Specifically, the major performance of the Model-Based Adaptive ROM will be shown when using a small subset of all the modes that can be extracted from the initial set of snapshots. Improvements will be reported in terms of contours comparison of the entire flow field and integral errors with respect to pure POD, since it is the most widely used ROM technique in the literature. For test-cases presenting a single geometry, performance of the Model-Based Adaptive framework and its major improvements with respect to POD will be also evaluated confining the analysis on the aerodynamic surfaces.

7.1 Unsteady problems typical of aeronautical field

Numerical experiments are presented to assess the performance of the proposed Model-Based Adaptive technique in the case of four impulsively started bodies such as a 30P30N high-lift configuration airfoil, a High-Lift Wing-Body configuration and a Delta Wing, and a configuration with multiple Delta Wing geometries in Formation Flight. A common feature of these flows, which makes them of interest also from a ROM per-

spective when a possible low-dimensional representation is looked for, is the presence of significant vortices interaction resulting from the shedding and coalescence of starting vortical structures, as well as convection of these structures. Therefore, the capabilities of the Model-Based Adaptive Framework will be tested in resolving this specific dynamics and a sampling will be limited to the time window where this dynamic of interest is happening. To obtain the High-Fidelity snapshots used to train the Adaptive ROM, CFD simulations are performed using the Finite Volume SU2 open source tool [155]. For the first three test-cases, featuring a single geometry in the computational domain, two separate analyses are performed. One analysis is performed considering a residual error evaluation integrated all over the computational domain and one considering only the surface of the aerodynamic body. Therefore, the capabilities of the Adaptive Framework are assessed on two different residual databases. The analysis limited only on the surface is meaningful when the main interest is on aerodynamic loads and aerodynamic coefficients. Having surface solutions available in real time manner is moreover important when performing shape optimization problems, where the distribution of a specific physical quantity, e.g. pressure, should be optimized. As already highlighted in Section 5.6, the entire set of conservative variables is considered to build the Adaptive Framework. Since all the simulations are run as viscous (no slip boundary condition), for the surface residual evaluation only density and energy are considered instead as conserved quantities, being the boundary condition of zero momentum identically satisfied by the Adaptive ROM. Indeed, each of the modes extracted respect the no slip boundary condition and therefore also their linear combination. The final test-case considered, namely a Formation Flight configuration with three equal Delta Wing geometries, shows the performance of the Adaptive Framework in describing the interaction of vortices detaching from the leader geometry with vortices generating from the followers' lifting surfaces. Since the focus for this last test-case is mainly on solving vortex structures' interactions happening in the flow field, only a volume analysis is performed.

According to the statement in Section 5.6, there are no constraints in the number and type of reduction algorithms to be used in the Adaptive Framework. For the applica-

tions presented in the current Chapter, an Adaptive ROM is built considering three linear methods, namely POD, DMD and RDMD. For each test-case, only a small subset of the entire set of modes that can be extracted from the collected snapshots will be considered, in order to exploit at best the improvements introduced by the Adaptive ROM. In particular, a suitable choice of the number of modes to be eventually retained in the Adaptive Framework is driven by the plots of $\epsilon_{R,T}$, following the analysis presented in Chapter 6. This quantity can provide valuable information in order to achieve a good trade-off between solution accuracy and dimensionality reduction of the problem.

The assessment of the proposed adaptive approach is presented in terms of its performance with respect to the pure POD-based method, since it is the most widely used method in the literature for implementing ROMs in the case of unsteady problems and it represents a good reference point for the community. The analysis is performed by comparing the contour levels of the CFD solution, the adaptive method and the pure POD algorithm for few time instants in the investigated time window. The database of residuals in time for all the methods included in the adaptive framework is also reported for each test-case, only for the volume for the Formation Flight test-case, and for both volume and surface for the first three test-cases.

7.2 30P30N

The impulsive start of a 30P30N airfoil is considered first [154]. For the details on the mesh used and the setup of the CFD simulation, the reader can refer to the same test-case presented in Section 3.4.2. For completeness, flow details in terms of time evolution of pressure contours are reported in Figure 7.1.

The reduced model is built within the time window $[0;0.03]$ s where the dynamics of interest is happening, with a sampling Δt of 6×10^{-4} s, which results in a number of snapshots $N_s = 50$ equispaced in time. For these settings, $\epsilon_{R,T}$ has been already computed varying the number of modes in the analysis presented in Section 6.3 (see Figure 6.4). On the basis of these plots, a number of 10 modes out of the initial 50

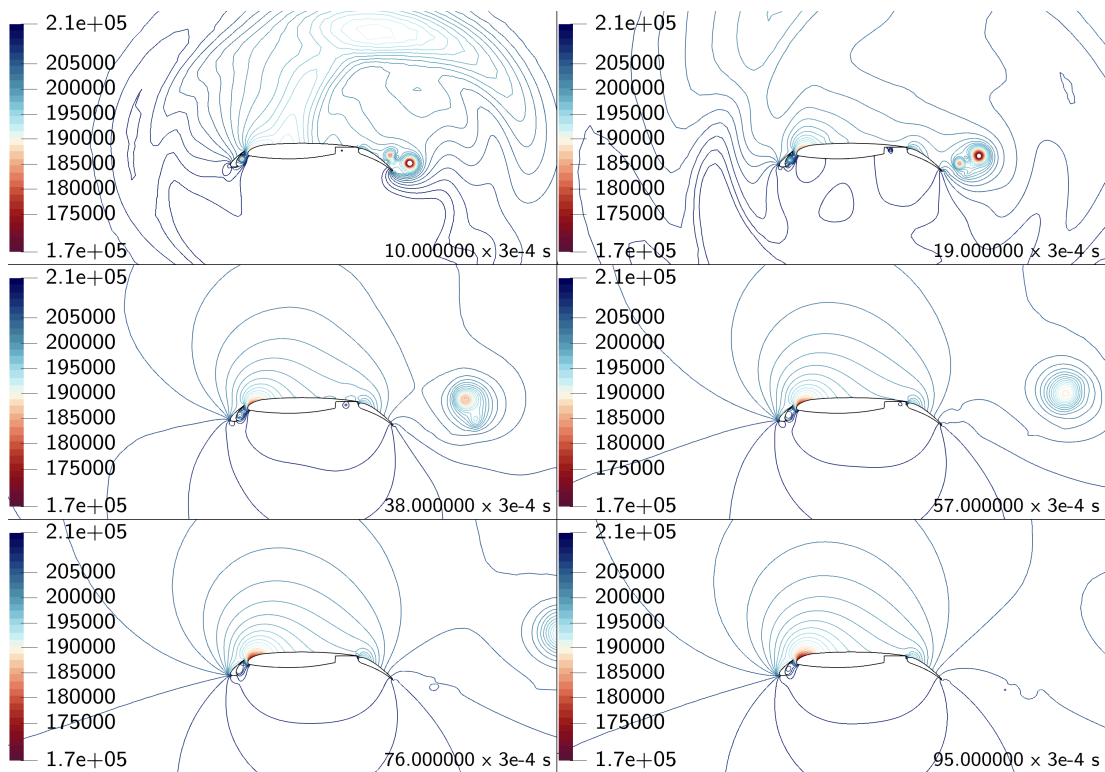


Figure 7.1: Contours of pressure for the impulsive start over the 30P30N airfoil at different instants of time.

are retained, selected for each method according to the procedures stated in Chapter 4. For the specific case of DMD, where different modes ranking can be used, as shown in Section 4.2, a simple truncation, based on the singular values computed in the first step of the algorithm (see Section 3.2.3), is used to perform the rank reduction, and it will be the procedure considered for all the test-cases presented in this Chapter.

As already highlighted in Section 6.1 the choice to retain only a small subset of modes is not driven by the impact it has on the time requirements of the online phase, which will remain practically unchanged. The further reduction is instead explored since it leads to two beneficial aspects: the final number of parameters to handle when optimisation steps are included in the process; a resulting Adaptive Framework that is able to introduce more improvements in preserving essential dynamics with respect to a single ROM as the number of modes retained is decreased. These two main aspects define also the choice of the number of modes for all the other test-cases presented hereafter.

For the test-case considered here, the time required for the database generation is approximately 3700 CH, considering a residuals' tolerance of 10^{-6} and a maximum of 10,000 iterations for the dual-time stepping scheme. The time required for the extraction of all the set of features for the adaptive framework and the computation of the residual database is approximately 2h, while the extraction of the POD basis only requires few seconds (no residual database required), both on a single core. Although these two time requirements are different, they are both negligible when compared to the cost of the database generation, which therefore dictates the computational effort of the offline phase. For the specific case of the Adaptive Framework, another valuable information to report is the time required to perform one residual evaluation to build the residual database. This time, indeed, provides the computational speedup achieved during the offline phase by an Adaptive Framework based on the residual error, as opposed to an Adaptive Framework based on the direct error, which instead requires to compute an additional high-fidelity reference solution. For this specific test-case, the time required for one residual evaluation to generate the residual database is 20s on a single core, as opposed to the 12.5 CH required to compute one additional CFD solution. Finally, the online phase requires for both the Adaptive Framework and the POD few tenths of a second to reconstruct the ROM solution at each desired time.

7.2.1 Volume Analysis

The residual evaluation all over the computational domain is performed first. Figure 7.2 reports the details of this residual evaluation for all the conservative variables considered (excluding turbulence) and the three methods included in the Adaptive Framework. Time evolutions of the single ROMs are not reported, since it is irrelevant for the definition of the Adaptive Framework. Indeed, the Adaptive ROM looks at the performance of each set of features extracted in its entirety, on the basis of the residual generated. This is why only the residuals are shown in Figure 7.2 and they will be the only quantities related to the various ROMs that are shown also for all the other test-cases presented hereafter. It can be noticed from Figure 7.2 how RDMD is the most used technique in the second-half of the time window. This result is in accordance

to the analysis reported in [44], highlighting the capability of RDMD in describing attractors, which, for this particular test-case, is represented by the convergence to the steady state flow as the strong transient linked to the impulsive start vanishes. The more pronounced oscillations at the end of the time window for the RDMD, which can be noticed from the blue curve in Figure 7.2, can be linked to interpolation issues at the border of the interval considered to build the ROM. The time evolution of RDMD modes reflects better than the other algorithms used the dynamics that is happening in the time window investigated. Therefore, it presents an almost constant trend towards the end of the time window when the solution is converging to a steady state flow condition, whereas it shows a more evident unsteady behaviour in the first part of the interval. This can cause oscillations to appear when the RBF interpolation is used on the slowly varying part, which are amplified when the residual evaluation of the ROM solution is performed. Overall, a slightly increasing trend with time, towards the end of the time window, can be observed in the residual error for all the three algorithms considered looking at Figure 7.2. This can still be linked to the particular dynamics investigated, where the most important unsteadiness is happening in the first part of the investigated time window ($t < 0.015$ s). The only modes retained might propagate information about the most important dynamics happening at previous time instants also at later stages, resulting in an increasing trend of the residual error. The improvements of the Adaptive framework are reported also in terms of contours of the entire flow field in Figure 7.3, where the conservative variable density is shown. In the very initial time window, some spurious oscillations are present for both the Adaptive ROM and the POD (first row in Figure 7.3), as a consequence of using only a small subset of modes to describe the very strong initial transient. The second row in Figure 7.3 still shows poor accuracy in resolving the starting vortex for both techniques, but presents overall slight improvements of the Adaptive ROM with respect to POD. Finally, for the last two instants represented (last two rows in Figure 7.3), the starting vortex is much better resolved while propagating downstream with respect to a pure POD, which instead reconstructs a structure highly stretched in the streamwise direction and loses accuracy in resolution. Also the reconstruction near the aerodynamic body shows

Chapter 7. Impulsively started lifting bodies

slight improvements when the Adaptive ROM is used in the last two instants of time represented.

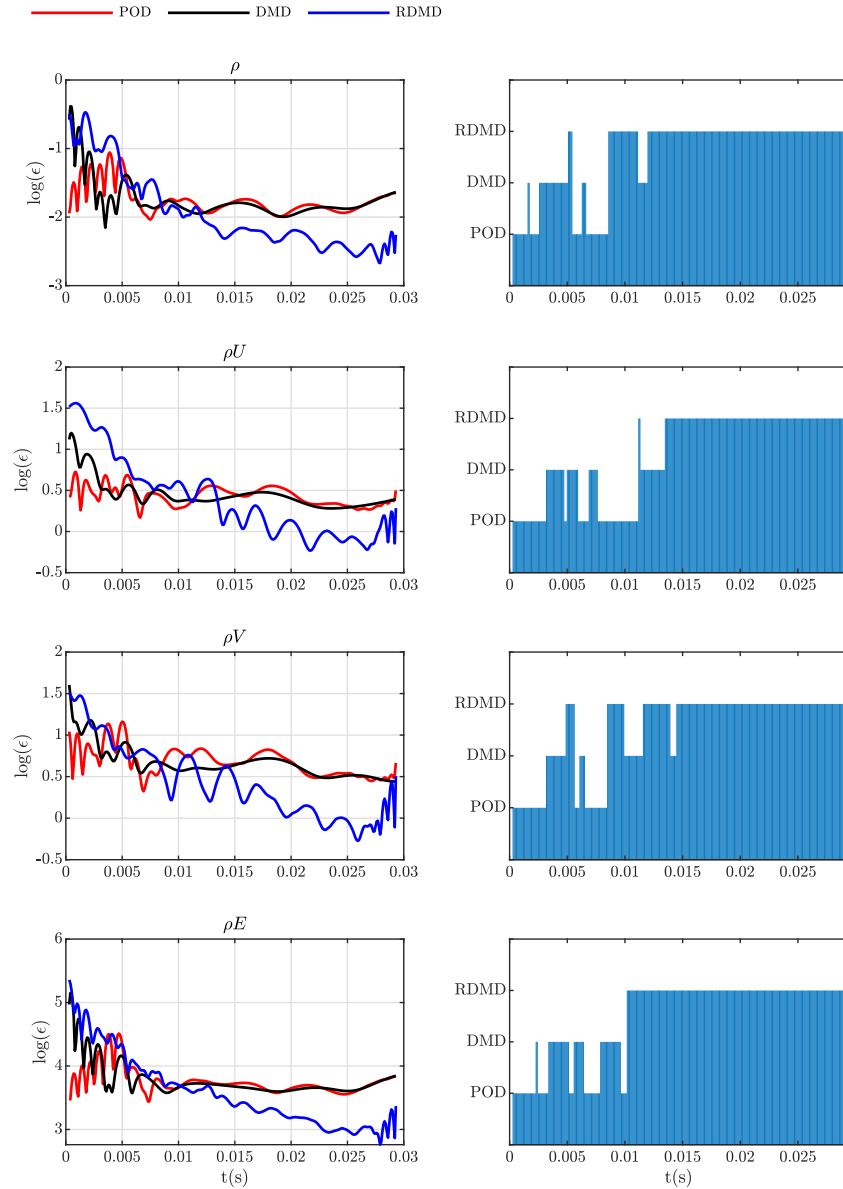


Figure 7.2: Volume residual evaluation (left column) and choice of methods (right columns) for all the conservative variables (excluding turbulence), fixed number of modes $N_m = 10$, 30P30N test-case.

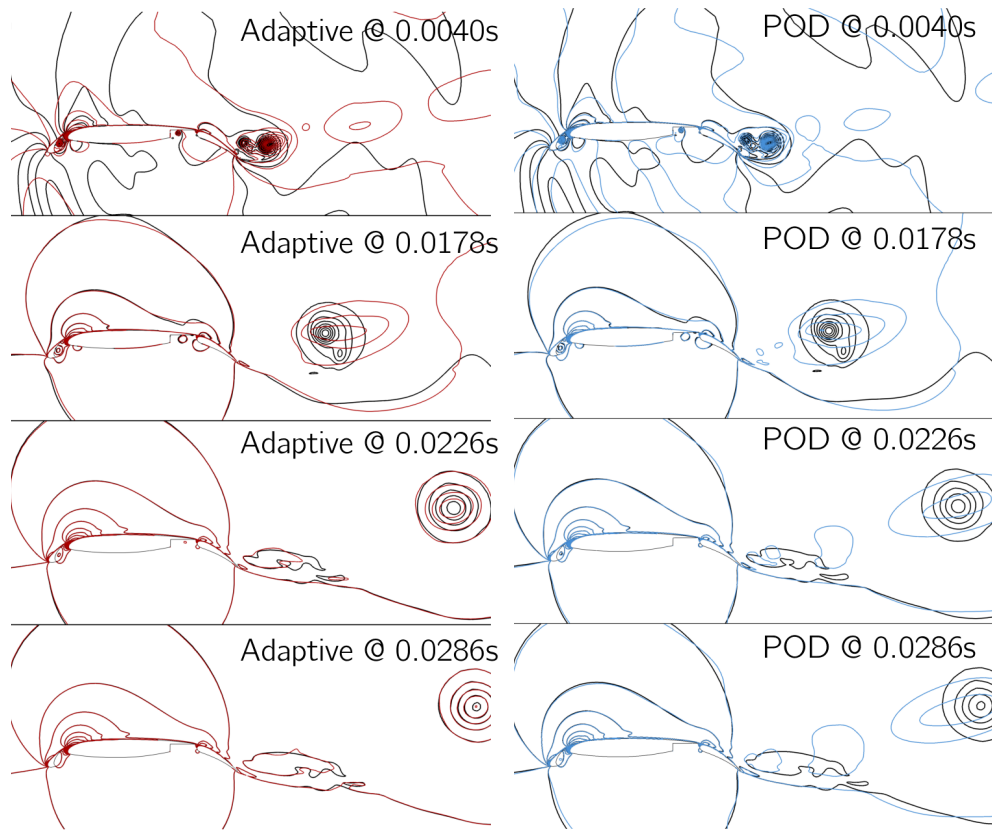


Figure 7.3: Comparison of the volume solution in terms of ρ . coloured lines show the ROM reconstruction while the black lines show the reference CFD solution. The left column shows the adaptive reconstruction, the right columns shows the pure POD reconstruction. Number of modes fixed, $N_m = 10$.

7.2.2 Surface Analysis

A residual evaluation considering only the body surface is now considered. Only the residual evaluation of conservative variables ρ and ρE is reported in Figure 7.4, as the no slip condition imposes a zero velocity, and therefore zero momentum, on the body surface (momentum equations are identically satisfied, residuals are equal to zero). The choice of the method is mostly limited to POD and RDMD. DMD might not be able to solve the very small structures near the wall with enough accuracy with the adopted truncation. Figure 7.6 reports few instants of time of the flow reconstructed on the surface in terms of the conservative variable ρE . A detail is reported in this Figure,

where the adaptive and pure POD reconstruction differ the most in describing the time dynamics on the surface. This detail is highlighted with a shaded rectangle in Figure 7.5, where both the airfoil geometry and a CFD reference solution at a particular time instant are reported. Slight improvements of the adaptive techniques are also present on the slat and flap region (not reported).

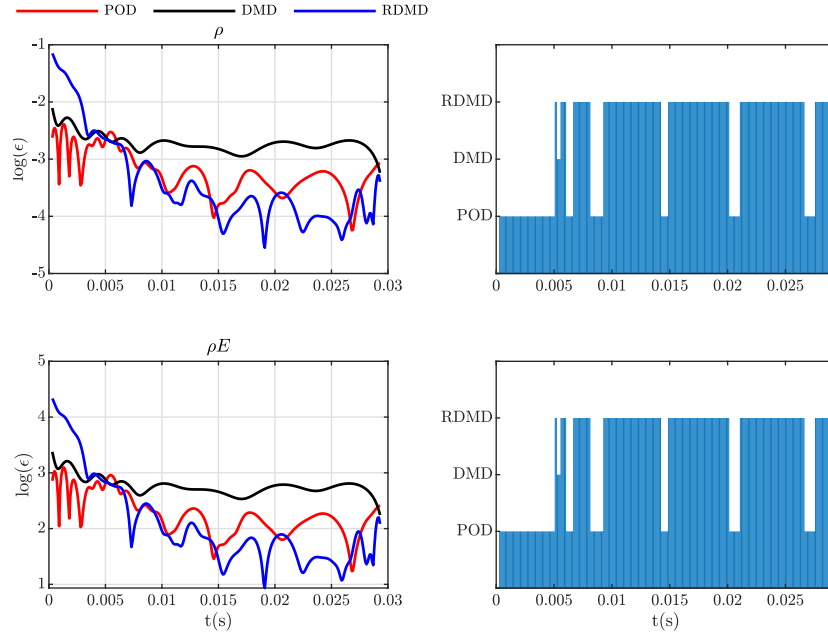


Figure 7.4: Surface residual evaluation (left column) and choice of methods (right columns) for the conservative variables ρ and ρE , fixed number of modes $N_m = 10$, 30P30N test-case.

7.3 High-Lift Wing-Body Configuration

The impulsive start of the High-Lift Wing-Body configuration from the AIAA 1st high-lift workshop is now considered [158]. Details on the mesh and the CFD setup can be retrieved from the 3D test-case presented in Section 4.1.1, the only difference being the physical time Δt used to advance the dual-time stepping simulation, namely $\Delta t = 5 \times 10^{-4}$ s. The flow is started from rest (boundary conditions on the farfield equal to freestream conditions), and it converges to a steady state in the vicinity of the wing, with one big vortex advecting downstream. Flow dynamics in terms of the

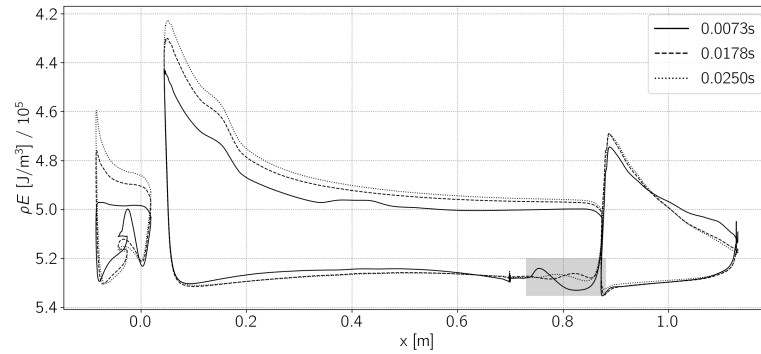


Figure 7.5: Surface reference solution in terms of ρE , 30P30N test-case. The shaded rectangle highlights the region where a zoomed comparison between methods is reported, see Figure 7.6.

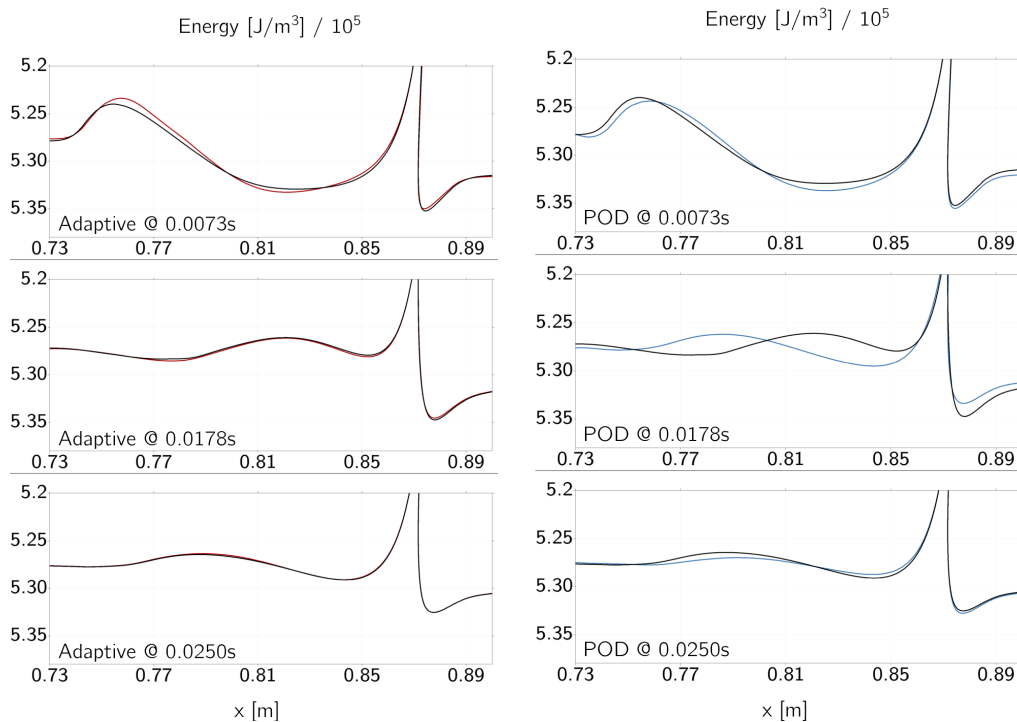


Figure 7.6: Contour comparison of the surface solution in terms of ρE for (top to bottom) $t = 0.0073s, 0.0178s, 0.0250s$ for the 30P30N test-case. Coloured lines show the ROM reconstruction while the black lines show the reference CFD solution. The left column shows the adaptive reconstruction, the right columns shows the pure POD reconstruction. Number of modes fixed, $N_m = 10$.

evolution in time of the Mach number is reported in Figure 7.7.

The reduced model is built within the time window $[0; 0.01]$ s where the dynamics of

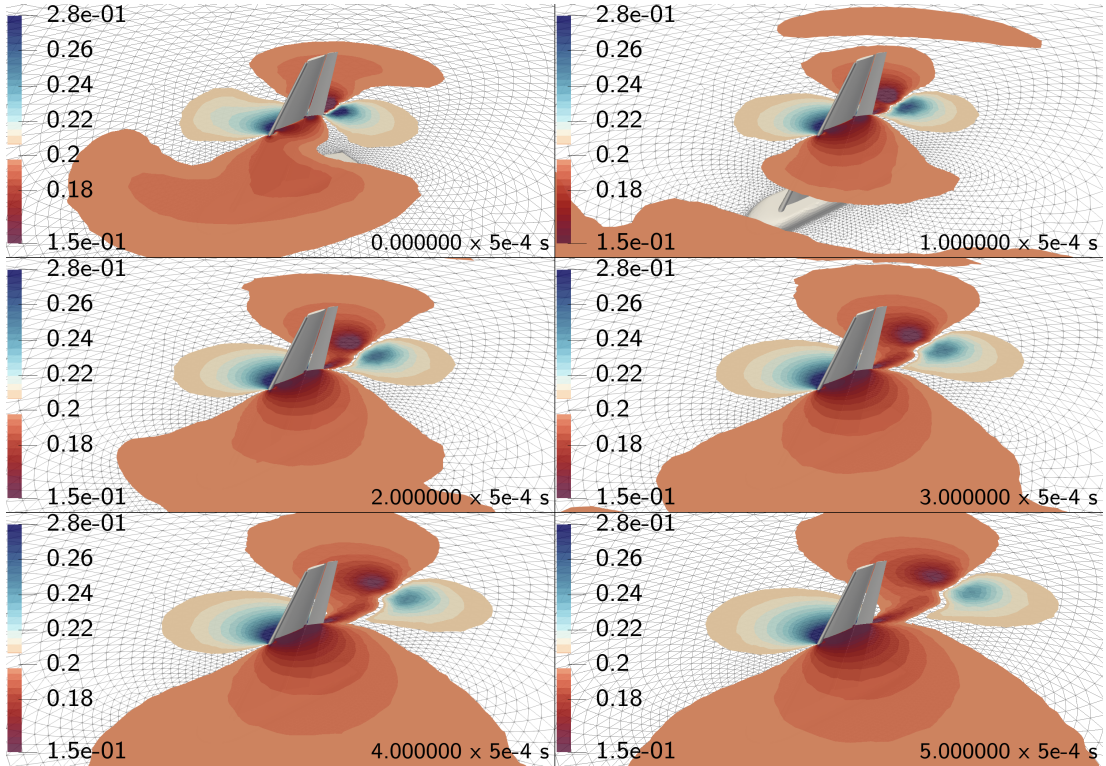


Figure 7.7: Contours of Mach number at different instants of time for the impulsive start of the High-Lift configuration.

interest is happening, with a sampling Δt of 2×10^{-3} s, which results in a number of snapshots $N_s = 50$ equispaced in time. Figure 7.8 reports the quantity $\epsilon_{R,T}$ varying the number of modes for all the primary conservative variables. Differently from what happens in the 2D test-cases analysed in Chapter 6 and according to the discussion reported in Section 6.4, there is no clearly visible hump in the plots reported. Indeed, the mesh spatial resolution for the 3D test-case considered is coarser in the region where vortex dynamics is happening, as it presents a highly refined region only close to the body surface. This leads to a situation where adding modes at the beginning does not introduce any spurious oscillations linked both to small spatial structures and the advective nature of the problem, as it happens instead for the 2D test-cases (see Figures 6.1-6.6). The lower resolution of the 3D test-cases is mainly dictated by the

computational resources available for the present work.

According to the $\epsilon_{R,T}$ plots, to exploit at best the improvements of the Adaptive Framework, a number of 10 modes out of 50 is retained to perform the complete analysis. Despite from these plots it appears that there is not a marked advantage in integral terms also when using the Adaptive Framework with a small subset of modes, it will be shown instead that, with the specific choice of number of modes, the Adaptive Framework is still capable of introducing improvements with respect to a single ROM in resolving local dynamics. These improvements are expected to increase as the mesh is refined and spatial structures are better resolved in the original snapshots used to train the ROM, according to the analysis reported in Section 6.4.

The time required for the database generation is approximately 16,000 CH, considering a residuals' tolerance of 10^{-6} and a maximum of 1,000 iterations for the dual-time stepping scheme. The time required for the extraction of all the set of features for the adaptive framework and the computation of the residual database is approximately 24h (most of the time is required to extract the RDMD basis), while the extraction of the POD basis requires less than one minute (no residual database required), both on a single core. The time required for one residual evaluation to generate the residual database is 800s on a single core, as opposed to the 80 CH required to compute one additional CFD solution. Finally, the online phase requires for both the Adaptive Framework and the POD few seconds to reconstruct the ROM solution at each desired time.

7.3.1 Volume Analysis

As in the previous test-case, a residual analysis over the full domain is carried out and Figure 7.9 shows the residual evaluation for all the conservative variables (excluding turbulence) and for the different methods (left column) and the choice of methods (bar plot on the right column). Again, there is a tendency of RDMD to perform better in the second half of the investigated time window, where the strong transient is vanishing, and the only structure left is a vortex, generated from the various lifting surfaces of the wing, that is propagating downstream. A behaviour similar to the one observed for

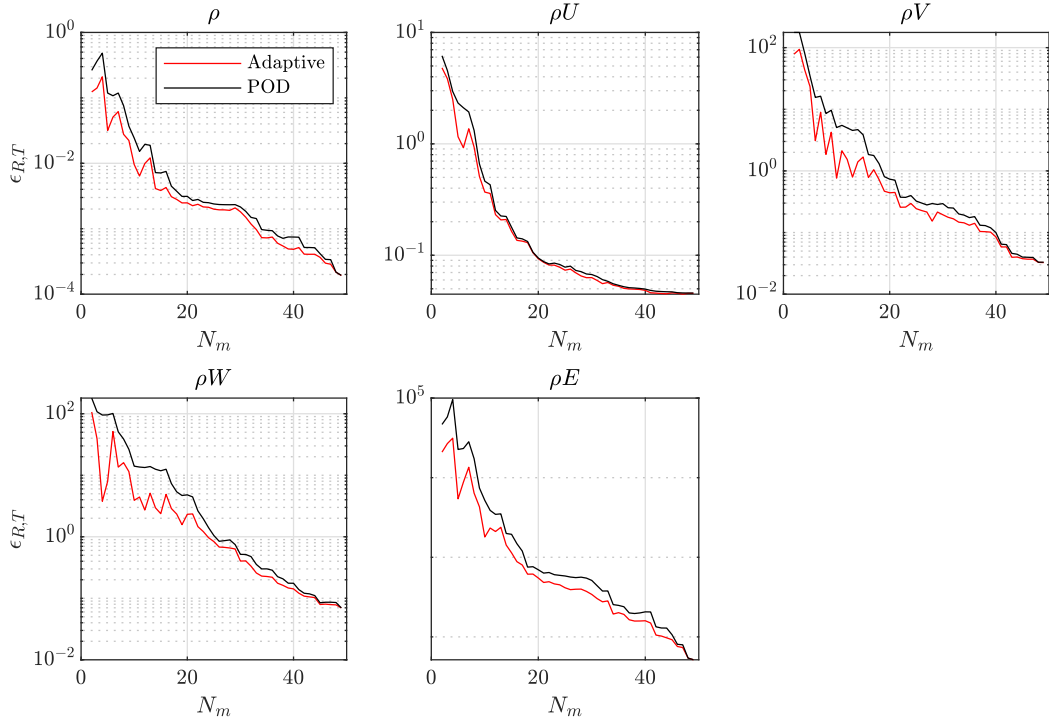


Figure 7.8: $\log_{10}(\epsilon_{R,T})$ varying the number of modes, for Adaptive ROM and POD, High-Lift Wing-Body Configuration test-case.

the previous test-case towards the end of the time window can be observed also for this specific case when looking at the residuals of RDMD and POD. This, again, can be both related to the physical information carried by the retained modes and the additional problem of interpolation issues at the border when the RBF is interpolating on a slowly varying dynamics. The DMD modes retained, instead, are almost completely dumped after the initial transient, which results in the quasi-constant behaviour of the residual after the initial time instants. It is worth highlighting that the DMD uses a different reconstruction formula (Equation 3.15), not based on interpolation, which dictates the different behaviour of the residuals. A detail of the better accuracy in resolving the vortex propagating in the second half of the time window, using the Adaptive Framework instead of pure POD, is reported in Figure 7.10, where the first column shows the Adaptive reconstruction, while the second column shows the pure POD reconstruction in terms of the conservative variable ρU . Although POD seems to provide enough accuracy to understand the dynamics, the Adaptive Framework shows

better accuracy both in time and space, i.e. the position of the vortex and its structure respectively. Indeed, structures resolved by POD appear slightly shifted in time and stretched in the streamwise direction.

7.3.2 Surface Analysis

A surface only residual evaluation is now carried out on the High-Lift Wing-Body surface. The residual evaluation for the only two meaningful quantities on the surface ρ and ρE are reported in Figure 7.11 and few surface reconstructions with both the adaptive technique and pure POD are reported in Figure 7.12. As for the previous case, in this figure a detail of the surface solution is shown, that is at the wing tip of the geometry, where the adaptive and pure POD reconstruction differ the most. It can be noticed from these details, how the adaptive reconstruction is able to resolve better surface structures at the wing tip as the solution is approaching a steady state. Not many differences are present on the rest of the surface in terms of contour comparisons.

7.4 Delta Wing

The impulsive start of a Delta Wing is considered. The geometry and the freestream flow conditions have been taken from the literature with the only difference being the exclusion of the model sting present in the original configuration[189]. The mesh used is a viscous hybrid mesh with 10,834,270 elements and 2,319,893 grid points. A dual-time stepping method is used for the CFD simulation with a $\Delta t = 10^{-4}$ s. The Mach number, Reynolds number and angle of attack are fixed respectively to $M = 0.4$, $Re = 6 \times 10^6$, $\alpha = 23$ deg. The simulation is run as fully turbulent, using the SST model [156]. Figure 7.13 reports few snapshots of the impulsive start where the vortical structures originating from the leading edge are represented by means of the Q-criterion. From the time evolution reported, it can be noticed the formation of the characteristic leading edge vortices and their breakdown in proximity of the Delta Wing trailing edge. A quasi-periodic behaviour is therefore established in the final instants of

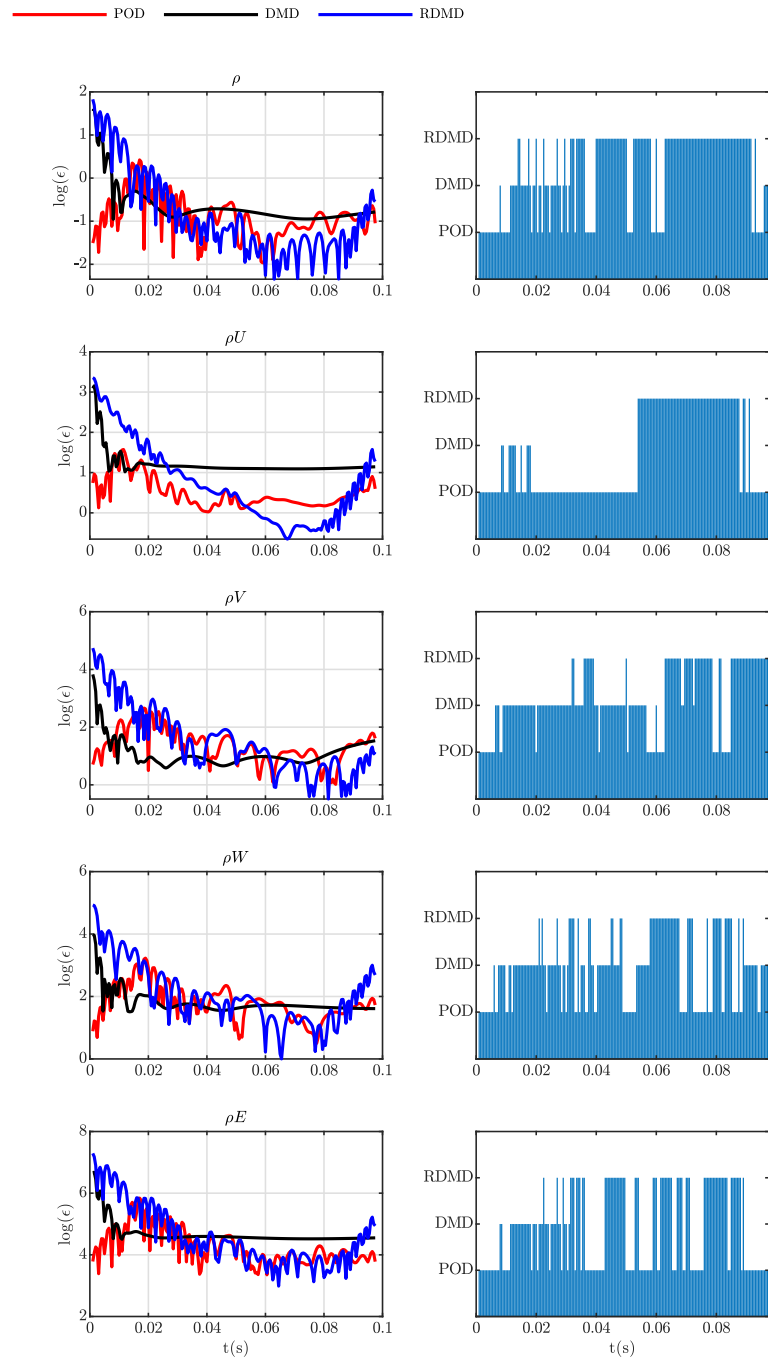


Figure 7.9: Volume residual evaluation (left column) and choice of methods (right columns) for all the conservative variables (excluding turbulence), fixed number of modes $N_m = 10$, High-Lift Wing-Body test-case.

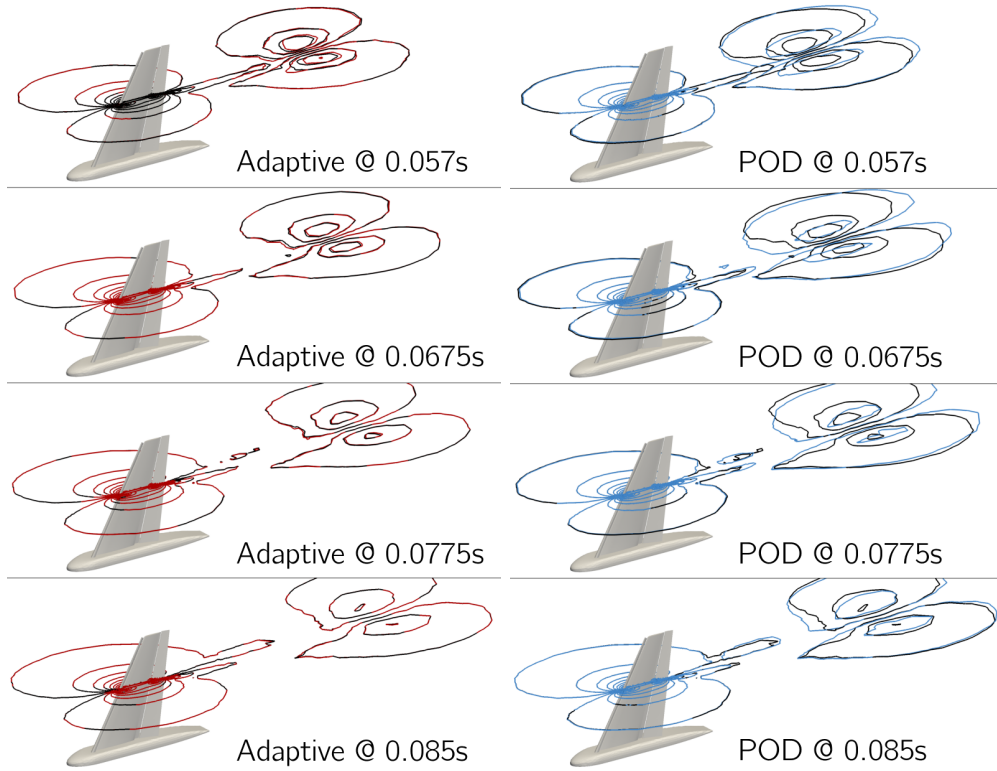


Figure 7.10: Contours comparison of volume solution in terms of ρU for the High-Lift Wing-Body test-case. Black contours show the CFD reference solution, colour contours report the ROM reconstruction. Left column shows the adaptive reconstruction, right column shows the POD pure reconstruction. Number of modes fixed, $N_m = 10$.

the investigated time-window, that shows the classical vortex breakdown phenomenon exhibited by Delta Wing Geometries at an angle of attack with respect to the freestream flow [190, 191].

In order to describe such dynamics in a low-dimensional manner, the reduced model is built within the time window $[0; 0.021]$ s, with a sampling Δt of 3×10^{-4} s, which results in a number of snapshots $N_s = 70$ equispaced in time. Figure 7.14 reports the quantity $\epsilon_{R,T}$ for all the primary conservative variables. According to the considerations already introduced for the previous test-case and the discussion reported in Section 6.4, the plots show a decreasing trend, as opposed to the non-monotonic trend observed for the 2D test-cases. Still according to these plots, a number of 10 modes out of the 70

Chapter 7. Impulsively started lifting bodies

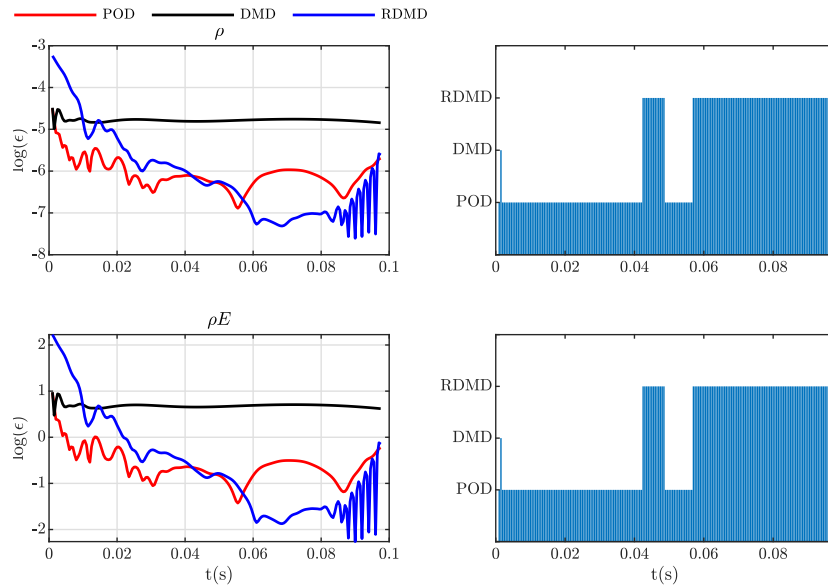


Figure 7.11: Surface residual evaluation (left column) and choice of methods (right columns) for the conservative variables ρ and ρE , fixed number of modes $N_m = 10$, High-Lift Wing-Body test-case.

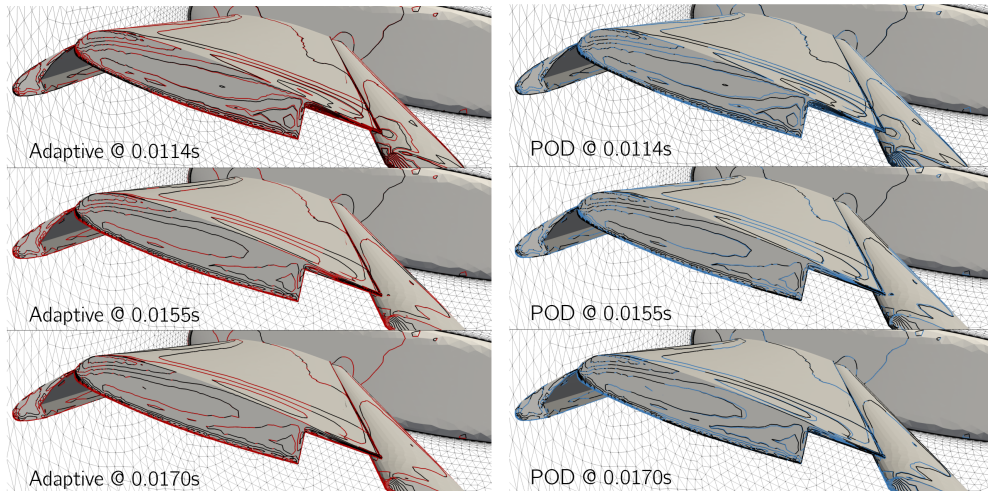


Figure 7.12: Detail of wing tip surface solution in terms of ρE for the High-Lift Wing-Body test-case. Black contours report the CFD reference solution, line contours show the ROM reconstruction. Left column is adaptive reconstruction, right column is pure POD reconstruction. Number of modes fixed, $N_m = 10$.

available is retained for each technique composing the adaptive framework. Although not strong improvements of the Adaptive Framework can be observed from the $\epsilon_{R,T}$

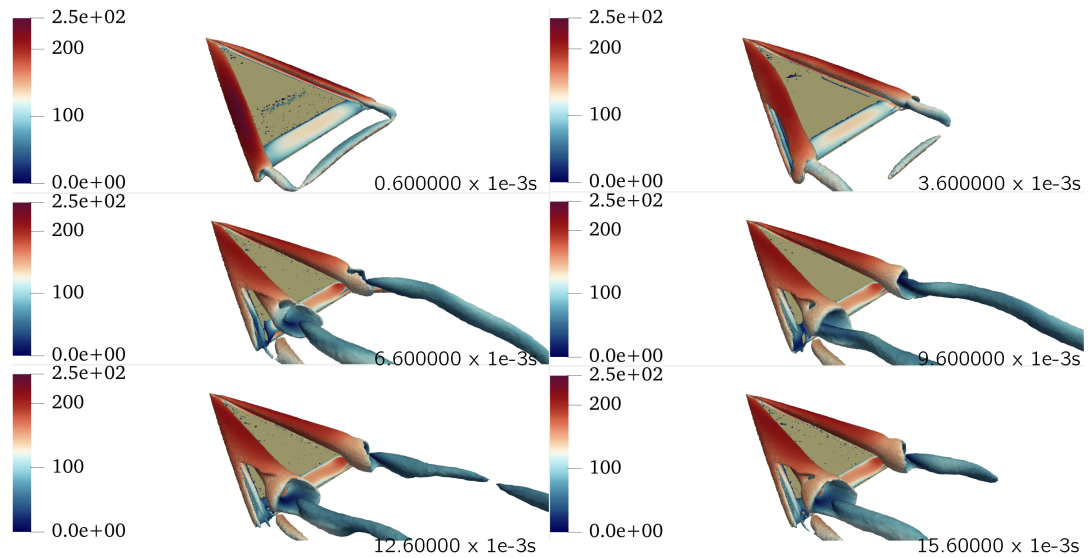


Figure 7.13: Contours of Q-criterion $Q = 800s^{-2}$ coloured with velocity magnitude for different time instants, Delta Wing test-case.

plots with respect to POD, it will be shown also for this test-case how the Adaptive Framework is able to better resolve local dynamics.

The time required for the database generation is approximately 10,500 CH, considering a residuals' tolerance of 10^{-6} and a maximum of 1,000 iterations for the dual-time stepping scheme. The time required for the extraction of all the set of features for the adaptive framework and the computation of the residual database is approximately 18h (most of the time is required to extract the RDMD basis), while the extraction of the POD basis requires less than one minute (no residual database required), both on a single core. The time required for one residual evaluation to generate the residual database is 700s on a single core, as opposed to the 50 CH required to compute one additional CFD solution. Finally, the online phase requires for both the Adaptive Framework and the POD few seconds to reconstruct the ROM solution at each desired time.

7.4.1 Volume Analysis

Also for this test-case, a residual evaluation all over the computational domain is first performed. Figure 7.15 reports this residual evaluation in time for the entire set of

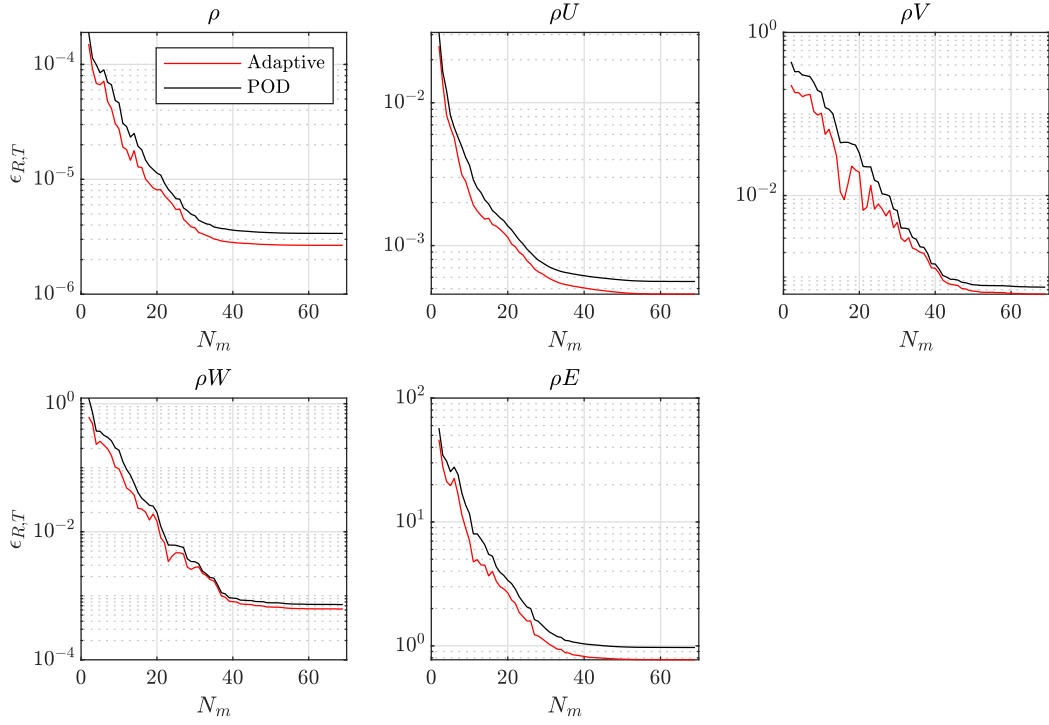


Figure 7.14: $\log_{10}(\epsilon_{R,T})$ varying the number of modes, for Adaptive ROM and POD, Delta Wing test-case.

conservative variables (excluding turbulence), for the three methods in the adaptive framework (left column) and the choice of these methods over the investigated time window (bar plot on the right column). For the specific case of the main component of momentum ρU and the two conservative variables ρ and ρE , RDMD performs better in the description of an attractor that is now quasi-periodic, namely the vortex breakdown happening very close to the trailing edge of the Delta Wing once the initial transient linked to the impulsive start vanishes. It is worth noting that, since the dynamics sampled is different from the two previous test-cases, the residuals of the various algorithms present a different behaviour in time, which is more oscillating than slowly increasing towards the end of the time window. Moreover, the characteristic oscillations at the border, usually appearing for the RDMD, are less pronounced than in the previous test-cases. This can be linked to the more varying dynamics of the modes, associated to the quasi-periodic dynamics dictated by the vortex breakdown. The better performance of the Adaptive Framework is clearly visible in terms of reconstruction of the entire flow

field in Figure 7.16, where a slice on the symmetry plane is reported and contours of the Adaptive and POD techniques are compared against the contours of the reference CFD solution, for the conservative variable density and for different instants of time. It can be noticed from this Figure how details of the trailing edge vortex advected downstream are completely lost with the POD reconstruction, while they are resolved, even if with not very good accuracy, by the Adaptive technique. Improvements are introduced by the Adaptive strategy also in the region near the aerodynamic body.

7.4.2 Surface Analysis

Finally, residual evaluation only on the surface of the Delta Wing is carried out. Figure 7.17 shows the residual evaluation for the meaningful conservative quantities ρ and ρE , while Figure 7.18 reports a detail of surface reconstruction for few time instants.

Slight improvements of the adaptive techniques can be noticed from this Figure, on the upper surface of the Delta Wing, especially in the central region. Adaptive reconstruction performs better also on the lower surface (details not shown). POD appears to provide enough accuracy in resolving surface dynamics. In particular, if integral quantities are required, the slight differences between Adaptive and POD method can be neglected. Nevertheless, when the focus is shifted more on resolving better local dynamics on the surface, e.g. if the exact location of the vortex breakdown is a required information of the analysis, which can be the case for flow control purposes, the Adaptive framework shows superior performance and it should be the one to consider.

7.5 Formation Flight featuring Delta Wing geometries

A configuration of three Delta Wings in Formation Flight is considered as the last test-case. Each Delta Wing has the same geometry of the one used for the Delta Wing test-case presented in Section 7.4. The configuration is symmetric, with one leader and two followers symmetrically positioned with respect to the leader longitudinal axis, next to the leader's wake. There is no relative rotation among the different

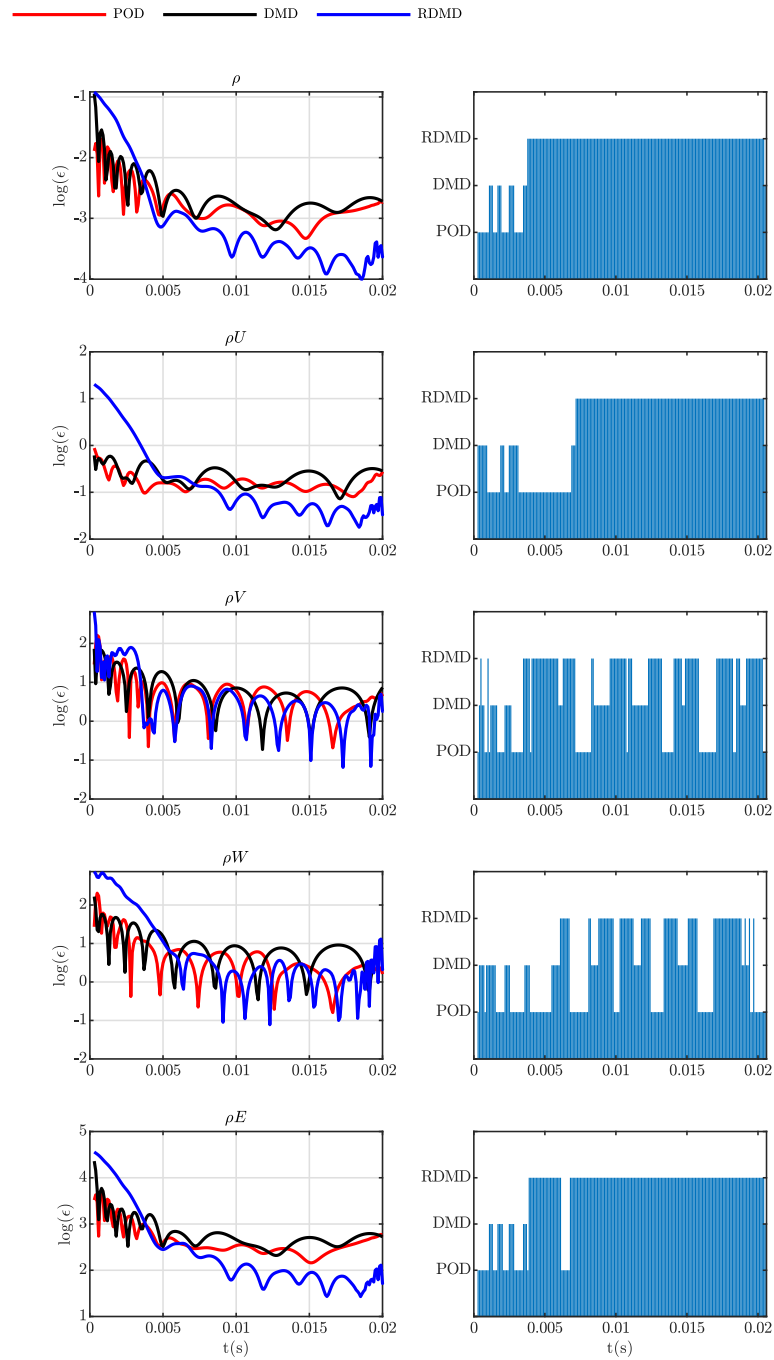


Figure 7.15: Volume residual evaluation (left column) and choice of methods (right columns) for all the conservative variables (excluding turbulence), fixed number of modes $N_m = 10$, Delta Wing test-case.

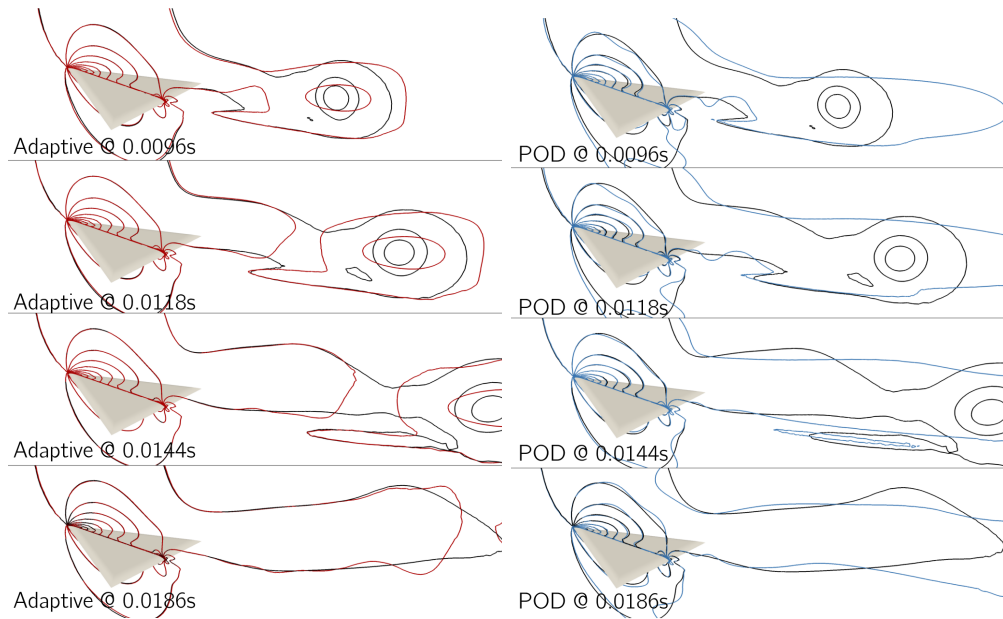


Figure 7.16: Comparison of volume solution in terms of ρ for the Delta Wing test-case. The black contours report the CFD reference solution, the coloured contour lines show the ROM reconstruction. Left column shows the adaptive reconstruction, right column shows the pure POD reconstruction. Number of modes fixed, $N_m = 10$.

bodies, which therefore exhibit the same angle of attack with respect to the free stream direction. The mesh has been built for half configuration, being it perfectly symmetric, and it is a viscous unstructured mesh with 15,911,216 elements and 3,824,705 grid points. A refinement is present in the region of the leader wake and near the interaction with the follower Delta Wing. A dual-time stepping method is used for the unsteady simulation and the time step is fixed to $\Delta t = 10^{-4}$ s. The Mach number, Reynolds number and angle of attack are fixed respectively to $M = 0.4$, $Re = 6 \times 10^6$, $\alpha = 15$ deg. The simulation is run as fully turbulent, using the SST turbulence model [156]. As initial condition for the CFD simulation, a freestream initialization of the entire computational domain has been considered, i.e. impulsive start. The sampling to build the reduced model is performed on the time window $[0; 0.0294]$ s, which contains both the strong initial transient and the dynamics linked to the interaction of the leading edge vortex detaching from the leader with the leading edge vortex forming on the followers' geometries. Few snapshots are reported in Figure 7.19 that describe the time

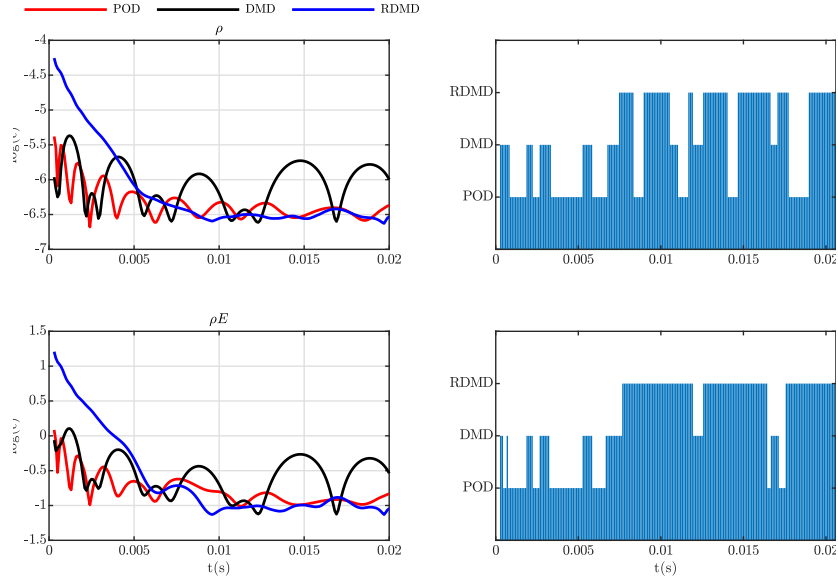


Figure 7.17: Surface residual evaluation (left column) and choice of methods (right columns) for the conservative variables ρ and ρE , fixed number of modes $N_m = 10$, Delta Wing test-case.

evolution of the flow field in terms of Q-criterion isosurfaces over the investigated time window. Since the computational mesh has been refined only in the wake of the leader Delta Wing and the early interaction region in proximity of the followers leading edge, resolution of vortices is poorer in the wake of the followers geometries.

In order to build the Adaptive Framework, snapshots have been sampled in the time window defined above, where the dynamic of interest is happening, using a sampling Δt equal to 3×10^{-4} , which results in a number of snapshots $N_s = 100$ equispaced in time. Figure 7.20 reports the quantity $\epsilon_{R,T}$ varying the number of modes for all the conservative variables, excluding turbulence. On the basis of these plots, to exploit the major improvements of the Adaptive Framework with respect to a single ROM, a number of 15 modes out of 100 is retained to carry out the complete analysis. The time required for the database generation is approximately 18,000 CH, considering a residuals' tolerance of 10^{-6} and a maximum of 1,000 iterations for the dual-time stepping scheme. The time required for the extraction of all the set of features for the adaptive framework and the computation of the residual database is approximately

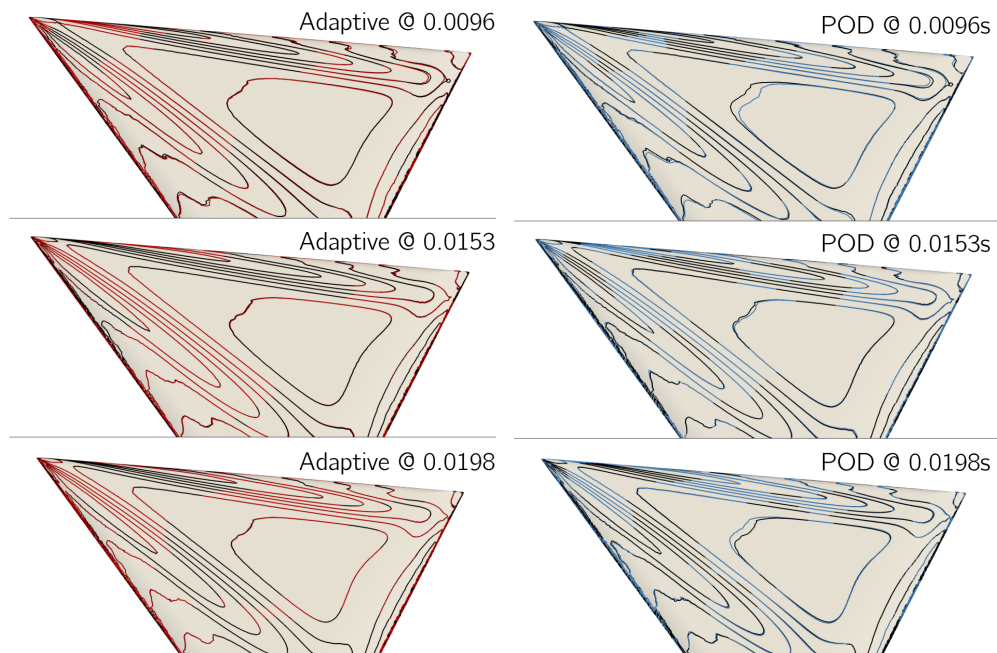


Figure 7.18: Detail of surface solution in terms of ρE for (top to bottom) $t = 0.0096s$, $0.0153s$, $0.0198s$ for the Delta Wing test-case. Black contours indicate the CFD reference solution, coloured contours show the ROM reconstruction. Left column is Adaptive reconstruction, right column is pure POD reconstruction. Number of modes fixed, $N_m = 10$.

20h (most of the time is required to extract the RDMD basis), while the extraction of the POD basis requires less than one minute (no residual database required), both on a single core. The time required for one residual evaluation to generate the residual database is 10^3s on a single core, as opposed to the 60 CH required to compute one additional CFD solution. Finally, the online phase requires for both the Adaptive Framework and the POD few seconds to reconstruct the ROM solution at each desired time. Figure 7.21 reports the residual evaluation in time for the entire set of conservative variables (excluding turbulence), for the three methods in the adaptive framework (left column) and the choice of these methods over the investigated time window (bar plot on the right column). It is clearly visible how RDMD presents better performance for almost the entire set of conservative variables in the second half of the investigated time window, where the interaction of vortices is happening. Only for the specific case

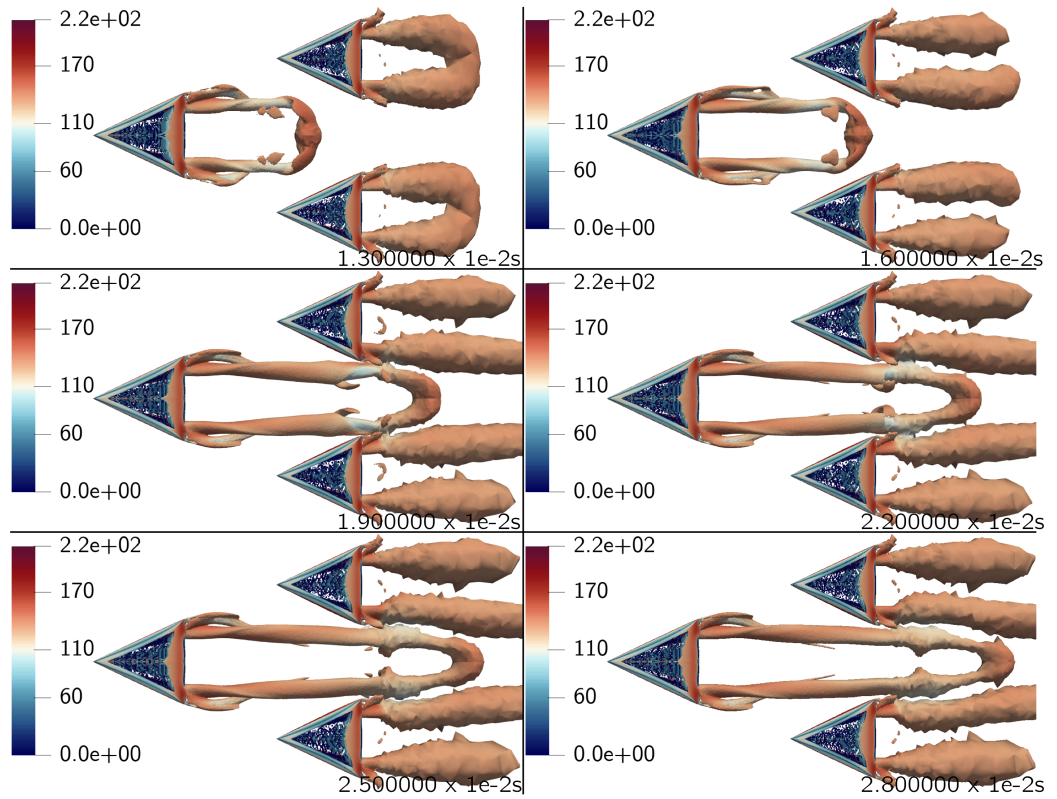


Figure 7.19: Contours of Q -criterion $Q = 800s^{-2}$ coloured with velocity magnitude (m/s) for different time instants, Formation Flight test-case.

of the Z component of momentum ρW , the different methods within the Adaptive framework are almost equally chosen across the entire time interval shown. The steep increase in the RDMD residual at the end of the time window can still be linked to interpolation issues of the RBF at the border, due to the slowly varying dynamics of the RDMD modes. The slightly increasing trend of the POD and DMD residual towards the end of the time window can be instead linked to the specific dynamics considered. The first half of the time window ($t < 0.017s$) contains the dynamics associated to the propagation of the trailing edge vortices and the main interaction of the trailing edge vortex of the leader with the two trailing edge vortices of the follower. The few POD and DMD retained modes are mainly describing such dynamics, whereas they are resolving with less accuracy the dynamics happening after the main interaction, which represents a less energetic dynamics for POD and it is also dumped by DMD eigenvalues as time increases. The major improvements of the RDMD, and therefore

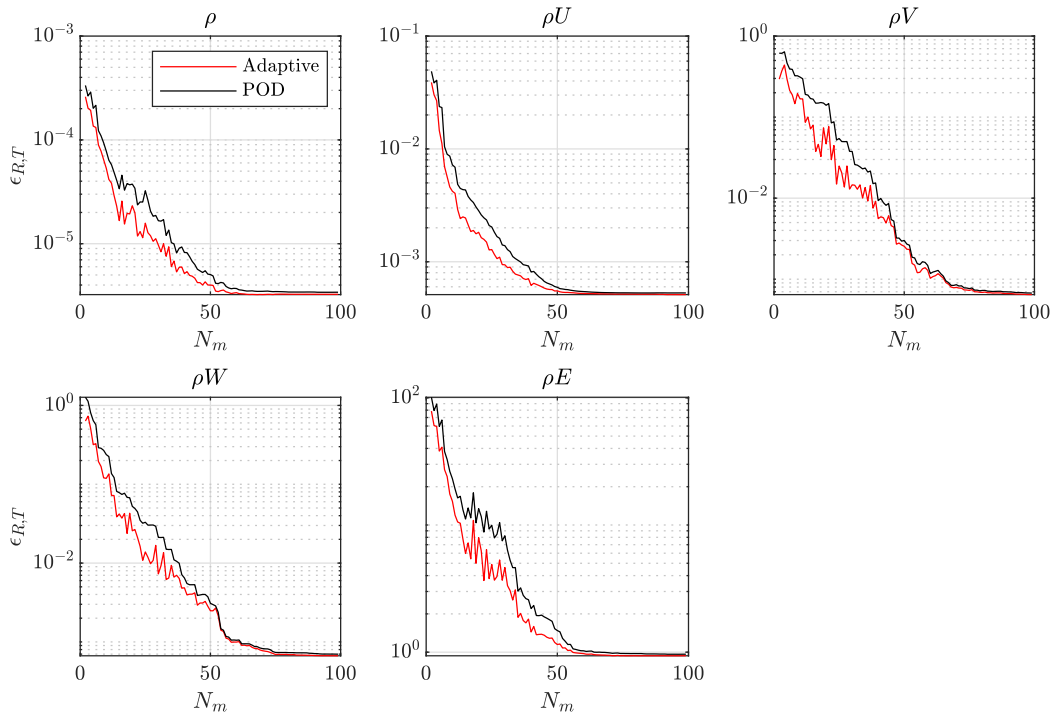


Figure 7.20: $\log_{10}(\epsilon_{R,T})$ varying the number of modes, for Adaptive ROM and POD, Formation Flight test-case.

of the Adaptive framework, in describing the dynamics of interacting vortices can be observed in Figure 7.22, where the contours of the CFD reference solutions are compared with the contours of the Adaptive and pure POD reconstruction on a specific slice, taken at 0.45m from the symmetry plane. Few instants of time are shown where the interaction of vortices is happening. Major accuracy is observed almost everywhere over the shown slice and for the various time instants. In particular, details of the interaction region are reported in Figure 7.23, where it is still clearly visible how the Adaptive ROM is able to resolve better the dynamics of the interaction. Again, the improvements are measured locally in terms of how close the contours of the ROM solution are to the CFD reference solution, and in integral terms using the residuals reported in Figure 7.21. Even if POD appears to be good enough for some time instants, the Adaptive Framework is still able to introduce more details in the description of the dynamics, which is believed to be important when problems related to flow control or design of aerodynamic surfaces is addressed.

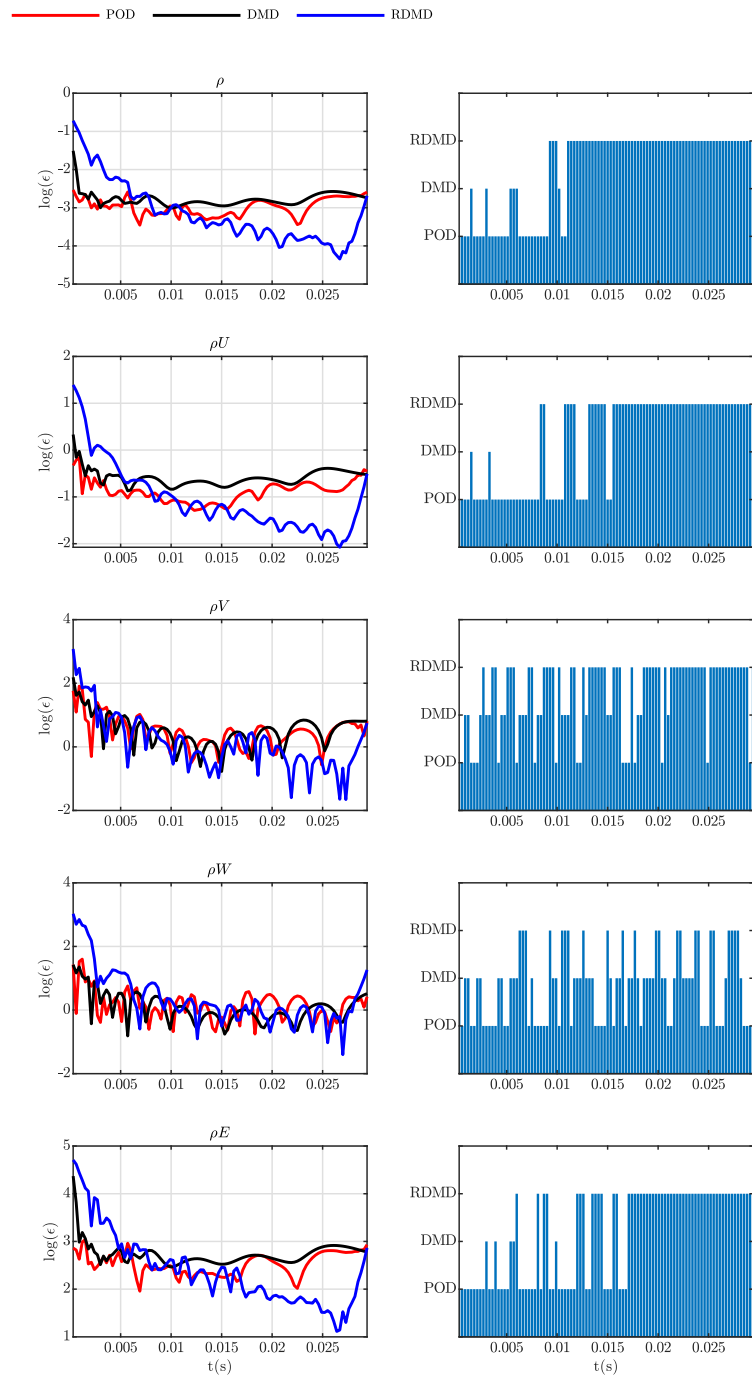


Figure 7.21: Volume residual evaluation (left column) and choice of methods (right columns) for all the conservative variables (excluding turbulence), fixed number of modes $N_m = 15$, Formation Flight test-case.

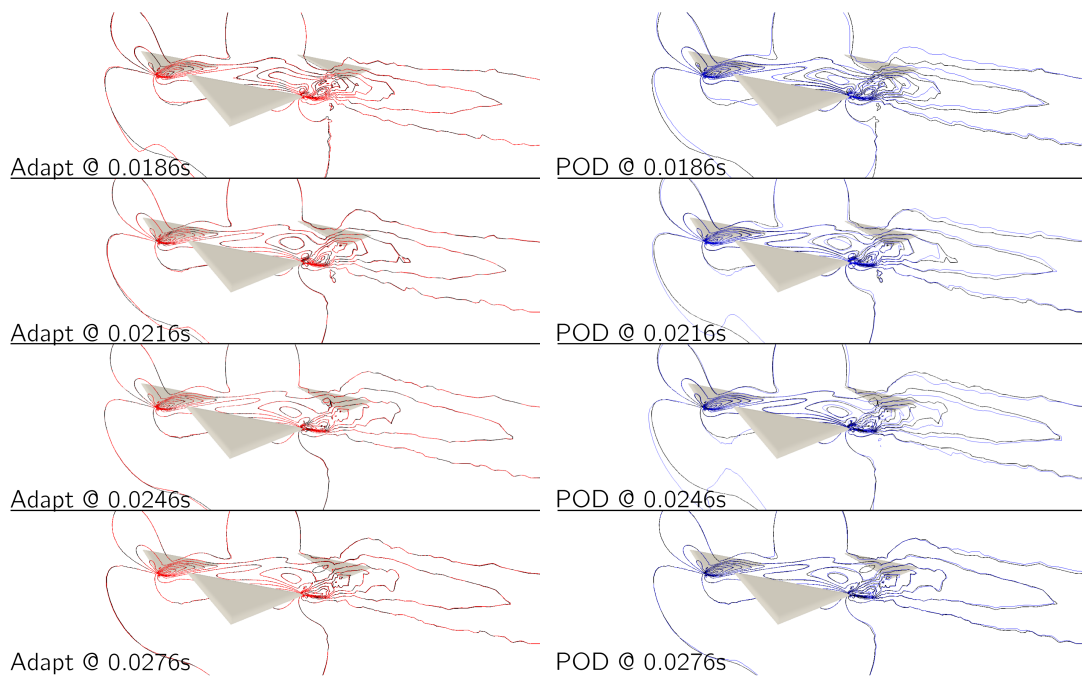


Figure 7.22: Comparison of volume solution in terms of ρ for the Formation Flight test-case. The black contours report the CFD reference solution, the coloured contour lines show the ROM reconstruction. Left column shows the adaptive reconstruction, right column shows the pure POD reconstruction. Slice taken at 0.45m from the plane of symmetry. Number of modes fixed, $N_m = 15$.

7.6 Remarks

The current Chapter presented few applications of the Model-Based Adaptive Reduced Basis framework introduced in Chapter 5 for unsteady complex flows. The complexity has been presented both in terms of the geometries considered, i.e. the 30P30N air-foil and the 3D High-Lift Wing-Body configuration test-case, and the complex vortex structures that can be generated from simple geometries in specific configurations, i.e. the Delta Wing at high angle of attack and Delta Wings in Formation Flight test-cases. For the various test-cases reported a rigorous grid convergence study is not reported, even if reasonable choices have been made on the space and time discretisation, according to the expected dynamics involved and the computational resources available. Performing a rigorous grid convergence study for all the test-cases presented is out of the scope of the present work, which focuses instead on resolving the physics carried

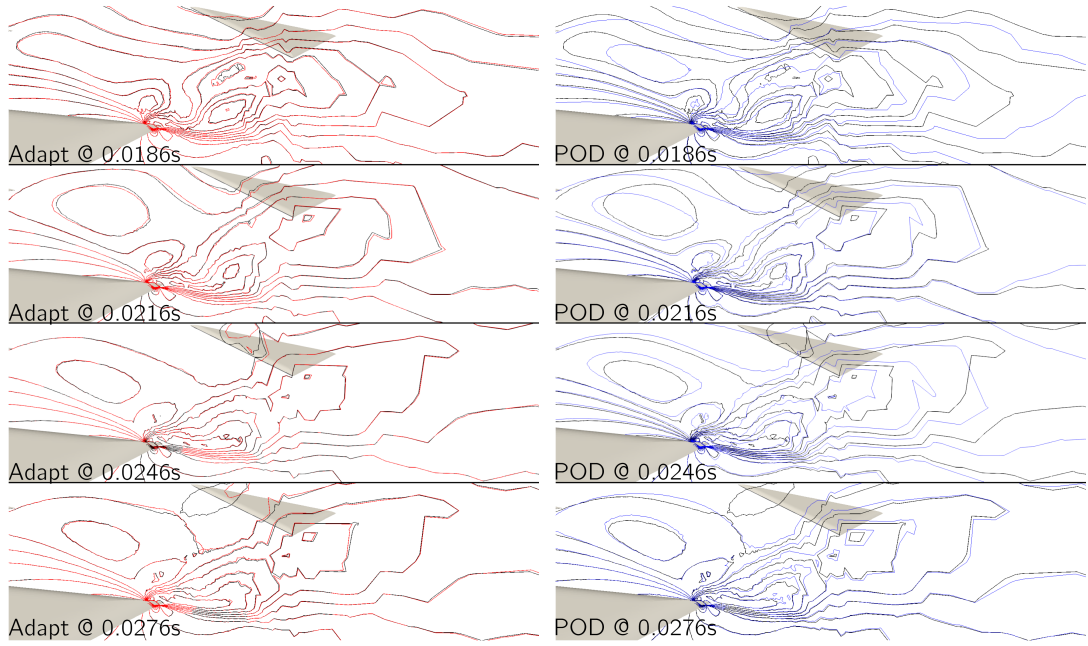


Figure 7.23: Detail of volume solution in the region of vortices interaction, in terms of ρ for the Formation Flight test-case. The black contours report the CFD reference solution, the coloured contour lines show the ROM reconstruction. Left column shows the adaptive reconstruction, right column shows the pure POD reconstruction. Slice taken at 0.45m from the plane of symmetry. Number of modes fixed, $N_m = 15$.

out by the collected snapshots. Therefore, the set of snapshots represents the target physics to be described by the ROMs with the best accuracy possible (see also the discussion reported in Section 3.4). The accuracy and physical consistency of the method has been assessed in reconstructing the entire flow field first and, for the first three test-cases only, conserved quantities on the body surface after. To perform this task, the residual evaluation has been considered all over the computational domain for the former and only on the body surface for the latter.

It is worth noticing that since the L^2 -norm of the residual is considered as the final value to drive the selection, the resulting performance indicator provides an integral measure of the quality of the method. Therefore, especially in the case of unsteady flows with complex dynamics in space and time, this might lead to a situation where the selected ROM might not be the best in solving all the spatial structures in the entire computational domain, despite being identified as the best method in terms of the

computed residual. Nevertheless, looking at the comparisons over the entire flow fields, it can be noticed a good improvement of the adaptive technique with respect to pure POD for the most part of the computational domain where important dynamics is happening. For the first three test-cases, the adaptive framework is able to solve better the advection of the starting vortex propagating downstream, Figures 7.3,7.10,7.16. This is mainly linked to the better performance RDMD is able to provide in defining attractors [44]. Moreover, the Adaptive Framework shows better accuracy also in resolving flow features near the aerodynamic bodies. For the last test-case of the Formation Flight configuration, the adaptive framework is introducing major improvements through the RDMD basis in solving the time evolution of vortices interaction at the trailing edge of the followers' geometries, Figure 7.23. Regarding the surface evaluation performed for the first three test-cases analysed, from Figures 7.6, 7.12 and 7.18 there are improvements of the adaptive framework with respect to pure POD in accordance with the residual evaluation confined only on the body surface. Specifically, for the 30P30N test-case, the resolution of the recirculation zone where the flap is retracted is improved with the adaptive framework, Figure 7.6, and there is improvement also on the slat and flap region. Major improvements from the High-Lift Wing-Body configuration are localized at the wing tip, Figure 7.12, while for the Delta Wing test-case there are slight improvements in the resolution of both upper, Figure 7.18, and lower surface.

Considering the entire analysis reported, the adaptive framework has shown to achieve significant reduction of the problem ($N_m < N_s \ll N_{\text{DOF}}$), while retaining good consistency and accuracy with the physics of unsteady aerodynamics problems. In particular, it has been shown that, using a small subset of the entire set of modes that can in principle be extracted from the original snapshots, the adaptive ROM is capable to provide major improvements with respect to the classical POD method. Indeed the truncation procedure, i.e. the number of modes finally retained, that is the fundamental step to promote dimensionality reduction, is the main responsible in POD for the lack of dynamic information, as the energy ranking might hide the dynamics of some low energy spatial structures. This dynamics can be recovered from the different sets of basis functions within the adaptive framework. Moreover, the residual evaluation reported

in Equation 5.12 has revealed to be a relevant measure to use in order to build the Adaptive ROM, showing enough physical consistency with the actual reconstruction of the flow field reported in the various test-cases.

It is worth noting again that the improvements of the Adaptive Framework with respect to a Single ROM are measured both in terms of how close the contours of the ROM solutions are to the CFD reference solution (local measure), and in terms of residual errors (integral measure). Even if for some instants of time the POD method appears to be good enough in describing some dynamics also locally, the Adaptive Framework always introduces a more detailed description of the flow field. This is believed to be of advantage for problems that require more refined solutions, e.g. flow control and design problems. When integral quantities are of interest instead, e.g. aerodynamic coefficients, no evident differences are expected between the Adaptive and a single ROM method. Finally, another important aspect is the computational time required for the

	T_{datagen} (CH)	$T_{\text{FE-RE}}$ (h)	$T_{\text{ROM-online}}$ (s)	$T_{\text{Res-Eval}}$ (s)	T_{CFD} (h)
Test-Case 1	3,700	2	$\sim 10^{-1}$	~ 20	12.5
Test-Case 2	16,000	24	< 10	~ 800	80
Test-Case 3	10,500	18	< 10	~ 700	50
Test-Case 4	18,000	20	< 10	$\sim 10^3$	60

Table 7.1: Comprehensive time breakdown for the Adaptive Framework in terms of time required for the database generation (T_{datagen}), time required for features extraction and residual database computation ($T_{\text{FE-RE}}$) and time required for the reconstruction of one ROM solution ($T_{\text{ROM-online}}$). The last two columns define the time requirements for the computation of the error database at one single point when a residual error ($T_{\text{Res-Eval}}$) or a direct error (T_{CFD}) are used. The time for the database generation is reported in CH, all the other times are considered on a single core.

online phase, which is able to provide low-dimensional solutions in real-time (less than 1s) and reproduce the high-dimensional solutions in less than 10s for the 3D test-cases. Table 7.1 reports a detailed summary of the computational time requirements needed by the different steps of the Adaptive ROM, namely offline (in the first two columns) and online phase (in the third column). Table 7.1 also reports, in the last two columns, details of the time required to perform one residual evaluation, $T_{\text{Res-Eval}}$, and the time required to compute one CFD physical time iteration, T_{CFD} . These two last quantities

highlight the computational speedup achieved by a residual based Adaptive ROM, as opposed to a direct error based Adaptive ROM, which requires to run an additional CFD time iteration to compute a reference solution. The CFD time requirements reported in the last columns can be improved acting on the numerical setup used for the unsteady simulation (e.g. turbulence models used, courant-friedrich-levy number, unsteady time step), but this is out of the scope of the present work. Nevertheless, it is expected that, also when introducing these improvements, the CFD time will still be at least one order of magnitude higher than the $T_{\text{Res-Eval}}$ when using a Dual-Time Stepping approach.

Chapter 8

Conclusions and Outlook

The implementation of reduced order models for unsteady fluid flows is a very challenging task. One of the main challenges is related to the following crucial aspect

“Defining a ROM framework able to reproduce in a strongly low-dimensional manner the dynamics of transient nonlinear aeronautical flows. The ROM framework should have the capability of preserving the essential dynamics linked to the advection, interaction and diffusion of characteristic vortical structures associated to this kind of flows.”

The strong dimensionality reduction refers to the number of modes finally retained in the ROM, i.e. a small subset of the entire set of modes available ($N_m < N_s \ll N_p$), which has an impact on the final number of DOFs to handle in order to describe the problem. The nonlinearity of the problem is referred in more general terms to the nonlinear nature of the original system of equations solved, i.e. the full set of Navier-Stokes equations. Therefore, the dynamics of the characteristic vortical structures of the flow fields considered is assumed to be nonlinear since it is originating from a system of nonlinear equations. It is finally worth noting that, although diverse sources of unsteadiness can be present in the flow (e.g. moving and/or deforming geometries), which are of equal interest in the fluid dynamics community, the present work focuses on the specific case of unsteady flows originating from fixed geometries. The main feature of this class of flows is the interaction and advection of vortices generated from

the various lifting surfaces.

To address the challenge reported above, three research questions have emerged that led to the following answers/findings.

Research Question 1

- Despite not covering all the possible impulsively started flows, the analyses presented in this work have given an heuristic yet conclusive evidence that there is not a unique best-in-class linear low-dimensional approach that can be used to describe the transient nonlinear dynamics associated to this class of flows. This is even true when explicitly considering specific time correlations among snapshots. Indeed, some of the most prominent and widely studied reduction approaches, based on different rationale for the identification of modes, have shown to identify different features of the essential dynamics over the investigated time window. The reduction techniques considered for the analysis have been specifically selected among the many algorithms introduced in the literature, based on their potential to address problems with certain degree of nonlinearities both in space and in time, while still preserving the linear assumption reported in Equation 2.1. The interest in impulsively started flows is related to the dynamics originating from specific geometries when an impulsive start is considered, i.e. various vortical structures that are advected and eventually interact. Although an impulse is technically something not real, it still represents a good assumption to reproduce dynamics of interest for aerodynamic bodies started from rest.
- The sorting, alias ranking, of dominant features is important from the point of view of the interpretation of the modes themselves with respect to the underlying physics, but it has proven to be also substantially important when looking at the reconstruction of a certain flow field with a very limited number of modes. Two aspects have emerged from the analysis performed on flow features ranking:
 1. For the specific case of POD-based approaches, an energy-based criterion that takes into account temporal correlation among snapshots is able to

recover also the dynamics of less energetic flow structures, improving the description of the overall time dynamics of the flow. In particular, the temporal-driven energy redistribution has proven to be a key point in reproducing the dynamics of both 2D and 3D impulsively started aeronautical geometries. Nevertheless, the energy redistribution has also shown to need more modes in order to reach a fixed energy content, in a measure that depends on the width of the time window to which the temporal correlation is applied. In particular, the more this width the more the modes needed to obtain the desired energy content. Therefore, although the technique shows better performance in reconstructing transient nonlinear dynamics, this also leads to more degrees of freedom in the final model. Even if the analysis has been limited to short periods of time, a similar behaviour is expected on larger time intervals, since the main parameter that influences the reconstruction is the relative size of the time filter applied to the temporal correlation matrix with respect to the size of the time interval where the sampling is performed. Nevertheless, an in-depth analysis on the influence of the initial span of the sampling interval has not been performed in the present work.

2. For the specific case of DMD-based methods, two different criteria have been considered for the modes ranking, namely the singular value truncation and a criterion purely based on time dynamics. For describing the dynamics of transient nonlinear aeronautical flows, a singular value truncation has been adopted, which is the most robust way to express the dynamics in a compact manner, i.e. with very few degrees of freedom, when neither enough/meaningful physical information can be extracted from the DMD algorithm nor they are known a-priori from the flow. For the specific case of transient quasi-linear dynamics, such as the early transition to turbulence in a channel flow, a criterion that is based exclusively on the time dynamics of the modes, i.e. the t -envelope method, has shown instead to be more effective in recovering time dynamics. The higher effectiveness of the novel

method stems from the ability to isolate better a subset of modes that are more dynamically important to describe the time evolution related to the early transition. This has been demonstrated by means of a comparative analysis of the t -envelope ranking criterion and a common energy ranking criterion. The reconstruction of the entire flow field when considering the modes selected through the t -envelope criterion showed improved accuracy with respect to the one obtained with modes selected through the energy ranking criterion.

Research Question 2.

- The residual error has been introduced as a measure to perform a quantitative assessment of how well a reduced solution is reproducing the dynamics underlying the collected snapshots. In particular, a Finite Volume discretisation of the full set of Navier-Stokes equations has been considered, and the residual produced by the reduced solutions when substituted in this discretisation has been defined as the residual measure. The quantitative assessment is, therefore, constrained to reduced solution computed only for conservative variables. Moreover, a fundamental assumption has been made, namely, that the reduced solution's accuracy is directly linked to how well a specific numerical discretisation of the corresponding conservation equation is satisfied. On the basis of this assumption, the residual error has shown to be quite a reliable measure to perform an assessment of different sets of reduced solutions. The conclusion has been supported by a comparative study of the assessment of various linear ROMs on the basis of the residual error and the direct error, that instead compares the reduced solution directly to the corresponding CFD reference solution. Indeed, only minor inconsistencies were reported. It is worth highlighting again that the residual error introduced here does not belong to the wide class of a-priori and a-posteriori error bounds widely studied in the literature to define certified and reliable ROMs. It represents instead an engineering tool to assess the performances of different sets of ROMs.

- The residual error revealed to be a good measure to drive the selection of the reduced solution depending on the time instant, when used within an Adaptive Framework that combines synergistically capabilities of various linear ROMs. Indeed, few applications of the framework to impulsively started aeronautical geometries have shown how the residual error is able to select the reduced solution that resolves most of the essential dynamics at each time instant.
- The trend of the residual error with the number of modes retained within a generic linear ROM has shown to be influenced by the initial mesh resolution. In particular, it has been shown how a non-monotonic trend on a well refined mesh can change to a monotonically decreasing behaviour when the mesh is coarsened. This has been linked to how many spatial features and how well these features are resolved in the snapshots used to train the ROM.

Research Question 3.

- A Model-Based Adaptive ROM has been identified as a means to combine the strengths of diverse existing linear methods in a unique and cohesive reduction framework. The novel framework exploits the capabilities of the residual error as a measure to drive the selection of the best linear method at each time instant desired for reconstruction. Different applications to 2D and 3D aeronautical problems, consisting of impulsively started airfoils and wings, have demonstrated the better performance of the Adaptive Framework with respect to a single ROM in describing all the essential dynamics. Indeed, flow features were overall better resolved both in space and time. The better resolution has been heuristically measured in terms of how close the contours of the field reconstructed by the ROM are to a CFD reference solution. This can be also practically quantified considering the relative reduction in the residual error when switching from a single ROM to the Adaptive Framework.
- The better performance of the Adaptive ROM with respect to a single ROM has been firstly identified in terms of the residual error considered in this work. Specif-

ically, an analysis changing the number of modes has shown how the Model-Based Adaptive ROM is able to introduce major improvements with respect to a single ROM when using only a small number of modes. This has been demonstrated through a series of 2D and 3D impulsively started airfoils and wings. Some reconstructions of the entire flow field for each of these test-cases have been also reported, that confirmed the capability of the Adaptive Framework to preserve dynamics of starting and interacting vortices even when using very few modes, as opposed to a single ROM. The number of modes finally used in the Adaptive Framework reflects the number of degrees of freedom needed to describe with enough accuracy and physical consistency the system dynamics. This last conclusion is therefore quite an important one, as unsteady analyses can be often involved in a design process that strongly benefits from a very low number of degrees of freedom to deal with.

- When the interest is on integral quantities, e.g. aerodynamic coefficients, the improvements of the Adaptive Framework with respect to a single ROM can be negligible. Indeed, it has been shown, especially for surface solutions, how the Adaptive Framework is able to introduce only slight improvements with respect to a single ROM and that POD can provide already satisfying accuracy in describing some dynamics. Nevertheless, when more details are requested, e.g. for problems involving design or problems that need exact localization and reconstruction of specific flow features (e.g. for flow control purposes), the Adaptive ROM introduced can make a difference when compared to a single ROM.
- The novel ROM framework introduced is not able to make predictions, i.e. the reconstruction of the flow field is limited within the interval where the sampling is performed. Although it has been applied only to a series of impulsively started geometries, the Adaptive Framework can be used for any kind of unsteady problem and for data originating from CFD solvers, where there is no change in mesh topology. This last aspect must be treated with more attention in terms of how the various set of basis functions are extracted when the collected snapshots are

computed on different meshes.

Contribution to knowledge. The list of contributions to the field of ROMs for unsteady flows reported in Section 1.2 is expanded here in terms of how these contributions were introduced:

- An analysis was performed on two specific test-cases, namely the impulsive start of a NACA0012 airfoil and a multi-element airfoil, in terms of accuracy in the reconstruction of few time instants considering different linear ROM methods;
- Two analyses were performed for the specific case of POD and DMD, investigating the influence of the ordering of the set of flow features extracted on the accuracy of the ROM reconstruction. In particular, the effects of the application of a filter to the POD temporal correlation matrix was investigated when describing transient nonlinear dynamics in time, and a novel criterion for DMD was tested, namely the t -envelope method, to select few meaningful modes capable of describing the early phase of transition to turbulence in a channel flow;
- An analysis was carried out on two specific test-cases, namely the impulsive start of a NACA0012 airfoil and a multi-element airfoil, in order to compare the performance of the residual error in the assessment of different linear ROMs with respect to a more robust definition of the error, namely the direct error, which uses reference solutions to be computed;
- The Model-Based Adaptive Framework was applied to a series of test-cases, consisting of impulsively started geometries that exhibit complex dynamics in time in terms of many interacting and advecting vortical structures. Details of the residual error based selection were provided and comparisons were made in terms of capabilities of the Adaptive Framework in reconstructing few CFD high-dimensional solutions in time.

Perspectives

The definition of the Model-Based Adaptive Framework paves the way to many other further investigations and developments that are out of the scope of the present work and are summarized in the following.

- **Ensuring continuity in time**

It would be worth performing a dedicated analysis on what happens in specific time windows, where the Model-Based Adaptive framework switches from one method to the other. In particular, investigate on smoothness and regularity of solutions when transitioning from one low-dimensional space to the other and if this regularity is an aspect actually required from a “practical” viewpoint (i.e. does it compromise the description and/or the understanding of the underlying time dynamics?).

- **Adaptivity in space**

The Model-Based Adaptive ROM has been implemented considering time as the only parameter for the adaptation. Since solutions coming from Navier-Stokes equations express dynamics happening on several temporal and spatial scales, a further development of the adaptive strategy would be introducing space variables as additional parameters for the adaptation. Therefore, instead of extracting few sets of global spatial basis functions, each one to use in specific sub-windows of time, the set of basis extracted would be also confined within particular sub-domains, on the basis of the spatial features and spatial scales they are able to solve. This would need to define a proper strategy for the decomposition of the original domain in sub-regions where to assign local basis functions, and constraints that ensure continuity in space, when the solution needs to be projected back to the high-dimensional space and the various sub-regions reassembled together.

- **Use the Model-Based Adaptive ROM for a non-conserved physical quantity**

The way the error measure is defined in the Model-Based Adaptive Framework needs the application of the method on the entire set of conservative variables. A relevant aspect to investigate would be how to adaptively select the ROMs when the quantity desired for reconstruction is not a conserved quantity (e.g. Pressure, Shear stress, etc.). There are two approaches that can be considered in this sense. The first is a conservative one and looks at building the reduced solutions for the conserved quantities first and then post-process them to obtain the primitive variables required. This is the same procedure followed when computing a Finite Volume solution for the conserved quantities, and then, for example, compute the pressure using the equations of state of the gas. While being conceptually straightforward, this approach might not be the most computationally efficient since, if Pressure is the only quantity required, the method would still need to compute four or five (depending on the spatial dimensions) reduced solutions. The second alternative approach would be to rely on the definition of appropriate relations connecting the residuals of the conserved quantities, as defined by Equation 5.12, to the residuals of the primitive quantities and use directly the latter to drive the selection within the Adaptive Framework. This would mean to define a Model-Based Adaptive ROM that processes directly the variable of interest, without having to pass through the computation of reduced solutions for the entire set of conservative variables.

- **Snapshots sampling procedure**

The present work has always used a uniform sampling of snapshots in time to train the low-dimensional model. Nevertheless, it has already been discussed how important can a specific sampling procedure be to elaborate more accurate and reliable ROMs (see also Chapter 1). Especially when time dynamics is strongly nonlinear and exhibits transient behaviour, a uniform sampling might not be the

best choice, as opposed to a non uniform sampling that accounts for nonlinearities in time. This aspect represents another important area of investigation for further improving the Model-Based Adaptive ROM. A first step in this direction could be to adaptively select the snapshots in time through an optimization algorithm that has as objective function an integral residual error to minimize, like the one introduced in Equation 6.1.

- **Extension to unsteady parametric problems**

The Model-Based Adaptive ROM has been implemented and tested for the specific case of unsteady fluid flows. The algorithms considered within the Adaptive Framework, excluding POD, are mainly conceived for unsteady problems, i.e. they use assumptions related to specific time dynamics represented by the collected snapshots to extract modes. Indeed, DMD assumes a linear dynamic in time to unveil time dynamics information carried by the snapshots. SPOD uses a filter applied to the POD temporal correlation matrix as a means to extract spatio-temporal flow features, i.e. modes that are related to spatial structures existing in specific time windows. RDMD, as a method derived from DMD, still retains its unsteady nature at the extraction level. A further development of the Adaptive ROM would therefore be to try extending its application also for unsteady problems with variable parameters. A first step in this direction could be a combined POD-Adaptive approach, where a first reduction is taken in the parameter space using POD. Then, an Adaptive framework is built for the time variable over the low-dimensional parameter space identified by POD. Specifically, the POD algorithm is applied at each time instant to find a low-dimensional linear embedding in the parameter space. The coefficients extracted at each time instant are then arranged in a matrix similar to the snapshots matrix \mathbf{U} (see Chapter 3) and an Adaptive Framework is built on it. A previous interpolation needs to be computed, if the set of parameters for which an Adaptive ROM has to be built is out of the training points.

Bibliography

- [1] David J Lucia, Philip S Beran, and Walter A Silva. Reduced-order modeling: new approaches for computational physics. *Progress in aerospace sciences*, 40 (1-2):51–117, 2004.
- [2] Athanasios C Antoulas. *Approximation of large-scale dynamical systems*. SIAM, 2005.
- [3] Alfio Quarteroni, Gianluigi Rozza, et al. *Reduced order methods for modeling and computational reduction*, volume 9. Springer, 2014.
- [4] Peng Li and Lawrence T Pileggi. Compact reduced-order modeling of weakly nonlinear analog and rf circuits. *IEEE Transactions on computer-aided design of integrated circuits and systems*, 24(2):184–203, 2005.
- [5] Roland W Freund. Krylov-subspace methods for reduced-order modeling in circuit simulation. *Journal of Computational and Applied Mathematics*, 123(1-2):395–421, 2000.
- [6] Patricia Astrid and Arie Verhoeven. Application of least squares mpe technique in the reduced order modeling of electrical circuits. In *Proceedings of the 17th Int. Symp. MTNS*, pages 1980–1986, 2006.
- [7] Yanchun Liang, Heow P Lee, Siakpiang Lim, Wuzhong Lin, Kwokhong Lee, and Chunguo Wu. Proper Orthogonal Decomposition and its applications—part i: Theory. *Journal of Sound and vibration*, 252(3):527–544, 2002.

Bibliography

- [8] Evgenii B Rudnyi and Jan G Korvink. Model order reduction of mems for efficient computer aided design and system simulation. In *Proc. International Symp. Mathematical Theory of Networks and Systems*, 2004.
- [9] Ali H Nayfeh, Mohammad I Younis, and Eihab M Abdel-Rahman. Reduced-order models for mems applications. *Nonlinear dynamics*, 41(1-3):211–236, 2005.
- [10] Siamak Niroomandi, Icíar Alfaro, David González, Elías Cueto, and Francisco Chinesta. Model order reduction in hyperelasticity: a proper generalized decomposition approach. *International Journal for Numerical Methods in Engineering*, 96(3):129–149, 2013.
- [11] Jin-Gyun Kim, Young-Jun Park, Geun Ho Lee, and Do-Nyun Kim. A general model reduction with primal assembly in structural dynamics. *Computer Methods in Applied Mechanics and Engineering*, 324:1–28, 2017.
- [12] Hector A Jensen, A Muñoz, Costas Papadimitriou, and E Millas. Model-reduction techniques for reliability-based design problems of complex structural systems. *Reliability Engineering & System Safety*, 149:204–217, 2016.
- [13] Chenlei Guo and Liming Zhang. A novel multiresolution spatiotemporal saliency detection model and its applications in image and video compression. *IEEE transactions on image processing*, 19(1):185–198, 2009.
- [14] Thierry Bouwmans, Sajid Javed, Hongyang Zhang, Zhouchen Lin, and Ricardo Otazo. On the applications of robust pca in image and video processing. *Proceedings of the IEEE*, 106(8):1427–1457, 2018.
- [15] Walter A Silva and Robert E Bartels. Development of reduced-order models for aeroelastic analysis and flutter prediction using the cfl3dv6. 0 code. *Journal of Fluids and Structures*, 19(6):729–745, 2004.
- [16] Thuan Lieu and Charbel Farhat. Adaptation of aeroelastic reduced-order models and application to an f-16 configuration. *AIAA journal*, 45(6):1244–1257, 2007.

Bibliography

- [17] Andrea Da Ronch, Ken Badcock, Y Wang, Andrew Wynn, and Rafael Palacios. Nonlinear model reduction for flexible aircraft control design. In *AIAA Atmospheric Flight Mechanics Conference*, page 4404, 2012.
- [18] Henrik Hesse and Rafael Palacios. Reduced-order aeroelastic models for dynamics of maneuvering flexible aircraft. *AIAA journal*, 52(8):1717–1732, 2014.
- [19] Juliano A Paulino, Andrea Da Ronch, Antonio B Guimarães Neto, Flavio J Silvestre, and Mauricio AV Morales. On real-time simulation of flexible aircraft with physics-derived models.
- [20] Clarence W Rowley and Scott TM Dawson. Model reduction for flow analysis and control. *Annual Review of Fluid Mechanics*, 49:387–417, 2017.
- [21] Kunihiro Taira, Steven L Brunton, Scott TM Dawson, Clarence W Rowley, Tim Colonius, Beverley J McKeon, Oliver T Schmidt, Stanislav Gordeyev, Vassilios Theofilis, and Lawrence S Ukeiley. Modal analysis of fluid flows: An overview. *AIAA Journal*, 55(12):4013–4041, 2017.
- [22] Kunihiro Taira, Maziar S Hemati, Steven L Brunton, Yiyang Sun, Karthik Duraisamy, Shervin Bagheri, Scott TM Dawson, and Chi-An Yeh. Modal analysis of fluid flows: Applications and outlook. *AIAA journal*, 58(3):998–1022, 2020.
- [23] Philip Holmes, John L Lumley, Gahl Berkooz, and Clarence W Rowley. *Turbulence, coherent structures, dynamical systems and symmetry*. Cambridge university press, 2012.
- [24] Patrick LeGresley and Juan Alonso. Airfoil design optimization using reduced order models based on Proper Orthogonal Decomposition. In *Fluids 2000 conference and exhibit*, page 2545, 2000.
- [25] Matteo Ripepi, Mark J Verveld, Niklas W Karcher, Thomas Franz, Mohammad Abu-Zurayk, Stefan Görtz, and Thiemo M Kier. Reduced-order models for aerodynamic applications, loads and mdo. *CEAS Aeronautical Journal*, 9(1):171–193, 2018.

Bibliography

- [26] Marco Tezzele, Nicola Demo, Mahmoud Gadalla, Andrea Mola, and Gianluigi Rozza. Model order reduction by means of active subspaces and Dynamic Mode Decomposition for parametric hull shape design hydrodynamics. *arXiv preprint arXiv:1803.07377*, 2018.
- [27] Angela Scardigli, Rocco Arpa, Alessandro Chiarini, and Haysam Telib. Enabling of large scale aerodynamic shape optimization through pod-based reduced-order modeling and free form deformation. In *Advances in Evolutionary and Deterministic Methods for Design, Optimization and Control in Engineering and Sciences*, pages 49–63. Springer, 2019.
- [28] Fazle AKM Hussain. Coherent structures and turbulence. *Journal of Fluid Mechanics*, 173:303–356, 1986.
- [29] Anatol Roshko. Structure of turbulent shear flows—a new look. In *14th Aerospace Sciences Meeting*, page 78, 1976.
- [30] Heinrich E Fiedler. Coherent structures in turbulent flows. *Progress in Aerospace Sciences*, 25(3):231–269, 1988.
- [31] John Leask Lumley. The structure of inhomogeneous turbulence. *Atmospheric turbulence and radio wave propagation*, pages 66–178, 1967.
- [32] George Haller. Lagrangian coherent structures. *Annual Review of Fluid Mechanics*, 47:137–162, 2015.
- [33] Clarence W Rowley. Model reduction for fluids, using balanced Proper Orthogonal Decomposition. *International Journal of Bifurcation and Chaos*, 15(03):997–1013, 2005.
- [34] Andrew Wynn, David S Pearson, Bharathram Ganapathisubramani, and Paul J Goulart. Optimal Mode Decomposition for unsteady flows. *Journal of Fluid Mechanics*, 733:473–503, 2013.
- [35] Mihailo R Jovanović, Peter J Schmid, and Joseph W Nichols. Sparsity-promoting Dynamic Mode Decomposition. *Physics of Fluids*, 26(2):024103, 2014.

Bibliography

- [36] Moritz Sieber, C Oliver Paschereit, and Kilian Oberleithner. Spectral Proper Orthogonal Decomposition. *Journal of Fluid Mechanics*, 792:798–828, 2016.
- [37] Miguel A Mendez, Mikhael Balabane, and Jean-Marie Buchlin. Multi-scale proper orthogonal decomposition of complex fluid flows. *arXiv preprint arXiv:1804.09646*, 2018.
- [38] Sivaguru S Ravindran. A reduced-order approach for optimal control of fluids using proper orthogonal decomposition. *International journal for numerical methods in fluids*, 34(5):425–448, 2000.
- [39] Oliver Lehmann, Mark Luchtenburg, Bernd R Noack, Rudibert King, Marek Morzynski, and Gilead Tadmor. Wake stabilization using pod galerkin models with interpolated modes. In *Proceedings of the 44th IEEE Conference on Decision and Control*, pages 500–505. IEEE, 2005.
- [40] Dirk M Luchtenburg, Katarina Aleksić, Michael Schlegel, Bernd R Noack, Rudibert King, Gilead Tadmor, Bert Günther, and Frank Thiele. Turbulence control based on reduced-order models and nonlinear control design. In *Active Flow Control II*, pages 341–356. Springer, 2010.
- [41] Bernd R Noack, Marek Morzynski, and Gilead Tadmor. *Reduced-order modelling for flow control*, volume 528. Springer Science & Business Media, 2011.
- [42] Arvind T Mohan and Datta V Gaitonde. A deep learning based approach to reduced order modeling for turbulent flow control using lstm neural networks. *arXiv preprint arXiv:1804.09269*, 2018.
- [43] Shervin Bagheri. Koopman-mode decomposition of the cylinder wake. *Journal of Fluid Mechanics*, 726:596–623, 2013.
- [44] Bernd R Noack, Witold Stankiewicz, Marek Morzyński, and Peter J Schmid. Recursive Dynamic Mode Decomposition of transient and post-transient wake flows. *Journal of Fluid Mechanics*, 809:843–872, 2016.

Bibliography

- [45] Jacob Page and Rich R Kerswell. Koopman mode expansions between simple invariant solutions. *Journal of Fluid Mechanics*, 879:1–27, 2019.
- [46] Peter J Schmid. Dynamic Mode Decomposition of numerical and experimental data. *Journal of Fluid Mechanics*, 656:5–28, 2010.
- [47] Peter J Schmid, Larry Li, Matthew P Juniper, and O Pust. Applications of the Dynamic Mode Decomposition. *Theoretical and Computational Fluid Dynamics*, 25(1-4):249–259, 2011.
- [48] Clarence W Rowley, Tim Colonius, and Richard M Murray. Model reduction for compressible flows using POD and Galerkin projection. *Physica D: Nonlinear Phenomena*, 189(1-2):115–129, 2004.
- [49] Matthew O Williams, Ioannis G Kevrekidis, and Clarence W Rowley. A data-driven approximation of the koopman operator: Extending Dynamic Mode Decomposition. *Journal of Nonlinear Science*, 25(6):1307–1346, 2015.
- [50] Benjamin Peherstorfer. Model reduction for transport-dominated problems via online adaptive bases and adaptive sampling. *arXiv preprint arXiv:1812.02094*, 2018.
- [51] Angelo Iollo and Damiano Lombardi. Advection modes by optimal mass transfer. *Physical Review E*, 89(2):022923, 2014.
- [52] Jörn Sesterhenn and Amir Shahripour. A lagrangian dynamic mode decomposition. *arXiv preprint arXiv:1603.02539*, 2016.
- [53] Rambod Mojjani and Maciej Balajewicz. Lagrangian basis method for dimensionality reduction of convection dominated nonlinear flows. *arXiv preprint arXiv:1701.04343*, 2017.
- [54] Karl Kunisch and Stefan Volkwein. Galerkin proper orthogonal decomposition methods for a general equation in fluid dynamics. *SIAM Journal on Numerical analysis*, 40(2):492–515, 2002.

Bibliography

- [55] Dirk M Luchtenburg, Bernd R Noack, and Michael Schlegel. An introduction to the pod galerkin method for fluid flows with analytical examples and matlab source codes. *Berlin Institute of Technology MB1, Muller-Breslau-Strabe*, 11, 2009.
- [56] Stefano Lorenzi, Antonio Cammi, Lelio Luzzi, and Gianluigi Rozza. Pod-galerkin method for finite volume approximation of navier–stokes and rans equations. *Computer Methods in Applied Mechanics and Engineering*, 311:151–179, 2016.
- [57] Kevin Carlberg, Charbel Bou-Mosleh, and Charbel Farhat. Efficient non-linear model reduction via a least-squares petrov–galerkin projection and compressive tensor approximations. *International Journal for numerical methods in engineering*, 86(2):155–181, 2011.
- [58] Irina Kalashnikova and Matthew Barone. Stable and efficient galerkin reduced order models for non-linear fluid flow. In *6th AIAA Theoretical Fluid Mechanics Conference*, page 3110, 2011.
- [59] Matthew F Barone, Irina Kalashnikova, Daniel J Segalman, and Heidi K Thornquist. Stable galerkin reduced order models for linearized compressible flow. *Journal of Computational Physics*, 228(6):1932–1946, 2009.
- [60] Francesco Ballarin, Andrea Manzoni, Alfio Quarteroni, and Gianluigi Rozza. Supremizer stabilization of pod–galerkin approximation of parametrized steady incompressible navier–stokes equations. *International Journal for Numerical Methods in Engineering*, 102(5):1136–1161, 2015.
- [61] Angelo Iollo, Stéphane Lanteri, and J-A Désidéri. Stability properties of pod–galerkin approximations for the compressible navier–stokes equations. *Theoretical and Computational Fluid Dynamics*, 13(6):377–396, 2000.
- [62] Mathieu Couplet, Claude Basdevant, and Pierre Sagaut. Calibrated reduced-order pod-galerkin system for fluid flow modelling. *Journal of Computational Physics*, 207(1):192–220, 2005.

Bibliography

- [63] Geoffrey M Oxberry, Tanya Kostova-Vassilevska, William Arrighi, and Kyle Chand. Limited-memory adaptive snapshot selection for proper orthogonal decomposition. *International Journal for Numerical Methods in Engineering*, 109(2):198–217, 2017.
- [64] Sugata Sen, Karen Veroy, Dinh Bao Phuong Huynh, Simone Deparis, Ngoc Cuong Nguyen, and Anthony T Patera. “natural norm” a posteriori error estimators for reduced basis approximations. *Journal of Computational Physics*, 217(1):37–62, 2006.
- [65] Gianluigi Rozza, Dinh Bao Phuong Huynh, and Anthony T Patera. Reduced basis approximation and a posteriori error estimation for affinely parametrized elliptic coercive partial differential equations. *Archives of Computational Methods in Engineering*, 15(3):1, 2007.
- [66] Karen Veroy, Christophe Prud’Homme, Dimitrios Rovas, and Anthony Patera. A posteriori error bounds for reduced-basis approximation of parametrized non-coercive and nonlinear elliptic partial differential equations. In *16th AIAA Computational Fluid Dynamics Conference*, page 3847, 2003.
- [67] Martin A Grepl and Anthony T Patera. A posteriori error bounds for reduced-basis approximations of parametrized parabolic partial differential equations. *ESAIM: Mathematical Modelling and Numerical Analysis*, 39(1):157–181, 2005.
- [68] Karsten Urban and Anthony T Patera. A new error bound for reduced basis approximation of parabolic partial differential equations. *Comptes Rendus Mathématique*, 350(3-4):203–207, 2012.
- [69] Gaetano Pascarella, Marco Fossati, and Gabriel Barrenechea. Adaptive reduced basis method for the reconstruction of unsteady vortex-dominated flows. *Computers & Fluids*, 190:382–397, 2019.
- [70] Gaetano Pascarella, Marco Fossati, and Gabriel Barrenechea. Model-based adaptive reduced basis methods for unsteady aerodynamics studies. In *AIAA Aviation 2019 Forum*, page 3332, 2019.

Bibliography

- [71] Bernd R Noack. From snapshots to modal expansions—bridging low residuals and pure frequencies. *Journal of Fluid Mechanics*, 802:1–4, 2016.
- [72] Toni Lassila, Andrea Manzoni, Alfio Quarteroni, and Gianluigi Rozza. Model order reduction in fluid dynamics: challenges and perspectives. In *Reduced Order Methods for modeling and computational reduction*, pages 235–273. Springer, 2014.
- [73] Benjamin Unger and Serkan Gugercin. Kolmogorov n-widths for linear dynamical systems. *Advances in Computational Mathematics*, 45(5-6):2273–2286, 2019.
- [74] Gavin Brown, Dai Feng, and Sun Yong Sheng. Kolmogorov width of classes of smooth functions on the sphere sd- 1. *Journal of Complexity*, 18(4):1001–1023, 2002.
- [75] Patrick L Combettes and Dinh Dũng. Kolmogorov n-widths of function classes induced by a non-degenerate differential operator: A convex duality approach. *Set-Valued and Variational Analysis*, 24(1):83–99, 2016.
- [76] Toni Lassila, Andrea Manzoni, Alfio Quarteroni, and Gianluigi Rozza. Generalized reduced basis methods and n-width estimates for the approximation of the solution manifold of parametric pdes. In *Analysis and numerics of partial differential equations*, pages 307–329. Springer, 2013.
- [77] Markus Bachmayr and Albert Cohen. Kolmogorov widths and low-rank approximations of parametric elliptic pdes. *Mathematics of Computation*, 86(304):701–724, 2017.
- [78] Peter Benner, Serkan Gugercin, and Karen Willcox. A survey of projection-based model reduction methods for parametric dynamical systems. *SIAM review*, 57(4):483–531, 2015.
- [79] Matthew O Williams, Peter J Schmid, and J Nathan Kutz. Hybrid reduced-order integration with proper orthogonal decomposition and dynamic mode decomposition. *Multiscale Modeling & Simulation*, 11(2):522–544, 2013.

Bibliography

- [80] Xuping Xie, Muhammad Mohebujjaman, Leo G Rebholz, and Traian Iliescu. Data-driven filtered reduced order modeling of fluid flows. *SIAM Journal on Scientific Computing*, 40(3):B834–B857, 2018.
- [81] Sk Rahman, Omer San, Adil Rasheed, et al. A hybrid approach for model order reduction of barotropic quasi-geostrophic turbulence. *Fluids*, 3(4):86, 2018.
- [82] M Mohebujjaman, LG Rebholz, and T Iliescu. Physically-constrained data-driven, filtered reduced order modeling of fluid flows. *arXiv preprint arXiv:1806.00350*, 2018.
- [83] Gal Berkooz, Philip Holmes, and John L Lumley. The proper orthogonal decomposition in the analysis of turbulent flows. *Annual review of fluid mechanics*, 25(1):539–575, 1993.
- [84] Giovanni Stabile, Saddam Hijazi, Andrea Mola, Stefano Lorenzi, and Gianluigi Rozza. POD-Galerkin reduced order methods for CFD using finite volume discretisation: vortex shedding around a circular cylinder. *Communications in Applied and Industrial Mathematics*, 8(1):210–236, 2017.
- [85] Giovanni Stabile and Gianluigi Rozza. Finite volume POD-Galerkin stabilised reduced order methods for the parameterised incompressible navier–stokes equations. *Computers & Fluids*, 173:273–284, 2018.
- [86] Michel Bergmann, C-H Bruneau, and Angelo Iollo. Enablers for robust pod models. *Journal of Computational Physics*, 228(2):516–538, 2009.
- [87] J Nathan Kutz, Steven L Brunton, Bingni W Brunton, and Joshua L Proctor. *Dynamic Mode Decomposition: data-driven modeling of complex systems*, volume 149. SIAM, 2016.
- [88] Bruce Moore. Principal component analysis in linear systems: Controllability, observability, and model reduction. *IEEE transactions on automatic control*, 26(1):17–32, 1981.

Bibliography

- [89] Miloš Ilak and Clarence W Rowley. Modeling of transitional channel flow using balanced proper orthogonal decomposition. *Physics of Fluids*, 20(3):034103, 2008.
- [90] Moritz Sieber, C Oliver Paschereit, and Kilian Oberleithner. On the nature of spectral Proper Orthogonal Decomposition and related modal Decompositions. *arXiv preprint arXiv:1712.08054*, 2017.
- [91] Aaron Towne, Oliver T Schmidt, and Tim Colonius. Spectral proper orthogonal decomposition and its relationship to dynamic mode decomposition and resolvent analysis. *arXiv preprint arXiv:1708.04393*, 2017.
- [92] Miguel A Mendez, David Hess, Bo B Watz, and Jean-Marie Buchlin. Multiscale proper orthogonal decomposition (mpod) of tr-piv data—a case study on stationary and transient cylinder wake flows. *Measurement Science and Technology*, 31(9):094014, 2020.
- [93] Jonathan H Tu, Clarence W Rowley, Dirk M Luchtenburg, Steven L Brunton, and J Nathan Kutz. On Dynamic Mode Decomposition: theory and applications. *arXiv preprint arXiv:1312.0041*, 2013.
- [94] Clarence W Rowley, Igor Mezić, Shervin Bagheri, Philipp Schlatter, and Dan S Henningson. Spectral analysis of nonlinear flows. *Journal of Fluid Mechanics*, 641:115–127, 2009.
- [95] Igor Mezić. Analysis of fluid flows via spectral properties of the Koopman operator. *Annual Review of Fluid Mechanics*, 45:357–378, 2013.
- [96] Scott TM Dawson, Maziar S Hemati, Matthew O Williams, and Clarence W Rowley. Characterizing and correcting for the effect of sensor noise in the Dynamic Mode Decomposition. *Experiments in Fluids*, 57(3):42, 2016.
- [97] J Nathan Kutz, Xing Fu, and Steven L Brunton. Multiresolution Dynamic Mode Decomposition. *SIAM Journal on Applied Dynamical Systems*, 15(2):713–735, 2016.

Bibliography

- [98] Soledad Le Clainche and José M Vega. Higher order Dynamic Mode Decomposition. *SIAM Journal on Applied Dynamical Systems*, 16(2):882–925, 2017.
- [99] Wu Mengmeng, Han Zhonghua, Nie Han, Song Wenping, Soledad Le Clainche, and Esteban Ferrer. A transition prediction method for flow over airfoils based on high-order dynamic mode decomposition. *Chinese Journal of Aeronautics*, 32(11):2408–2421, 2019.
- [100] Soledad Le Clainche, Zhong-Hua Han, and Esteban Ferrer. An alternative method to study cross-flow instabilities based on high order dynamic mode decomposition. *Physics of Fluids*, 31(9):094101, 2019.
- [101] Francisco J Gonzalez and Maciej Balajewicz. Deep convolutional recurrent autoencoders for learning low-dimensional feature dynamics of fluid systems. *arXiv preprint arXiv:1808.01346*, 2018.
- [102] Steven L Brunton, Bernd R Noack, and Petros Koumoutsakos. Machine learning for fluid mechanics. *Annual Review of Fluid Mechanics*, 52:477–508, 2020.
- [103] Samuel E Otto and Clarence W Rowley. Linearly recurrent autoencoder networks for learning dynamics. *SIAM Journal on Applied Dynamical Systems*, 18(1):558–593, 2019.
- [104] Benjamin E Souda, Amit Singer, C William Gear, and Ioannis G Kevrekidis. Manifold learning techniques and model reduction applied to dissipative pdes. *arXiv preprint arXiv:1011.5197*, 2010.
- [105] Dalton Lungu, Saurabh Prasad, Melba M Crawford, and Okan Ersoy. Manifold-learning-based feature extraction for classification of hyperspectral data: A review of advances in manifold learning. *IEEE Signal Processing Magazine*, 31(1):55–66, 2013.
- [106] Cosimo Solidoro, Vinko Bandelj, Pierluigi Barbieri, Gianpiero Cossarini, and Serena Fonda Umani. Understanding dynamic of biogeochemical properties in

Bibliography

- the northern adriatic sea by using self-organizing maps and k-means clustering. *Journal of Geophysical Research: Oceans*, 112(C7), 2007.
- [107] Thomas Franz, Ralf Zimmermann, Stefan Görtz, and Niklas Karcher. Interpolation-based reduced-order modelling for steady transonic flows via manifold learning. *International Journal of Computational Fluid Dynamics*, 28(3-4): 106–121, 2014.
- [108] Sam T Roweis and Lawrence K Saul. Nonlinear dimensionality reduction by locally linear embedding. *science*, 290(5500):2323–2326, 2000.
- [109] Arthur Ehlert, Christian N Nayeri, Marek Morzynski, and Bernd R Noack. Locally linear embedding for transient cylinder wakes. *arXiv preprint arXiv:1906.07822*, 2019.
- [110] John A Lee and Michel Verleysen. *Nonlinear dimensionality reduction*. Springer Science & Business Media, 2007.
- [111] Susan S Schiffman, M Lance Reynolds, and Forrest W Young. *Introduction to multidimensional scaling*. Academic press New York, 1981.
- [112] J Nathan Kutz. Deep learning in fluid dynamics. *Journal of Fluid Mechanics*, 814:1–4, 2017.
- [113] Yoshua Bengio, Aaron Courville, and Pascal Vincent. Representation learning: A review and new perspectives. *IEEE transactions on pattern analysis and machine intelligence*, 35(8):1798–1828, 2013.
- [114] David J Lucia and Philip S Beran. Projection methods for reduced order models of compressible flows. *Journal of Computational Physics*, 188(1):252–280, 2003.
- [115] Stefan Volkwein. Model reduction using proper orthogonal decomposition. *Lecture Notes, Institute of Mathematics and Scientific Computing, University of Graz*. see <http://www.uni-graz.at/imawww/volkwein/POD.pdf>, 1025, 2011.

Bibliography

- [116] Alfio Quarteroni, Andrea Manzoni, and Federico Negri. *Reduced basis methods for partial differential equations: an introduction*, volume 92. Springer, 2015.
- [117] Youngsoo Choi and Kevin Carlberg. Space–time least-squares petrov–galerkin projection for nonlinear model reduction. *SIAM Journal on Scientific Computing*, 41(1):A26–A58, 2019.
- [118] Willem Cazemier, Roel WCP Verstappen, and Arthur EP Veldman. Proper Orthogonal Decomposition and low-dimensional models for driven cavity flows. *Physics of Fluids*, 10(7):1685–1699, 1998.
- [119] Alfonso Caiazzo, Traian Iliescu, Volker John, and Svetlana Schyschlowa. A numerical investigation of velocity–pressure reduced order models for incompressible flows. *Journal of Computational Physics*, 259:598–616, 2014.
- [120] Riccardo Rubini, Davide Lasagna, and Andrea Da Ronch. 11-based calibration of pod-galerkin models of two-dimensional unsteady flows. *Chinese Journal of Aeronautics*, 34(1):226–236, 2021.
- [121] Saifon Chaturantabut and Danny C Sorensen. Nonlinear model reduction via discrete empirical interpolation. *SIAM Journal on Scientific Computing*, 32(5): 2737–2764, 2010.
- [122] Irina Tezaur, Jeffrey Fike, Kevin Carlberg, Matthew Barone, Danielle Maddix, Erin Mussoni, and Maciej Balajewicz. Advanced fluid reduced order models for compressible flow. Technical report, Sandia National Lab.(SNL-NM), Albuquerque, NM (United States), 2017.
- [123] David Amsallem, Charbel Farhat, and Matthew Zahr. On the robustness of residual minimization for constructing pod-based reduced-order cfd models. In *Proceedings of the 43rd AIAA fluid dynamics conference and exhibit, San Diego, CA*, 2013.
- [124] Steven L Brunton, Joshua L Proctor, and J Nathan Kutz. Discovering govern-

Bibliography

- ing equations from data by sparse identification of nonlinear dynamical systems. *Proceedings of the national academy of sciences*, 113(15):3932–3937, 2016.
- [125] Jean-Christophe Loiseau, Steven L Brunton, and Bernd R Noack. From the pod-galerkin method to sparse manifold models. *Handbook of Model-Order Reduction*, 2:1–47, 2019.
- [126] Niall M Mangan, Steven L Brunton, Joshua L Proctor, and J Nathan Kutz. Inferring biological networks by sparse identification of nonlinear dynamics. *IEEE Transactions on Molecular, Biological and Multi-Scale Communications*, 2(1):52–63, 2016.
- [127] Manyu Xiao, Piotr Breitkopf, Rajan Filomeno Coelho, Catherine Knopf-Lenoir, Maryan Sidorkiewicz, and Pierre Villon. Model reduction by cpod and kriging. *Structural and multidisciplinary optimization*, 41(4):555–574, 2010.
- [128] David JJ Toal. *Proper orthogonal decomposition & kriging strategies for design*. PhD thesis, University of Southampton, 2009.
- [129] Marco Fossati and Wagdi G Habashi. Multiparameter analysis of aero-icing problems using proper orthogonal decomposition and multidimensional interpolation. *AIAA journal*, 51(4):946–960, 2013.
- [130] Vladimir Buljak. Proper orthogonal decomposition and radial basis functions for fast simulations. In *Inverse Analyses with Model Reduction*, pages 85–139. Springer, 2012.
- [131] Sean Walton, Oubay Hassan, and Ken Morgan. Reduced order modelling for unsteady fluid flow using proper orthogonal decomposition and radial basis functions. *Applied Mathematical Modelling*, 37(20-21):8930–8945, 2013.
- [132] Dunhui Xiao, Fangxin Fang, Christopher Pain, and Guangdao Hu. Non-intrusive reduced-order modelling of the navier–stokes equations based on rbf interpolation. *International Journal for Numerical Methods in Fluids*, 79(11):580–595, 2015.

Bibliography

- [133] Christopher KI Williams and Carl Edward Rasmussen. *Gaussian processes for machine learning*, volume 2. MIT press Cambridge, MA, 2006.
- [134] Mengwu Guo and Jan S Hesthaven. Data-driven reduced order modeling for time-dependent problems. *Computer methods in applied mechanics and engineering*, 345:75–99, 2019.
- [135] Ada Cammilleri, Florimond Guéniat, Johan Carlier, Luc Pastur, Etienne Mémin, François Lusseyran, and Guillermo Artana. Pod-spectral decomposition for fluid flow analysis and model reduction. *Theoretical and Computational Fluid Dynamics*, 27(6):787–815, 2013.
- [136] Vassilios Theofilis. Global linear instability. *Annual Review of Fluid Mechanics*, 43:319–352, 2011.
- [137] Qiong Liu, Francisco Gómez, and Vassilios Theofilis. Linear instability analysis of low-*re* incompressible flow over a long rectangular finite-span open cavity. *Journal of Fluid Mechanics*, 799, 2016.
- [138] We He, Rafael dos Santos Gioria, José Miguel Pérez, and Vassilis Theofilis. Linear instability of low reynolds number massively separated flow around three naca airfoils. *Journal of Fluid Mechanics*, 811:701, 2017.
- [139] Jinah Jeun, Joseph W Nichols, and Mihailo R Jovanović. Input-output analysis of high-speed axisymmetric isothermal jet noise. *Physics of Fluids*, 28(4):047101, 2016.
- [140] Ati S Sharma, Rashad Moarref, Beverley J McKeon, Jae Sung Park, Michael D Graham, and Ashley P Willis. Low-dimensional representations of exact coherent states of the navier-stokes equations from the resolvent model of wall turbulence. *Physical Review E*, 93(2):021102, 2016.
- [141] Bernard O Koopman. Hamiltonian systems and transformation in hilbert space. *Proceedings of the national academy of sciences of the united states of america*, 17(5):315, 1931.

Bibliography

- [142] Igor Mezić. Spectral properties of dynamical systems, model reduction and decompositions. *Nonlinear Dynamics*, 41(1):309–325, 2005.
- [143] Marko Budišić, Ryan Mohr, and Igor Mezić. Applied koopmanism. *Chaos: An Interdisciplinary Journal of Nonlinear Science*, 22(4):047510, 2012.
- [144] Zheng Wang, Dunhui Xiao, Fangxin Fang, Rajesh Govindan, Christopher C Pain, and Yike Guo. Model identification of reduced order fluid dynamics systems using deep learning. *International Journal for Numerical Methods in Fluids*, 86(4):255–268, 2018.
- [145] Jan S Hesthaven and Stefano Ubbiali. Non-intrusive reduced order modeling of nonlinear problems using neural networks. *Journal of Computational Physics*, 363:55–78, 2018.
- [146] Zhen Gao, Qing Liu, Jan S Hesthaven, Baoshan Wang, Wai S Don, and Xiao Wen. Non-intrusive reduced order modeling of convection dominated flows using artificial neural networks with application to rayleigh-taylor instability.
- [147] Arvind Mohan, Don Daniel, Michael Chertkov, and Daniel Livescu. Compressed convolutional lstm: An efficient deep learning framework to model high fidelity 3d turbulence. *arXiv preprint arXiv:1903.00033*, 2019.
- [148] Lawrence Sirovich. Method of snapshots. *Quarterly of Applied Mathematics*, 45(3):561–571, 1987.
- [149] Gaël Guennebaud, Benoît Jacob, et al. Eigen v3. <http://eigen.tuxfamily.org>, 2010.
- [150] Robert M Gray et al. Toeplitz and circulant matrices: A review. *Foundations and Trends[®] in Communications and Information Theory*, 2(3):155–239, 2006.
- [151] J Wise. The autocorrelation function and the spectral density function. *Biometrika*, 42(1/2):151–159, 1955.

Bibliography

- [152] Matan Gavish and David L Donoho. The optimal hard threshold for singular values is $4/\sqrt{3}$. *IEEE Transactions on Information Theory*, 60(8):5040–5053, 2014.
- [153] Jonathan C Carr, Richard K Beatson, Jon B Cherrie, Tim J Mitchell, W Richard Fright, Bruce C McCallum, and Tim R Evans. Reconstruction and representation of 3d objects with radial basis functions. In *Proceedings of the 28th annual conference on Computer graphics and interactive techniques*, pages 67–76. ACM, 2001.
- [154] Christopher L Rumsey, Thomas B Gatski, Susan X Ying, and Arild Bertelrud. Prediction of high-lift flows using turbulent closure models. *AIAA journal*, 36(5):765–774, 1998.
- [155] Thomas D Economon, Francisco Palacios, Sean R Copeland, Trent W Lukaczyk, and Juan J Alonso. Su2: An open-source suite for multiphysics simulation and design. *AIAA Journal*, 54(3):828–846, 2015.
- [156] Florian R Menter. Improved two-equation k-omega turbulence models for aerodynamic flows. *NASA Technical Memorandum*, 103975, 1992.
- [157] Erik Adler Christensen, Morten Brøns, and Jens Nørkær Sørensen. Evaluation of proper orthogonal decomposition–based decomposition techniques applied to parameter-dependent nonturbulent flows. *SIAM Journal on Scientific Computing*, 21(4):1419–1434, 1999.
- [158] Christopher L Rumsey, JP Slotnick, M Long, RA Stuever, and TR Wayman. Summary of the first aiaa CFD high-lift prediction workshop. *Journal of Aircraft*, 48(6):2068–2079, 2011.
- [159] Gilles Tissot, Laurent Cordier, Nicolas Benard, and Bernd R Noack. Model reduction using Dynamic Mode Decomposition. *Comptes Rendus Mécanique*, 342(6-7):410–416, 2014.

Bibliography

- [160] Jiaqing Kou and Weiwei Zhang. An improved criterion to select dominant modes from dynamic mode decomposition. *European Journal of Mechanics-B/Fluids*, 62:109–129, 2017.
- [161] Kevin K Chen, Jonathan H Tu, and Clarence W Rowley. Variants of Dynamic Mode Decomposition: boundary condition, koopman, and fourier analyses. *Journal of Nonlinear Science*, 22(6):887–915, 2012.
- [162] Travis Askham and J Nathan Kutz. Variable projection methods for an optimized dynamic mode decomposition. *SIAM Journal on Applied Dynamical Systems*, 17(1):380–416, 2018.
- [163] Ioannis W Kokkinakis and Dimitris Drikakis. Implicit large eddy simulation of weakly-compressible turbulent channel flow. *Computer Methods in Applied Mechanics and Engineering*, 287:229 – 261, 2015. ISSN 0045-7825. doi: 10.1016/j.cma.2015.01.016. URL <http://www.sciencedirect.com/science/article/pii/S0045782515000365>.
- [164] Xiaohua Wu, Parviz Moin, and Jean-Pierre Hickey. Boundary layer bypass transition. *Physics of Fluids*, 26(9):091104, 2014. doi: 10.1063/1.4893454. URL <https://doi.org/10.1063/1.4893454>.
- [165] Thierry Braconnier, Marc Ferrier, J Christophe Jouhaud, Marc Montagnac, and Pierre Sagaut. Towards an adaptive pod/svd surrogate model for aeronautic design. *Computers & Fluids*, 40(1):195–209, 2011.
- [166] Marco Fossati. Evaluation of aerodynamic loads via reduced-order methodology. *AIAA Journal*, 53(8):2389–2405, 2015.
- [167] Jian Yu, Chao Yan, Zhenhua Jiang, Wu Yuan, and Shusheng Chen. Adaptive non-intrusive reduced order modeling for compressible flows. *Journal of Computational Physics*, 397:108855, 2019.
- [168] Qiang Du, Vance Faber, and Max Gunzburger. Centroidal voronoi tessellations: Applications and algorithms. *SIAM review*, 41(4):637–676, 1999.

Bibliography

- [169] Jerome Sacks, William J Welch, Toby J Mitchell, and Henry P Wynn. Design and analysis of computer experiments. *Statistical science*, pages 409–423, 1989.
- [170] Alexander Forrester, Andras Sobester, and Andy Keane. *Engineering design via surrogate modelling: a practical guide*. John Wiley & Sons, 2008.
- [171] Michal Rewienski and Jacob White. A trajectory piecewise-linear approach to model order reduction and fast simulation of nonlinear circuits and micromachined devices. *IEEE Transactions on computer-aided design of integrated circuits and systems*, 22(2):155–170, 2003.
- [172] Michał Rewieński and Jacob White. Model order reduction for nonlinear dynamical systems based on trajectory piecewise-linear approximations. *Linear algebra and its applications*, 415(2-3):426–454, 2006.
- [173] Kyle Washabaugh, David Amsallem, Matthew Zahr, and Charbel Farhat. Nonlinear model reduction for cfd problems using local reduced-order bases. In *42nd AIAA Fluid Dynamics Conference and Exhibit*, page 2686, 2012.
- [174] Zhao Zhan, Wagdi G Habashi, and Marco Fossati. Local reduced-order modeling and iterative sampling for parametric analyses of aero-icing problems. *AIAA Journal*, 53(8):2174–2185, 2015.
- [175] David Amsallem, Matthew J Zahr, and Charbel Farhat. Nonlinear model order reduction based on local reduced-order bases. *International Journal for Numerical Methods in Engineering*, 92(10):891–916, 2012.
- [176] Omer San and Jeff Borggaard. Principal interval decomposition framework for pod reduced-order modeling of convective boussinesq flows. *International Journal for Numerical Methods in Fluids*, 78(1):37–62, 2015.
- [177] Kevin Carlberg. Adaptive h-refinement for reduced-order models. *International Journal for Numerical Methods in Engineering*, 102(5):1192–1210, 2015.

Bibliography

- [178] Philip A Etter and Kevin T Carlberg. Online adaptive basis refinement and compression for reduced-order models via vector-space sieving. *Computer Methods in Applied Mechanics and Engineering*, 364:112931, 2020.
- [179] Muruhan Rathinam and Linda R Petzold. A new look at proper orthogonal decomposition. *SIAM Journal on Numerical Analysis*, 41(5):1893–1925, 2003.
- [180] Chris Homescu, Linda R Petzold, and Radu Serban. Error estimation for reduced-order models of dynamical systems. *SIAM Journal on Numerical Analysis*, 43(4):1693–1714, 2005.
- [181] James P Fink and Werner C Rheinboldt. On the error behavior of the reduced basis technique for nonlinear finite element approximations. *ZAMM-Journal of Applied Mathematics and Mechanics/Zeitschrift für Angewandte Mathematik und Mechanik*, 63(1):21–28, 1983.
- [182] Bernard Haasdonk and Mario Ohlberger. Reduced basis method for finite volume approximations of parametrized linear evolution equations. *ESAIM: Mathematical Modelling and Numerical Analysis-Modélisation Mathématique et Analyse Numérique*, 42(2):277–302, 2008.
- [183] Kevin Carlberg, Youngsoo Choi, and Syuzanna Sargsyan. Conservative model reduction for finite-volume models. *Journal of Computational Physics*, 371:280–314, 2018.
- [184] Ralf Zimmermann and Sanne Goertz. Improved extrapolation of steady turbulent aerodynamics using a non-linear pod-based reduced order model. *Aeronautical Journal*, 116(1184):1079, 2012.
- [185] Michel Bergmann, C Henri Bruneau, and Angelo Iollo. Improvement of reduced order modeling based on pod. In *Computational fluid dynamics 2008*, pages 779–784. Springer, 2009.
- [186] Hrvoje Jasak. Error analysis and estimation for the finite volume method with applications to fluid flows. 1996.

Bibliography

- [187] Francisco Palacios, Juan Alonso, Karthikeyan Duraisamy, Michael Colonna, Jason Hicken, Aniket Aranake, Alejandro Campos, Sean Copeland, Thomas Economon, Amrita Lonkar, et al. Stanford university unstructured (su 2): an open-source integrated computational environment for multi-physics simulation and design. In *51st AIAA aerospace sciences meeting including the new horizons forum and aerospace exposition*, page 287, 2013.
- [188] Alejandro Allendes, Gabriel R Barrenechea, and Richard Rankin. Fully computable error estimation of a nonlinear, positivity-preserving discretization of the convection-diffusion-reaction equation. *SIAM Journal on Scientific Computing*, 39(5):A1903–A1927, 2017.
- [189] Julio Chu and James M Luckring. *Experimental surface pressure data obtained on 65 delta wing across Reynolds number and Mach number ranges*. National Aeronautics and Space Administration, Langley Research Center, 1996.
- [190] Jungchang Lin and Donald Rockwell. Transient structure of vortex breakdown on a delta wing. *AIAA Journal*, 33(1):6–12, 1995.
- [191] Anand Kumar. On the structure of vortex breakdown on a delta wing. *Proceedings of the Royal Society of London. Series A: Mathematical, Physical and Engineering Sciences*, 454(1968):89–110, 1998.